ABSTRACT

In recent years, electromagnetic compatibility (EMC) problems associated with high frequency and high speed interconnects are becoming of increasing concern. Coaxial cables are a popular form of interconnect. In this thesis, the crosstalk coupling between two parallel coaxial cables in free space and above a ground plane is investigated. The degree of coupling is usually formulated analytically in the frequency domain. In this thesis, a method for time domain simulation is proposed using the TLM technique. Results are compared with frequency domain solutions and experimental results. Also; the standard model has been improved by including the skin depth effect in the coaxial cable braid.

The crosstalk between the two coaxial cables is observed through the induced voltages on the loads of the adjacent cable, which is deemed to be the usual measureable form of cable coupling. The equivalent circuit developed for the coupling path of two coaxial cables in free space takes account of the differential mode (DM) current travelling in the braids of the cables. As for the coupling path of the cables via a ground plane, the equivalent circuit is developed based on the flow of differential mode (DM) and common mode (CM) currents in the braid, where the coaxial braid's transfer impedance is modelled using Kley's model.

The radiated electric (E) field from the coaxial cable above a ground plane is also deduced from the predicted cable sheath current distribution and by the Hertzian dipoles' approach. Results are validated against the radiated electric field of a single copper wire above ground. Both the simulated and experimental results are presented in the time and frequency domains and good agreement is observed thus validating the accuracy of the model.

LIST OF PUBLICATIONS

[1] Y. X. Teo, D. W. P. Thomas and C. Christopoulos, "The effects of end plates on coaxial cable coupling," Proceedings of PIERS 2012, Kuala Lumpur, Malaysia, 27th – 30th March 2012, pp. 15.

[2] Yu Teo, D. W. P. Thomas and Christos Christopoulos, "Time-domain simulation of crosstalk between coaxial cables," Asia-Pacific Intl. Symposium and Exhibition on EMC: APEMC 2013, Melbourne, Australia, 20th – 23rd May 2013, pp. 189 – 192.

[3] Yu Xian Teo, D. W. P. Thomas and C. Christopoulos, "A time domain numerical model for crosstalk between coaxial cables including skin depth effects," IEEE Trans. on EMC. – Submitted.

[4] Yu Xian Teo, Jin Meng, D. W. P. Thomas and C. Christopoulos, "Predicted electromagnetic fields radiated by cables from time domain models," IEEE Trans. on EMC. – To be submitted.

[5] Jin Meng, Yu Xian Teo, D. W. P. Thomas and Christos Christopoulos, "Fast prediction of transmission line radiated emissions using the Hertzian dipole method and line-end discontinuities models," IEEE on EMC. – Accepted.

ACKNOWLEDGEMENTS

First and foremost, I would like to extend my deepest gratitude to both my supervisors, Professor D. W. P. Thomas and Professor C. Christopoulos for their endless guidance and support throughout the period of my research degree. I am also grateful to them for their tireless effort in emptying their busy schedules to provide answers and to help with my many questions. This thesis would not have been completed without their immeasurable contributions.

I would also like to extend my appreciation to my colleagues at the School of Electrical and Electronic Engineering for the friendships and support we shared. A special mention to Dr. John Paul for his many helpful experimental ideas and suggestions. Also, a special thanks to Professor Jin Meng from the Naval University of Engineering, Wuhan, China, for his endless assistance in the collaboration project for our department.

On a more personal note, I wish to thank my dear friends scattered all over the world, for putting up with my endless rambling and consistent procrastination to work on my research. Not to mention the countless times of wondering if I was still sane while talking to myself.

Last but not least, this thesis is dedicated to my family members, especially my parents, who have showered me with blessings and love, providing me the very foundation for me in completing this thesis. The countless encouragement I received gave me a reason to follow through the hardships I encounter along the way and therefore, I am truly grateful.

LIST OF SYMBOLS

The following symbols are used throughout this thesis:

b	hole width
c	speed of light
d	wire diameter
e	number of carriers
f	frequency
h	height of cable
h_r	radial spindle separation
j	$\sqrt{-1}$
k	time step (iteration) number
l	lay length
n	node (iteration) number
s	separation between cables
t	time
z	Z transform variable
B	magnetic flux density
C	capacitance
C_d	line capacitance
C_m	mutual capacitance
C_S	self capacitance
C_{td}	tertiary circuit capacitance
D_0	outer diameter of dielectric
D_m	mean braid diameter
E	electric field
E_{rad}	radiated electric field
G	conductance
H	magnetic field
I	current
I_S	source circuit current
I_t	tertiary circuit current
I_V	victim circuit current
L	inductance
L_d	line inductance
L_S	self inductance
L_{td}	tertiary circuit inductance
M	mutual inductance
N	number of wires in each carrier
P	number of carrier crossings per unit length
Q	charge carried by pulses
R	resistance

R_L	source circuit terminated resistance
R_S	source resistance
R_{0L}	victim circuit terminated resistance
R_{VL}	victim circuit terminated resistance
V	voltage
V_S	source voltage
VR	voltage to the right
VL	voltage to the left
Y_T	transfer admittance
Z	line characteristic impedance
Z_C	tertiary circuit characteristic impedance
Z_P	end plate impedance (differential mode)
Z_{ts}, Z_{tv}	end plate impedance (common mode)
Z_T	transfer impedance
α	braid angle
δ	skin depth
λ	wavelength
μ_0	permeability of free space
μ_r	relative permeability
ε_0	permittivity of free space
ε_r	relative permittivity
σ	conductivity
ω	angular frequency
Δf	frequency step (df)
Δl	space step (dl)
Δt	time step (dt)
Δx	node spacing in x-direction (dx)
Δy	node spacing in y-direction (dy)
Δz	node spacing in z-direction (dz)

Additional symbols are used to clarify such quantities as certain line parameters, voltages and currents. These symbols are generally defined where they are used in their respective sections.

Prefixes

A subscript prefix $_k$ is used to denote the time step (iteration) number.

A subscript prefix $_n$ is used to denote the node (iteration) number.

Suffixes

The following superscript suffixes are used:

^{i} pulse incident upon a node

^{r} pulse scattered from a node

Subscript suffixes are often used to denote a direction. In the case of a multiple character suffix, the last character gives the function of the symbol while the first character gives the direction of the function of the symbol.

Accents

The $\vec{\ }$ symbol is used to denote a vector quantity.

The $\tilde{\ }$ symbol is used to denote a Fourier Transformed quantity

TABLE OF CONTENTS

CHAPTER 1

INTRODUCTION

1.1 Electromagnetic Compatibility

Since the early days of radio and telegraph communications, there have been sources of electromagnetic interference from electronic devices [1.5]. These particular electromagnetic waves inevitably cause interference which might cause other systems to fail. Electromagnetic interference is concerned with a wide variety of systems ranging from the human body to large electrical power systems, such as the national grid, which are subject to interference as diverse as lightning, electrostatic discharge, radio and television transmissions etc. Numerous other sources of electromagnetic emissions such as DC electric motors and fluorescent lights also generate interference virtually in all equipment powered by electrical supplies. The subject of electromagnetic compatibility (EMC) is the branch of science and engineering concerned with the ability of systems to function correctly in their electromagnetic (EM) environment, making them immune to certain amounts of electromagnetic interference (EMI), while at the same time keeping the interference they generate within specified limits [1.2]. Subject areas within the EMC field include coupling to and from external fields or within equipment design, emission tests such as radiation from cables and other current carrying conductors; and susceptibility tests. This thesis is concerned with the various electromagnetic emissions from one current carrying conductor coupled onto another.

Interest in EMC is largely associated with military, aircraft and other heavy machinery systems and limits were initially set for radio interference for commercial and domestic EMC purposes [1.1]. However, due to the rapid increase in the use of radio communications, digital systems, fast processors and the introduction of new design practices, the sensitivity and susceptibility limits were established. The study of EMC in all systems eventually became more important.

For example, a strong transmission from a FM radio station or TV station may be picked up by a digital computer. The received transmission then interferes with the data or control signals resulting in incorrect function of the device. Conversely, a digital computer may create emissions that couple into a TV, causing interference [1.5]. Thus, in the design of electronic systems, it is crucial to minimise the interference from and into the particular equipment. EMC compliance is required for all types of electrical and electronic equipments during design, development, production, installation and operational phases. On 3rd May 1989, the EEC adopted a directive on EMC: electrical and electronic equipments brought on to the market must, by 1st January 1992, meet certain EMC requirements (emission and immunity limits) [1.3].

EMC problems can be divided into a number of issues such as EMI, Crosstalk, Susceptibility and Emission. Due to EMC disturbances, the equipment will generally be surrounded by some form of metallic enclosure, or shield, which contains apertures through which EM radiation can penetrate and couple into circuits within the equipment. The susceptibility to EMI is partly determined by the strength of signals coupled into the equipment. The relative strength of the penetrating field is known as the shielding effectiveness. The effectiveness of a shield can be viewed as being the ratio of the magnitude of the electric (magnetic) field that is incident on the barrier to the magnitude of the electric (magnetic) field that is transmitted to the barrier and is computed in units of dB, given by:

$$SE = 20 \log \frac{E_i}{E_t} \text{ ; in dB} \qquad (1.1)$$

where E_i represents a field incident on one side of a shielding layer and E_t represents the field on the other side.

Shielding effectiveness, ideally, should be of the order of hundred dB. For example, a shielding effectiveness of 100dB means that the incident field has been reduced by a factor of 100k as it exits the shield. In order to realise an ideal shielding effectiveness, the shield must completely enclose the electronics and must have no penetrations such as holes, seams, slots or cables. Any penetrations in a shield unless properly treated, may drastically reduce the effectiveness of the shield; therefore, generating EMI such as the crosstalk, onto surrounding devices.

1.2 A Review of Coaxial Cable Coupling

Many installations use coaxial cables to transmit signal from one device to another. Unless a solid homogeneous tube is superconductive, it possesses finite impedance, resulting in a non-zero external longitudinal electric field intensity produced by the current in the tube [1.8]. Since the shield in coaxial lines is not ideal, a leakage of the electric and magnetic fields contained within the area enclosed by the outer conductor is inevitable, thus electromagnetically affecting external conductors in close proximity. The transfer impedance of the braided shield cables can be accurately determined; hence the primary objective in validating such phenomenon is to develop the equivalent circuit for the corresponding system. Quantitative estimates of the screening performances are determined by developing a general coupling model for the crosstalk between braided coaxial cables, using circuit-based approach that employs distributed parameters [1.16]. The specific feature of crosstalk study of shielded cables in a wide frequency band is that, while the propagation regime in the dielectric remains quasistatic, the shield works in the wave propagation regime in conductors [1.7]. Mohr [1.27] states that when the coupled interference is determined solely on the basis of magnetic coupling, it is shown that the interference is dependent only on the character of the current in the source line. Many different analytical approaches [1.10], [1.11] and [1.16] – [1.32] were developed to model the crosstalk between two coaxial cables. Paul [1.9] theoretically explains that the coupling system of two current carrying conductors in general can be modelled by deriving the transmission line equations from a representation of the line as lumped circuit elements distributed along the line using three methods:

- From the integral forms of Maxwell's equations.
- From the differential forms of Maxwell's equations.
- From the usual distributed parameter, per-unit-length equivalent circuit.

Paul's theory [1.9] works basically for ideal situations by assuming that the two conductors are perfect cylindrical conductors. The only approximate realistic manner of this system is adjusted by including the per-unit length resistive loss in series with the inductive element. Nonetheless, the per-unit-length parameters, ie: inductance, capacitance and conductance, theoretically derived by Paul [1.9] can be implemented into the cable coupling system (see Chapter 2, sections 2.3.1 and 2.3.2).

Some of the earliest researches done on this subject were carried out by Bell System Technologies on the crosstalk between coaxial telephone lines [1.12] – [1.15]. Schelkunoff and Oradenko [1.12] derived analytical formulas to model the crosstalk of the said system in free space. The effects of the braid's transfer admittance on the crosstalk analysis were studied extensively by Sali [1.6] and [1.16]; by using an optimized (HLE-45) and a standard (URM-43) coaxial cable. Kley [1.18]; and Badr et al. [1.17] confirmed the accuracy of Sali's [1.6] and [1.16] formulation through experimental measurements in the frequency domain, proving that the inclusion of the transfer admittance is not necessary for optimized cable braids as it has negligible effects (described in detail in Chapter 2, section 2.2).

A further development of coupling between shielded cables above a common metallic ground plane was introduced by Mohr [1.27] using 4 different configurations, ie: open-to-open, shielded-to-open, open-to-shielded; and shielded-to-shielded wire coupling. However, the use of a lumped circuit model limited his work to low frequencies for which the cables are shorter when compared with a quarter of its wavelength [1.17]. Ellinas [1.26] confirmed Mohr's [1.27] analytical study under the boundary condition of a short circuited outer sheaths of the cables (tertiary circuit). The major part of Ellinas' [1.26] contribution was the development of the crosstalk analysis at high frequencies. A modification to Mohr's [1.27] analysis was also done by taking into account a finite resistance of the metallic ground plane.

The concept of tertiary circuit is analytically studied by Schelkunoff and Odarenko [1.12]; and Tsalovich [1.8]. This coupling mechanism is applied for both cases of the coupling system mentioned, and is shown in Figure 1.2.1.

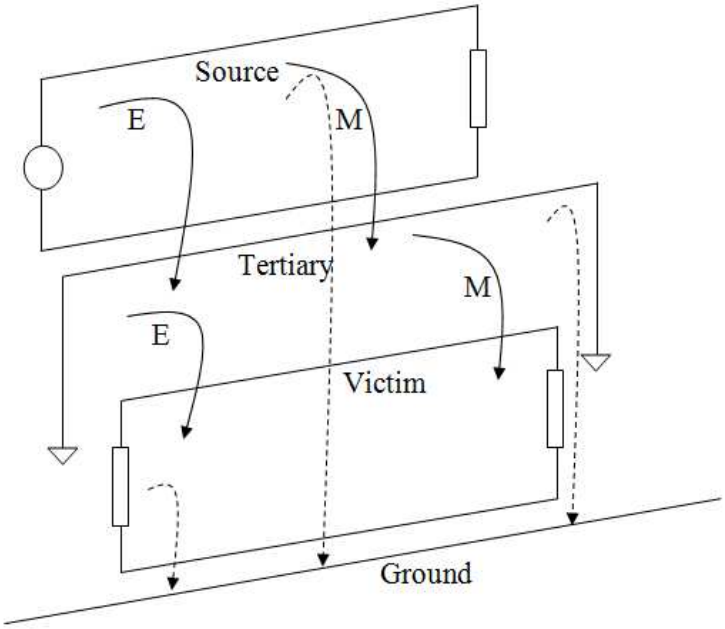

Figure 1.2.1: The concept of tertiary circuit illustrated by Tsalovich [1.8]

Schelkunoff and Odarenko [1.12] explain that a source line does not directly affects a given victim line but also other circuits, if present. The signal from the source line is instead transferred through the additional circuitry, and finally to the victim line. Numerical analyses widely used which apply the same concept are Thomas et al. [1.10]; Badr et al. [1.17], [1.22] and [1.25]; and Sali [1.6], [1.16] and [1.33].

1.3 Relevance of the Thesis

In practical situations such as aircraft, automotive and heavy machinery; large amounts of cables are used, inevitably causing large amount of coupling. This thesis is specifically concerned with the importance of time domain modelling of multiconductor lines (mainly coaxial cables) and its radiated field emissions, where few researchers have explored. It is therefore evident to describe time domain results showing time domain effects such as jitter and general signal integrity. This thesis also shows improvement in the accuracy of crosstalk in multiconductor lines associated with several aspects where previous work has failed to explain. While most work discussed with relevance to the cables itself, this work has successfully proved the importance of the cables' connections and terminations (vertical supports) and its effects in detail. The accuracy of the coupling effects are further improved when time

domain skin effect is implemented in the coaxial cable braids, where this loss factor is often ignored.

1.4 Overview

The purpose of this section is to describe the structure of the work presented in the following chapters. The work can be divided into two parts: the theoretical derivation of the numerical model simulations and experimental measurements of the system. Results are presented throughout to illustrate specific points but the major results for the total coupling effect in the system have been compiled in **Chapter 5**.

Chapter 2 reviews the theory in detail behind different techniques modelling the surface transfer impedance of a coaxial cable and also coupling configuration between coaxial cables via a tertiary circuit, including their per-unit length parameters used in this work:

- Coupling between two coaxial cables in free space
- Coupling between two coaxial cables via a perfect ground plane

Chapter 3 is concerned with the crosstalk experimental measurements of the two coupling configurations in **Chapter 2**. Experimental arrangement using RG-58 coaxial cables and the utilized equipments are described in detail. Experimental measurements are carried out and presented to describe the impact of end plates on coupling.

Chapter 4 reviews the theory of the 1-Dimensional TLM models and presents the implementation techniques for the two coupling configurations used in the numerical model. Results comparing numerical predictions and experimental measurements are presented both in time and frequency domains. Results are compared between the numerical predictions and measurements, showing the effects of a lossless tertiary circuit against the effects of the vertical supports (brass end plates).

Chapter 5 describes a feature not normally included in published studies of the characterization of the tertiary circuit, namely the skin depth. It presents the analysis of two different techniques to model the skin depth in the time domain together with

its implementation into the tertiary circuit model. Results are compared between numerical predictions against measurements, showing the effects of skin depth effect for all configurations presented in this research work.

Chapter 6 is concerned with the radiated electromagnetic field analysis. The experimental arrangement of the antenna and the cable in a screened room is described. It also presents a comparison between the numerical predictions and experimental measurement of the radiated interference for two different configuration systems:

- A simple bare wire above a perfect ground plane
- A single coaxial cable above a perfect ground plane

Chapter 7 presents the conclusions of this research work and possible future research is discussed.

The main achievement of this research in the modelling of interconnects can be summarised below:

1. Time domain modelling of coaxial cable coupling.
2. The inclusion of cable termination effects (ie: brass end plates).
3. The loss factor; specifically due to the skin effect, included in the tertiary circuit and modelled in the time domain showing significant impact.
4. Time domain simulation validated against time domain measurements and through Fourier transform of the results validated against frequency domain measurements.
5. Technique for predicting radiated fields in the time domain using the Hertzian dipole approach developed for coaxial cables and validated against frequency domain measurements after Fourier transforming the time domain data.

References

[1.1] A. C. Marvin, "New developments in EMC education," Proc. of the 10th Intl. Zurich Symposium on EMC, March 1993, pp. 403 – 406.

[1.2] Christopoulos, C, Principles and Techniques of Electromagnetic Compatibility, second edition, CRC Press, Taylor & Francis Group, 2007.

[1.3] Jasper Goedbloed, Electromagnetic Compatibility, Philips Research Laboratories, Eindhoven, Prentice Hall International (UK) Ltd, 1992.

[1.4] John D. Kraus, Electromagnetics, Fourth Edition, McGraw-Hill, Inc, 1991.

[1.5] Clayton R. Paul, Introduction to Electromagnetic Compatibility, Wiley Series in Microwave and Optical Engineering, 1992.

[1.6] S. Sali, F.A. Benson and J.E. Sitch, "General crosstalk equations between two braided coaxial cables in free space," IEE Proceedings, vol. 130, pt. a, no. 6, September 1983.

[1.7] Christopoulos, C., Principles and Techniques of Electromagnetic Compatibility, second edition, CRC Press, Taylor & Francis Group, 2007.

[1.8] Anatoly Tsaliovich, Cable Shielding for Electromagnetic Compatibility, Van Nostrand Reinhold, 1995.

[1.9] Clayton R. Paul, Analysis of Multiconductor Transmission Lines, John Wiley & Sons, Inc, 1994.

[1.10] D. W. P. Thomas, C. Christopoulos, F. Leferink and H. Bergsma, "Practical measure of cable coupling," Intl. Conf. on Electromagnetics in Advanced Applications, September 2009, pp. 803 – 806.

[1.11] E. F. Vance, Coupling to Shielded Cables, Pub. A Wiley, 1978.

[1.12] S. A. Schelkunoff and T. M. Odarenko, "Crosstalk between coaxial transmission lines," Bell Syst. Tech. J., 1937, 26, pp. 144 – 164.

[1.13] J. C. Isaacs, Jr. and N. A. Strakhov, "Crosstalk in uniformly coupled lossy transmission lines," Bell Syst. Tech. J., January 1973, pp. 101 – 115.

[1.14] R. P. Booth and T. M. Odarenko, "Crosstalk between conductors in cable," Ibid., 1940, 19, pp. 358 – 384.

[1.15] K. E. Gould, "Crosstalk in coaxial cables – analysis based on short-circuited and open tertiaries," Ibid., 1940, 19, pp. 341 – 357.

[1.16] S. Sali, "A circuit-based approach for crosstalk between coaxial cables with optimum braided shields," IEEE Transactions on EMC, vol. 35, no. 2, May 1993.

[1.17] A. H. Badr, Prof. F.A. Benson and J. E. Stitch, "Interference between braided coaxial cables," IEE Proceedings, vol. 128, no. 5, July 1981, pp. 347 – 353.

[1.18] Thomas Kley, "Optimized single-braided cable shields," IEEE Transactions on Electromagnetic Compatibility, vol. 35, no. 1, February 1993.

[1.19] S. Sali, Prof. F.A. Benson and J.E. Sitch, "Coupling in a dielectric-coated multicoaxial-cable system, an analysis based on a quasi-tem model," IEE Proceedings, vol. 131, no. 1, January 1984.

[1.20] C. Smartt, S. Greedy, D.W.P. Thomas, C. Christopoulos, P. Sewell, "Modelling and measurement of crosstalk between shielded cables," EMC-Europe, Wroclaw, 2010.

[1.21] Clayton R. Paul, "Computation of crosstalk in a multiconductor transmission line," IEEE Transactions on EMC, vol. EMC-23, no. 4, November 1981.

[1.22] A. H. Badr, Prof. F.A. Benson and J.E. Sitch, "Coupling between a pair of coaxial cables in a multicable system," IEE Proc, vol. 128, pt. A, no.8, November 1981, pp. 547 – 551.

[1.23] S. Sali, F. A. Benson and J. E. Sitch, "Coupling between multicoaxial systems – I General considerations and efficient numerical method for crosstalk," IEE Proc., vol. 129, pt. A, no. 3, May 1982, pp. 162 – 166.

[1.24] S. Sali, F. A. Benson and J. E. Sitch, "Coupling between multicoaxial systems – II Theoretical predictions of crosstalk and experimental results," IEE Proc., vol. 129, pt. A, no. 3, May 1982, pp. 167 – 171.

[1.25] A. H. Badr, Prof. F.A. Benson and J.E. Sitch, "Coupling between coaxial cables over a ground place at low frequencies," IEE Proc. vol. 127, pt. A, no. 8, November 1980.

[1.26] John N. Ellinas, "Coupling between braided coaxial cables over a ground plane," Dept. Of Computer Engineering, TEI of Pireaus, P. Ralli & Thivon 250, Athens, Greece.

[1.27] R. J. Mohr, "Coupling between open and shielded wire lines over a ground plane," IEEE Transactions on EMC, vol. EMC-9, no. 2, September 1967.

[1.28] C. J. Smartt, S. Greedy, D.W.P. Thomas, C. Christopoulos and P. Sewell, "Shielded cable model development for time domain CEM techniques," IET 8th Intl. Conf. on Computation in EMC (CEM 2011), April 2011, pp. 1 – 2.

[1.29] A. S. De C. Fernandes, "Propagation characteristics of a loose braid coaxial cable in free space," The Radio and Electronic Engineer, vol. 49, no. 5, pp. 255-260, May 1979.

[1.30] J. M. Tealby, P. A. Cudd and Prof. F. A. Benson, "Coupling between jacketed braided coaxial cables," IEE Proceedings, vol. 134, pt. A, no. 10, Dec. 1987.

[1.31] C. Gordon, "Time-domain simulation of multiconductor transmission lines with frequency-dependent losses," IEEE Proc. Intl. Conf. on Computer Design: VLSI in Computers and Processors, Oct. 1992, pp. 222 – 228.

[1.32] Colin Gordon, Thomas Blazeck and Raj Mittra, "Time-domain simulation of multiconductor transmission lines with frequency-dependent losses," IEEE Transactions on Computer-Aided Design, vol. 11, no. 11, pp. 1372-1387, Nov. 1992.

[1.33] S. Sali, "Modal technique for the time domain analysis of crosstalk between coaxial cables," IEEE in Electronics and Communication Engineering Journal, vol. 1, no. 6, Nov. 1989, pp. 254 – 260.

CHAPTER 2

THEORY OF CABLE COUPLING

2.1 Coaxial Cables

The coaxial cable was invented in 1929 and first used commercially in 1941 [2.1]. AT&T established its first cross-continental coaxial transmission system in 1940 [2.1]. Depending on the carrier technology used together with other factors, the alternatives to the coaxial cable are the twisted pair copper wire and the optical fibre cables. Coaxial cable is the type of copper cable used by cable TV companies between the community antenna and user homes and businesses. It is sometimes used by telephone companies from their central office to telephone poles near users, and also widely installed for use in business and corporation such as Ethernet and other types of local area network. A coaxial cable comprises two conductors that share a common axis, an inner conductor (copper wire) and an outer cylindrical conductor, which is usually earthed and provides the return path. The outer conductor is usually braided (commonly copper material) to allow for a more flexible cable. It is used to carry various signals, ie radio signals and is an extremely popular form of interconnect in the rapidly developing electronics industry. Figure 2.1.1 shows the cross section area of a RG-58 coaxial cable.

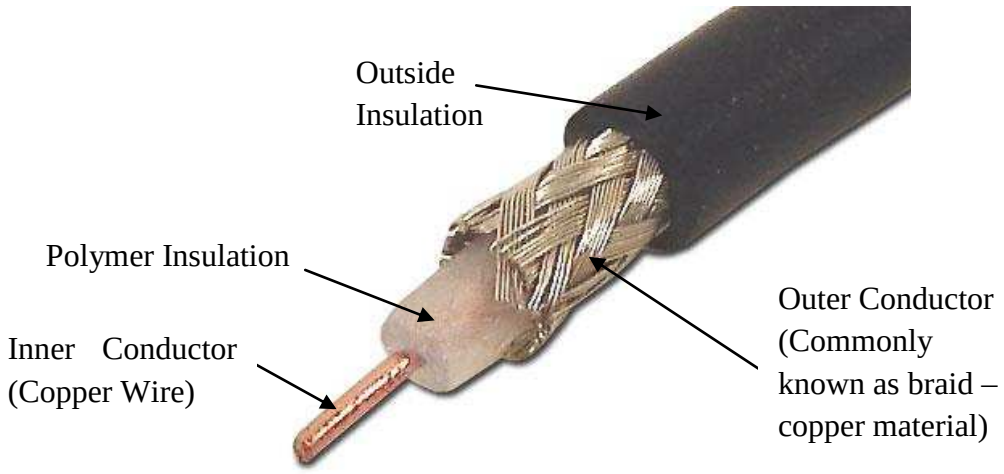

Figure 2.1.1: Cross section area of a RG-58 coaxial cable

2.2 Surface Transfer Impedance of Coaxial Cables

Coaxial cables are light and flexible but still possess a relatively high degree of shielding effectiveness. Systems connected to coaxial cables are not ideal. The outer conductor functions as a shield to reduce coupling of the signal into adjacent wiring. In general, the choice of cable type for a particular application is a compromise between various aspects, such as cost, diameter, weight, flexibility, RF losses and shielding [2.2]. The factors affecting these parameters include the structure of the inner and outer conductor, dielectric insulation layer and the sheath of the cable. More shield coverage means less radiation of energy. However, it does not necessarily mean less signal attenuation. The terms 'shielding' and 'screening' of a coaxial system is often used. It concerns mainly with the leakage from the woven characteristics of the braid. This leakage of energy into the coaxial cable when the exterior of the braided shield is subjected to interference of an electromagnetic field is described by Sali et al. in [2.3]. The penetration of such energy depends on the frequency of the incident source (wave or signal pulses). The penetration of energy into the braid at low frequencies is due to the diffusion of energy of the electromagnetic field whereas at high frequencies, the penetrations are due to:

- Electric coupling parameters causing the penetration of electric field (Transfer Admittance)
- Magnetic coupling parameters causing the penetration of magnetic field (Transfer Impedance) [2.3]

The penetration of the magnetic field may be modelled by the concept of surface transfer impedance per unit length, Z_T, which essentially behaves like an inductive reactance at high frequencies [2.3]. The term surface transfer impedance was used in the literature as long ago as the 1930s, and one of the first authors to define it was Schelkunoff [2.5]. Cable shields are important in overall system performance as they can be of significant length and can run through electromagnetically hostile environments. The basic general concept of a cable shield's surface transfer impedance is explained in [2.4]. For example, consider a cylindrical shield of a cable with thickness, D, as shown in Figure 2.2.1.

(a)

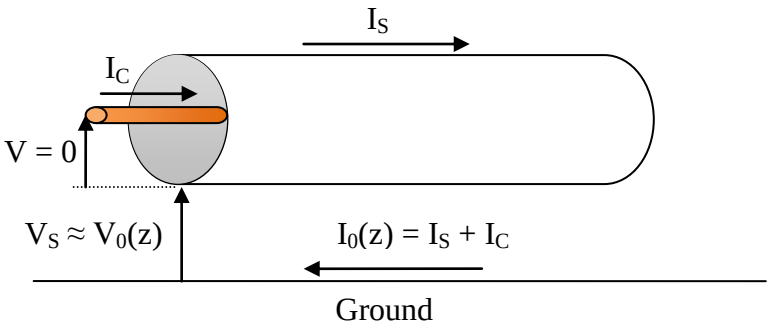

(b)

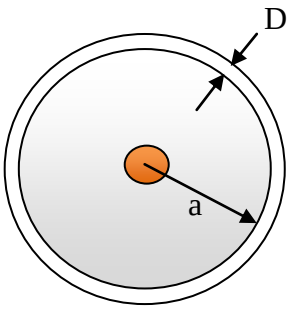

Figure 2.2.1: Configuration used to calculate transfer impedance (a) Currents and voltages for a shielded cable analysis. (b) A cross section area of a cylindrical shield with radius a

The transfer impedance of the shield is one measure of the effectiveness of the shield and in its most general form the transfer impedance can be defined as:

$$Z_T = \frac{1}{I_0}\frac{dV}{dz} \tag{2. 1}$$

where I_0 is the total current flowing in the shield and $\frac{dV}{dz}$ is the change in open circuit voltage generated by this current along the transmission line formed by the shield and the conductors enclosed by the shield [2.11]. Metal braided shields allow the penetration of electromagnetic field through holes, cracks, etc. and are characterised by mutual-coupling components as well as the diffusion components. This is illustrated in Figure 2.2.2 [2.11].

(a)

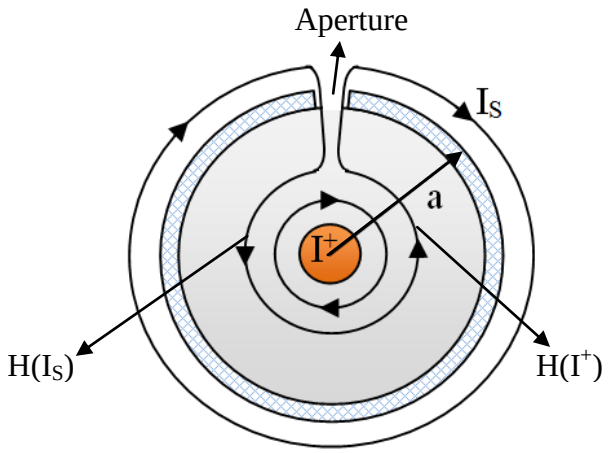

(b)

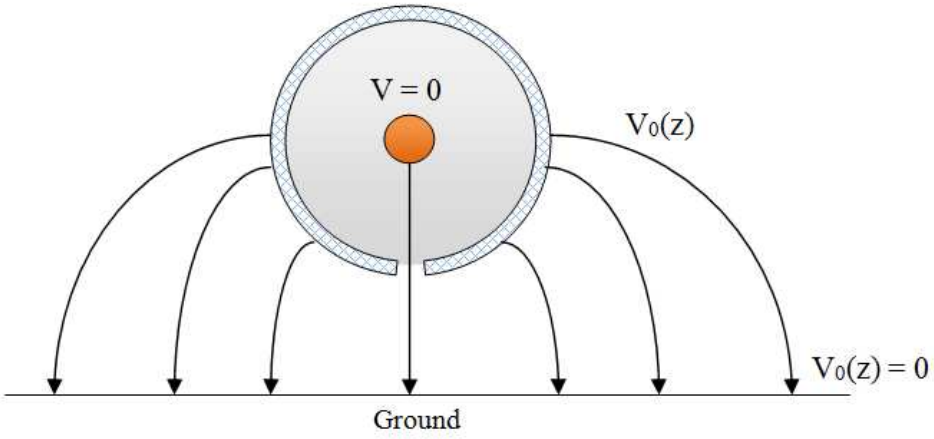

Figure 2.2.2: Penetration of electromagnetic fields through the apertures of the *cable's braided shield through (a) Magnetic coupling. (b) Electric coupling* [2.11].

In addition to the diffusion of energy due to magnetic field at high frequencies, the electric coupling produced by an electric field, which would otherwise terminate on the outer surface of the shield, penetrate through the holes in the shield and terminating on the inner conductor. The penetrating of this electric field may be represented by the concept of transfer admittance, Y_T, between the inner conductor and the return path for the shield, which essentially behaves like a capacitive reactance at high frequencies. As implied in Figure 2.2.2, the effects of electric coupling requires that the external circuit of the shield current be considered, as well as the internal circuit of the shielded conductor. In its most general form, the transfer admittance can be defined as:

$$Y_T = \frac{1}{V_0}\frac{dI_0}{dz} \tag{2. 2}$$

where V_0 denotes the voltage between the shield and the return path for the shield current. $\frac{dI_0}{dz}$ defines the change in short circuit internal circuit current along the shield per unit length [2.11]. The analogy of the derivation of the transfer admittance gives rise to the equivalent electric dipole developed by Kaden [2.6] and Marcuvitz [2.7]. This derivation is associated with the assumption, where the hole and charge from the outer shield from the return path is induced into the inner conductor by this dipole. This analysis yields a mutual capacitance, C_{12}, between the inner conductor and the return path of the shield. Therefore, the mutual coupling of the transfer impedance, Z_T, and transfer admittance, Y_T, is expressed by the mutual inductance, M_{12}, and mutual capacitance, C_{12}, caused by the apertures between the inner conductor and the external circuits enclosed by the shield, giving [2.6], [2.7]:

$$C_{12} = v\frac{pC_1C_2}{4\pi^2a^2\varepsilon} \tag{2. 3}$$

$$M_{12} = v\frac{\mu_0 m}{4\pi^2a^2} \tag{2. 4}$$

where a denotes the outer shield radius; μ and ε denotes the permeability and permittivity of the internal polymer insulation respectively; and v denotes the number of identical apertures per unit length of the shield. p and m represent the electric and magnetic polarization of the apertures respectively. C_1 is the capacitance per unit length between the internal conductors and the shield while C_2 is the capacitance per unit length between the outer shield and the shield's return path. The assumption made for equations (2.3) and (2.4) to be valid is that the dimensions of the apertures are far smaller than the outer shield radius, a, and the wavelength of the current path, λ.

Many improvements to the models for transfer impedance and transfer admittance of the braid have been proposed [2.5] – [2.17], which serve as the usual practical measure of the shielding properties of the shielded cables [2.8], [2.10] and [2.11]. This aspect will be discussed and compared further in this chapter. The best solution for the modelling of the geometrical properties in the braided shield is then selected to model the transfer impedance of the RG-58 coaxial cable.

2.2.1 Vance Model [2.11]

(a)

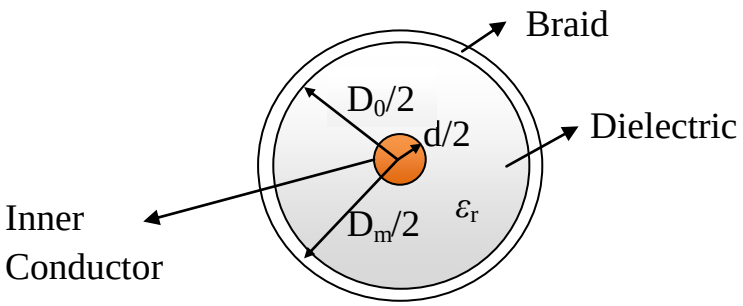

(b)

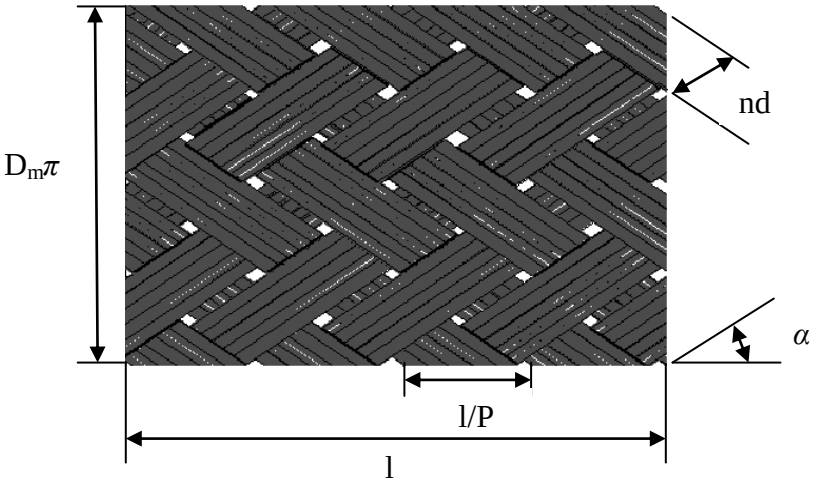

Figure 2.2.3: (a) A cross-section of a coaxial cable. (b) A detailed braided shield with defined basic parameters

A typical coaxial cable with a braided shield has a conducting shield containing a large number of small diamond-shaped openings owing to the criss-crossing belts of conductors, illustrated in Figure 2.2.3. The analysis of braided wire shields widely used in RF transmission lines and shielded multiconductor cables for electronic systems is based on the theory of coupling through electrically small apertures or irises of the braid, derived by Kaden [2.6] and Marcuvitz [2.7]. The aperture theory is adapted to the single-layer braided shield so that the transfer impedance of the braided shield can be expressed in terms of physical parameters such as wire size, number of wires per carrier, number of carriers, and braid angle. The transfer impedance expressions and shield parameters are expressed in a way that the effect of varying such parameters as shield coverage, ie: wire size, braid angle, etc. can be assessed [2.7]. Many authors have worked on the calculation of the coupling parameters of

shielded cables. However, this chapter concentrates mainly on the important contributions made towards the development of the surface transfer impedance, presented by Tyni [2.10], Vance [2.11], and Kley [2.8].

Tyni [2.10] identified two magnetic coupling processes to account for the inductive rise of Z_T at high frequencies. The coupling by direct penetration of the external fields to the interior through the holes in the braid give rise to hole inductance. The magnetic flux coupling in the circuits between the inner and outer layers in the braid results in another inductance, known as the braid inductance. Measurements were performed [2.13] and established that when the hole inductance of the braid is greater than the braid inductance, Z_T has a positive value and vice versa. It has been suggested by Tyni [2.10] that for braid angle less than 45˚, the hole and the braid inductances oppose each other and greatly reduced Z_T values may be obtained for a particular optical coverage in the shield where the difference between the two inductances is minimum [2.9].

Benson et al. [2.14], Homann [2.15], McDowell et al. [2.16] and Sali [2.36] proved that it is theoretically possible to design a coaxial braid with a minimum of Z_T, where the braids are considered to be optimized braids. Optimized cable braids such as the RG-400 coaxial cable have very low optical coverage and they require much lower fillings, allowing low Z_T values to be obtained. The low optical coverage in the braid reduces braid inductance but increases hole inductance due to the increased number of holes and their increased sizes. Therefore, this accounts for the much higher electric field coupling within the braid. Since optimized braids have low optical coverage that is much smaller than a standard URM-43 coaxial cable, they do give rise to increased electric field coupling. Therefore, Y_T, represented by capacitive coupling impedance may assume values that are comparable to the values of Z_T and hence, impossible to be ignored, especially when the analysis for various field coupling and crosstalk is concerned.

The Vance model [2.11] is one of the earliest and simplest models for the transfer impedance. Similar to Tyni, it is suggested by Vance [2.11] that the transfer characteristics of a braided shield can be defined in terms of D_m, N, P and d. A typical braid pattern is illustrated in Figure 2.2.3. From the given parameters, the fill factor of the braid can be equated as:

$$F = \frac{PNd}{\sin\alpha} = \frac{nNd}{2\pi D_m \cos\alpha} \tag{2. 5}$$

The optical coverage of the braid is given by:

$$\mathcal{X} = 2F - F^2 \tag{2. 6}$$

Braid angle, α, plays an important role in determining the shape of the braid and its magnetic field coupling, which mainly affects the value of Z_T. For braid angle, $\alpha < 45^{\circ}$, the major axis of the diamond-shaped holes is perpendicular to the magnetic field, where the shape is oriented for a minimum magnetic coupling through the aperture of the braid. As for braid angle, $\alpha > 45^{\circ}$, the major axis of the diamond-shaped holes is parallel to the magnetic field, orienting the shape for a maximum magnetic field coupling through the shield's aperture.

Finally, the transfer impedance of the braided shield can be approximated using two components. The first component determines the diffusion of the electromagnetic leakage energy through the shield. Meanwhile, the second component determines the penetration of the magnetic field coupling through the shield's aperture. Vance [2.11] further develops the diffusion of the low frequency resistive component, R_{dc}, of Z_T, in (2.9). This DC resistance per unit length of each conductor is approximated by assuming that the conductor of d diameter is isolated from all other conductors, in which the contact resistance between the cables is large compared to the cable resistance, giving:

$$R_0 = \frac{4}{\pi d^2 \sigma \cos\alpha} \tag{2. 7}$$

The DC resistance per unit length of the shield is:

$$R_{dc} = \frac{R_0}{nN} = \frac{4}{\pi d^2 nN\sigma \cos\alpha} \tag{2. 8}$$

It is found in [2.5] that by assuming that this DC resistive component behaves in the same manner as the diffusion term in a cylindrical tube with thickness d, the skin depth effect implemented together with the DC resistance of the braid, giving a total screen impedance of:

$$Z_d = \frac{4}{\pi d^2 n N \sigma \cos\alpha}\left(\frac{(1+j)\,{}^{d}/_{\delta}}{\sinh\left((1+j)\,{}^{d}/_{\delta}\right)}\right) = R_{dc}\left(\frac{(1+j)\,{}^{d}/_{\delta}}{\sinh\left((1+j)\,{}^{d}/_{\delta}\right)}\right) \quad (2.9)$$

where the skin depth, δ, can be equated as:

$$\delta = \sqrt{\frac{2}{\omega\mu_0\sigma}} \quad (2.10)$$

From (2.4), similar shapes such as ellipses with semicircular ends, the polarizability of the diamond-shaped aperture can be represented by the polarizability of an equivalent elliptical aperture. The magnetic polarizability of the elliptical aperture has been derived in closed form for parallel to both the major and minor axis of the ellipse [2.12]. Hence, for the major axis, the magnetic polarizability of the ellipse is given by:

$$m_l = \frac{\pi l^3}{24}\left(\frac{e^2}{K(e) - E(e)}\right) \quad (2.11)$$

As for the minor axis, the magnetic polarizability of the ellipse is given by:

$$m_w = \frac{\pi l^3}{24}\left(\frac{(1-e^2)}{K(e) - (1-e^2)E(e)}\right) \quad (2.12)$$

where e represents the ellipse's eccentricity, given by:

$$e = \sqrt{\left[1 - \left(\frac{w}{l}\right)^2\right]} \quad (2.13)$$

where w and l denote the minor and major axis of the ellipse respectively.

K(e) and E(e) are complete elliptic integrals of the first and second kind, respectively, and can be defined as:

$$K(e) = \int_0^{\frac{\pi}{2}} \frac{d\varphi}{\sqrt{(1 - e^2\sin^2\varphi)}} \quad (2.14)$$

$$E(e) = \int_0^{\frac{\pi}{2}} \left[\sqrt{(1 - e^2\sin^2\varphi)}\right] d\varphi \quad (2.15)$$

Assuming that the braided shield pattern can be simulated by ellipses having similar major and minor axes to the rhombic holes, the mutual inductive coupling which represents Z_T associated with the apertures can be approximately equated as:

$$M_{12} \approx \frac{\pi\mu_0}{6N}(1-\mathcal{X})^{\frac{3}{2}}\left\{\frac{e^2}{K(e)-(1-e^2)E(e)}\right\};\ \alpha < 45^{\circ}$$
$$e = \sqrt{(1-\tan^2\alpha)} \qquad (2.16)$$

or

$$M_{12} \approx \frac{\pi\mu_0}{6N}(1-\mathcal{X})^{\frac{3}{2}}\left\{\frac{\frac{e^2}{\sqrt{(1-e^2)}}}{K(e)-E(e)}\right\};\ \alpha > 45^{\circ}$$
$$e = \sqrt{(1-\cot^2\alpha)} \qquad (2.16)$$

The total transfer impedance for the braided shield cable can then finally be expressed as:

$$Z_T = Z_d + j\omega M_{12} \qquad (2.17)$$

2.2.2 Tyni Model [2.10]

Apart from the Vance model [2.11], the Tyni model [2.10] is studied extensively in [2.14] and found to be reasonably accurate in modelling the transfer impedance of coaxial cables. In [2.14], detailed measurements were carried out based on theoretical model developed by Tyni [2.10], which demonstrated good agreement. The braided cable shield provides a certain increase in attenuation compared to a continuous conductor. As mentioned, the contribution to this leakage is from the inductive coupling between the internal and outer conductor of the coaxial cable. Hence, the transfer impedance can be expressed in terms of an inductive term, giving:

$$Z_T = R + j\omega L \qquad (2.18)$$

where R in (2.18), is expressed as the resistive component of the braid at low frequencies.

Tyni's prediction of the leakage from coaxial cables is based on the theoretical analysis of a non-optimized braided cable, which uses a minimised electric (capacitive) leakage. In the Tyni model [2.10], the transfer impedance is found from two inductances, ie: braid and hole inductances. It is a further development from Vance [2.11], which only considers the braid inductance. The braid inductance, L_b, arises from the woven nature of the braid. The principal idea behind this qualitative inductance is that L_b is treated as an inner inductance between the two interlaced halves of the braid, relating it only to the geometry of the braid. The leakage or gap inductance, L_h, is the hole inductance due to the apertures in the shield. L_b and L_h can be equated as [2.10]:

$$L_b = \frac{\mu_0 h_r}{4\pi D_m}(1 - \tan^2 \alpha) \tag{2. 19}$$

$$L_h = \frac{2\mu_0 N}{\pi \cos \alpha}\left(\frac{b}{\pi D_m}\right)^2 e^{\left(\frac{-\pi d}{b}-2\right)} \tag{2. 20}$$

Given information of the braid picks P, outer diameter of dielectric D_0 and number of conductors n (see Figure 2.2.3), the parameters l, α, D_m, h_r and b can be given by [2.10]:

$$l = \frac{N}{2P} \tag{2. 21}$$

$$\alpha = \tan^{-1}\left(\frac{2\pi D_m P}{N}\right) \tag{2. 22}$$

$$D_m = D_0 + 2d \tag{2. 23}$$

$$b = \frac{2\pi D_m}{N}\cos \alpha - nd \tag{2. 24}$$

$$h = \frac{2d^2}{b + d} \tag{2. 25}$$

Further modification was proposed by Katakis [2.17], the following equations (2.26) and (2.27) suggest that D_m is also a function of h_r. The equations represent a non-linear relationship. Thus, a solution is found by using a Newton-Raphson iteration process.

$$D_m = D_0 + 2d + h_r \tag{2. 26}$$

where h_r can be obtained through:

$$\left[\frac{2\pi}{N}\right] + \left[(1-n)d + \frac{2\pi}{N}(D_0 + 2d)\cos\alpha\right] h_r - 2d^2 = 0 \tag{2. 27}$$

Z_T can then finally be expressed as:

$$Z_T = Z_d + j\omega(L_b + L_h) \tag{2. 28}$$

2.2.3 Kley Model [2.8]

The Kley model [2.8] is a further development of the characteristics of the transfer impedance of a braided shield cable. According to Kley, the known approaches, such as [2.6], [2.7], [2.10] and [2.11], for the calculation of the internal coupling parameters of single-braided shields are still lacking in comparison with the measured values. The Kley model is found to be based on analytical approaches by Kaden [2.6], Vance [2.11], and Tyni [2.10], which plans to eliminate the problem causing the slight drawback when comparing with measurement values. Similarly, Kley concentrates on the important insights on the braid inductance of the transfer impedance's dependence on the inductive coupling through the apertures of the braid. Implementing the screen impedance by Vance [2.11] in (2.29), giving:

$$Z_T = Z_d + j\omega(L_h - L_b) \tag{2. 29}$$

It is suggested by Kley that there are two effects which contribute to the coupling inductance, M_T. These two factors comprise of the mutual inductance due to the apertures allowing for the curvature of the tube (hole inductance), M_L; and the mutual inductance between carriers in the braid (braid inductance), M_G.

$$M_T = M_L + M_G \tag{2. 30}$$

This term is adjusted by Kley, originated from the mutual inductive coupling due to the apertures in the braid, derived from the magnetic polarizability of the elliptical aperture in the Vance model [2.11]. Kley approximated this elliptic function in (2.16) by $2 - \cos\alpha$, with an exponential attenuation factor of τ_H, and also considering the factor of 0.875 due to the curvature of the braid, to give:

$$M_L \approx 0.875\mu_0 \frac{\pi(2-\cos\alpha)}{6N}(1-F)^3 e^{-\tau_H} \tag{2. 31}$$

where the attenuation factor is derived as:

$$\tau_H = 9.6F\sqrt[3]{\frac{\chi^2 d}{D_m}} \tag{2. 32}$$

The hole inductance can be related to the braid parameters for circular apertures, assuming that the proximity effects are ignored and uniform current distribution assumed.

It is elaborated by Kley that the braid inductance varies with the braid angle α (no induced voltage if $\alpha = 45^\circ$; and maximal induced voltage if $\alpha = 0^\circ$) [2.8]. From (2.16), Tyni's [2.10] braid inductance in (2.19) was validated by the triaxial configuration measurement in [2.18], to give an approximate formula derived by Kley:

$$M_G \approx -\mu_0 \frac{0.11}{Nn}\cos(2K_1\alpha) \tag{2. 33}$$

where

$$K_1 = \frac{\pi}{4}\left[\frac{2}{3}F_0 + \frac{\pi}{10}\right]^{-1} \tag{2. 34}$$

and F_0 represents the minimal fill factor of the braid, derived from (2.16), given by:

$$F_0 = F\cos\alpha \tag{2. 35}$$

Kley introduced a third inductance in the braid, known as the skin inductance, L_S. As the magnetic field penetrates through the apertures of the braid, it generates eddy

currents on the surface of the apertures. This effect is taken into account by an ohmic-inductive component of the transfer impedance [2.8]. This said inductance includes the skin effect on the aperture surface, which can be equated as:

$$L_S = \frac{1}{\omega\pi\sigma\delta}[D_L^{-1} + D_G^{-1}] \tag{2. 36}$$

where D_L and D_G are fictitious diameters that model the corresponding skin effect. The evaluation of the measurements done by Kley [2.8] yields for D_L an approximated formula given by:

$$D_L^{-1} \approx \frac{10\pi F_0^2 \cos\alpha}{D_m}[1 - F]e^{-\tau_E} \tag{2. 37}$$

where the attenuation factor can be equated as:

$$\tau_E = 12F\sqrt[3]{\frac{\chi^2 d}{D_m}} \tag{2. 38}$$

and the fictitious parameter D_G is approximated by:

$$D_G^{-1} \approx -\frac{3.3}{2\pi F_0 D_m}\cos(2K_2\alpha) \tag{2. 39}$$

where

$$K_2 = \frac{\pi}{4}\left[\frac{2}{3}F_0 + \frac{3}{8}\right]^{-1} \tag{2. 40}$$

The evaluation of the measurements found by Kley showed that the thickness, d_R, of the equivalent tube is proportional to the wire diameter, d. The said thickness is also found to be slightly dependent on the braid angle, α. Therefore, from (2.9), the screen impedance of the tube can be equated as:

$$Z_R = R_{dc}\left[\frac{(1+j)\,{}^{d_R}/_{\delta}}{\sinh\left((1+j)\,{}^{d_R}/_{\delta}\right)}\right] \tag{2. 41}$$

where d_R is defined as:

$$d_R \approx \frac{0.67d}{\sqrt{\cos\alpha}} \tag{2. 42}$$

Finally, the formula for Z_T of a single-braided shield cable is written in its entirety as:

$$Z_T = Z_R + j\omega(M_L + M_G + L_S) \tag{2. 43}$$

2.2.4 Comparison of the Transfer Impedance Models

The predicted transfer impedance as given by Tyni [2.10], Vance [2.11], and Kley [2.8] models for the standard non-optimized coaxial cable RG-58 with the parameters as supplied by the manufacturers (RG-58 in Appendix D) are plotted in Figure 2.2.4. The predicted transfer impedance models are validated via measurements using the trixial configuration in [2.19]. There is a significant difference between the models but they are comparable to the typical results shown in Figure 2.2.5 [2.27]. Research done by Benson et al. [2.14] and Thomas et al. [2.26] both found that Kley model provides the best accuracy in modelling the transfer impedance of braided shield cables since all possible aspects of the inductances in the braid were considered. Therefore, the Kley model forms the basis of modelling the surface transfer impedance for the RG-58 coaxial cable in this thesis.

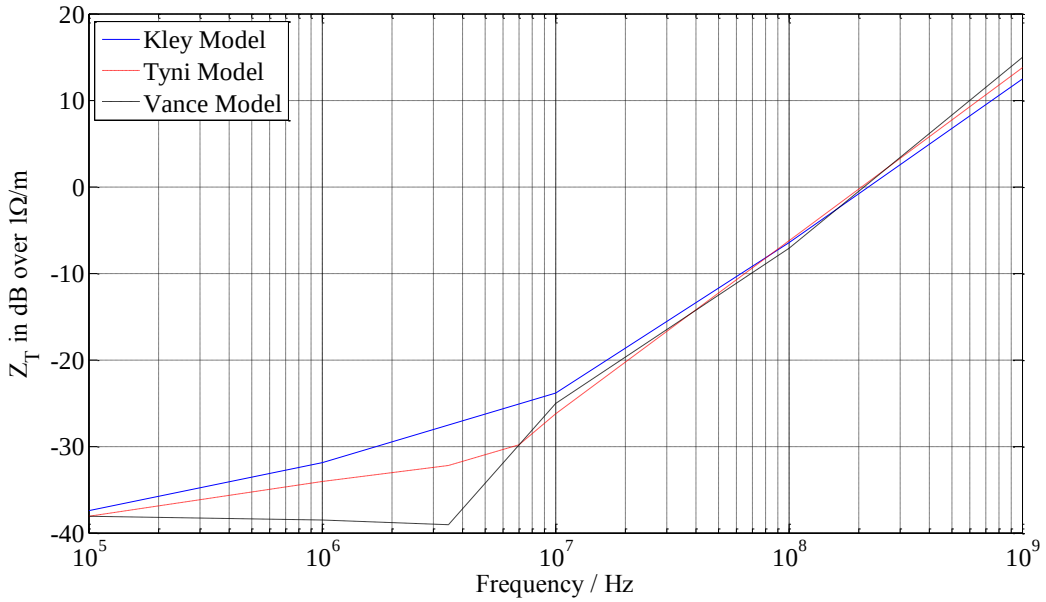

Figure 2.2.4: Comparison between predicted and measured transfer impedance, Z_T, using RG-58 parameters

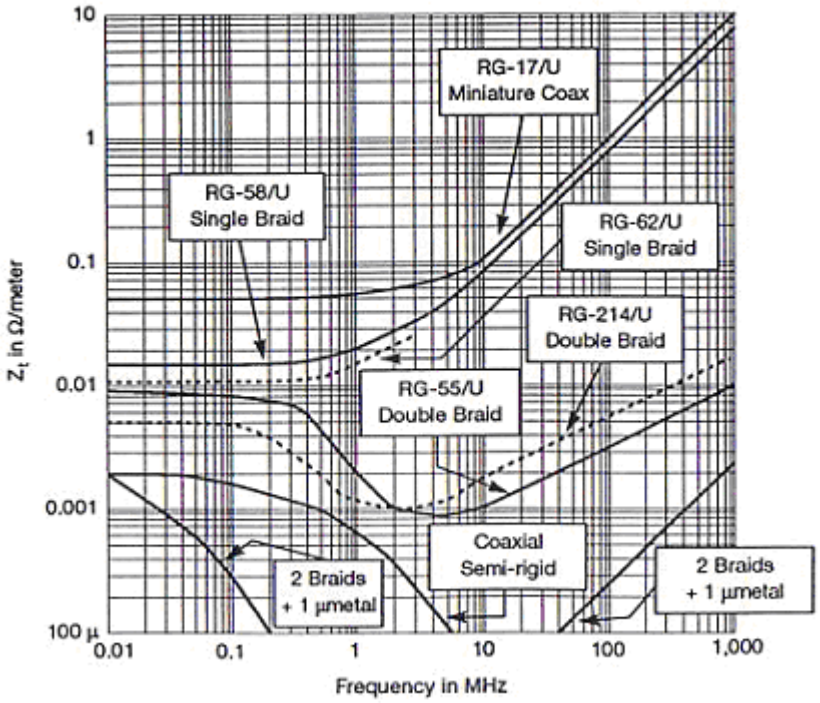

Figure 2.2.5: Transfer Impedances, Z_T, of different types of coaxial cables [2.27]

2.3 Crosstalk

A transmission line is a structure that guides the transmission of energy. This energy form could be electromagnetic waves or acoustic waves, or other propagating phenomenon. The components which make up an electrical transmission line include wires, coaxial cables, dielectric slabs, optical fibres, electric power lines and waveguides.

Crosstalk is an important aspect of the design for an electromagneticly compatible product. Electrical signals can be coupled onto a transmission line via different paths. One of the most common cases is where the transmission line shares a common path with another transmission line. The crosstalk phenomenon is due to near-field coupling. A current flowing, which exists in one line, produces an interference signal on the other line that is in close proximity (induced interference). This interference is caused by an electromagnetic field surrounding the transmission line and does not involve a physical connection between the two circuits. Crosstalk refers to the unintended electromagnetic coupling between wires, traces, trace to wire, electrical components etc. [2.22]. The crosstalk between two cables can induce signals on the adjacent cable that may radiate externally to the product, potentially causing the latter to exceed permitted radiated emission regulatory limits. Due to internal coupling to the power cord of the product, these coupled signals may also cause the product to fail the conducted emission regulatory requirements [2.23]. Crosstalk is generally considered to be a functionality concern to all engineering design by causing electromagnetic and can be a major contributor to the propagation of EMI.

Schelkunoff and Odarenko [2.32] explain that the crosstalk between any two transmission lines depends upon the existence of mutual impedances and mutual admittances between the lines. The two types of crosstalk are introduced in [2.32], ie: impedance crosstalk and admittance crosstalk. Impedance crosstalk is produced by an electromotive force in series with the disturbed line in consequence of mutual impedances between the lines; whereas admittance crosstalk is produced by an electromotive force in shunt with the disturbed line, induced by virtue of mutual admittances.

Given the definition of crosstalk in [2.32], Christopoulos [2.4] describes that crosstalk subjects to inductive coupling (impedance crosstalk) as well as capacitive coupling (admittance crosstalk); followed by a basic example shown in Figure 2.3.1. Capacitive coupling usually results from traces lying close to each other above a reference plane, where only the electric coupling is considered. This coupling depends on the distance between traces and the overlapping area. It is particularly evident when two high impedance circuits are in close proximity to each other, carrying low frequency signals. As for inductive coupling, it normally appears dominant in low impedance circuits in close proximity to each other, carrying low frequency signals, where only the magnetic components of the field is considered [2.4].

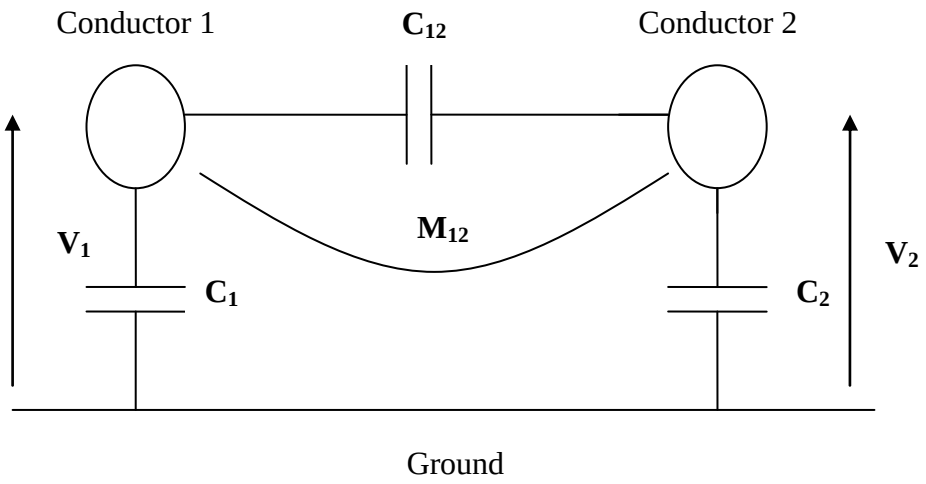

Figure 2.3.1: Configuration of a two-conductor transmission line system

Figure 2.3.1 shows a system of two parallel conductors. The potential difference V_1 in conductor 1 with respect to ground will cause an interference signal to appear in conductor 2, given by:

$$V_2 = \frac{C_{12}}{C_{12} + C_2} V_1 \tag{2. 44}$$

where C_1 denotes the capacitance of conductor 1 to ground; C_2 denotes the capacitance of conductor 2 to ground; and C_{12} denotes the mutual capacitance between conductors 1 and 2.

With addition of a shield around conductor 2, depicted in Figure 2.3.2, capacitive coupling can be described in the following way. If the shield has no DC connection to ground, its potential is given by [2.4]:

$$V_{12S} = \frac{C_{12S}}{C_{12S} + C_{2S}} V_1 \tag{2. 45}$$

where C_{12S} denotes the mutual capacitance between conductor 1 to the shield of conductor 2 and C_{2S} denotes the capacitance of the shield of conductor 2 to ground.

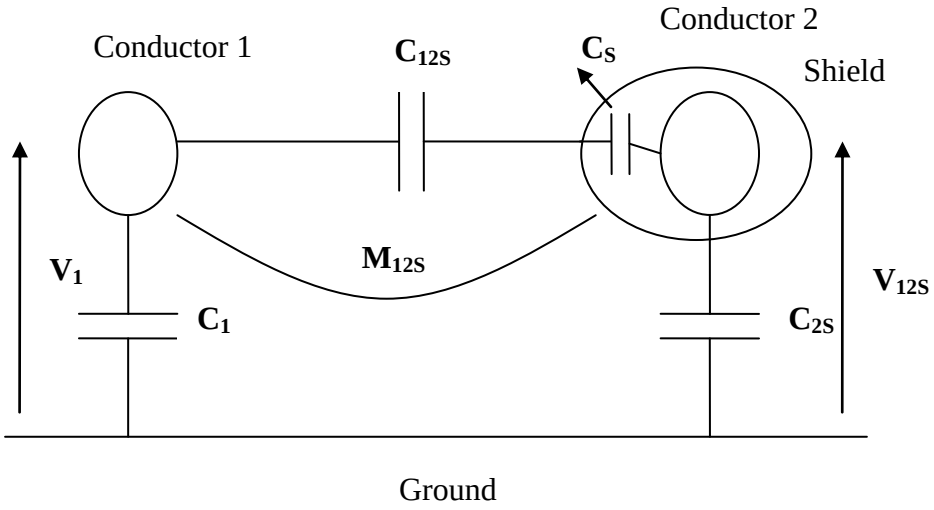

Figure 2.3.2: Shielding effect on conductor 2 [2.4]

Referring to Figure 2.3.2, the voltage induced on conductor 2 when current I_1 flows in conductor 1 is given by:

$$V_2 = M_{12} \frac{dI_1}{dt} \tag{2. 46}$$

where M_{12} denotes the mutual impedance between the two transmission lines. Inductive coupling is can be described when a magnetic shield is implemented on conductor 2, shown in Figure 1.2.2, in the following way. The voltage induced on the shield, V_{12S}, would then be:

$$V_{12S} = M_{12S} \frac{dI_1}{dt} \tag{2. 47}$$

where M_{12S} denotes the mutual inductance between conductor 1 and the shield of conductor 2.

However, if the shield is connected to ground, shown in Figure 2.3.3, V_S and the voltage induced on conductor 2 are zero. The initial current I_1 driven in conductor 1 given by (2.47) will then induce an additional voltage, V_{Shield}, given by:

$$V_{Shield} = M_{12S}\frac{dI_1}{dt} \tag{2. 48}$$

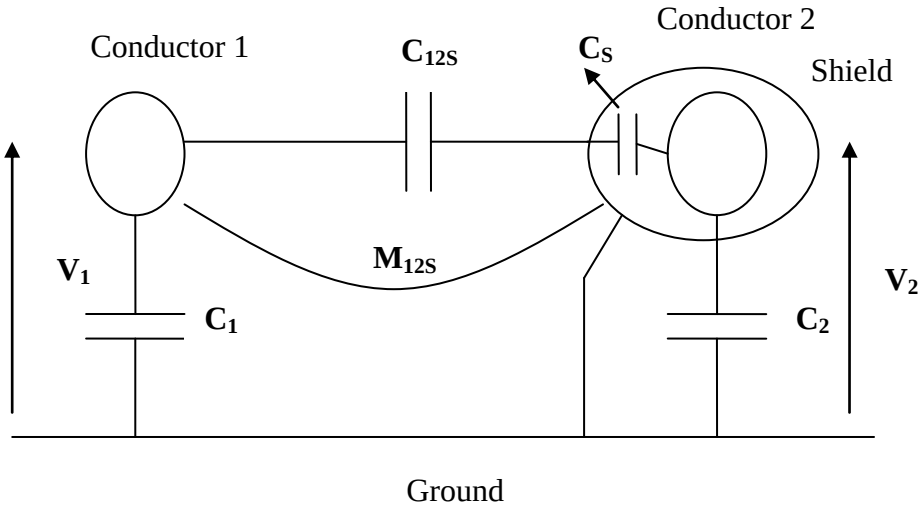

Figure 2.3.3: Grounded shield on conductor 2

where M_{12S} denotes the mutual inductance between the shield and conductor 2. If the geometry of the shield allows no magnetic field to be established within the shield, then all the magnetic flux induced by I_S within the shield is linked to conductor 2.

$$M_{12S} = \frac{\varphi}{I_S} = L_S \tag{2. 49}$$

where φ denotes the magnetic flux induced in the shield and L_S denotes the self inductance of the shield connected to ground. Assuming that the induced voltage on conductor 2 can be expressed in the frequency domain using:

$$V_2 = j\omega(M_{12}I_2 + L_S) \tag{2. 50}$$

By assuming that the induction due to I_2 on conductor 2 can be neglected, the mutual inductance between conductor 1 and the shield would be:

$$M_{12S} \approx M_{12} \tag{2. 51}$$

Thus,

$$I_S = \frac{j\omega M_{12} I_1}{R_S + j\omega L_S} \tag{2. 52}$$

where R_S denotes the resistance of the shield. By substituting (2.52) into (2.50), the total induced voltage on conductor 2 can be simplified to be:

$$V_2 = j\omega M_{12} I_1 \frac{\frac{R_S}{L_S}}{\frac{R_S}{L_S} + j\omega} \tag{2. 53}$$

From (2.53), at low frequencies, where the induced voltage is not affected by the shield, the induced voltage is given by:

$$\omega \approx 0;$$

$$V_2 = j\omega M_{12} I_1 \tag{2. 54}$$

Whereas at high frequencies, the induced voltage is given by:

$$\omega \approx \frac{R_S}{L_S}; \tag{2. 55}$$

$$V_2 = j\omega M_{12} I_1 \frac{R_S}{L_S} \tag{2. 56}$$

The calculations in the example described are not valid if the lines become electrically long as it happens at very high frequencies. If the conductors are not in close proximity, ie: separated by a larger distance, the coupling is not regarded as simply capacitive or inductive coupling. At greater separations, energy from the sources of interference propagates in the form of electromagnetic waves that penetrate onto the victim line, thus causing EMI, ie: radiated interference. Depending on the distance between the source and the victim line, the radiated interference is further subdivided to near-field and far-field radiated interference.

This thesis presents the coupling effects between coaxial cables both in the time and frequency domain. It describes the development of a shielded cable model suitable for implementation within a numerical model, based on the Transmission-Line

Modelling Method (TLM). The model incorporates the appropriate coupling theory for the analysis of shielded cables, subject to crosstalk and radiated interference (EMI). Results presented here are concerned with identifying and quantifying factors affecting electromagnetic coupling through the construction of numerical models and their validation against measurements.

2.3.1 Coupling between Two Coaxial Cables in Free Space

The circuit topology used for this work is described by Thomas et al. [2.26]. The typical layout of a general case of near-end coupling between two coaxial lines in parallel to each other along a common path is shown in Figure 2.3.4.

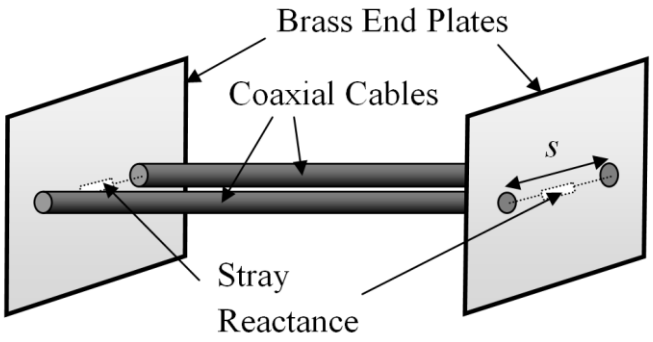

Figure 2.3.4: A layout of two coaxial cables along a common path in free space

The cables have a constant separation, s, along the length, l, between the terminations. The nature of the terminations strongly affects the degree of cable coupling at high frequencies due to the stray reactance they introduce. In this case, the stray reactance introduced would mostly be inductive since the cables are terminated by a common brass connector plate at each end, creating an extra current loop. However, the effect of the terminations can only be estimated due to the geometric complexity of the terminations and insufficient information. Nevertheless, an experimental analysis is carried out to define the characteristics of the connector plates and its approximate inductance (see Chapter 3). The effect of the coupling path due to transfer admittance, Y_T, has not been included in this thesis since for a optimized braided shield cable (RG-58) its effects are deemed to be negligible (see section 2.2.1).

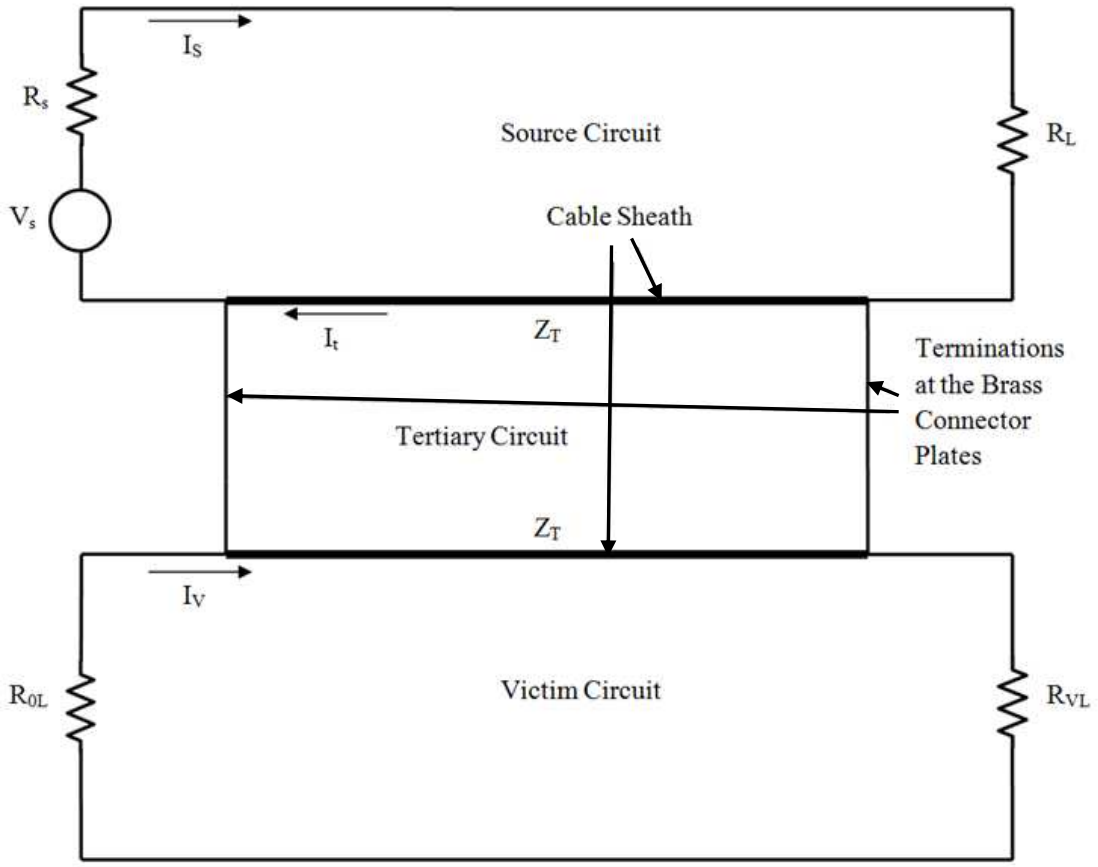

Figure 2.3.5: The equivalent circuit between two coaxial cables in parallel in free space [2.26]

The equivalent circuit for the coupling path created by the cable braid's transfer impedance is shown in Figure 2.3.5. In these analysis [2.3], [2.35] – [2.41], which will be the main concern for this investigation, only the source circuit is driven by V_S. The coupling path between the two circuits is described by the current in the source circuit, I_S, inducing a current in the tertiary circuit, I_t, which in turn induces a current, I_V, in the victim circuit. The tertiary circuit is the conducting path formed by the outer sheath of the cables and the terminations. The victim current, I_V, will then create a voltage across the terminations of the victim circuit, V_{V0}. This voltage, V_{V0}, is the usual measurable form of cable coupling. Splitting the three circuits (Source, Tertiary and Victim Circuits), the currents and voltages can be derived individually as depicted in Figure 2.3.6.

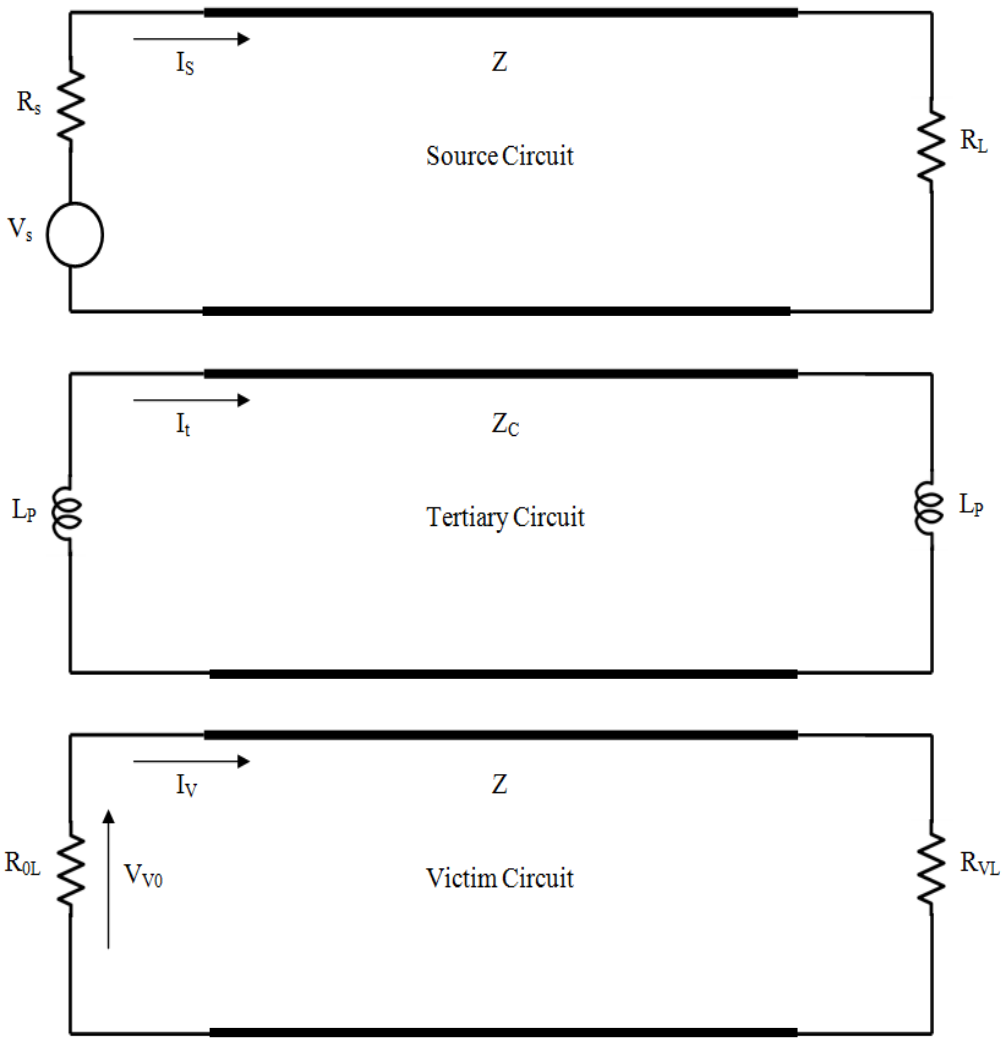

Figure 2.3.6: The individual source, tertiary and victim circuits

Based on the analytical solution given by Thomas et al. [2.26], for low frequencies ($\lambda \gg l$), the voltage induced in the adjacent circuit is independent of the distance along the cable sheath, x. Thus, the equivalent circuit transmission line for low frequency coupling (Source, Tertiary and Victim) can be illustrated in Figure 2.3.7.

(a)

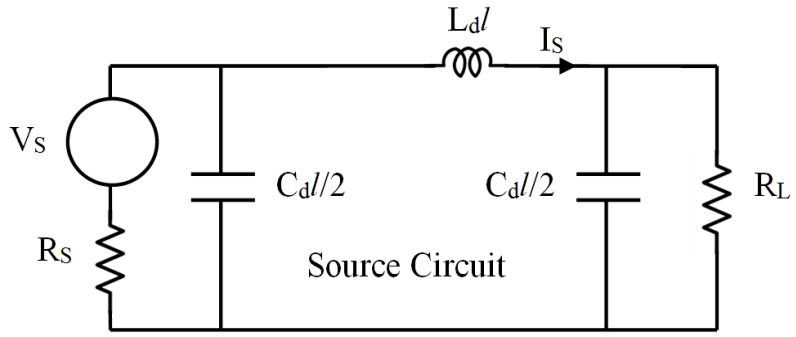

(b)

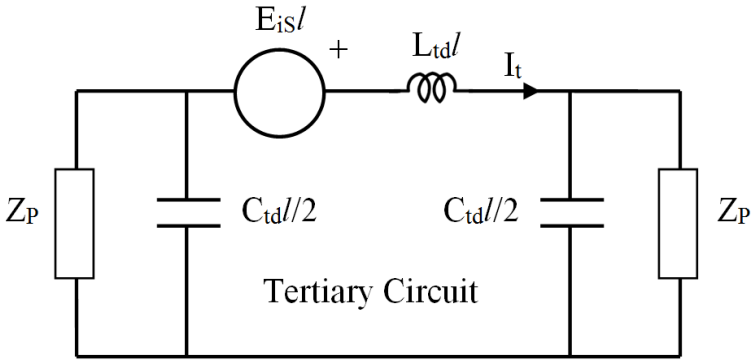

(c)

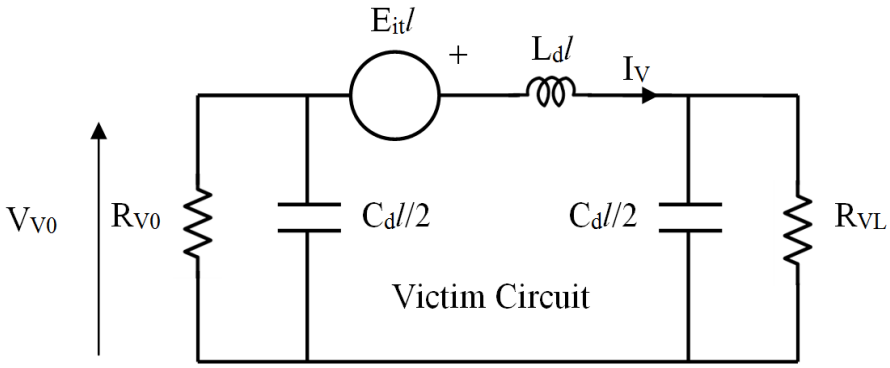

Figure 2.3.7: Equivalent circuit for low frequency cable coupling for (a) Source (b) Tertiary (c) Victim circuits

The current I_S, runs along the source circuit, and is given by:

$$I_S = \frac{V_S}{(j\omega L_d l) + R_S + R_L} \quad (2.57)$$

Assuming that both cables are identical, Z_T denotes the coaxial braid transfer impedance and x is the distance along the cable braid, the voltage gradient, $E_{iS}(x)$, induced by I_S in (2.58) along the braid, with respect to x, can be equated as:

$$E_{iS}(x) = Z_T I_S(x) \quad (2.58)$$

Since the tertiary circuit is terminated by a brass connector plate at each end, it is assumed that the connector plates possess finite impedance, which is approximated by an arbitrary inductive reactance, Z_P (see Chapter 3). The induced current I_t due to the voltage gradient in (2.59) is then given by:

$$I_t = \frac{E_{iS} l}{(j\omega L_{td} l + 2Z_P)} \quad (2.59)$$

Similarly, the voltage gradient, $E_{it}(x)$, induced by I_t in (2.47) can be equated by:

$$E_{it}(x) = Z_T I_t(x) \quad (2.60)$$

Finally, the induced current I_V and voltage V_{V0} due to the voltage gradient in (2.61) and (2.62) are respectively given by:

$$I_V = \frac{E_{it} l}{(j\omega L_d l) + R_{V0} + R_{VL}} \quad (2.61)$$

$$V_{V0} = I_V E_{it}(0) \quad (2.62)$$

2.3.2 Coupling between Two Coaxial Cables via a Perfect Conducting Ground Plane

Based on the configuration used in section 2.3.1, the presence of another cable or a ground plane will enable other current paths to form and reduce the coupling between two cables [2.41]. The typical layout of a general case of near-end coupling between two coaxial lines in parallel above a ground plane is shown in Figure 2.3.8.

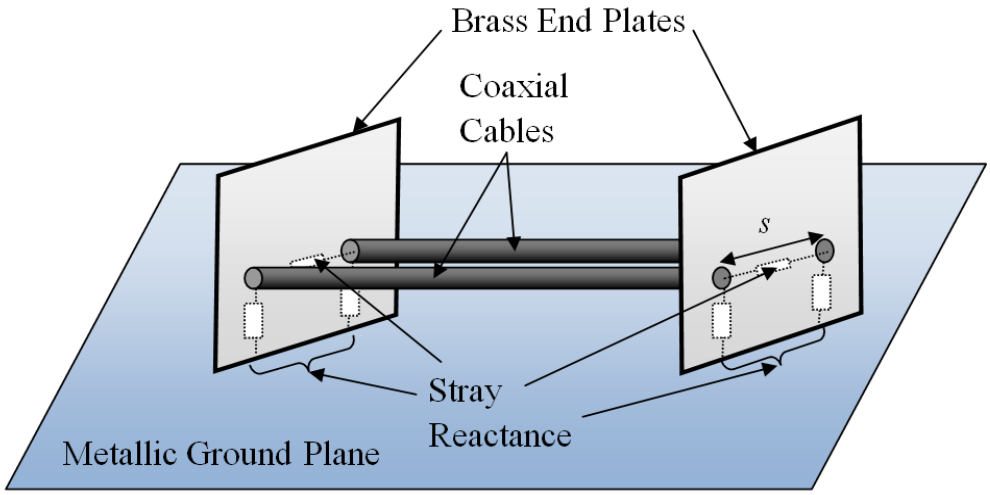

Figure 2.3.8: A layout of two coaxial cables along a common path above a conducting ground plane

Similar to the coupling mechanism in section 2.3.1, the source line is driven by V_S, and the coupling path between the two circuits can be observed using the voltage at the termination across the victim line, V_{V0}. As illustrated in Figure 2.3.8, the two coaxial lines are terminated by a brass end plate at each end. However, the plates now provide an extra return current path between the coaxial braids and the third conductor – ground. The current I_t in section 2.3.1 has a form of a differential mode as the victim and source currents are of opposite signs. In the case of an additional metallic ground plane, the induced tertiary circuit current comprises two modes in the form of differential and common mode currents. The differential mode current, I_{td}, represents the circulating current loop between the two coaxial braids while the common mode current, I_{tc}, represents the return path of the current loop between the coaxial braids and the metallic ground plane [2.4]. Therefore, the general equivalent coupling circuit for the two coaxial cables above a ground plane can be illustrated in Figure 2.3.9.

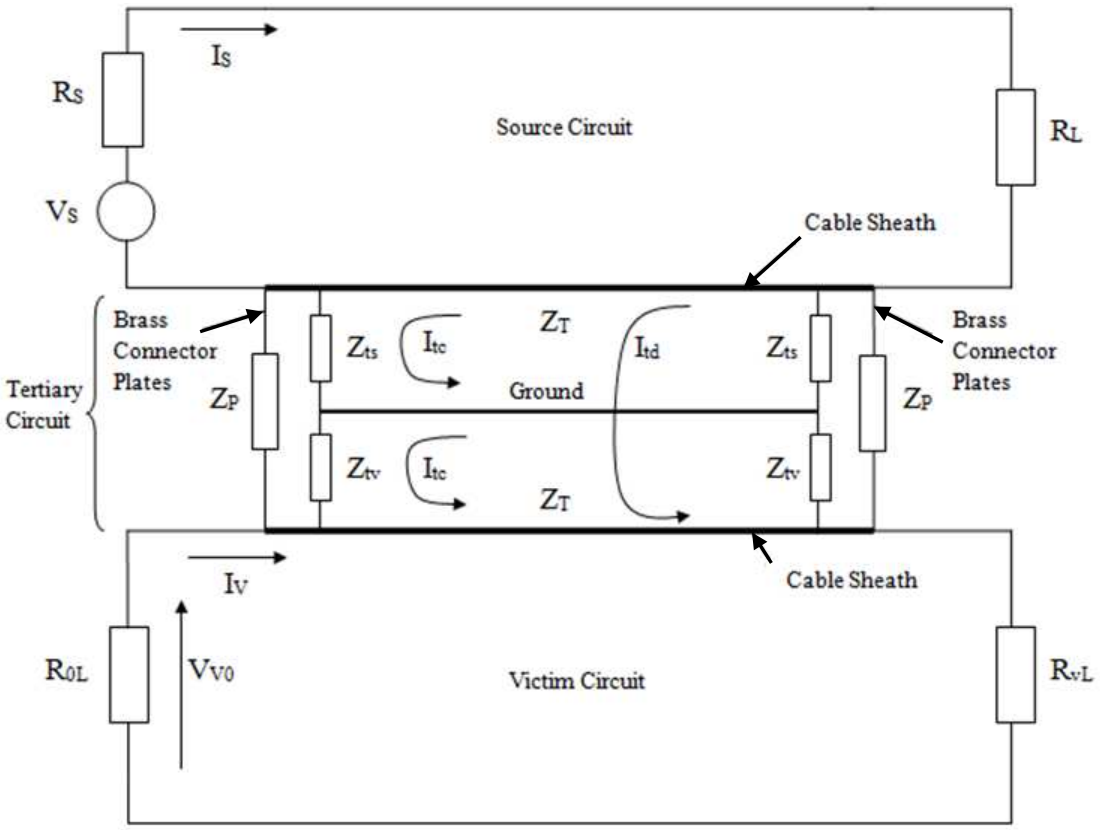

Figure 2.3.9: The equivalent circuit between two coaxial cables in the presence of a third conductor (ground plane)

It is assumed that the brass end plates possess a finite impedance for both the common and differential modes. It is approximated in section 2.3.1 that the arbitrary impedance (differential mode) between the coaxial braids is represented by Z_P. Another set of arbitrary impedances (common mode) approximated are Z_{ts} and Z_{tv}, which represent the finite impedance between the coaxial braids and ground plane (see Chapter 3). If the coaxial lines are identical, assuming that the current and charge is uniformly distributed around the surface area of the end plates, it can be deduced that:

$$Z_{ts} = Z_{tv} \tag{2. 63}$$

Thomas et al. [2.26] derived an analytical solution to determine the degree of coupling of this system. Differential and common mode currents, I_{td} and I_{tc}, on the cable sheaths are equated with respect to the currents on the sheaths of the source and victim cables, I_S and I_V; respectively, giving:

$$\begin{bmatrix} I_S \\ I_V \end{bmatrix} = \begin{bmatrix} -1 & 1 \\ 1 & 1 \end{bmatrix} \begin{bmatrix} I_{td} \\ I_{tc} \end{bmatrix} = [S] \begin{bmatrix} I_{td} \\ I_{tc} \end{bmatrix} \tag{2. 64}$$

where [S] represents the modal transformation matrix derived using the multimode model as described by Naylor and Christopoulos [2.4] and [2.52] (See Chapter 4). For low frequencies ($\lambda \gg l$), the induced common and differential mode currents on the tertiary circuit cable sheaths are equated with respect to $E_{iS}l$, derived from (2.46), giving:

$$\begin{bmatrix} E_{iS}l \\ 0 \end{bmatrix} = \left[j\omega \begin{bmatrix} L_S & L_M \\ L_M & L_S \end{bmatrix} + [Z_{td}] \right] \begin{bmatrix} I_{tS} \\ I_{tV} \end{bmatrix} \tag{2. 65}$$

where L_S is the self inductance of the source and victim cable shields; L_M is the mutual inductance between the source and victim cable shields; and $[Z_{td}]$ is the impedance matrix of the tertiary circuit terminations as depicted in Figure 2.3.7, in the form of:

$$[Z_{td}] = \begin{bmatrix} \dfrac{Z_{ts}(Z_{tv}+Z_P)}{Z_P+Z_{ts}+Z_{tv}} & \dfrac{Z_{ts}Z_{tv}}{Z_P+Z_{ts}+Z_{tv}} \\ \dfrac{Z_{ts}Z_{tv}}{Z_P+Z_{ts}+Z_{tv}} & \dfrac{Z_{tv}(Z_{ts}+Z_P)}{Z_P+Z_{ts}+Z_{tv}} \end{bmatrix} \tag{2. 66}$$

From (2.64), the victim current, I_V, can be solved to obtain the induced voltage across the termination at the victim circuit using (2.62).

2.3.3 Cable Coupling at High Frequencies

For higher frequencies, the voltage per-unit length along the source cable braid will have a significant variation along the cable length due to propagation effects, which lead to resonances in the tertiary circuit and a significant increase in the degree of cable coupling. In this case, the coaxial line currents are no longer uniform and the high frequency analytical solution proposed by Thomas et al. [2.26] is derived. Based on Figure 2.3.6, for a general source cable with a series supply resistance, R_S, and a load resistance of R_L, the input source current, $I_S(0)$, with respect to source voltage, V_S, is given by:

$$I_S(0) = \frac{V_S}{R_S + Z\left[\dfrac{R_L + Z\tanh\ \gamma_S l}{Z + R_L\tanh\ \gamma_S l}\right]} \tag{2. 67}$$

where Z denotes the characteristic impedance of the source cable and γ_S denotes the propagation constant of the coaxial cable, usually defined as:

$$\gamma_S = \frac{j\omega}{u} \tag{2. 68}$$

where u is the propagation velocity of the coaxial line, typically defined as two-thirds of c. Current $I_S(0)$ comprises of forward and backward propagating waves, giving:

$$I_S(0) = I_S^+ \ (forward) + I_S^- \ (backward)$$
$$I_S^- = \rho_S I_S^+ \tag{2. 69}$$

where ρ_S denotes the boundary travelling wave reflection at the supply end, defined as:

$$\rho_S = \left[\frac{Z - R_L}{R_L + Z}\right] e^{-2\gamma_s l} \tag{2. 70}$$

The current along the length of the source cable is then given by:

$$I_S(x) = [e^{-\gamma_S x} + \rho_S e^{\gamma_S x}] I_S^+ \tag{2. 71}$$

where I_S^+ is derived from (2.67) and (2.70):

$$I_S^+ = \frac{I_S(0)}{1 + \rho_S} = \frac{[Z + R_L] e^{\gamma_S l} V_S}{2\left[R_L\left(Z \cosh \ \gamma_S l + R_L \sinh \ \gamma_S l\right) + Z\left(R_L \cosh \ \gamma_S l + Z \sinh \ \gamma_S l\right)\right]} \tag{2. 72}$$

The tertiary circuit involving the coaxial braids and the victim cable will be equivalent to a segment of transmission lines with a distributed voltage source in series, illustrated in Figure 2.3.10.

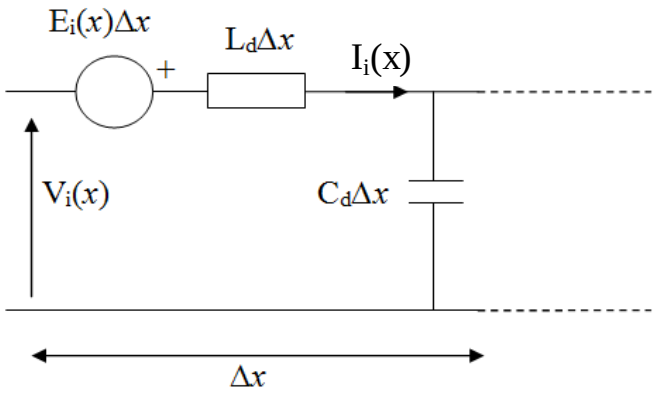

Figure 2.3.10: Equivalent circuit *of a section* Δx *of a transmission line with a* distributed series voltage source $E_i(x)$ [2.26]

The differential equations describing the induced voltage, $V_i(x)$, and current, $I_i(x)$, on the transmission line with a distributed series voltage source, $E_i(x)$, are derived by Vance [2.31] and implemented by Thomas et al. [2.26], giving a general solution for the tertiary circuit to be:

$$I_t(x) = [K_1 + P(x)]e^{-\gamma x} + [K_2 + Q(x)]e^{\gamma x} \tag{2. 73}$$

where

$$P(x) = \frac{1}{2Z_C}\int_0^x e^{\gamma u}E_i(u)\,du \tag{2. 74}$$

$$Q(x) = \frac{1}{2Z_C}\int_0^x e^{-\gamma u}E_i(u)\,du \tag{2. 75}$$

where Z_C denotes the characteristic impedance of the tertiary circuit and K_1 and K_2 satisfies the boundary conditions; $x = 0$ and $x = l$, to give:

$$K_1 = \rho_1\left[\frac{\rho_2 P(l)e^{-\gamma l} - Q(0)e^{\gamma l}}{e^{\gamma l} - \rho_1\rho_2 e^{-\gamma l}}\right] \tag{2. 76}$$

$$K_2 = \rho_2 e^{-\gamma l}\left[\frac{\rho_2 Q(0)e^{-\gamma l} - P(l)}{e^{\gamma l} - \rho_1\rho_2 e^{-\gamma l}}\right] \tag{2. 77}$$

where the boundary travelling wave reflection coefficients, ρ_1 and ρ_2, are given by:

$$\rho_1 = \rho_2 = \frac{Z_P - Z_C}{Z_P + Z_C} \tag{2. 78}$$

Equation (2.73) is first applied to obtain the current of the surface of the coaxial braids, I_t, before applying it to obtain the current on the victim line, I_V. The induced voltage across the termination of the victim line, V_{V0}, can then be equated as:

$$V_{V0} = R_{0L} I_V(0) \tag{2. 79}$$

The cable coupling, C, is often quantified by the ratio of the received victim voltage to the source voltage, expressed as:

$$C = 20 \log_{10}\left(\frac{V_{V0}}{V_S}\right);\ \text{in } dB \tag{2. 80}$$

2.4 Analysis of the Tertiary Circuit Parameters

Both the RG-58 coaxial cables of same length are arranged in parallel to each other as shown in Figure 2.3.2. Since the current in source circuit is coupled to the tertiary circuit, which is eventually coupled to the victim circuit, it is crucial to model the tertiary circuit as realistically as possible. The modelling of the tertiary circuit is complex since all possible losses in the tertiary circuit can only be predicted through measurements due to the stray reactance the cables introduce. Assuming that the signal in the tertiary circuit is in free space, its velocity would be approximately the speed of light, c:

$$c = 2.998 \times 10^8\ ;\ \text{in } ms^{-1}$$

2.4.1 Per-Unit Length Characteristic Impedance of the Tertiary Circuit

A. Two-Conductor Transmission Line System

The parameters of the parallel conductor lines shown in Figure 2.4.1 may be easily derived if the conditions are met, where the current and charge distribution on each conductor's periphery is uniform. Therefore, the approximate equations are

clearly true when the separation between the coaxial lines, s, is significantly greater than the coaxial braid radius, r_m ($s \gg r_m$), for each coaxial line, assuming that both cables are identical, given by [2.4]:

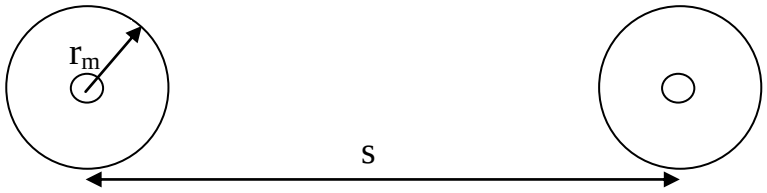

$$L_{td} = \frac{\mu_0}{\pi} \ln\left(\frac{s}{r_m}\right) \text{ ; in } H/m \tag{2. 81}$$

$$C_{td} = \frac{\pi\varepsilon}{\ln\left(\frac{s}{r_m}\right)} \text{ ; in } F/m \tag{2. 82}$$

Figure 2.4.1: Two-conductor transmission line in free space

For conditions when s is not symmetrically greater than r_m, the currents and charges will not be uniformly distributed around the circumference, exact equations can be derived in [2.23] to give:

$$L_{td} = \frac{\mu_0}{\pi} \cosh^{-1}\frac{s}{r_m} \text{ ; in } H/m \tag{2. 83}$$

$$C_{td} = \frac{\pi\varepsilon_0}{\cosh^{-1}\frac{s}{r_m}} \text{ ; in } F/m \tag{2. 84}$$

$$Z_C = \sqrt{\frac{L_{td}}{C_{td}}} \text{ ; in } \Omega/m \tag{2. 85}$$

Finally, the characteristic impedance, Z_C, of the tertiary circuit can be obtained as:

B. Two-Conductor Transmission Line System via an Infinite, Conducting Ground Plane

The parameters of a two parallel conductor lines above ground can then be easily derived from Figure 2.4.2. Due to the metallic ground plane, an image of the two

conductors is reflected by the metallic ground plane, creating inductive and capacitive impedance between the real and the image of the conductors. Again, for conditions when s is significantly greater than r_m ($s \gg r_m$); and assuming that the ground plane is perfect and infinitely large, the inductance and capacitance per-unit length of the entire system is derived by [2.4]:

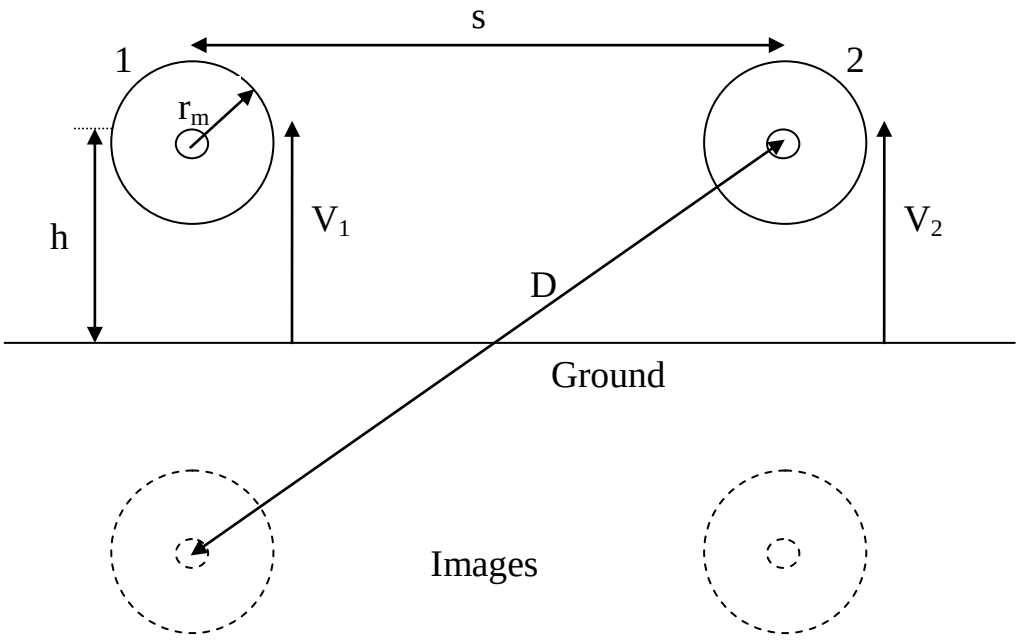

Figure 2.4.2: Two-conductor transmission line above ground

$$[q] = [c][v] = \begin{bmatrix} c_{11} & c_{12} \\ c_{21} & c_{22} \end{bmatrix} \begin{bmatrix} V_1 \\ V_2 \end{bmatrix} \tag{2. 86}$$

Assuming that both coaxial lines are identical, the capacitance coefficients are:

$$c_{11} = c_{22} = \frac{\ln\left(\frac{2h}{r_m}\right)}{A} \; ; \text{ in } F/m \tag{2. 87}$$

$$c_{12} = c_{21} = -\frac{\ln\left(\frac{D}{s}\right)}{A} \; ; \text{ in } F/m \tag{2. 88}$$

where A can be derived as:

$$A^{-1} = \frac{2\pi\varepsilon_0}{\left\{\ln\left(\frac{2h}{r_m}\right)\right\}^2 - \left\{\ln\left(\frac{D}{s}\right)\right\}^2} \tag{2. 89}$$

Therefore, the inductance matrix in per-unit length is given by:

$$[L_{td}] = \frac{\mu}{2\pi}\begin{bmatrix} \ln\frac{2h}{r_m} & \ln\frac{D}{s} \\ \ln\frac{D}{s} & \ln\frac{2h}{r_m} \end{bmatrix};\ \text{in } H/m \qquad (2.90)$$

2.5 Conclusions

In this chapter, the theoretical knowledge of coaxial cable coupling via the characterisation of the tertiary circuit is presented. The cable coupling due to transfer impedance alone is considered as the effect of transfer admittance is negligible for non-optimised cable braids. A comparison is made between three different techniques (Tyni, Vance and Kley models) of the coaxial cable, where the best accuracy model by Kley is chosen. The coupling due to the transfer impedance occurs when the cables are laid in parallel along a common path. The two configuration investigated in this chapter were the coupling between two coaxial cables in free space and the coupling between two coaxial cables over a perfect conducting ground plane. By assuming that both cables are identical; and the metallic ground plane is perfect and infinitely large, the tertiary circuit were correspondingly derived in [2.4] for the two configurations investigated.

References

[2.1] Nahin, Paul J. (2002), Oliver Heaviside: The life, Work, and Times of an Electrical Genius of the Victorian Age, ISBN 0-8018-6909-9.

[2.2] "Study of literature on coaxial cables and connectors with reference to RF losses and leakage," ERA report 2848/1, August 1975.

[2.3] S. Sali, F.A. Benson and J.E. Sitch, "General crosstalk equations between two braided coaxial cables in free space," IEE Proceedings, vol. 130, pt. a, no. 6, September 1983.

[2.4] Christopoulos, C., Principles and Techniques of Electromagnetic Compatibility, second edition, CRC Press, Taylor & Francis Group, 2007.

[2.5] Schelkunoff. SA, "The electromagnetic theory of coaxial transmission lines and cylindrical shields," Bell Syst. Tech. J., 1934, 13, (14), pp. 532 – 579.

[2.6] H. Kaden, Wirbelstrome und Schirmung in der Nachrichtentechnik (Springer-Verlag, Berlin, 1959).

[2.7] N. Marcuvitz, Waveguide Handbook, MIT Rad. Lab. Ser., Vol. 10 (McGraw-Hill, New York, 1951).

[2.8] Thomas Kley, "Optimized single-braided cable shields," IEEE Transactions on Electromagnetic Compatibility, vol. 35, no. 1, February 1993.

[2.9] S. Sali, "Experimental and analytical investigations of crosstalk between leaky cables," Conference on Precision Electromagnetic Measurements Digest, June 1996, pp. 439 – 440.

[2.10] M. Tyni, "The transfer impedance of coaxial cables with braided outer conductor," in Wroclow EMC Symposium, 1976, pp. 410 – 419.

[2.11] Edward F. Vance, "Shielding effectiveness of braided-wire shields," IEEE Transactions on Electromagnetic Compatibility, vol. EMC-17, no. 2, May 1975, pp. 71 – 77.

[2.12] Noel A. McDonald, "Simple approximations for the longitudinal magnetic polarizabilities of some small apertures," IEEE Transactions on Microwave Theory and Techniques, vol. 36, no. 7, July 1988, pp. 1141 – 1144.

[2.13] S. Sali, "Screening efficiency of triaxial cables with optimum braided shields," IEEE Trans. EMC, vol. 32, 1990, pp. 125 – 136.

[2.14] F. A. Benson, P. A. Cudd and J. M. Tealby, "Leakage from coaxial cables," IEE Proc-A, vol. 139, no. 6, 1992, pp. 285-303.

[2.15] E. Homann, "Geschirmte kabel mit optimalen geflectschirmen," Nachrichtentechishe Zeitschrift, vol. 21, no. 3, pp. 155-161, 1968.

[2.16] Charles N. McDowell and Melvin J. Bernstein, "Surface transfer impedance measurements on subminiature coaxial cables," IEEE Transactions on EMC, vol. EMC-15, no. 4, Nov. 1973.

[2.17] J. N. Katakis, Transfer Impedance of Wire Braided Coaxial Cables at Radio and Microwave Frequencies, MEng thesis, University of Sheffield, Feb. 1983.

[2.18] Thomas Kley, "Measuring the coupling parameters of shielded cables", IEEE Trans. in EMC, vol. 35, no. 1, pp. 10 – 20, Feb. 1993.

[2.19] N. Akeam and M. H. Karatas, "Measurement of transfer impedance and screening attenuation effects on cables using tri-axial method," Intl. Journal on Technical and Physical Problems of Engineering, (IJTPE), iss. 10, vol. 4, no. 1, Mar. 2012, pp. 103 – 107.

[2.20] Jasper Goedbloed, Electromagnetic Compatibility, Philips Research Laboratories, Eindhoven, Prentice Hall International (UK) Ltd, 1992.

[2.21] John D. Kraus, Electromagnetics, Fourth Edition, McGraw-Hill, Inc, 1991

[2.22] Clayton R. Paul, Introduction to Electromagnetic Compatibility, Wiley Series in Microwave and Optical Engineering, 1992.

[2.23] C. R. Paul and S. A. Nasar, Introduction to Electromagnetic Fields, 2nd Edition, McGraw Hill, NY, 1987.

[2.24] Anatoly Tsaliovich, Cable Shielding for Electromagnetic Compatibility, Van Nostrand Reinhold, 1995.

[2.25] Clayton R. Paul, Analysis of Multiconductor Transmission Lines, John Wiley & Sons, Inc, 1994.

[2.26] D. W. P. Thomas, C. Christopoulos, F. Leferink and H. Bergsma, "Practical measure of cable coupling," Intl. Conf. on Electromagnetics in Advanced Applications, September 2009, pp. 803 – 806.

[2.27] D. R. J. White and M. Mardiguian, A Handbook Series on EMI and Compatibility, Volume 3: Electromagnetic Shielding, 1988, Pub. Don White Consultants Inc.

[2.28] David C. Chang, "Theory on small radiating apertures in the outer sheath of a coaxial cable," IEEE Transactions on Antennas and Propagation, vol. AP-26, no. 5, September 1978, pp. 674 – 682.

[2.29] Lothar O. Hoeft, "A simplified relationship between surface transfer impedance and more stirred chamber shielding effectiveness of cables and connectors," EMC Europe 2002 International Symposium on EMC, Sorrento, Italy, September 2002, pp. 441 – 446.

[2.30] Kendall F. Casey and Edward F. Vance, "EMP coupling through cable shields," IEEE Transactions on Antennas and Propagation, vol. AP-26, no. 1, January 1978.

[2.31] E. F. Vance, Coupling to Shielded Cables, Pub. A Wiley, 1978.

[2.32] S. A. Schelkunoff and T. M. Odarenko, "Crosstalk between coaxial transmission lines," Bell Syst. Tech. J., 1937, 26, pp. 144 – 164.

[2.33] J. C. Isaacs, Jr. and N. A. Strakhov, "Crosstalk in uniformly coupled lossy transmission lines," Bell Syst. Tech. J., January 1973, pp. 101 – 115.

[2.34] R. P. Booth and T. M. Odarenko, "Crosstalk between conductors in cable," Ibid., 1940, 19, pp. 358 – 384.

[2.35] K. E. Gould, "Crosstalk in coaxial cables – analysis based on short-circuited and open tertiaries," Ibid., 1940, 19, pp. 341 – 357.

[2.36] S. Sali, "A circuit-based approach for crosstalk between coaxial cables with optimum braided shields," IEEE Transactions on EMC, vol. 35, no. 2, May 1993.

[2.37] A. H. Badr, Prof. F.A. Benson and J. E. Stitch, "Interference between braided coaxial cables," IEE Proceedings, vol. 128, no. 5, July 1981, pp. 347 – 353.

[2.38] S. Sali, Prof. F.A. Benson and J.E. Sitch, "Coupling in a dielectric-coated multicoaxial-cable system, an analysis based on a quasi-tem model," IEE Proceedings, vol. 131, no. 1, January 1984.

[2.39] C. Smartt, S. Greedy, D.W.P. Thomas, C. Christopoulos, P. Sewell, "Modelling and measurement of crosstalk between shielded cables," EMC-Europe, Wroclaw, 2010.

[2.40] Clayton R. Paul, "Computation of crosstalk in a multiconductor transmission line," IEEE Transactions on EMC, vol. EMC-23, no. 4, November 1981.

[2.41] A. H. Badr, Prof. F.A. Benson and J.E. Sitch, "Coupling between a pair of coaxial cables in a multicable system," IEE Proc, vol. 128, pt. A, no.8, November 1981, pp. 547 – 551.

[2.42] S. Sali, F. A. Benson and J. E. Sitch, "Coupling between multicoaxial systems – I General considerations and efficient numerical method for crosstalk," IEE Proc., vol. 129, pt. A, no. 3, May 1982, pp. 162 – 166.

[2.43] S. Sali, F. A. Benson and J. E. Sitch, "Coupling between multicoaxial systems – II Theoretical predictions of crosstalk and experimental results," IEE Proc., vol. 129, pt. A, no. 3, May 1982, pp. 167 – 171.

[2.44] A. H. Badr, Prof. F.A. Benson and J.E. Sitch, "Coupling between coaxial cables over a ground place at low frequencies," IEE Proc. vol. 127, pt. A, no. 8, November 1980.

[2.45] John N. Ellinas, "Coupling between braided coaxial cables over a ground plane," Dept. Of Computer Engineering, TEI of Pireaus, P. Ralli & Thivon 250, Athens, Greece.

[2.46] R. J. Mohr, "Coupling between open and shielded wire lines over a ground plane," IEEE Transactions on EMC, vol. EMC-9, no. 2, September 1967.

[2.47] C. J. Smartt, S. Greedy, D.W.P. Thomas, C. Christopoulos and P. Sewell, "Shielded cable model development for time domain CEM

techniques," IET 8th Intl. Conf. on Computation in EMC (CEM 2011), April 2011, pp. 1 – 2.

[2.48] A. S. De C. Fernandes, "Propagation characteristics of a loose braid coaxial cable in free space," The Radio and Electronic Engineer, vol. 49, no. 5, pp. 255-260, May 1979.

[2.49] J. M. Tealby, P. A. Cudd and Prof. F. A. Benson, "Coupling between jacketed braided coaxial cables," IEE Proceedings, vol. 134, pt. A, no. 10, Dec. 1987.

[2.50] C. Gordon, "Time-domain simulation of multiconductor transmission lines with frequency-dependent losses," IEEE Proc. Intl. Conf. on Computer Design: VLSI in Computers and Processors, Oct. 1992, pp. 222 – 228.

[2.51] Colin Gordon, Thomas Blazeck and Raj Mittra, "Time-domain simulation of multiconductor transmission lines with frequency-dependent losses," IEEE Transactions on Computer-Aided Design, vol. 11, no. 11, pp. 1372-1387, Nov. 1992.

[2.52] P. Naylor and Christopoulos C., "Coupling between electromagnetic fields and multimode transmission systems using TLM," Intl. Journal of Numerical Modelling: Electronic Networks, Devices and Fields, vol. 2, pp. 227 – 240, 1989.

[2.53] S. Sali, "Modal technique for the time domain analysis of crosstalk between coaxial cables," IEEE in Electronics and Communication Engineering Journal, vol. 1, no. 6, Nov. 1989, pp. 254 – 260.

CHAPTER 3

EXPERIMENTAL MEASUREMENTS

3.1 Introduction to Measurement Facilities and Instruments

The crosstalk experiments presented in this chapter involve measurements in the frequency domain (FD) and the time domain (TD). The facilities and instruments used for the FD and TD measurements are shown in Figures 3.1.2 and 3.1.3, respectively. Experimental verifications are also carried out to estimate the stray reactance of the brass end plates for both common and differential modes of the tertiary circuit mentioned in Chapter 2. The instruments for this measurement are shown in Figure 3.1.4. Standard connecting cables (SMA/BNC) are mainly used to provide input and output connections from one device to another, depicted in Figure 3.1.1.

Figure 3.1.1: Typical SMA/BNC cables used to provide connections

3.1.1 Frequency Domain (FD) Measurement Instruments

Frequency domain measurements were performed with the following instruments and depicted in Figure 3.1.2:

I Vector Network Analyser (VNA)

- Series: E8326B
- Frequency Range: 10MHz – 20GHz

- Input/output Impedance: 50Ω
- Electronic Calibration Module: N4691-60003

II SMA/BNC Connecting Cables

Two connecting cables of 1m in length are used to connect to the two ports of the VNA. The cables are calibrated with an electronic calibration module N4691-60003 before conducting the experiment. The FD crosstalk (in dB) is obtained from the scattering parameter, S_{21}, of the VNA readings.

(a) (b)

Figure 3.1.2: (a) Vector Network Analyser. (b) Electronic Calibration Module.

3.1.2 Time Domain (TD) Measurement Instruments

Time domain measurements were carried out using the following instruments and depicted in Figure 3.1.3:

I Time-Domain Oscilloscope (TDO)

- Series: MSO810A
- Maximum Frequency: 1GHz
- Minimum Voltage Scale: 1mV/div
- Input/output Impedance: 50Ω

II Broadband Power Amplifier (AMP)

- Series: ENI 604L

- Maximum Radio Frequency (RF) Input: 13dBm
- Gain (G): 45dB
- Frequency Range: 0.5 – 1000MHz

III Pulse Function Arbitrary Generator (PFAG)

- Series: 81150A
- Maximum Frequency: 120MHz
- Input/output Impedance: 50Ω

IV Attenuator (ATT)

- Attenuation: -30dB
- Frequency Range: 0 – 18GHz

V SMA/BNC Connecting Cables

Two connecting cables of 2 meters and one connecting cable of 1m in length are used to connect to the input and output ports of the PFAG, TDO and AMP. The TD crosstalk (in V) is obtained from the TDO readings.

(a) (b)

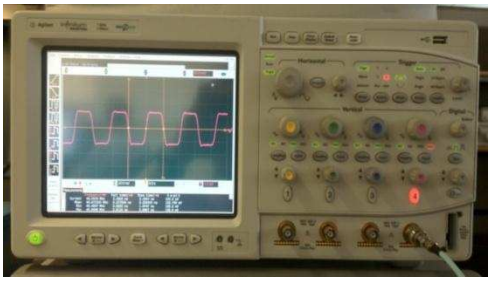

(c) (d)

Figure 3.1.3: (a) MSO series Time Domain Oscilloscope. (b) ENI series Broadband Power Amplifier. (c) Pulse Function Arbitrary Generator. (c) Attenuator

3.1.3 Stray Reactance Measurement in the Brass Plates Instruments

Stray reactance of the brass end plates were measured using the following instruments and shown in Figure 3.1.4:

I Time Domain Wide Bandwidth Oscilloscope (TDR)

- Series: DCA 86100B
- Time Domain Reflectometer Module Series Installed: 54754A
- Input/output Impedance: 50Ω

II SMA/BNC Connecting Cables

One connecting cable of 1m in length is used to connect to the output of the TDR module. The cable losses are ignored in the measurements.

The stray reactance of the cable is observed through the reflection of the cable's scattering properties shown on the TDR screen.

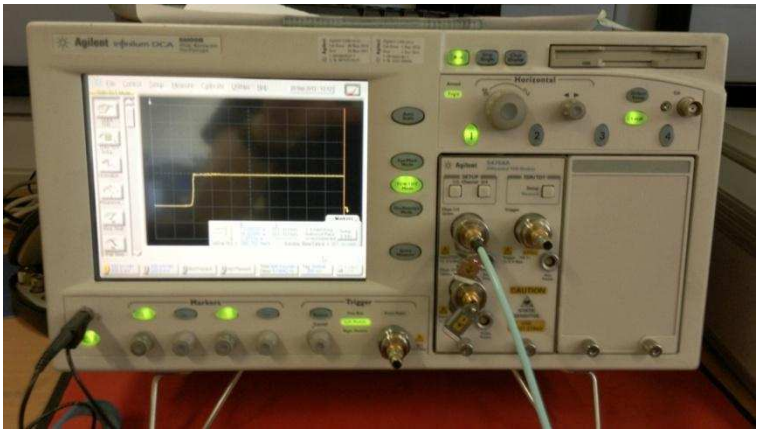

Figure 3.1.4: DCA series Time Domain Wide Bandwidth installed with a Time Domain Reflectometer Module

3.2 The Crosstalk Measurement Set Up

The crosstalk measurement is carried out throughout using two RG-58 coaxial cables. The said coaxial cables are both 1.22m in length and clamped with a SMA bulk head male-connector at each end, shown in Figure 3.2.1. The coaxial cables are fixed through two brass connector end plates, where each plate has dimensions of

30cm in width by 30cm in length, which complete the current return path and act as means of physical support for the cables. The end plates used are made of brass, where multiple holes are drilled to allow for varying different centre-to-centre separations, ie: 2cm, 5cm, 10cm and 15cm between the two cables; and varying heights from the ground plane, ie: 11cm, 16.5cm, 21.5cm and 26.5cm; as illustrated in Figure 3.2.2.

Figure 3.2.1: The two RG-58 coaxial cables with 1.22m in length

(a)

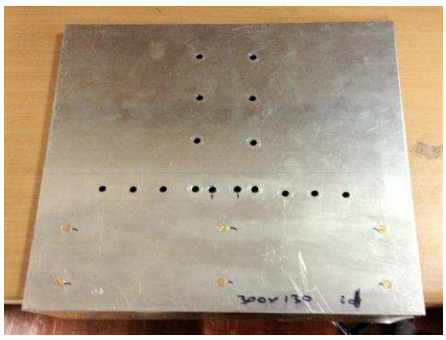

(b)

(c)

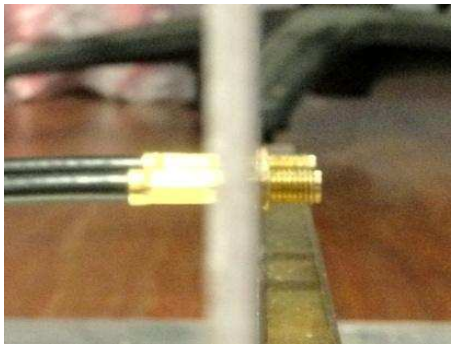

Figure 3.2.2: (a) Brass connector end plate. (b) The SMA bulk head connectors clamped onto the cables. (c) The SMA connectors fixed through the brass end plate.

3.2.1 Frequency Domain (FD) Measurement

A. Coupling between Two RG-58 Coaxial Cables in Free Space

The measurement arrangement used to obtain the crosstalk between two coaxial cables in free space is illustrated by Smartt et al. [3.1]. Figure 3.2.3 shows the actual experimental arrangement of two RG-58 coaxial cables in parallel to each other. The crosstalk measurements between the two cables are performed in an open laboratory space on a wooden bench top, clear from all possible external sources. The arrangement comprises of the source and victim cables terminated with 50Ω loads at each end. Note that there is no metallic ground plane involved in this experiment.

(a)

(b)

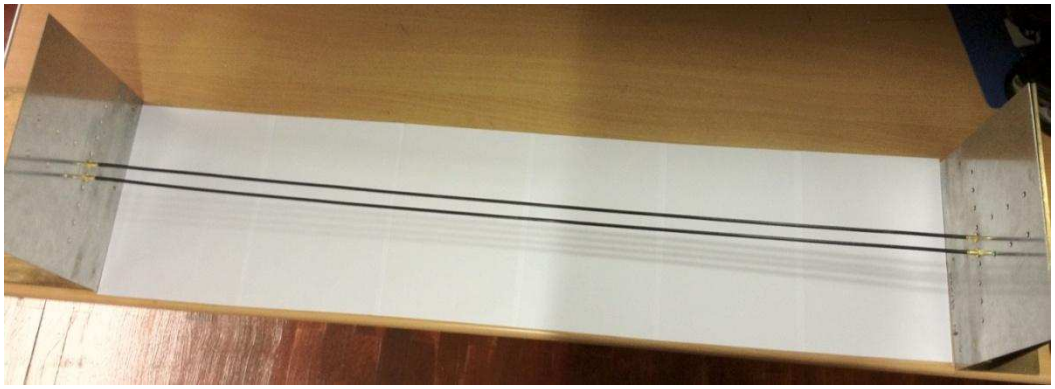

(c)

(d)

Figure 3.2.3: The arrangement of two RG-58 coaxial cables in free space. (a) Side *view. (b) Plan view. (c) Back view. (d) 50Ω loads*.

The VNA is used to provide the signal source and detection. The source cable is connected to Port 1, where it acts as a transmitter, of the VNA and the victim cable is

in turn connected to Port 2 of the VNA, where it acts as a receiver. The VNA is set up to measure the degree of cable coupling or crosstalk, S_{21}, in dB, sweeping over a frequency range of 10MHz to 1GHz with 1601 sample points. The instrument and test leads were calibrated with an electronic calibration module N4691-60003. The measurement set up together with the details of the brass connector end plates are illustrated in Figure 3.2.4.

(a)

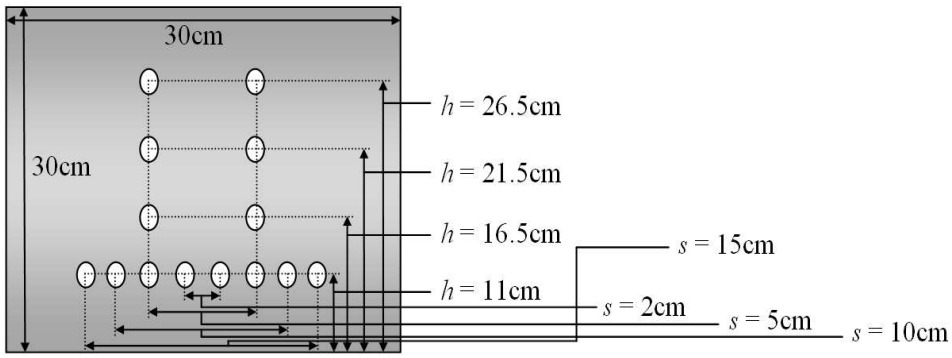

(b)

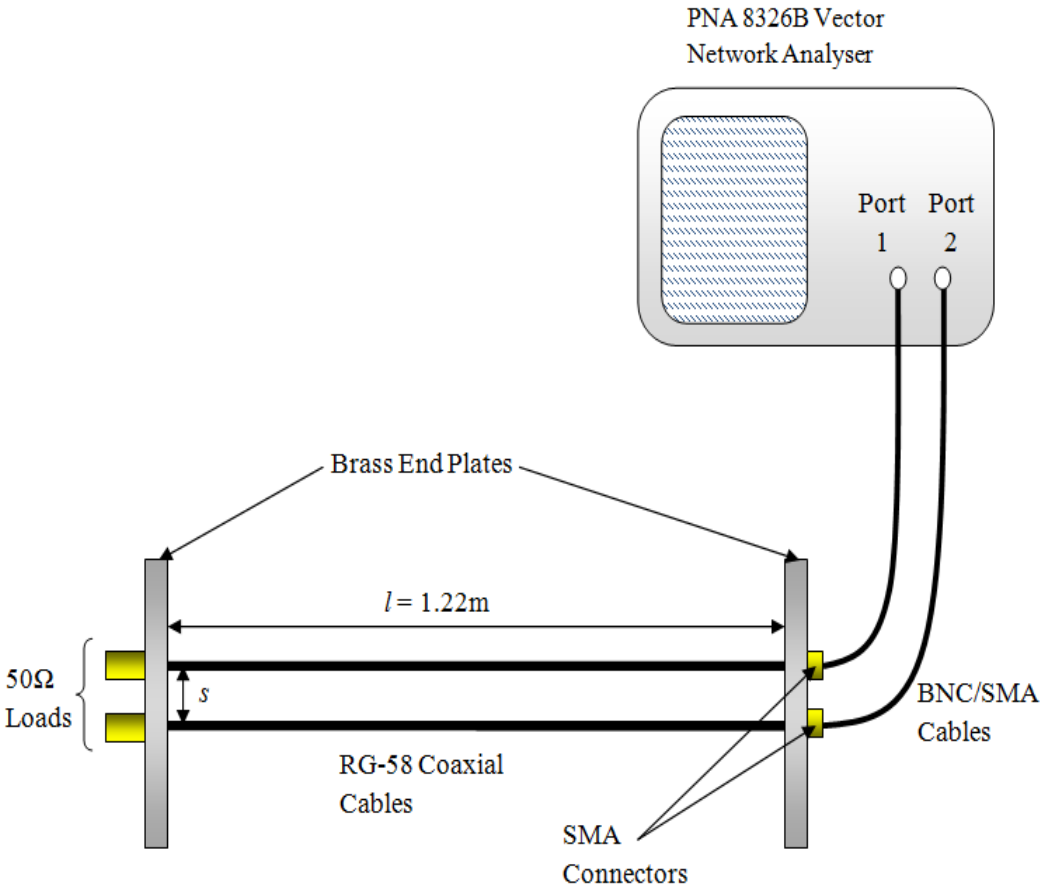

Figure 3.2.4: (a) Details of the brass connector end plates. (b) The frequency domain crosstalk measurement set up for two RG-58 coaxial cables in free space.

Figures 3.2.5 – 3.2.8 show frequency domain measurement results of the coupling between two RG-58 coaxial cables in free space, with frequencies ranging from 10MHz to 1GHz.

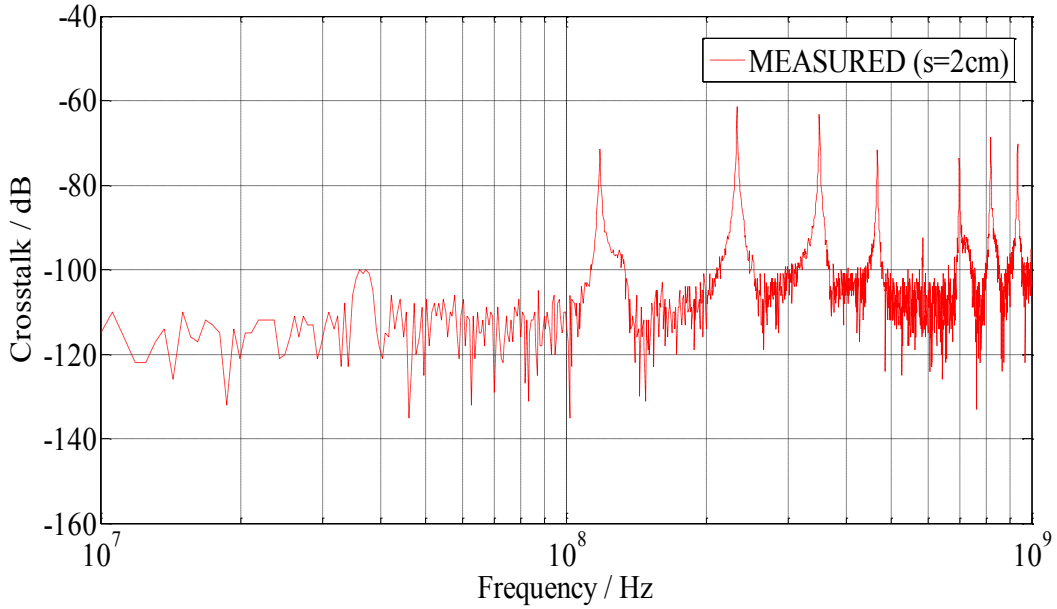

Figure 3.2.5: FD measurement – Crosstalk between two RG-58 coaxial cables in free space with separation, s = 2cm

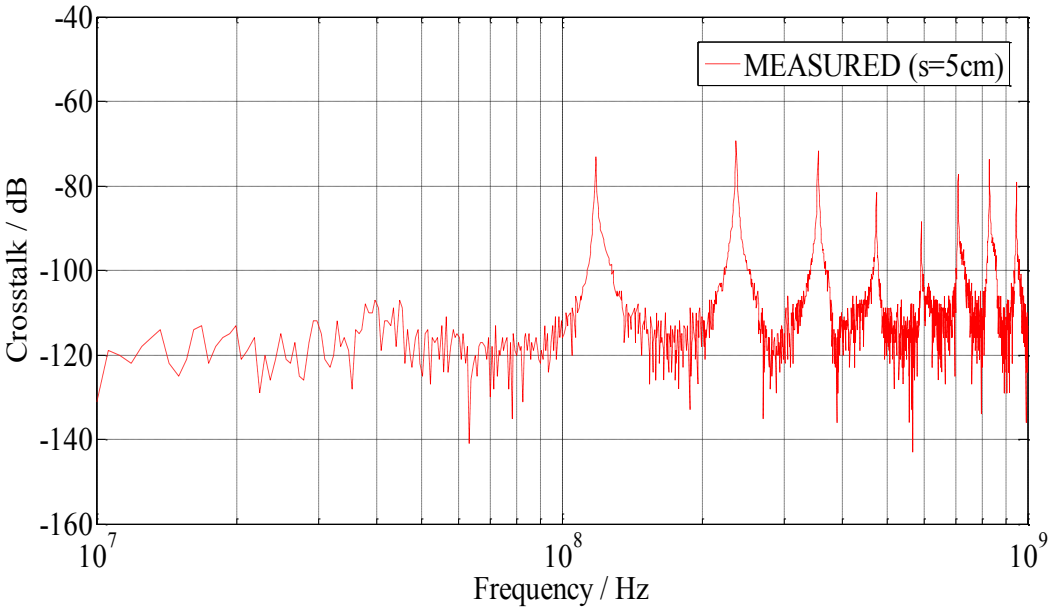

Figure 3.2.6: FD measurement – Crosstalk between two RG-58 coaxial cables in free space with separation, s = 5cm

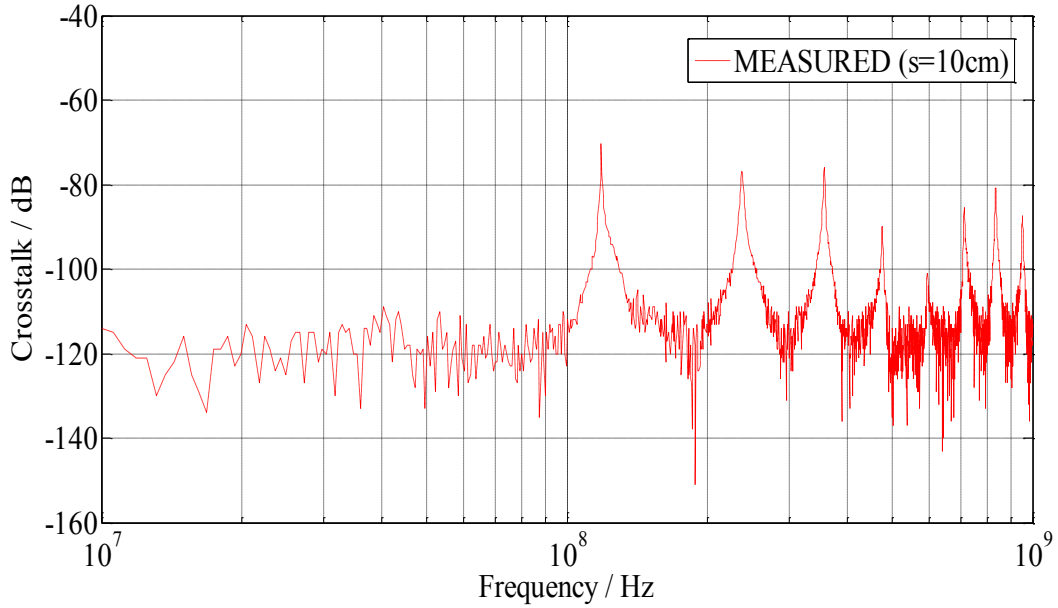

Figure 3.2.7: FD measurement – Crosstalk between two RG-58 coaxial cables in free space with separation, s = 10cm

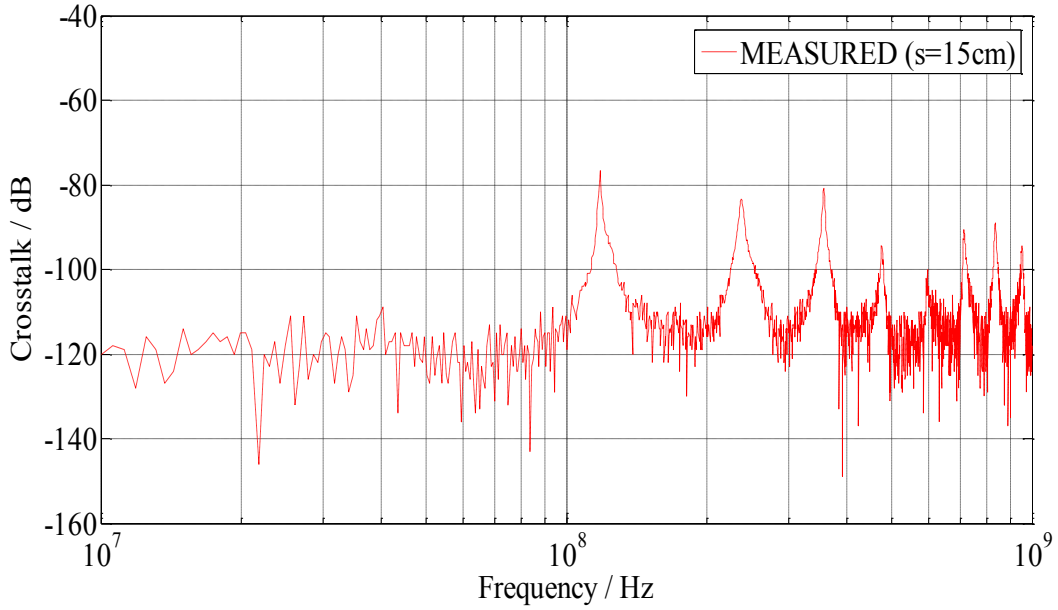

Figure 3.2.8: FD measurement – Crosstalk between two RG-58 coaxial cables in free space with separation, s = 15cm

B. Coupling between Two RG-58 Coaxial Cables via a Metallic Ground Plane

The measurement arrangement used to obtain the crosstalk between two coaxial cables via a metallic ground plane is illustrated by Badr et al. [3.1] and [2.41]. Figure 3.2.9 shows the actual experimental arrangement of two RG-58 coaxial cables in parallel to each other over an aluminium ground sheet of dimensions 0.5m in width by 2m in length, which the brass connector end plates are placed on. The crosstalk measurements between the two cables are performed on the floor of an open laboratory space. The arrangement comprises of the source and victim cables terminated with 50Ω loads at each end. Note that this experiment involves a metallic ground plane.

(a)

(b)

(c) (d)

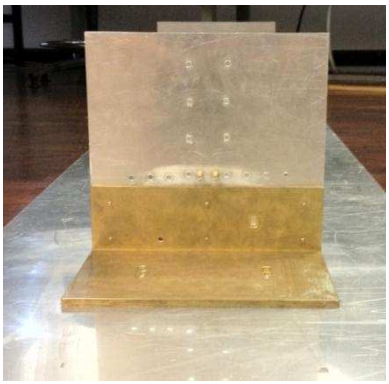

Figure 3.2.9: The arrangement of two RG-58 coaxial cables above an aluminium ground plane. (a) Side view. (b) Plan view. (c) Back view. (d) Brass end plate placed on the aluminium ground plane.

Similar to section 3.2.1A, Port 1 of the VNA is connected to the source cable while Port 2 is connected to the victim cable. The measurement set up is illustrated in Figure 3.2.10.

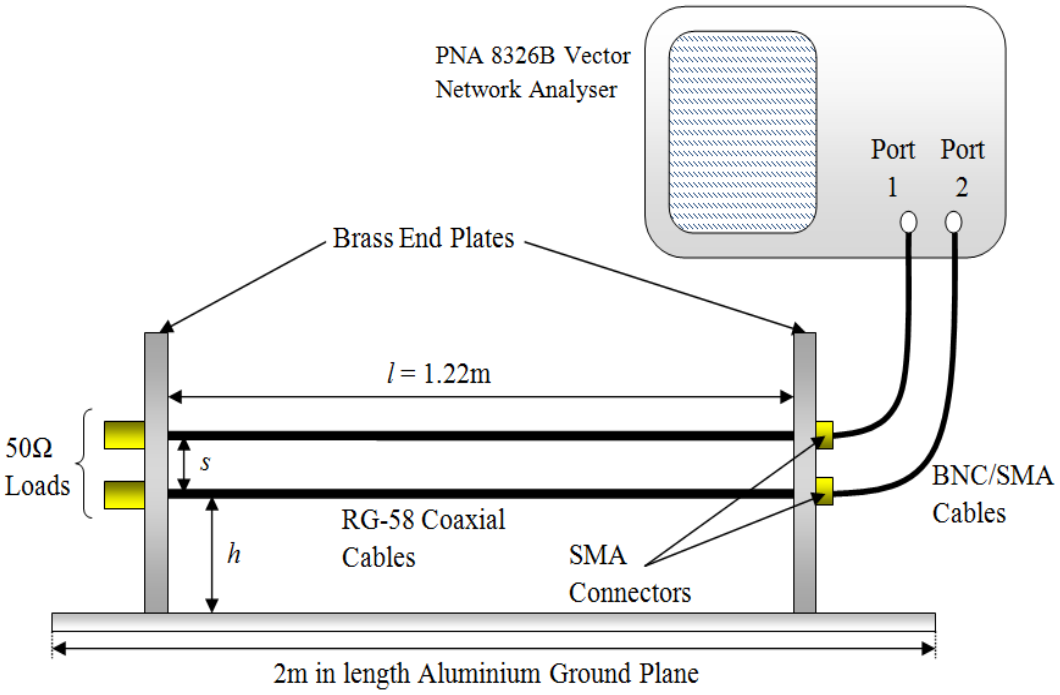

Figure 3.2.10: The frequency domain crosstalk measurement set up for two RG-58 coaxial cables over an aluminium ground plane

With frequencies ranging from 10MHz to 1GHz and keeping the height of the cables from the ground plane, h, constant at 11.5cm; Figures 3.2.11 – 3.2.14 show frequency domain measurement results for varying separations between the cables, s, (2, 5, 10 and 15cm). In conjunction, by keeping the separation, s, constant at 5cm, Figures 3.2.15 – 3.2.17 show frequency domain measurement results by varying h (16.5, 21.5 and 26.5cm).

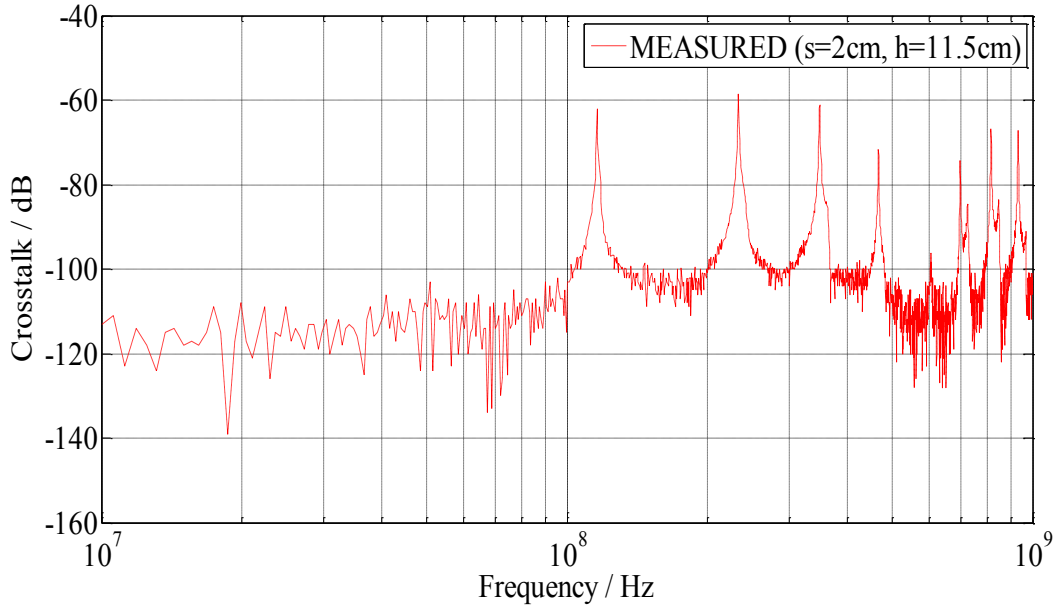

Figure 3.2.11: FD measurement – Crosstalk between two RG-58 coaxial cables in free space with separation, s = 2cm and height, h = 11.5cm

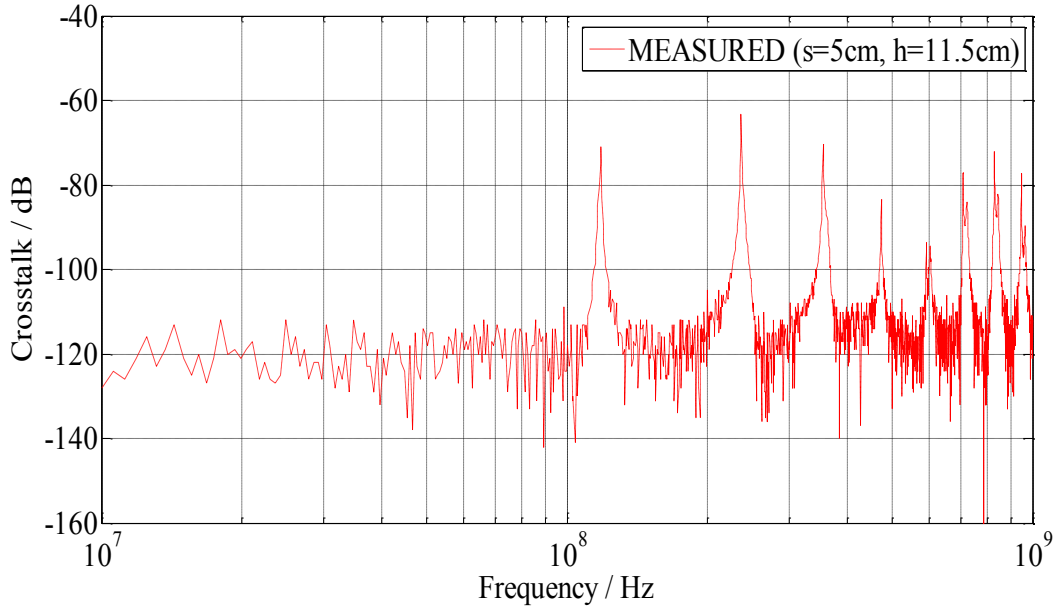

Figure 3.2.12: FD measurement – Crosstalk between two RG-58 coaxial cables in free space with separation, s = 5cm and height, h = 11.5cm

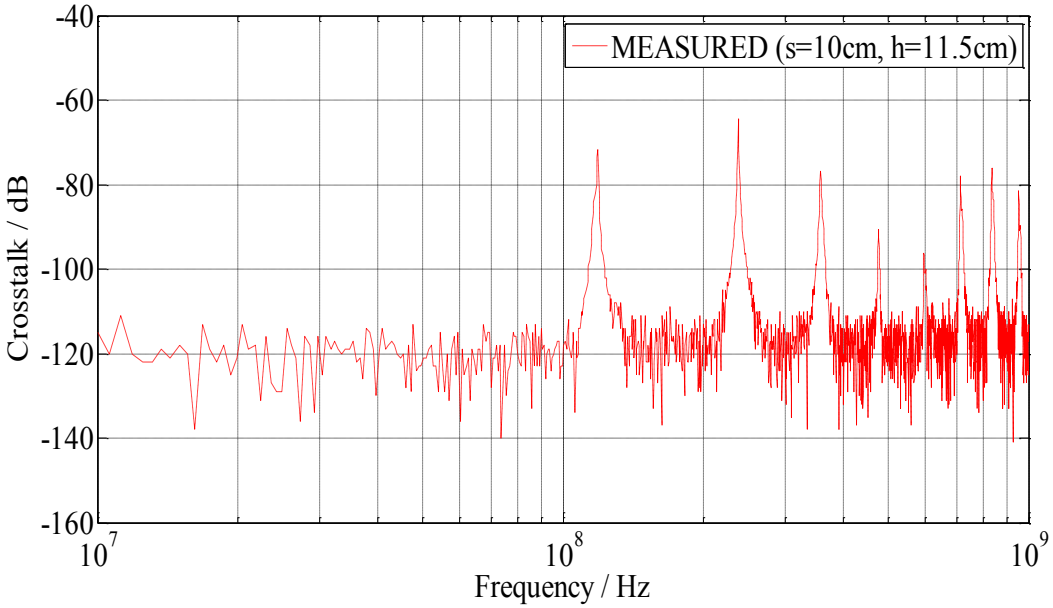

Figure 3.2.13: FD measurement – Crosstalk between two RG-58 coaxial cables in free space with separation, s = 10cm and height, h = 11.5cm

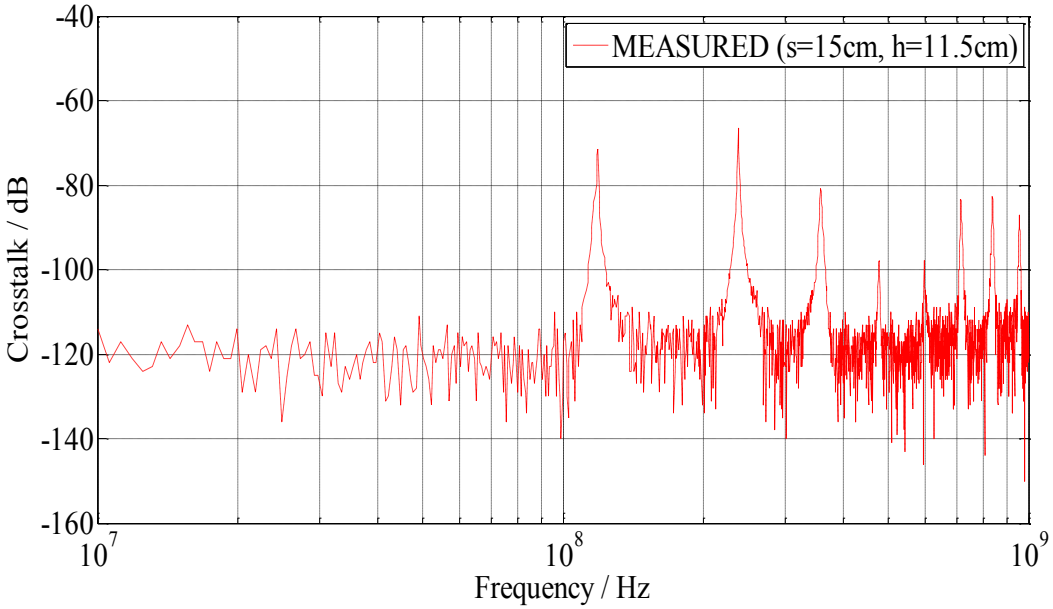

Figure 3.2.14: FD measurement – Crosstalk between two RG-58 coaxial cables in free space with separation, s = 15cm and height, h = 11.5cm

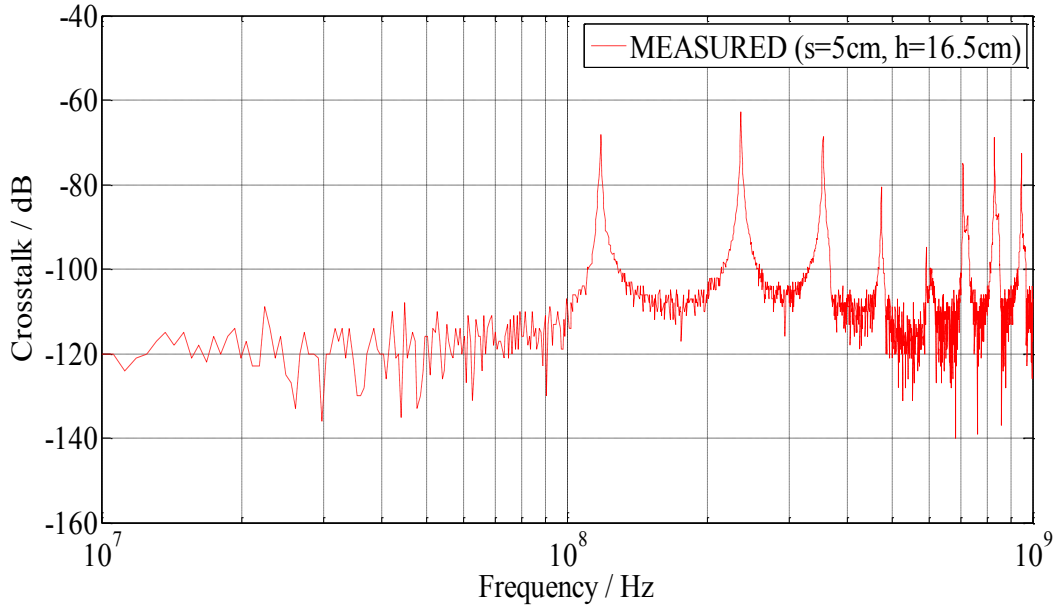

Figure 3.2.15: FD measurement – Crosstalk between two RG-58 coaxial cables in free space with separation, s = 5cm and height, h = 16.5cm

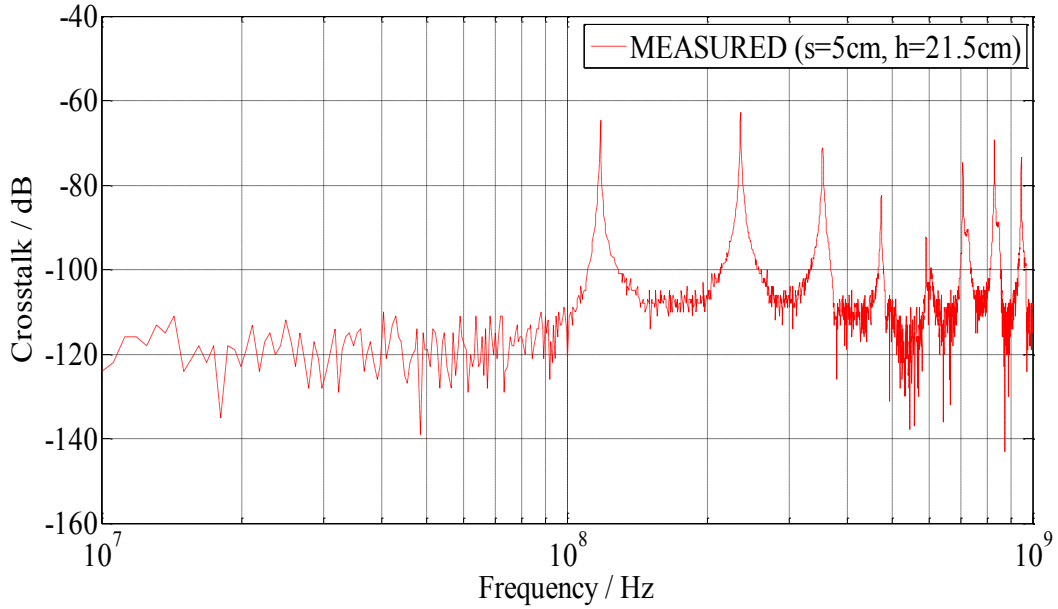

Figure 3.2.16: FD measurement – Crosstalk between two RG-58 coaxial cables in free space with separation, s = 5cm and height, h = 21.5cm

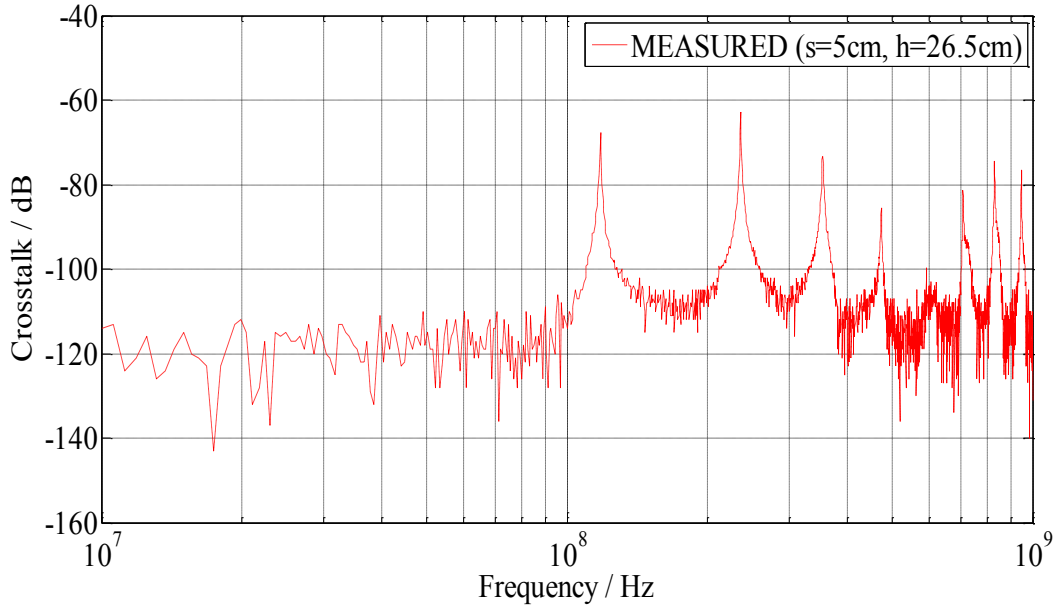

Figure 3.2.17: FD measurement – Crosstalk between two RG-58 coaxial cables in free space with separation, s = 5cm and height, h = 26.5cm

3.2.2 Time Domain (TD) Measurement

A. Coupling between Two RG-58 Coaxial Cables in Free Space

The experimental environment and measurement tools remained the same as the FD measurements carried out in section 3.2.1, the same configuration from Figure 3.2.4 is used to obtain the time domain crosstalk measurement results for the coupling of two RG-58 coaxial cables in free space. The objective is to further validate the accuracy of the time domain numerical model. However, the VNA is replaced by a PFAG instead, where it functions to generate a signal source to one of the RG-58 coaxial cables. A square wave source signal has been investigated, where the significance of the broadband frequency (square) waveforms can be observed (see Chapter 5). Since the crosstalk signal is relatively small, the AMP is used to amplify the source signal to a desired amplitude, which allows the output to then be observed from the adjacent cable on the same end using the TDO. The corresponding measurement set up is depicted as a flow diagram in Figure 3.2.18 and illustrated in Figure 3.2.19.

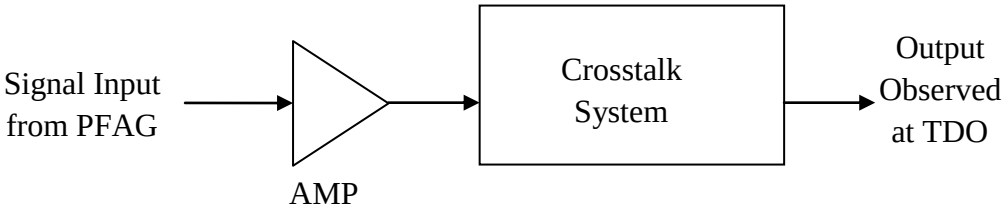

Figure 3.2.18: Flow diagram of the time domain crosstalk system

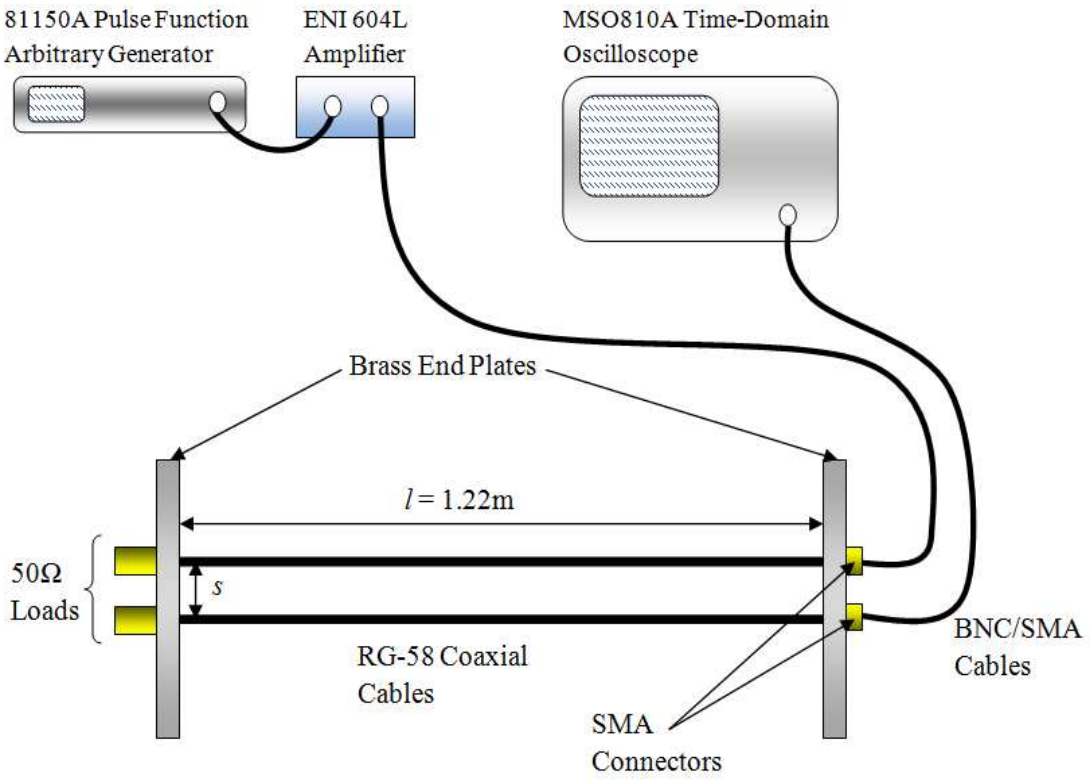

Figure 3.2.19: The time domain crosstalk measurement set up for two RG-58 coaxial cables in free space

Note that the distance between the two connecting cables (BNC/SMA cables) leading from the RG-58 coaxial cables to the test equipments must be significantly larger than the separation s to prevent unwanted crosstalk interference. The first 2 peak resonant frequencies were observed to be at approximately 118MHz and 233MHz; as depicted in section 3.2.1A. With fundamental frequencies, 39.33MHz and 46.67MHz, fed into the amplified square wave in Figure 3.2.18, Figures 3.2.20 – 3.2.22 present their corresponding time domain measurement results for separations, s (2, 5 and 10cm), respectively.

(a)

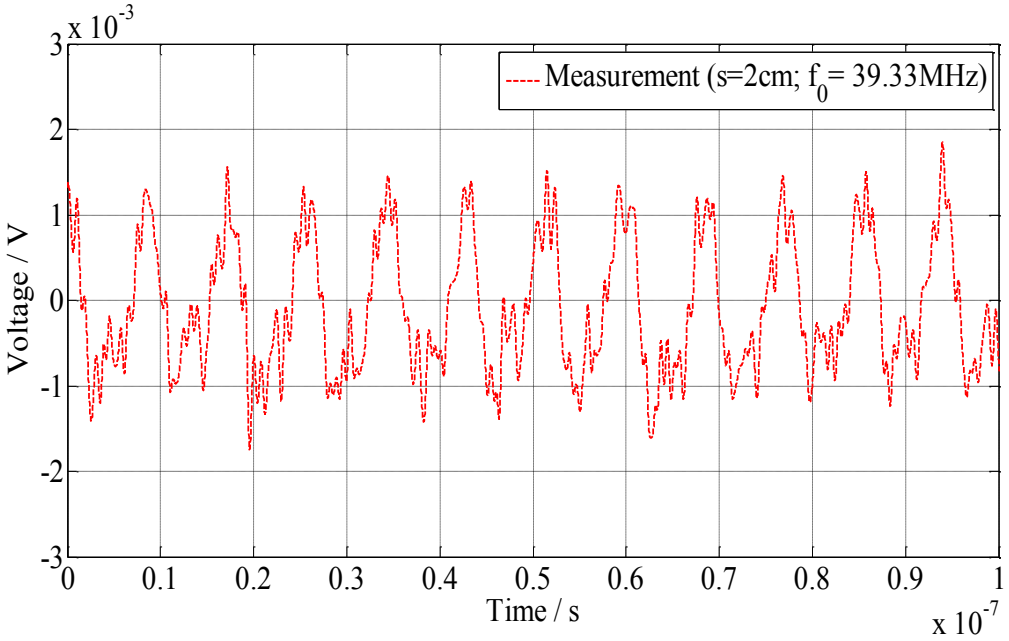

(b)

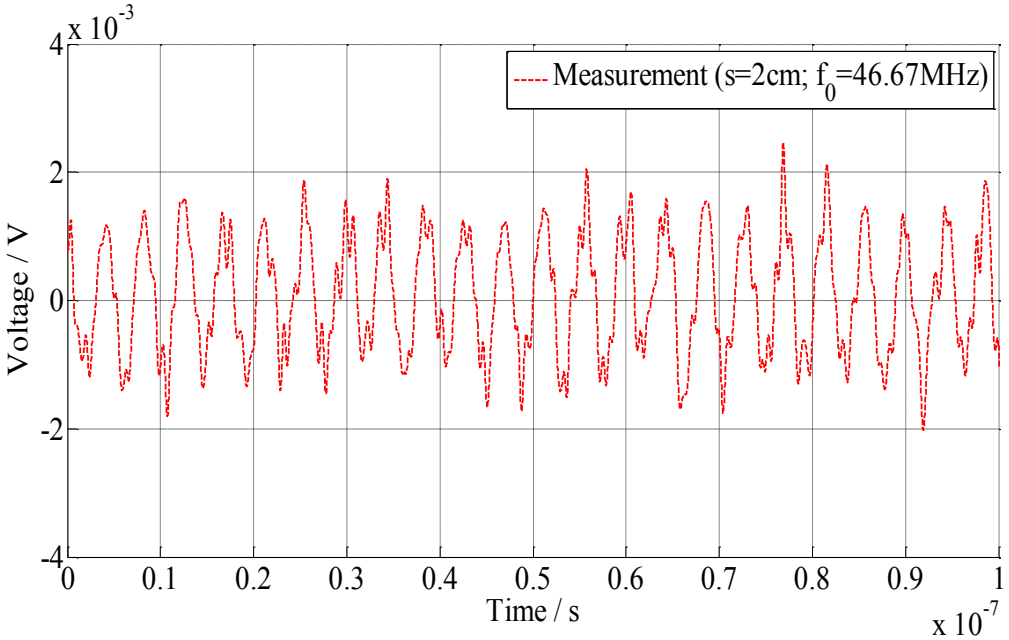

Figure 3.2.20: TD measurement – Crosstalk of two RG-58 coaxial cables in free space for a separation, s = 2cm, and input of fundamental frequency (a) 39.33MHz. (b) 46.67MHz.

(a)

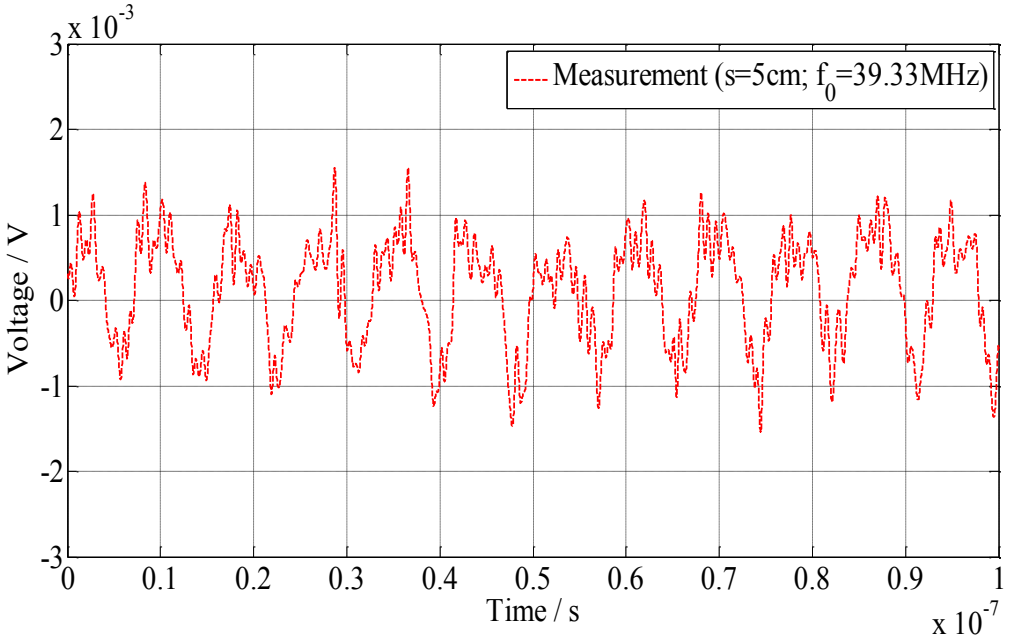

(b)

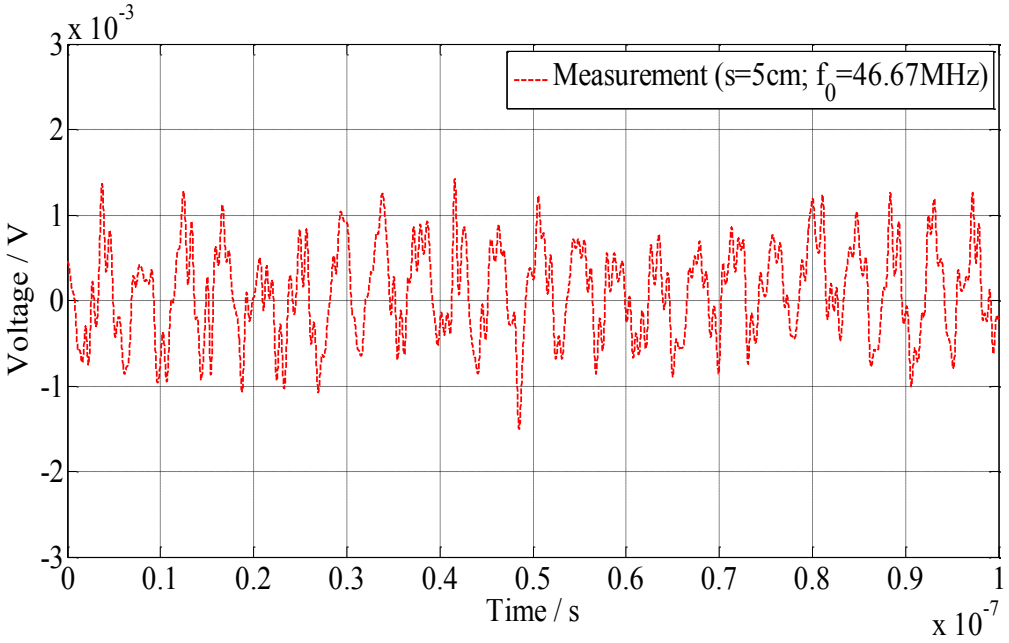

Figure 3.2.21: TD measurement – Crosstalk of two RG-58 coaxial cables in free space for a separation, s = 5cm, and input of fundamental frequency (a) 39.33MHz. (b) 46.67MHz.

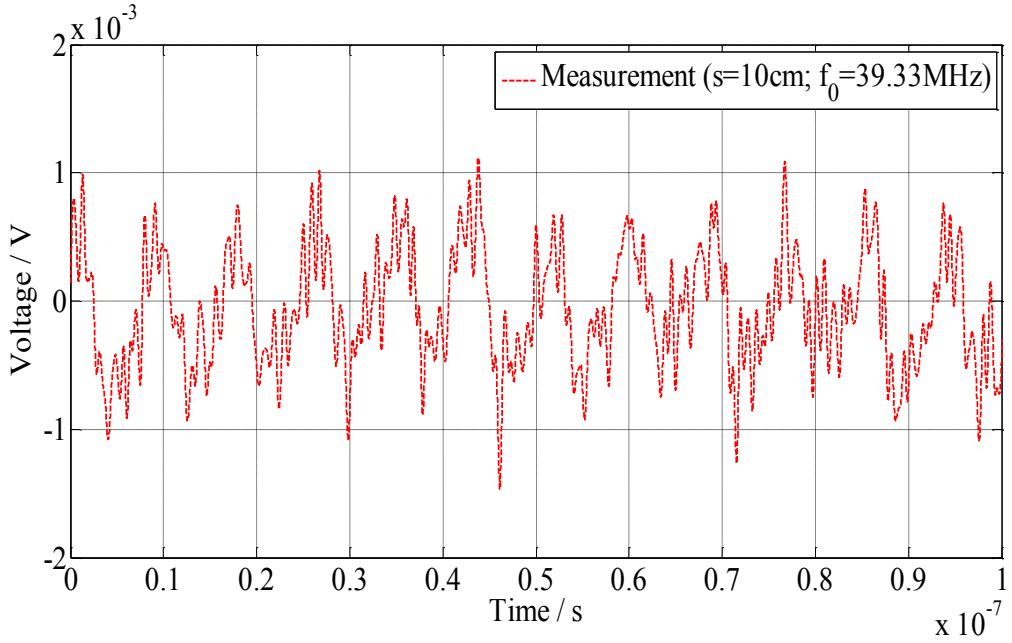

Figure 3.2.22: TD measurement – Crosstalk of two RG-58 coaxial cables in free space for a separation, s = 10cm, and input of fundamental frequency 39.33MHz.

B. Coupling between Two RG-58 Coaxial Cables via a Metallic Ground Plane

Similarly, the TD measurement set up for the coupling of two RG-58 coaxial cables via a ground plane follows the same configuration from Figure 3.2.6. Using the experimental instruments and flow diagram illustrated in section 3.2.2A, the corresponding measurement set up can be illustrated in Figure 3.2.23.

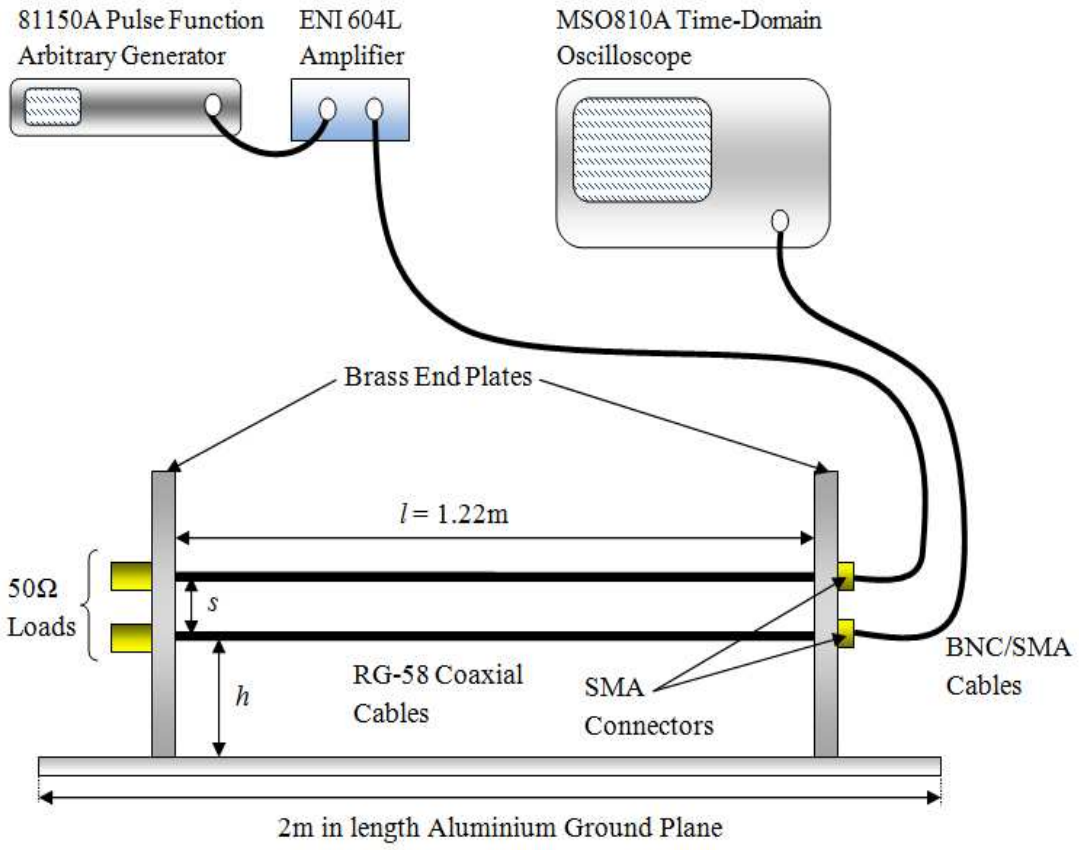

Figure 3.2.23: The time domain crosstalk measurement set up for two RG-58 coaxial cables over an aluminium ground plane

With an extra ground plane, this measurement set up applies the necessary conditions in section 3.2.2A. The first 2 peak resonant frequencies were observed to be at approximately 118MHz and 235MHz; as depicted in section 3.2.1B. With fundamental frequencies, 38.4MHz and 46.1MHz, fed into the amplified square wave; keeping the height, h, constant at 11.5cm, Figures 3.2.24 – 3.2.26 present time domain measurement results for various separations, s (2, 5 and 10cm); whereas Figures 3.2.27 and 3.2.28 present time domain measurement results for various h (16.5cm and 26.5cm) while keeping s constant at 5cm.

(a)

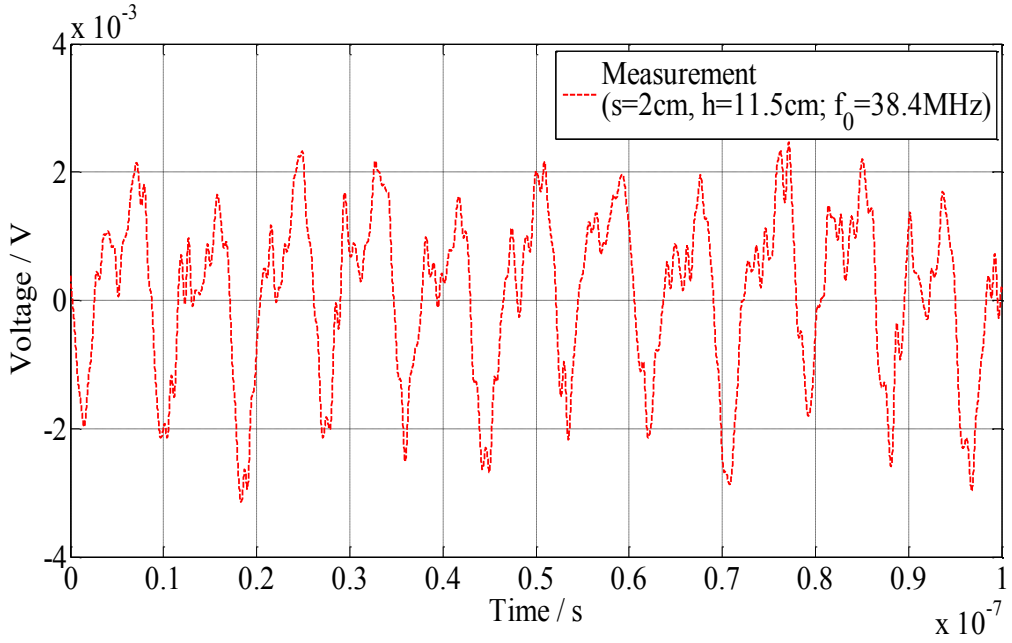

(b)

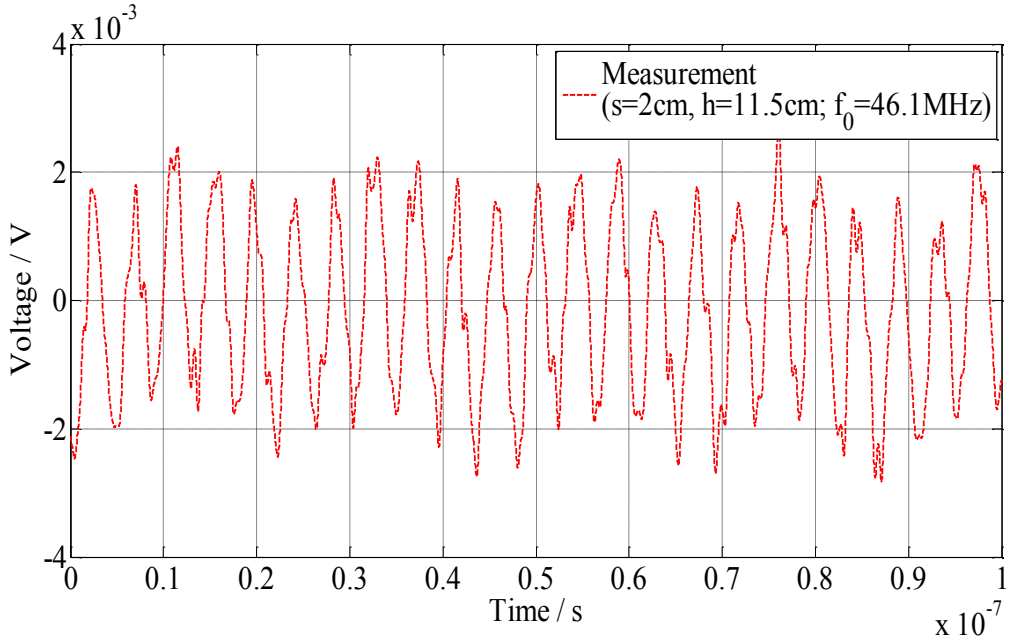

Figure 3.2.24: TD measurement – Crosstalk of two RG-58 coaxial cables via ground plane for separation, s = 2cm and height, h = 11.5cm; and input of fundamental frequency (a) 38.4MHz. (b) 46.1MHz.

(a)

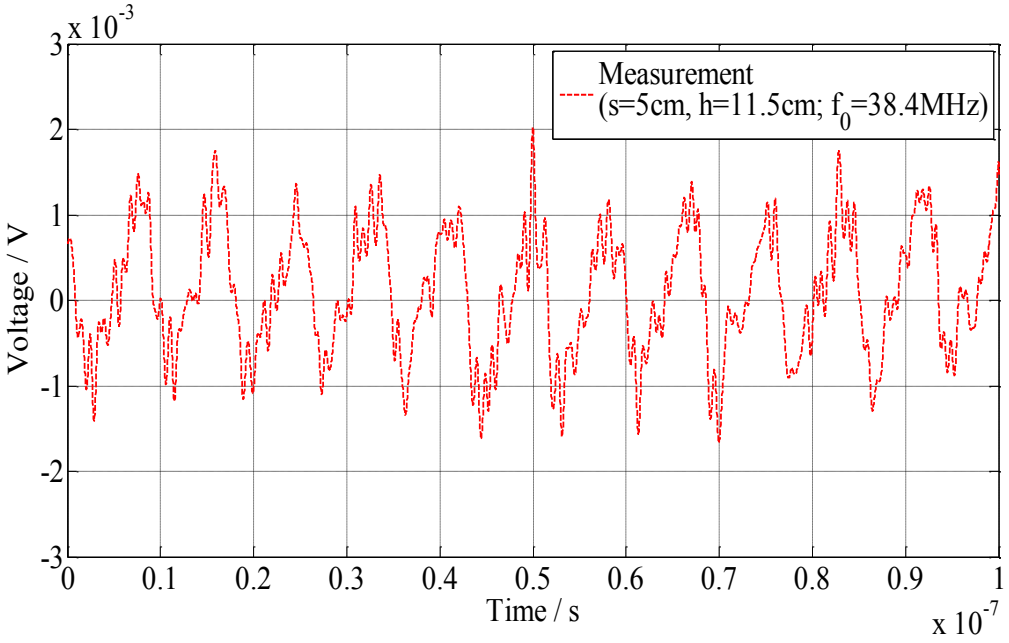

(b)

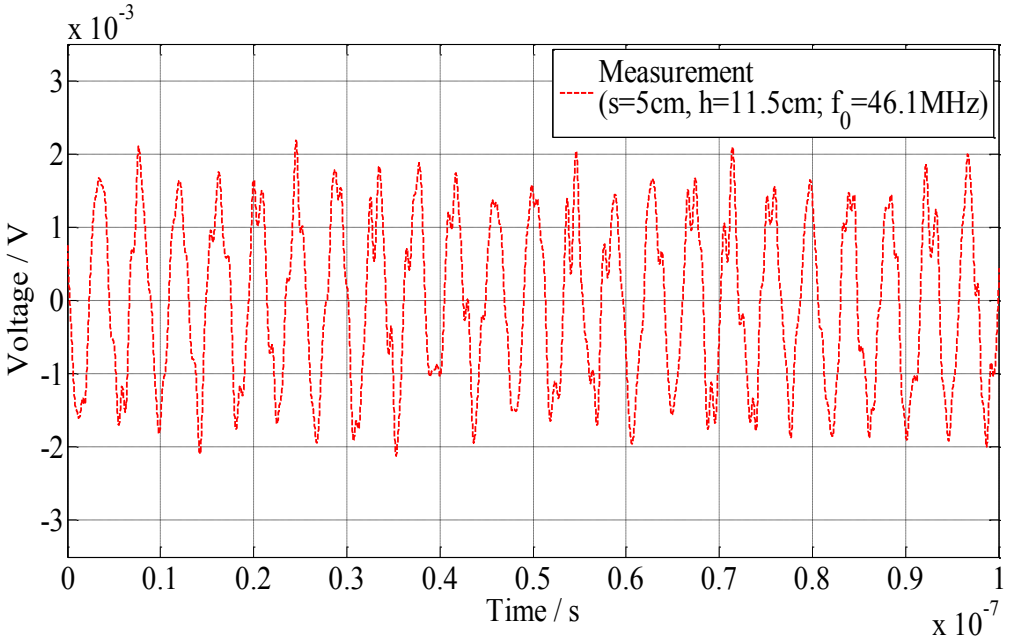

Figure 3.2.25: TD measurement – Crosstalk of two RG-58 coaxial cables via ground plane for separation, s = 5cm and height, h = 11.5cm; and input of fundamental frequency (a) 38.4MHz. (b) 46.1MHz.

(a)

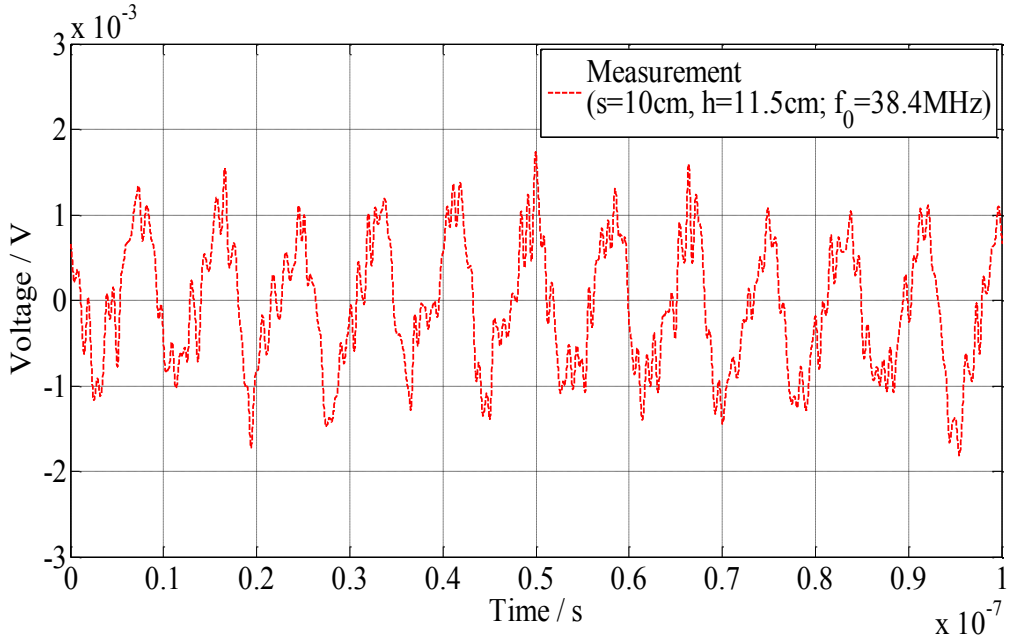

(b)

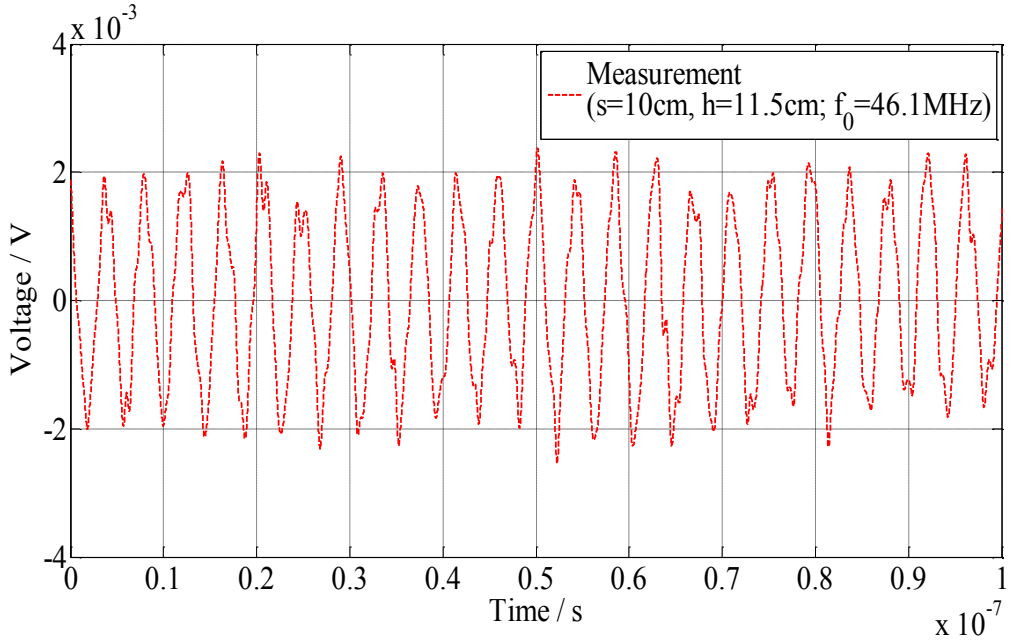

Figure 3.2.26: TD measurement – Crosstalk of two RG-58 coaxial cables via ground plane for separation, s = 10cm and height, h = 11.5cm; and input of fundamental frequency (a) 38.4MHz. (b) 46.1MHz.

(a)

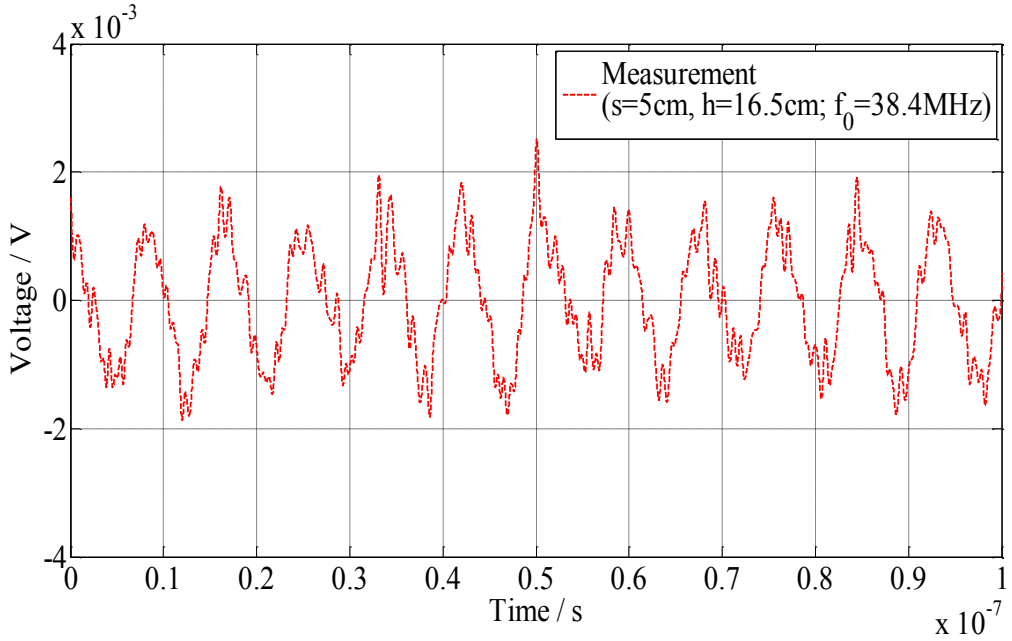

(b)

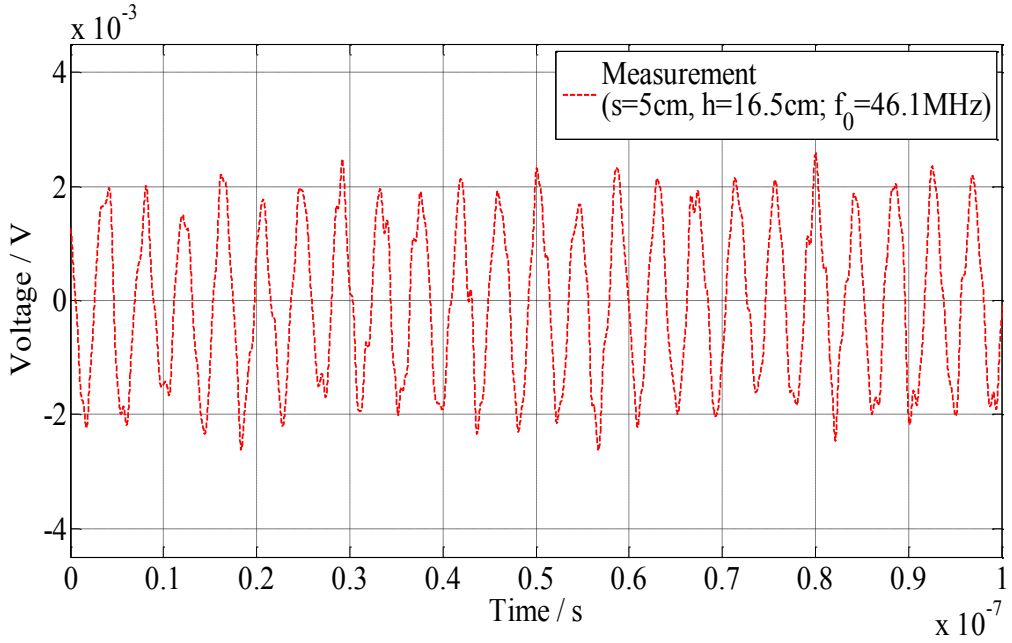

Figure 3.2.27: TD measurement – Crosstalk of two RG-58 coaxial cables via ground plane for separation, s = 5cm and height, h = 16.5cm; and input of fundamental frequency (a) 38.4MHz. (b) 46.1MHz.

(a)

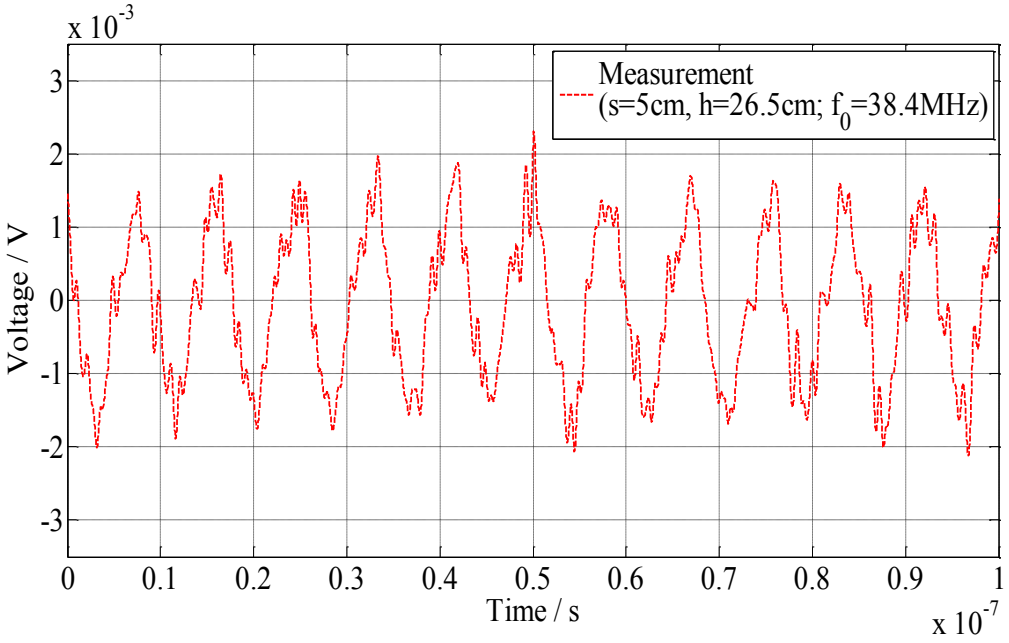

(b)

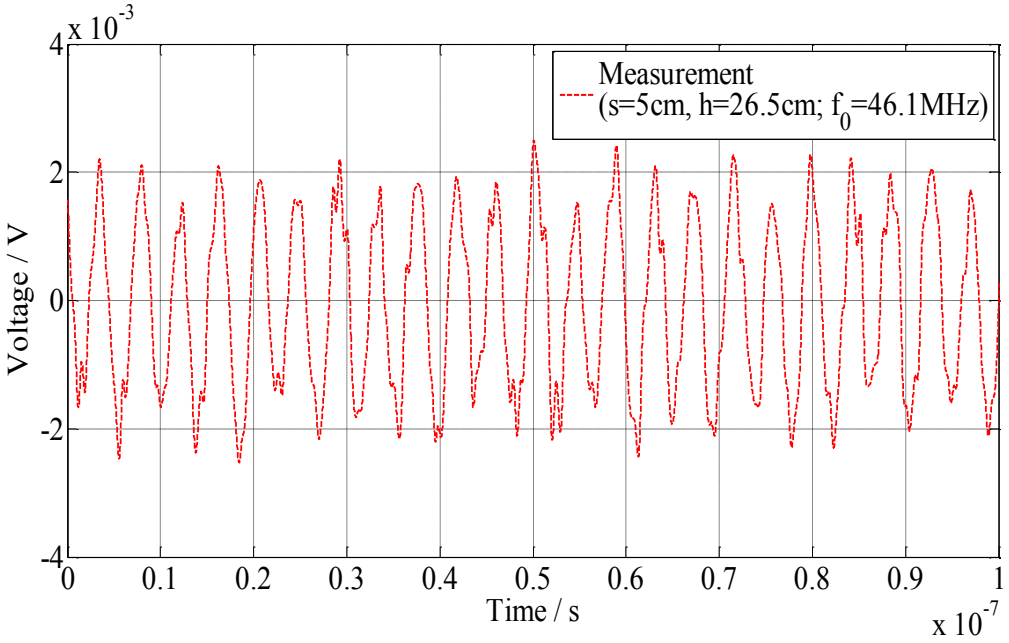

Figure 3.2.28: TD measurement – Crosstalk of two RG-58 coaxial cables via ground plane for separation, s = 5cm and height, h = 26.5cm; and input of fundamental frequency (a) 38.4MHz. (b) 46.1MHz.

C. Non-Linearity of the Broadband Power Amplifier

Throughout the experiment, it has been discovered that the ENI 604L broadband power amplifier does not provide a linear gain of 45dB. This effect can be observed through the change in the input signal after amplifying the signal through the amplifier, illustrated in Figure 3.2.29.

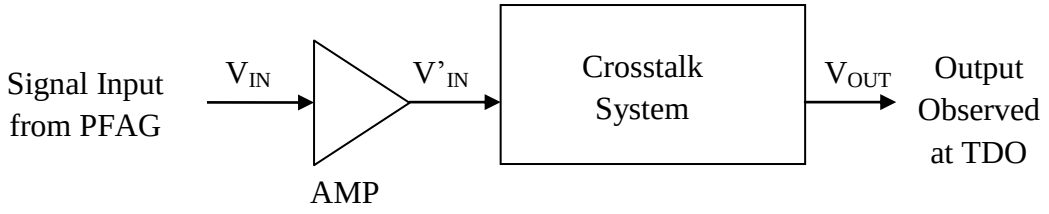

Figure 3.2.29: Flow diagram showing the non-linearity effect of the broadband power amplifier

where V_{IN} represents the signal source input from the PFAG and V'_{IN} represents the signal input distortion after passing through the amplifier; and V_{OUT} represents the signal output on the TDO.

For an example, suppose a 64mV peak voltage square wave of fundamental frequency 46.67MHz serves as an input signal from the PFAG, the signal is amplified through the AMP with a gain of approximately 45dB. However, to prevent the TDO from being damaged, the ATT of -30dB is connected to the output port of the AMP after signal amplification to attenuate the input signal. The flow diagram can be illustrated in Figure 3.2.30.

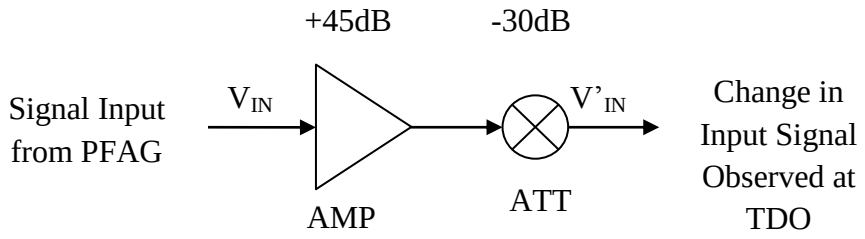

Figure 3.2.30: An addition of an attenuator to observe the change in the input signal after amplification

Figure 3.2.31(a) shows the original input signal directly from the PFAG with a square wave of mean voltage peak at 64mV, V_{IN}, while Figure 3.2.31(b) shows the distorted square wave after amplification with a voltage gain of 15dB, V'_{IN}.

(a)

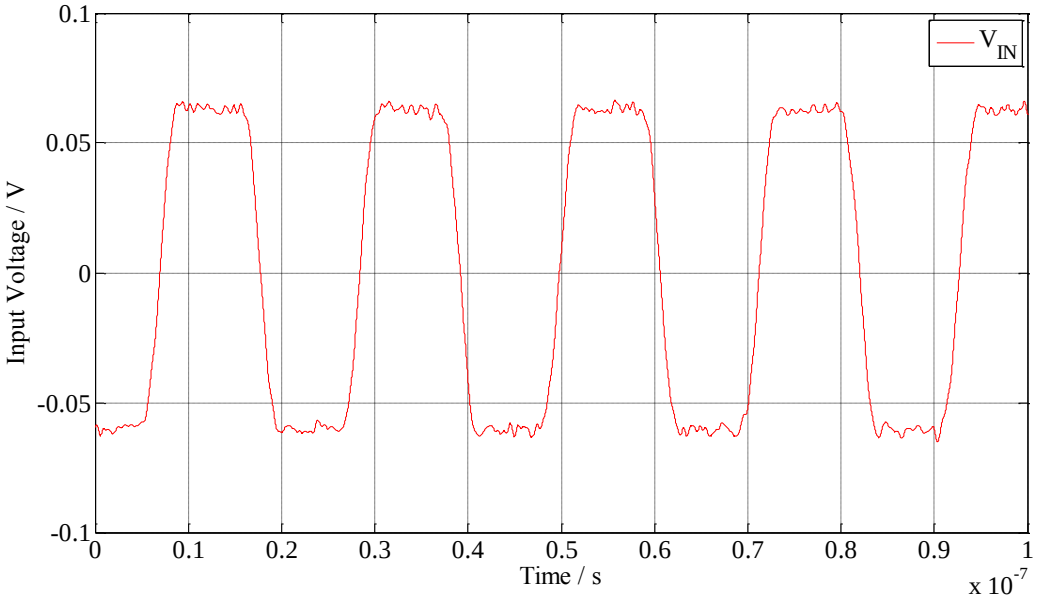

(b)

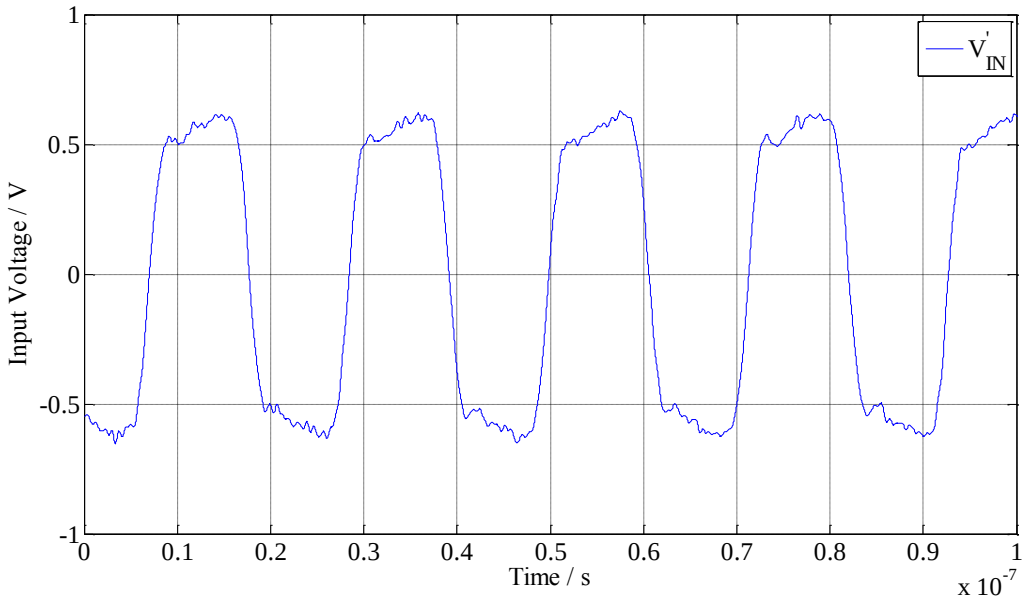

Figure 3.2.31: Comparison between the square waves input signal (a) V_{IN}. *(b)* V'_{IN}.

3.3 External Impedance at the Brass Connector End Plates

As presented in Chapter 2, both the source and victim circuits are the inner conductors and loads of the RG-58 coaxial cables while the tertiary circuit is an equivalent circuit between the braids, where it is terminated by a finite impedance due to the stray reactance the brass plates introduce. Brass is an alloy, made of copper and zinc, which serves as a good current carrying conductor and possess similar permittivity value with copper.

Significant research has been done to measure and predict the crosstalk between two coaxial cables [3.3] – [3.22]. However, not much has been mentioned and explained about the terminations of the tertiary circuit, despite their significant effect on the degree of cable coupling. In most cases, the tertiary circuit is assumed to be connected together by either an arbitrary impedance or a short circuit at each end [3.3], [3.6], [3.7], [3.15], [3.16] and [3.19] – [3.22]. Therefore, in order to accurately model a more realistic cable coupling system, measurements are carried out to estimate the inductance associated with the termination, both for the differential and common mode tertiary circuit. The TDR module is used to detect reflections and calculation of the characteristic impedance of the cables as well as detecting the termination reflection and estimating the reactance due to discontinuities in the system, as a function of cable length [3.23].

3.3.1 Experimental Set Up to Measure the Excess Reactance in the Brass End Plates

Since the tertiary circuit of the cable coupling system is formed from the outer braids of the two coaxial cables, the measurement set up is done by only connecting the outer braids of the coaxial cables to the brass end plates. This is done by cutting the inner conductor of one of the coaxial cables with the outer braid still intact. The outer braid is then soldered to a SMA connector centre pin using a copper wire since the inner conductor of a RG-58 coaxial cable is of copper material. This is shown in Figure 3.3.1. The return is then the outer braid of the victim cable or the ground plane.

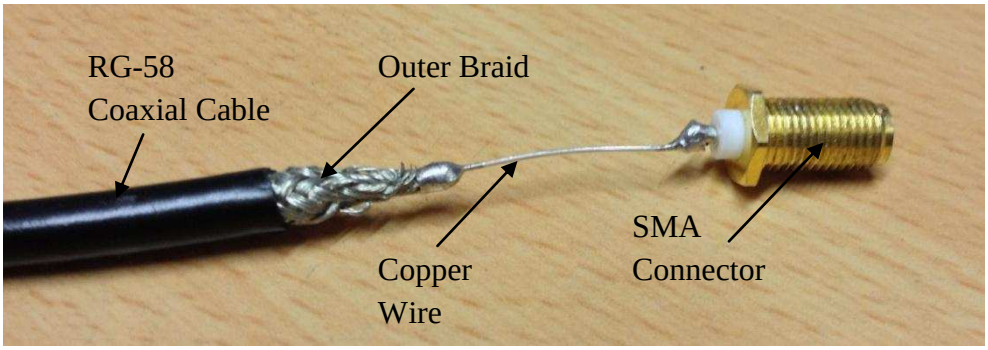

Figure 3.3.1: Connection of the RG-*58 coaxial cable's* outer braid to the SMA connector through a copper wire

The reflections in the braids of the coaxial cables together with the approximation value of excess reactance are provided by the TDR module. Theoretically, a larger current loop yields larger characteristic reactance within the loop. This phenomenon causes a slight shift in the peaks of the crosstalk at resonant frequencies. Therefore, the separation between the cables, s, is varied to obtain its respective differential mode inductive reactance; while the height of the cable above ground, h, is varied to obtain its respective common mode inductive reactance. Figure 3.3.2 shows the direction of the tertiary current, I_t, in its differential and common modes, through the brass end plates.

(a)

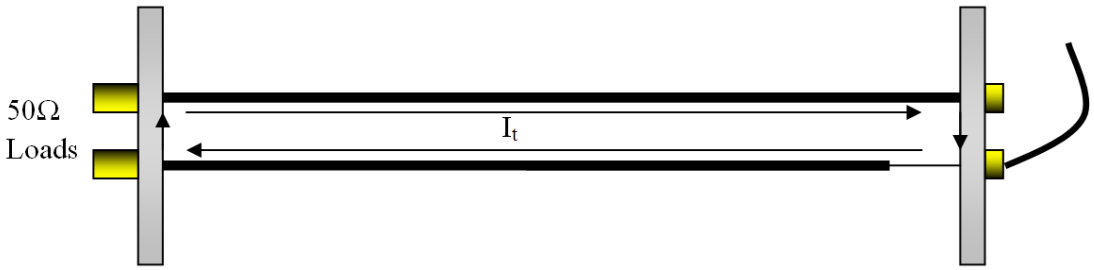

(b)

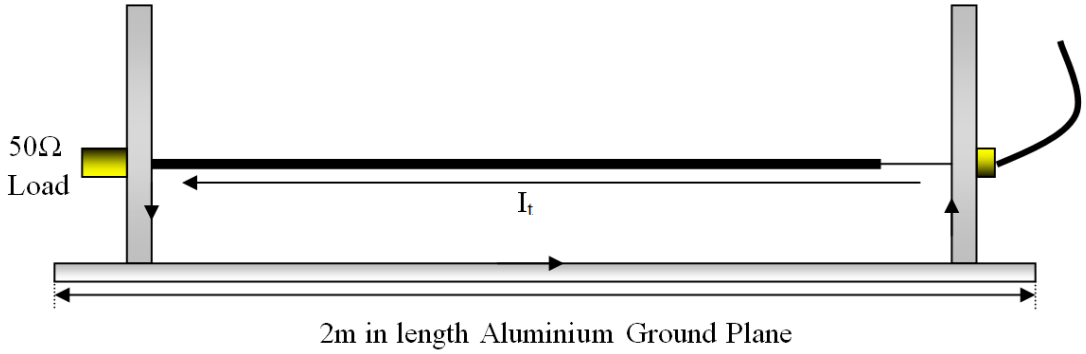

Figure 3.3.2: Direction of the tertiary current, I_t. (a) Differential mode. (b) Common mode.

A. Differential Mode

The experimental set up for the differential mode excess inductance measurement is illustrated in Figure 3.3.3. In this experiment, two RG-58 coaxial cables are used. The length of the cables, l, used is 2m long and the separation of the two cables, s, is varied. The cables are connected to the brass end plates and one of them is connected to the TDR module. The excess reactance measured by the TDR module represents the differential mode complex impedance, Z_P, in the brass plates.

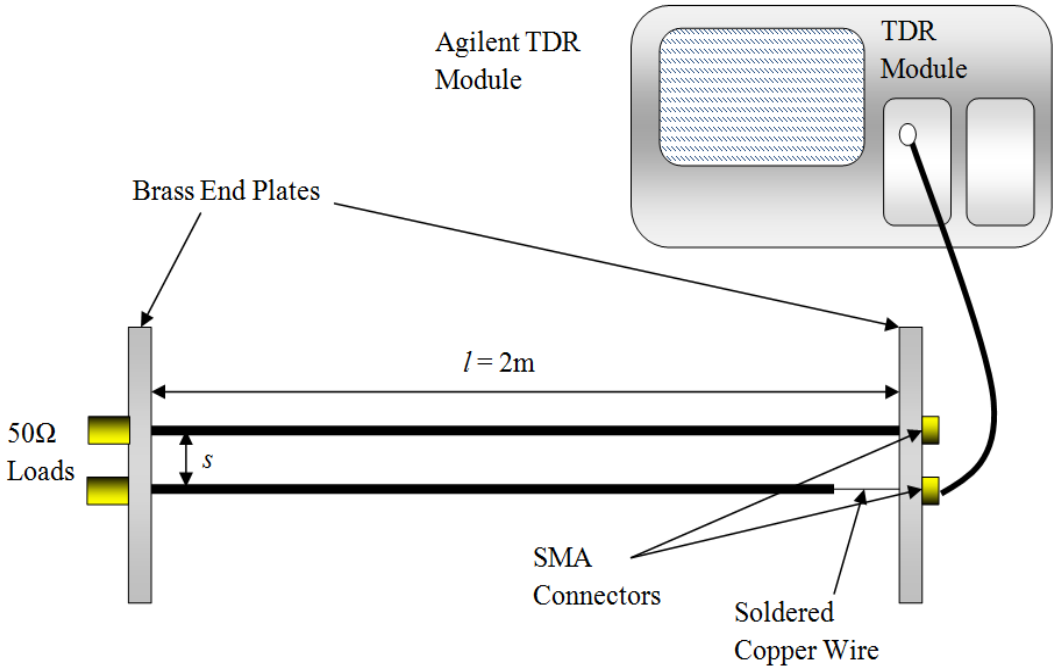

Figure 3.3.3: Differential mode measurement set up to measure the excess reactance in the brass end plates

B. Common Mode

The experimental set up for the common mode excess inductance measurement is illustrated in Figure 3.3.4. In this experiment, one RG-58 coaxial cable is used. The length of the cable, l, used is 2m long and the height between the cable and the ground plane, h, is varied. The cable is connected to the brass end plates and to the TDR module. The excess reactance measured by the TDR module represents the common mode complex impedance, Z_{ts} and Z_{tv}, in the brass plates.

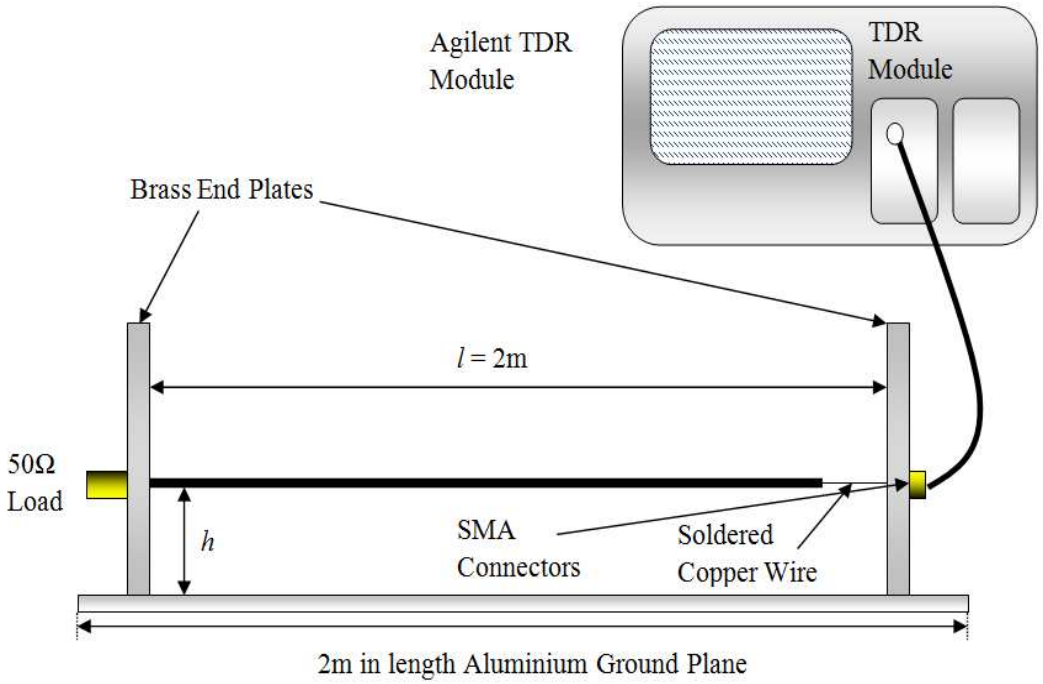

Figure 3.3.4: Common mode measurement set up to measure the excess reactance in the brass end plates

3.3.2 Results

The results obtained show many reflections on the screen of the TDR module and is rather complicated. This is expected since the configurations actually form the tertiary circuit itself. Using the same connecting cables for all configurations, the connecting cable's length is given by the region of the TDR plot showing its characteristic impedance, 50Ω. As defined in section 2.4.1 in Chapter 2, the characteristic impedance of each configuration is dependent on the height and separation between the cables. A pulse signal is transmitted from the TDR Module and is reflected back via the braid of the coaxial cables. The excess reactance in the brass end plates can be estimated from the spike of the reflection at the 50Ω load end of the cable.

Since the brass end plates are assumed to be identical, the excess reactance measured at the far end of the brass plate is assumed to be similar to the near end brass plate. The TDR module includes a built in "excess reactance" feature where the parameter values can be extracted directly from the screen using markers. It models

the transmission line as a uniform transmission line having a single discontinuity, either a lumped inductor or lumped capacitor [3.23]. The position of the markers will define the region of discontinuity (at the terminations) where the capacitance or inductance will be extracted and the value can be determined. Since there are a lot of reflections, the excess reactance value presented on the screen varies. Hence, it is recommended that an average or approximate value is noted in order to implement this excess reactance in the numerical model.

A. Differential Mode

Figures 3.3.5 to 3.3.8 show the differential mode reflection of the cables in the tertiary circuit (see Figure 3.3.2a), with markers indicating the separation between the cables and its excess reactance in the brass plates for separations 2cm, 5cm, 10cm and 15cm.

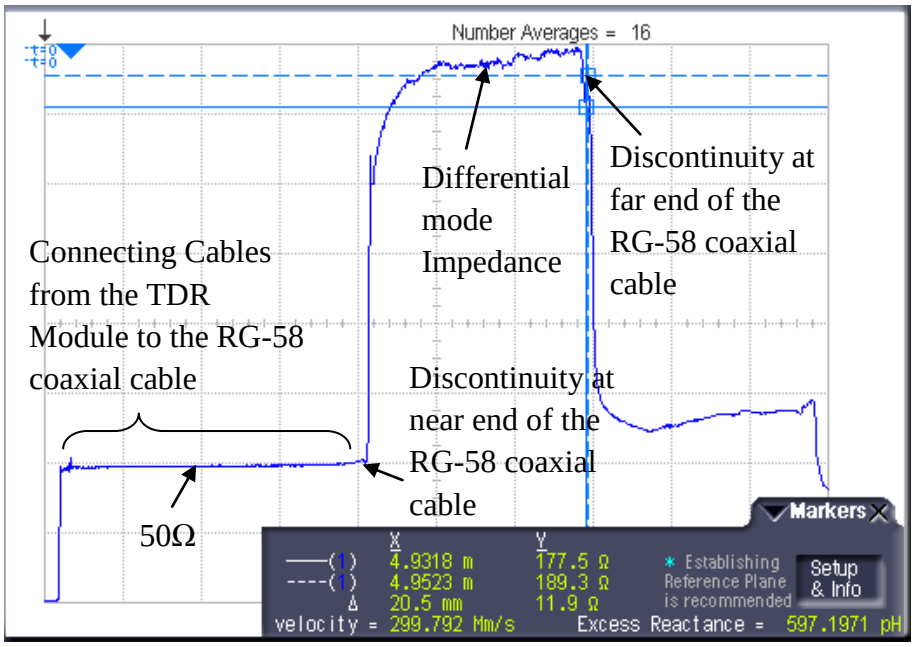

Figure 3.3.5: The reflection of the tertiary circuit shown on the TDR module; distance between markers indicating a 2cm separation and an excess inductance of approximately 0.6nH in the brass plate, between the cables

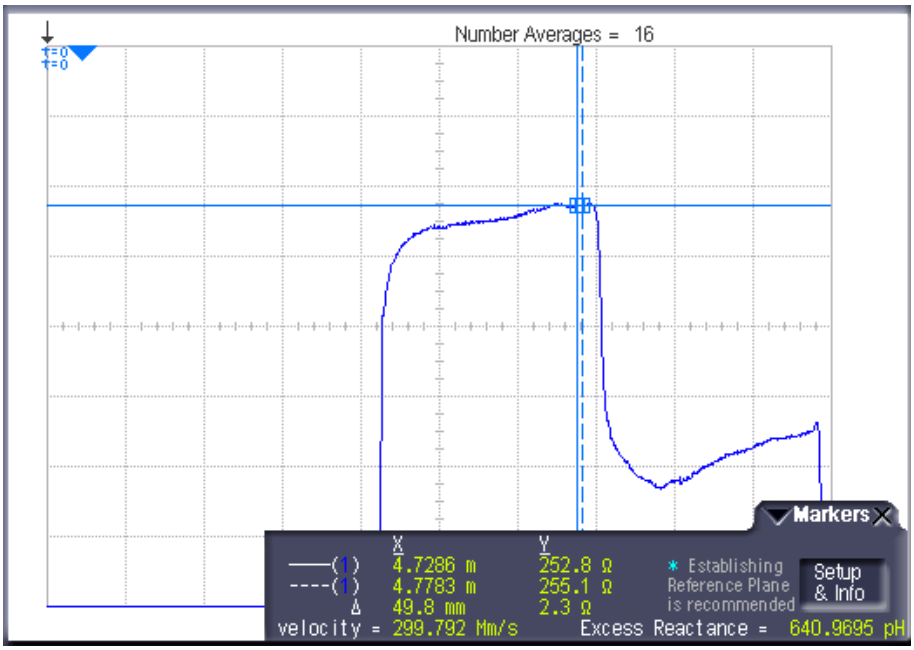

Figure 3.3.6: The reflection of the tertiary circuit shown on the TDR module; distance between markers indicating a 5cm separation and an excess inductance of approximately 0.65nH in the brass plate, between the cables

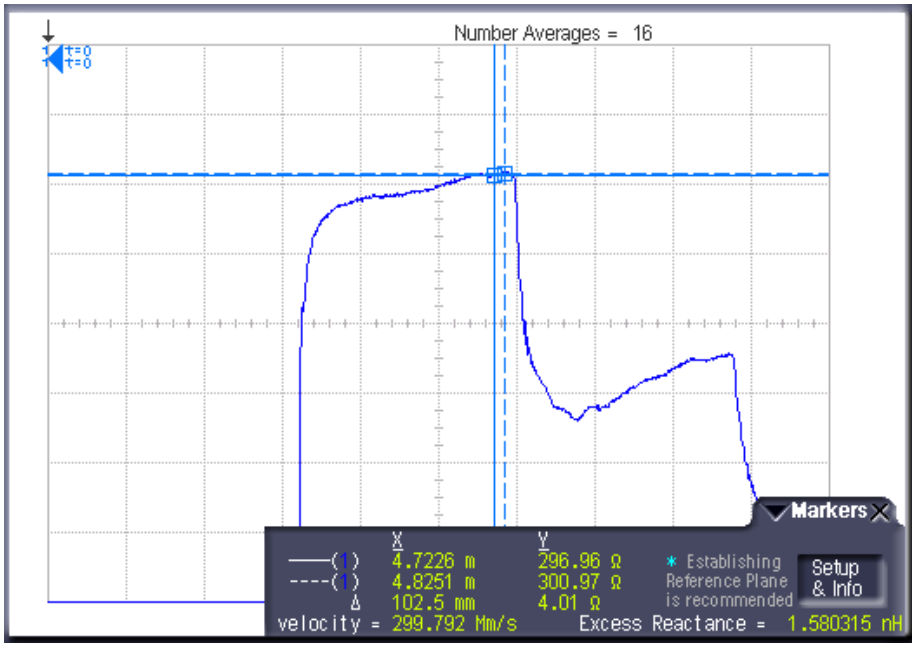

Figure 3.3.7: The reflection of the tertiary circuit shown on the TDR module; distance between markers indicating a 10cm separation and an excess inductance of approximately 1.5nH in the brass plate, between the cables

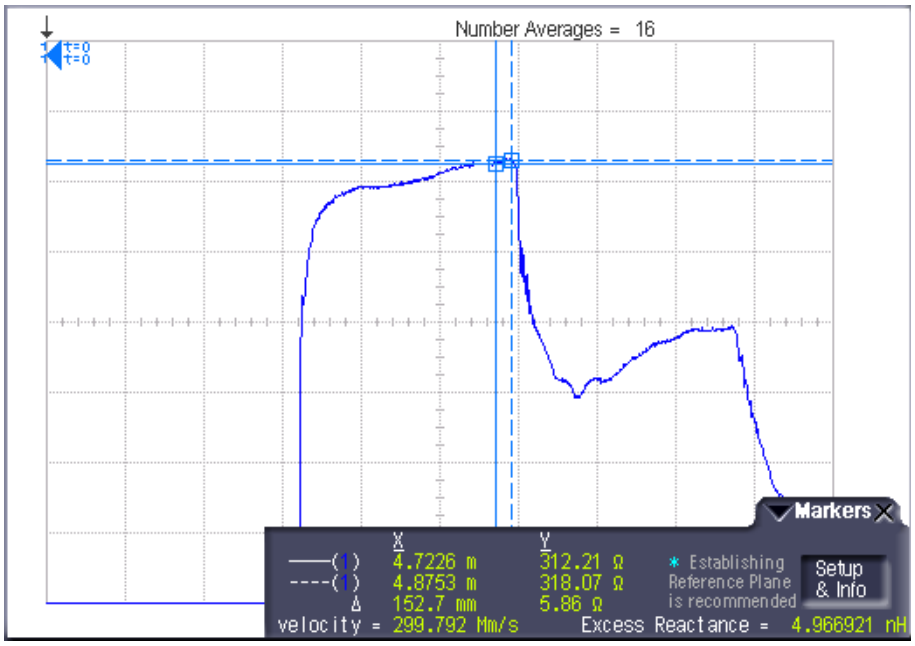

Figure 3.3.8: The reflection of the tertiary circuit shown on the TDR module; distance between markers indicating a 15cm separation and an excess inductance of approximately 5nH in the brass plate, between the cables

The relationship between the differential mode excess inductance, L_P, and the separation between the two RG-58 coaxial cables, s, is depicted in Figure 3.3.9 (see Chapter 2, section 2.3.1 for system configuration).

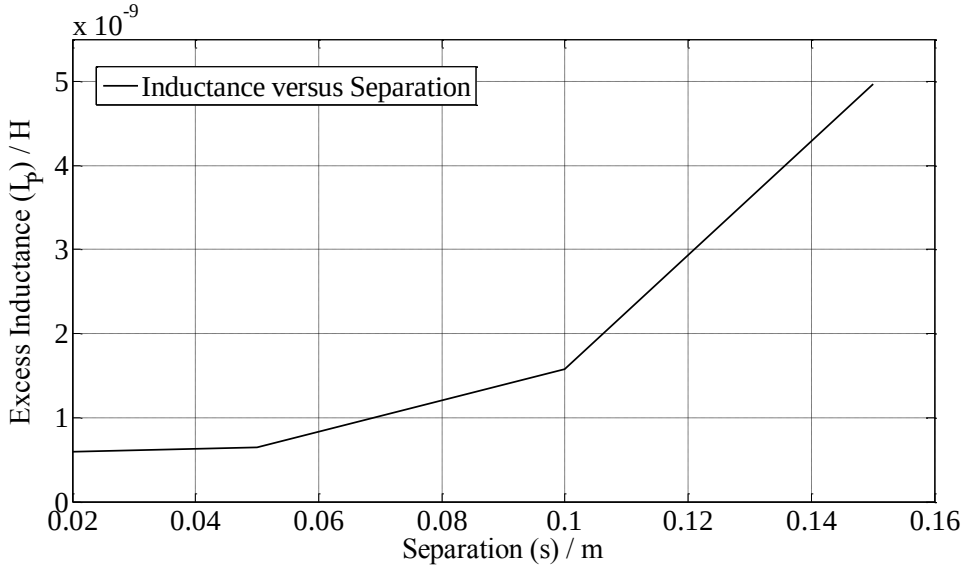

Figure 3.3.9: Graph showing the relationship between differential mode excess inductance, L_P, and the separation between the RG-58 coaxial cables, s

B. Common Mode

Figures 3.3.10 to 3.3.13 show the common mode reflection of the cables in the tertiary circuit (see Figure 3.3.2b), with markers indicating the height of the cables over the metallic ground plane and its excess reactance in the brass plates for heights 11.5cm, 16.5cm, 21.5cm and 26.5cm.

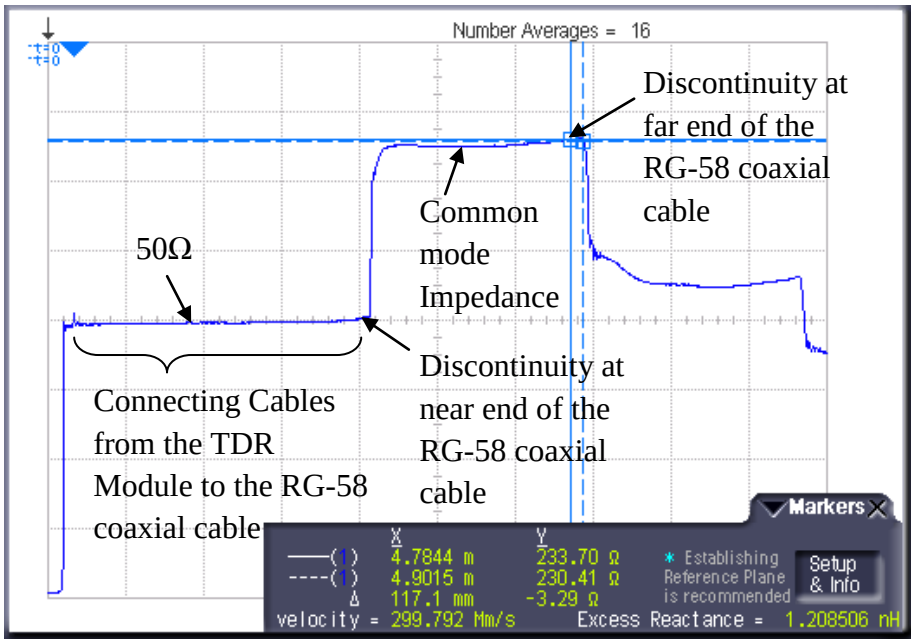

Figure 3.3.10: The reflection of the tertiary circuit shown on the TDR module; distance between markers indicating a 11.5cm height and an excess inductance of approximately 1.2nH in the brass plate, over a metallic ground plane

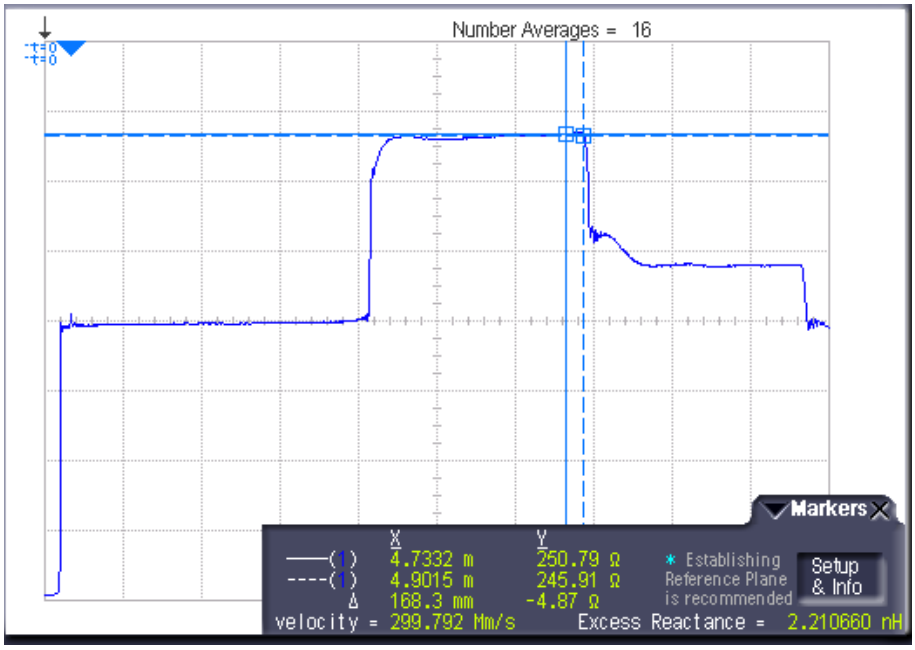

Figure 3.3.11: The reflection of the tertiary circuit shown on the TDR module; distance between markers indicating a 16.5cm height and an excess inductance of approximately 2.2nH in the brass plate, over a metallic ground plane

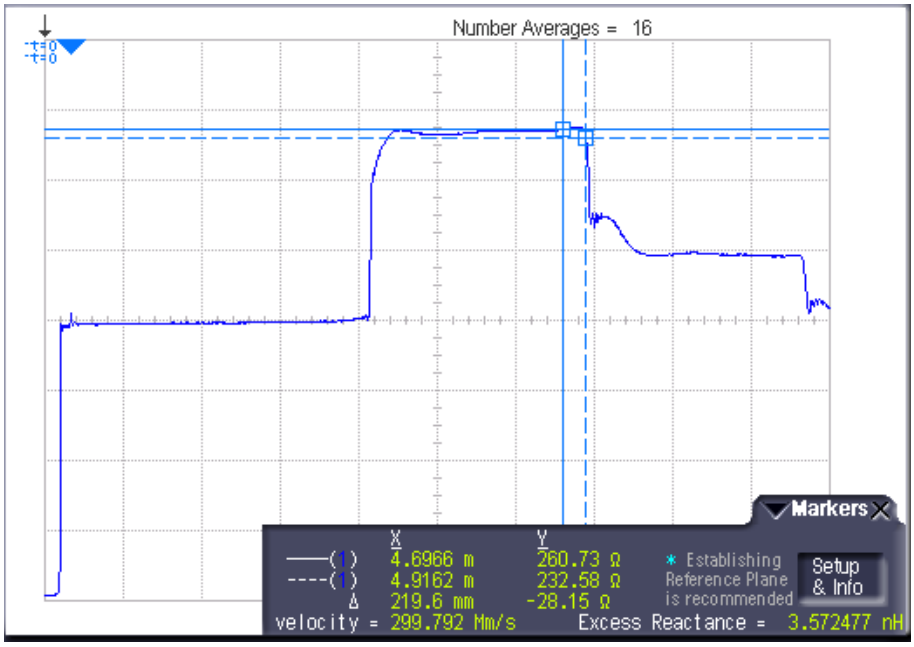

Figure 3.3.12: The reflection of the tertiary circuit shown on the TDR module; distance between markers indicating a 21.5cm height and an excess inductance of approximately 3.6nH in the brass plate, over a metallic ground plane

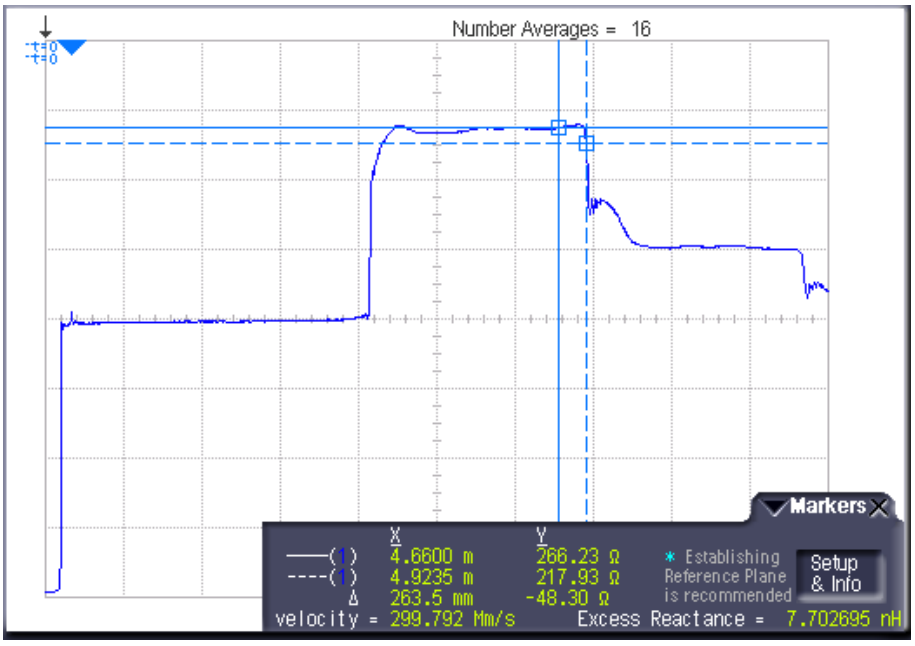

Figure 3.3.13: The reflection of the tertiary circuit shown on the TDR module; distance between markers indicating a 26.5cm height and an excess inductance of approximately 7.7nH in the brass plate, over a metallic ground plane

The relationship between the common mode excess inductance, L_{ts}, and the height of the RG-58 coaxial cable, h, above a metallic ground plane is depicted in Figure 3.3.14 (see Chapter 2, section 2.3.2 for system configuration).

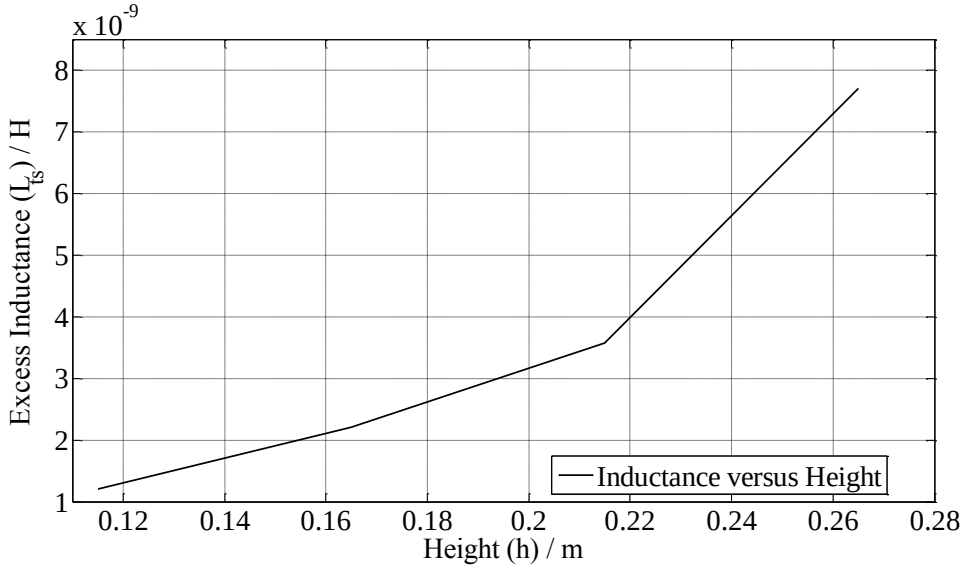

Figure 3.3.14: Graph showing the relationship between common mode excess inductance, L_{ts}, and the height of the RG-58 coaxial cable above a metallic ground plane, h

Since the excess inductances are successfully obtained from the TDR module, it is subsequently implemented into the numerical model presented in Chapter 4. Instead of using an arbitrary impedance values, the excess inductances extracted from the TDR module provide a more accurate tertiary circuit termination of the system for each case.

3.4 Conclusions

The crosstalk experiment together with the measurement configurations are introduced and presented. The configuration involves coupling measurements between two RG-58 coaxial cables in free space and over a metallic ground plane; with results obtained in both the time and frequency domains. Various measurement results were taken by varying the separation between the two cables and the height between the cables and the metallic ground plane. The external impedance of the connector plates are also measured using a Time Domain Reflectometer (TDR) to obtain an approximation of the tertiary circuit termination's stray inductance, as presented in Chapter 2. Measurements were taken for both modes; the differential mode, formed by the external surfaces of the two cable braids as well as the connector plates; and the common mode, formed by the return path between the cable braid and the metallic ground plane.

References

[3.1] N. Akeam and M. H. Karatas, "Measurement of transfer impedance and screening attenuation effects on cables using tri-axial method," Intl. Journal on Technical and Physical Problems of Engineering, (IJTPE), iss. 10, vol. 4, no. 1, Mar. 2012, pp. 103 – 107.

[3.2] F. A. Benson, P. A. Cudd and J. M. Tealby, "Leakage from coaxial cables," IEE Proc-A, vol. 139, no. 6, 1992, pp. 285-303.

[3.3] C. J. Smartt, S. Greedy, D.W.P. Thomas, C. Christopoulos and P. Sewell, "Shielded cable model development for time domain CEM

techniques," IET 8th Intl. Conf. on Computation in EMC (CEM 2011), April 2011, pp. 1 – 2.

[3.4] Clayton R. Paul, Introduction to Electromagnetic Compatibility, Wiley Series in Microwave and Optical Engineering, 1992.

[3.5] Clayton R. Paul, Analysis of Multiconductor Transmission Lines, John Wiley & Sons, Inc, 1994.

[3.6] D.W.P. Thomas, C. Christopoulos, F. Leferink and H. Bergsma, "Practical measure of cable coupling," IEEE Computer Science Press, September 2005.

[3.7] S. A. Schelkunoff and T. M. Odarenko, "Crosstalk between coaxial transmission lines," Bell Syst. Tech. J., 1937, 26, pp. 144 – 164.

[3.8] J. C. Isaacs, Jr. and N. A. Strakhov, "Crosstalk in uniformly coupled lossy transmission lines," Bell Syst. Tech. J., January 1973, pp. 101 – 115.

[3.9] R. P. Booth and T. M. Odarenko, "Crosstalk between conductors in cable," Ibid., 1940, 19, pp. 358 – 384.

[3.10] K. E. Gould, "Crosstalk in coaxial cables – analysis based on short-circuited and open tertiaries," Ibid., 1940, 19, pp. 341 – 357.

[3.11] S. Sali, "A circuit-based approach for crosstalk between coaxial cables with optimum braided shields," IEEE Transactions on EMC, vol. 35, no. 2, May 1993.

[3.12] A.H. Badr, Prof. F.A. Benson and J. E. Stitch, "Interference between braided coaxial cables," IEE Proceedings, vol. 128, no. 5, July 1981, pp. 347 – 353.

[3.13] S. Sali, Prof. F.A. Benson and J.E. Sitch, "Coupling in a dielectric-coated multicoaxial-cable system, an analysis based on a quasi-TEM model," IEE Proceedings, vol. 131, no. 1, January 1984.

[3.14] C. Smartt, S. Greedy, D.W.P. Thomas, C. Christopoulos, P. Sewell, "Modelling and measurement of crosstalk between shielded cables," EMC-Europe, Wroclaw, 2010.

[3.15] Clayton R. Paul, "Computation of crosstalk in a multiconductor transmission line," IEEE Transactions on EMC, vol. EMC-23, no. 4, November 1981.

[3.16] A.H. Badr, Prof. F.A. Benson and J.E. Sitch, "Coupling between a pair of coaxial cables in a multicable system," IEE Proc, vol. 128, pt. A, no.8, November 1981, pp. 547 – 551.

[3.17] S. Sali, F. A. Benson and J. E. Sitch, "Coupling between multicoaxial systems – I General considerations and efficient numerical method for crosstalk," IEE Proc., vol. 129, pt. A, no. 3, May 1982, pp. 162 – 166.

[3.18] S. Sali, F. A. Benson and J. E. Sitch, "Coupling between multicoaxial systems – II Theoretical predictions of crosstalk and experimental results," IEE Proc., vol. 129, pt. A, no. 3, May 1982, pp. 167 – 171.

[3.19] A.H. Badr, Prof. F.A. Benson and J.E. Sitch, "Coupling between coaxial cables over a ground place at low frequencies," IEE Proc. vol. 127, pt. A, no. 8, November 1980.

[3.20] John N. Ellinas, "Coupling between braided coaxial cables over a ground plane," Dept. Of Computer Engineering, TEI of Pireaus, P. Ralli & Thivon 250, Athens, Greece.

[3.21] R.J. Mohr, "Coupling between open and shielded wire lines over a ground plane," IEEE Transactions on EMC, vol. EMC-9, no. 2, September 1967.

[3.22] John Paul, Christos Christopoulos and David W. P. Thomas, "Time-domain simulation of multiconductor transmission-lines,"

[3.23] Agilent Signal Integrity Series, Part 1: Single-Port TDR, TDR/TDT, and 2-Port TDR, Application Note.

CHAPTER 4

NUMERICAL MODELLING

The solution of electromagnetic problems can be found using two distinctive methods; analytical or numerical approach. Although the analytical method provides the most accurate solutions to most EMC problems, its application is limited to a selection of simple cases. In order to formulate solutions in most practical situations iterative numerical modelling is used. Thus, this leads to the development of computational electromagnetics, applied to a wide variety of practical EMC solutions [4.1] and [4.2].

In a general case, the constitutive analytical equations and boundary conditions significantly complicate both the formulation and solution of electromagnetic problems. It becomes more complicated when the medium is inhomogeneous and time-varying [4.5]. For example, the propagation of electromagnetic signals in dielectrics and semiconductor structures, such as interconnects. The solution of such EMC problems demands efficient time-domain numerical techniques.

Numerical modelling is concerned with the representation of physical systems by specific quantities which are obtained by numerical methods [4.4]. For electromagnetic systems, it is generally required to obtain the electric and magnetic field within a volume of space, subject to specified boundary conditions. The investigation of these physical systems in time-varying media have led to the requirements of accurate, reliable and powerful computational tools in order to analyse the electromagnetic wave's propagation, providing an insight into the interaction of both electric and magnetic fields with the physical properties of the specified space volume.

4.1 Time-Domain Numerical Techniques

Maxwell's equations are related to time and spatial variation of electromagnetic fields, but self-consistent only to electromagnetic fields in an infinite medium [4.6]. With modifications done by Maxwell to Gauss', Ampere and Faraday's laws [4.6] and with the assumption that the equations only depend on free charges and currents in their differential forms are given by:

- Gauss' law for electricity:

$$\nabla . \vec{D} = \rho \tag{4. 1}$$

- Gauss' law for magnetism:

$$\nabla . \vec{B} = 0 \tag{4. 2}$$

- Faraday's law of induction:

$$\nabla \times \vec{E} = -\frac{\partial \vec{B}}{\partial t} \tag{4. 3}$$

- Ampere's law:

$$\nabla \times \vec{H} = J + \frac{\partial \vec{D}}{\partial t} \tag{4. 4}$$

Numerical methods can be used to approximate solutions for Maxwell's equations to a required good accuracy. The most commonly used time-domain numerical techniques include the Finite Difference Time Domain Method (FDTD) [4.2] and the Transmission Line Modelling Method (TLM) [4.1]. These methods are considered to be flexible and applicable to a wide range of EMC applications with a possible preference for a particular method being dependent on the structure under consideration. However, the studies require a fine mesh and for large dimensions these iterative numerical modelling techniques would be limited by the cost of long computational times and expensive memory requirements.

In this chapter, numerical solutions based on the TLM method for the description of the coupling degree between two coaxial cables are presented. Using 1-Dimensional TLM method, the system is modelled based on structures and factors

measured experimentally, resulting in a practical numerical solution in predicting the crosstalk of the system, as described in Chapters 2 and 3.

4.2 One-Dimensional Transmission Line Modelling

The theory of modelling a transmission line is overviewed to present the idea of interaction of the propagation of a signal in a basic transmission line, modelling procedure and computation for the one-dimensional case. The method of the basic one-dimensional TLM model is developed and described in great detail by Christopoulos [4.1]. This theory forms the basis of the following algorithm used within this thesis.

The TLM method is a numerical differential time domain technique which employs a network of discrete transmission lines connected at scattering junctions in order to simulate the behaviour of a distributed system [4.7]. This is based on the analogy between the field quantities and lumped circuit equivalents, where the transmission line is discretized into mesh of segments, connected by nodes [4.1]. The field, represented by wave pulses are scattered in the nodes and propagate in the transmission lines, generating incident and reflected voltages. The TLM method can be logically implemented in four stages, which consists of the initial problem definition and housekeeping tasks, followed by the calculation of voltages and currents through a repetitive iteration of scattering and connection [4.1]. Initialization defines the sources and initial incident voltage wave values; scattering determines the reflected voltage waves at all nodes and connection exchanges the voltage pulses between adjacent nodes.

A simple transmission line network is shown in Figure 4.2.1.

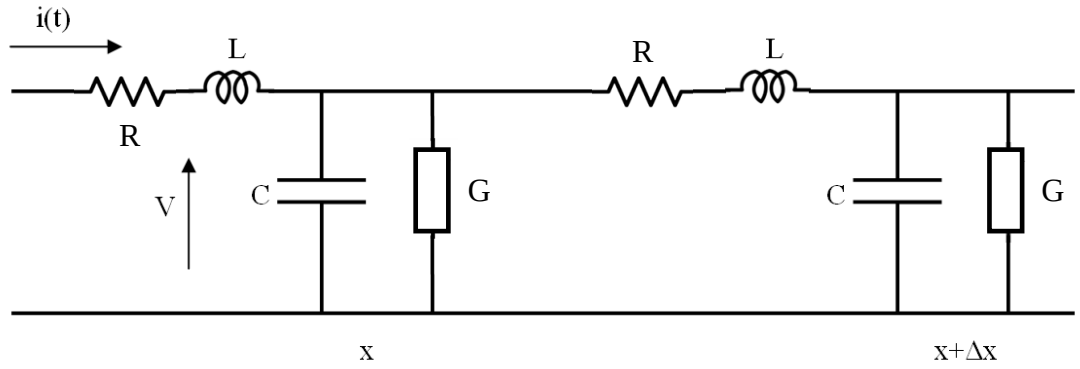

Figure 4.2.1: A simple section of transmission line network [4.1]

Figure 4.2.1 gives the equivalent circuit of a section of a transmission line network system where L is the series inductance per-unit length; C as the shunt capacitance per-unit length and R as the series resistance per-unit length; and G is shunt conductance per-unit-length. For a lossless line the equivalent reduces to that given in Figure 4.2.2 with a fundamental line segment given in Figure 4.2.3.

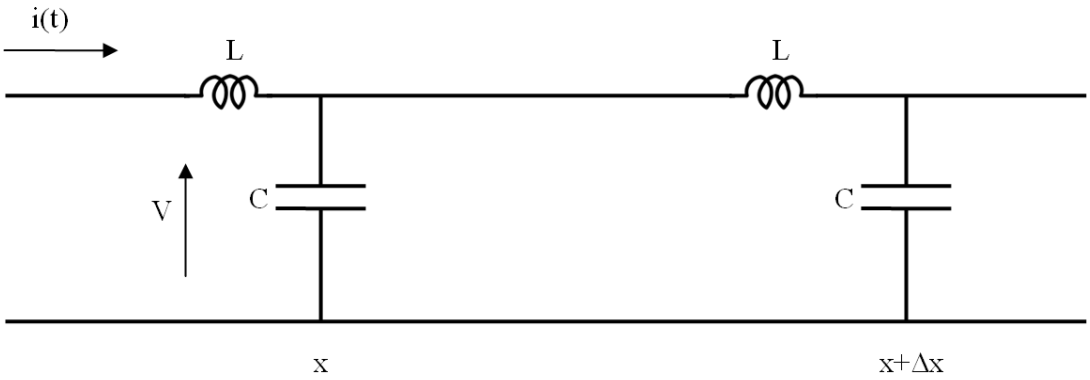

Figure 4.2.2: A simple lossless transmission line network

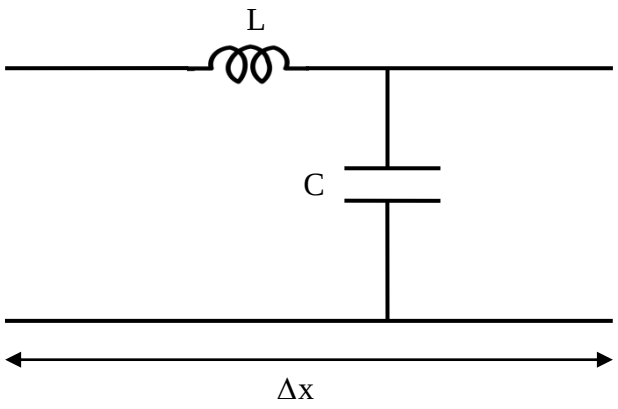

Figure 4.2.3: A basic line segment

The basic line segment in the transmission line can be produced with a TLM equivalent as shown in Figure 4.2.4, with L and C replaced with a link line of impedance, Z, where

$$Z = \sqrt{\frac{L}{C}} \tag{4. 5}$$

and the propagation velocity along a line section is:

$$u = \frac{1}{\sqrt{LC}} \tag{4. 6}$$

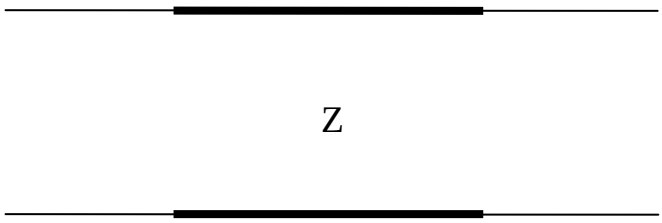

Figure 4.2.4: The TLM model of the basic line segment [4.1]

Let each section be of length Δx such that the propagation time along the section is:

$$\Delta t = \frac{\Delta x}{u} \tag{4. 7}$$

The simulation of the voltages and currents can then be achieved by representing them as propagating waves or voltage pulses in each section as shown in Figure 4.2.5.

An illustration of part of the transmission line with several nodes taken into consideration is as shown in Figure 4.2.5.

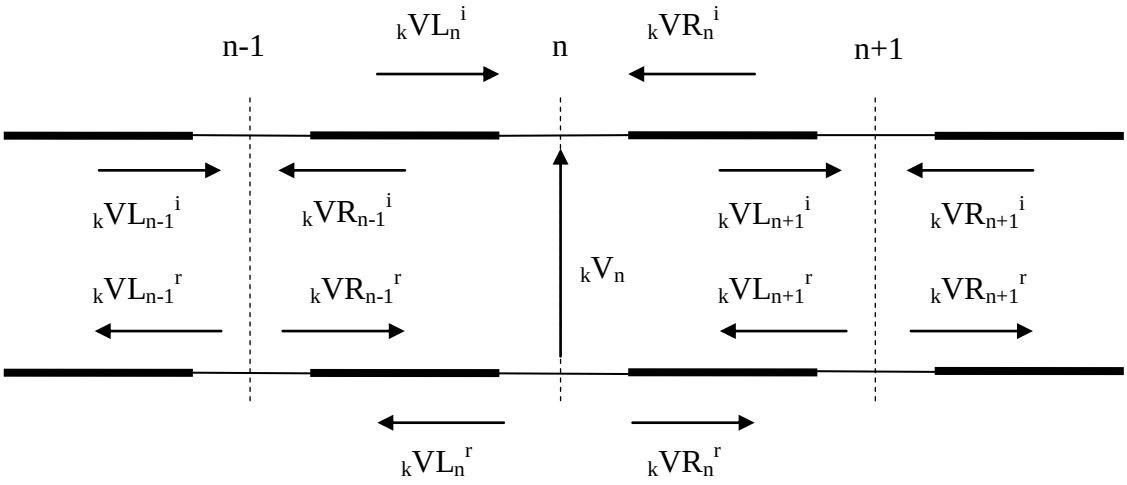

Figure 4.2.5: Four segments of nodes in a transmission line network

For time-step k, there are voltage pulses going in from the right and left of each of the node known as the incident voltages while the reflected voltage pulses are going out from the right and left of each of the node. For example, in Figure 4.2.5, taking node n as a reference, $_kVL_n^i$ (left) and $_kVR_n^i$ (right) are the incident voltages going into the termination, node n. $_kVL_n^r$ (left) and $_kVR_n^r$ (right) are reflected voltages going out from the termination, node n. The Thevenin equivalent circuit for one node can be illustrated in Figure 4.2.6.

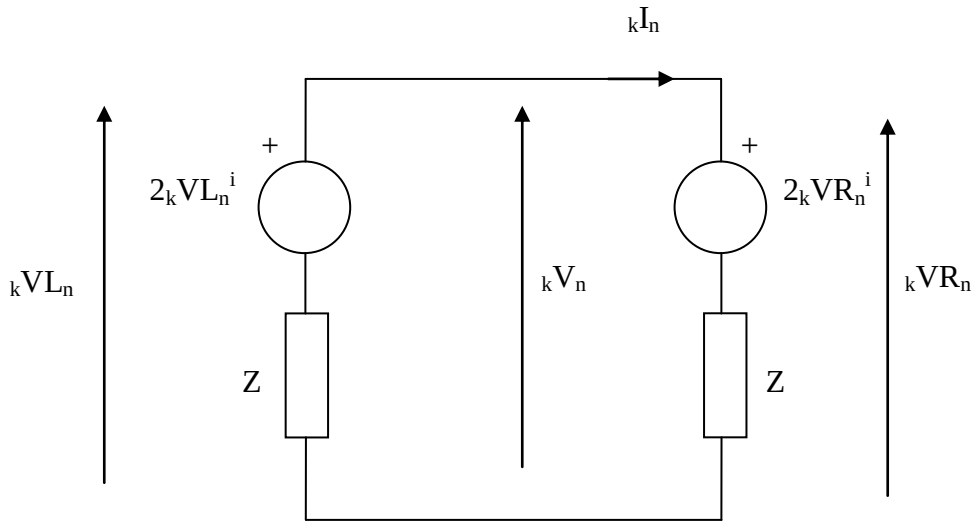

Figure 4.2.6: The Thevenin Equivalent of a node, n, in a transmission line

Solving the Thevenin Equivalent circuit as illustrated in Figure 4.2.7 above, for each node, the following equation is obtained for the voltages and currents [4.8].

$$ {}_kV_n = {}_kVL_n^i + {}_kVR_n^i \tag{4. 8}$$

Similarly, the current of the node is given by:

$$ {}_kI_n = \frac{{}_kV_n - 2\,{}_kVR_n^i}{Z} \tag{4. 9}$$

By observing Figure 4.2.6, the reflected voltages into the lines on the left and on the right can be equated where:

$$ {}_kVR_n^r = {}_kV_n - {}_kVR_n^i \tag{4. 10}$$

$$ {}_kVL_n^r = {}_kV_n - {}_kVL_n^i \tag{4. 11}$$

The equations (4.10) and (4.11) provide the scattering properties in a transmission line. With the knowledge of the incident voltages known at the first time-step, k, from the initial conditions of the equations, the incident voltages at the next consecutive time-step, which is k+1, can be obtained. The scattered pulses are then transmitted (or connected) to the adjacent nodes for the next time step using:

$$ {}_{k+1}VL_n^i = {}_kVR_{n-1}^r \tag{4. 12}$$

$$ {}_{k+1}VR_n^i = {}_kVL_{n+1}^r \tag{4. 13}$$

The general principles employed to find the conditions of each of the nodes on the transmission line, as explained above using node, n, as the reference node, can also be applied to find the source node, n = 1; and the load node, n = NT, with some small modifications.

The equivalent circuit for the source node, n = 1, is illustrated in Figure 4.2.7.

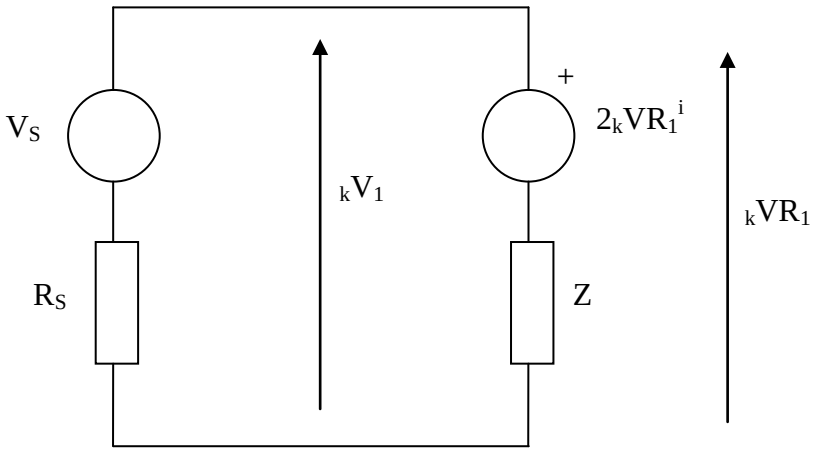

Figure 4.2.7: The Thevenin Equivalent circuit of a source node, n = 1

From the Thevenin Equivalent circuit presented in Figure 4.2.7, by applying the same principles discussed above, it can be readily shown that:

$$_kV_1 = \frac{\frac{V_S}{R_S} + \frac{2\ _kVR_1^i}{Z}}{\frac{1}{R_S} + \frac{1}{Z}} \tag{4. 14}$$

For the scattering property of the source node, by applying similar principles, it can be readily shown that:

$$_kVR_1^r = {}_kV_n - {}_kVR_1^i \tag{4. 15}$$

The equivalent circuit for the load node, n = NT, is illustrated in Figure 4.2.8.

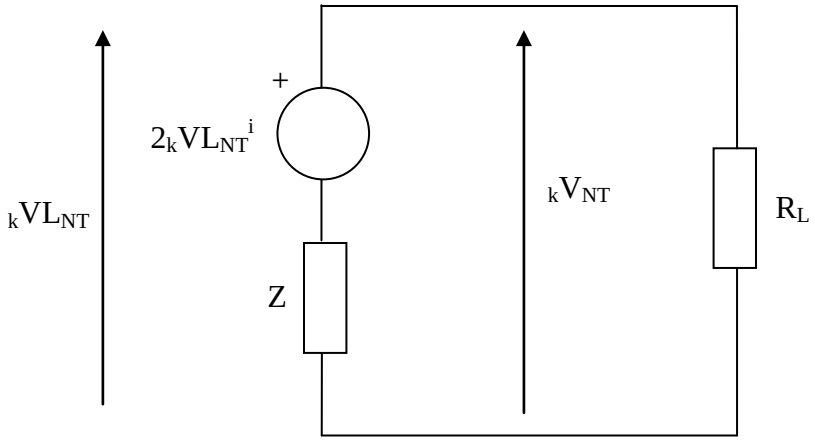

Figure 4.2.8: The Thevenin Equivalent circuit of a load node, n = NT

Similarly, from the Thevenin Equivalent circuit in Figure 4.2.8, by applying the same principles, it is given that:

$$_kV_{NT} = \frac{\frac{2\ _kVL_{NT}^{i}}{Z}}{\frac{1}{Z}+\frac{1}{R_L}} \tag{4. 16}$$

For the scattering property of the load node, by applying similar principles, it is given that:

$$_kVL_{NT}^{r} = \ _kV_n - \ _kVL_{NT}^{i} \tag{4. 17}$$

4.2.1 Time Synchronisation

For the problem of cable coupling described in Chapter 2, the source, tertiary and victim circuits are modelled individually using the 1-D TLM method. For ease of computation it is necessary for the time and space steps to be the same for all circuits in the transmission lines. The tertiary circuit insulation is mostly air in contrast to both the source and victim coaxial lines which have polymer insulation. The propagating velocities in both the source and victim circuits will then be different to the tertiary circuit. A method is required to synchronise the time steps used for modelling each of the circuit since the space step, Δx, is fixed. By introducing a transmission line stub in

the source and victim lines to increase the capacitance per-unit length, it causes the total wave travelling along the mesh to travel at a velocity lower than that of the individual transmission lines. The amount of dispersion introduced by the transmission stub is calculated using the method presented by Naylor et al. [4.9]. Since the source circuit and the victim circuit both have a slower propagation speed due to the dielectric permittivity of the polymer insulation, a stub capacitance is implemented in each node of the source and victim circuit transmission lines in order to synchronise the propagation speed in all three circuits as shown in Figure 4.2.9. The propagation speed of both the source and victim lines can be calculated as:

$$u = \frac{c}{\sqrt{\varepsilon_r}} \tag{4. 18}$$

(a)

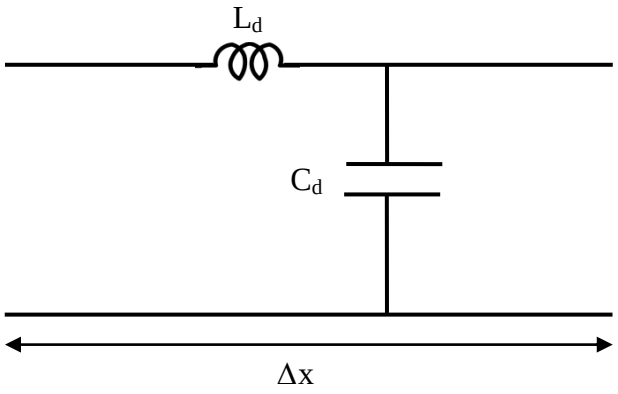

(b)

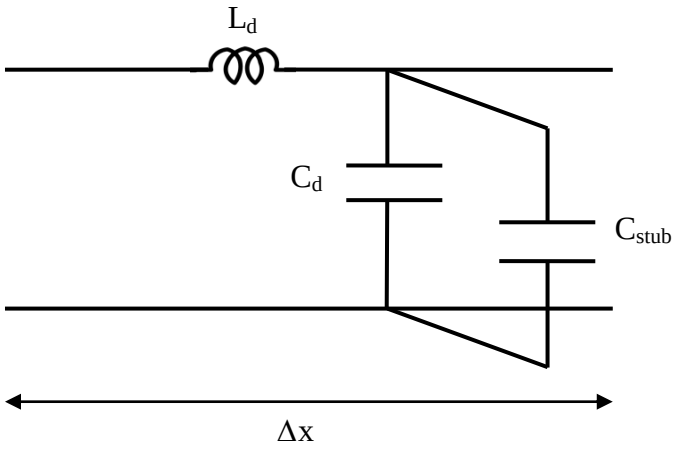

Figure 4.2.9: Addition of a transmission line stub to reduce the propagation velocity of signal. (a) Transmission line. (b) Adjusted transmission line with a stub capacitance.

The propagation velocity of a transmission line in free space is:

$$u_{(a)} = \frac{1}{\sqrt{L_d C_d}} = c \tag{4. 19}$$

The propagation velocity of a transmission line with stub capacitance can in turn be given as:

$$u_{(b)} = \frac{1}{\sqrt{L_d C_t}} = \frac{c}{\sqrt{\varepsilon_r}} \tag{4. 20}$$

The difference between the total capacitance (a) and the characteristic capacitance per unit length (b) is the value of the capacitance of the additional transmission line stub, which is given by:

$$C_{stub} = C_t - C_d \tag{4. 21}$$

Therefore, since the value of ε_r and c are known and $u_{(b)}$ can be calculated from (4.20), then the values of L_d and C_t can be found, giving the value C_{stub} in (4.21). Therefore, the new characteristic impedance can be calculated as:

$$Z = \sqrt{\frac{L_d}{C_d}} \tag{4. 22}$$

Applying the above method with the TLM concept, the incident and scattering properties are calculated by constructing its Thevenin equivalent circuit shown in Figure 4.2.10:

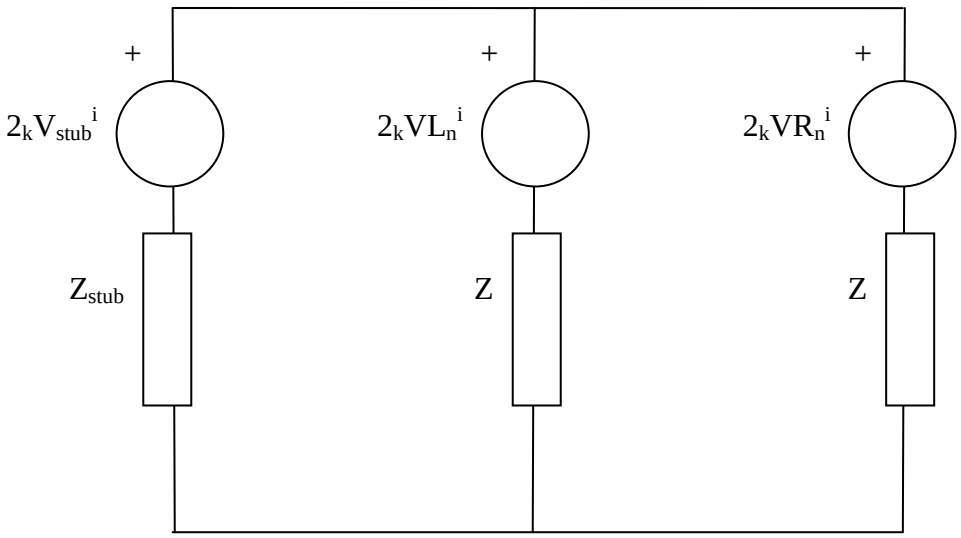

Figure 4.2.10: The Thevenin equivalent circuit of the implementation of a stub capacitance in the source and victim lines

where the stub impedance Z_{stub} is formulated as:

$$Z_{stub} = \frac{\Delta t}{2C_{stub}\Delta x} \tag{4. 23}$$

The total voltage can then be calculated as:

$$_kV_n = \frac{\frac{2V_{stub}^{i}}{Z_{stub}} + \frac{2VL^{i}}{Z} + \frac{2VR^{i}}{Z}}{\frac{1}{Z_{stub}} + \frac{1}{Z} + \frac{1}{Z}} \tag{4. 24}$$

The scattering properties would then be:

$$VL^{r} = {}_kV_n - VL^{i} \tag{4. 25}$$

$$VR^{r} = {}_kV_n - VR^{i} \tag{4. 26}$$

$$V_{stub}^{i} = {}_kV_n - V_{stub}^{i} \tag{4. 27}$$

4.2.2 Numerical Modelling of the Surface Transfer Impedance

As presented in Chapter 2, the transfer impedance of the coaxial lines braid is modelled using the Kley model [2.8]. The coupling path from one circuit to another is

numerically modelled through the frequency dependent models of the transfer impedance. Typically, the coupling path of the coaxial cables is driven by the source circuit, leading to an additional source voltage in the tertiary and victim circuits in each node, which also applies for the transition between tertiary to the victim circuit. Current driven voltage source model is depicted in Figure 4.2.11, for which the absolute value of the braid's transfer impedance, Z_T, is used to describe the coupling path driven by the source circuit with current, I_S.

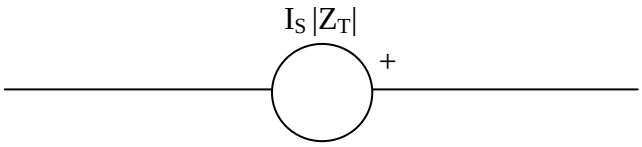

Figure 4.2.11: Single frequency model

Two different broadband frequency models are considered to validate the modelling of the transfer impedance, Z_T: stub inductance model and digital filter. This then describes the coupling path between the source circuit and tertiary circuit and the coupling path between the tertiary circuit and the victim circuit, where the value of Z_T is frequency dependent.

A. Stub Inductance Model

Adapted from Christopoulos [4.1], a stub inductor is used to describe Z_T, where it is designed to be frequency dependent in TLM methods. The stub representing the inductance of the braid's transfer impedance, L_T, is terminated by a short circuit.

From Figure 4.2.11, Z_T is described as an L-R circuit with a source current flowing, I_S, giving:

$$Z_T = R_T + L_T \tag{4. 28}$$

Figure 4.2.12 illustrates how the stub inductance is introduced.

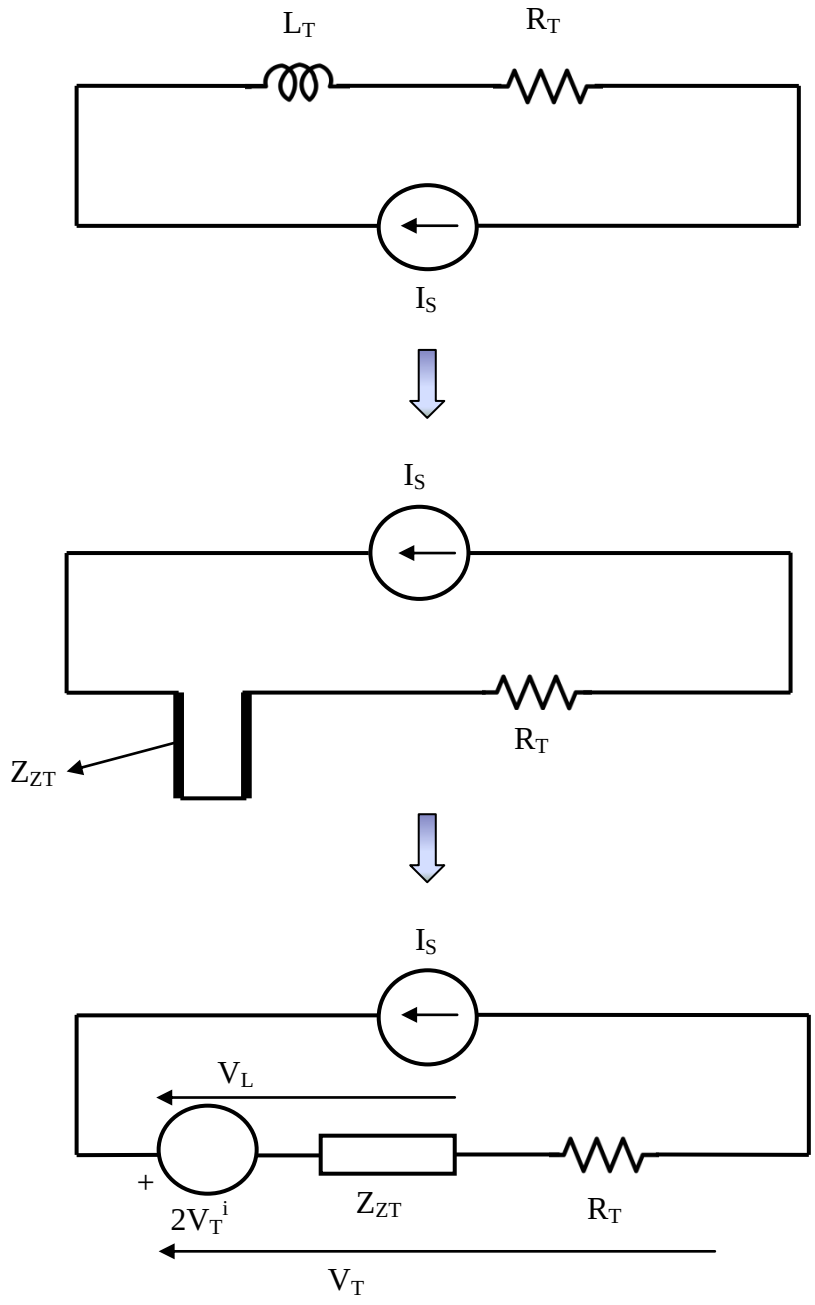

Figure 4.2.12: Implementing a stub inductance to the transfer impedance

where R_T and L_T are defined from (4.28) as:

$$R_T = Z_R \tag{4. 29}$$

$$L_T = M_L + M_G + L_S \tag{4. 30}$$

where Z_R, M_L, M_G and L_S are as described by the Kley model in Chapter 2, section 2.2.3.

The voltages from Figure 4.2.12 are calculated as follows:

$$V_L = 2V_T^i + I_S Z_{ZT} \tag{4. 31}$$

$$V_T = V_L + I_S R_T \tag{4. 32}$$

where Z_{ZT} is given by:

$$Z_{ZT} = \frac{2L_T}{\Delta t} \tag{4. 33}$$

The scattering property is obtained as follows:

$$V_T^r = V_L - V_T^i \tag{4. 34}$$

The incident voltage at the next time-step is then:

$${}_{k+1}V_T^i = -{}_kV_T^r \tag{4. 35}$$

where V_T is then the source voltage for the victim circuit node.

B. Digital Filter Model

The digital filter is another technique of modelling the broadband frequency of the coaxial braid's transfer impedance. Similar to the stub inductance technique developed by Christopoulos [4.1], the digital filter operates by using the bilinear z-transform method. The bilinear transform is a first-order approximation of the natural algorithm function that is an exact mapping of the z-plane to the s-plane. When Laplace transform is performed on a discrete-time signal, with each element of the discrete-time sequence attached to a correspondingly delayed unit impulse, the result is precisely the z-transform of the discrete-time sequence with a substitution of [4.12]:

$$z = e^{s\Delta t} = \frac{e^{\frac{s\Delta t}{2}}}{e^{-\frac{s\Delta t}{2}}} \approx \frac{1 + \frac{s\Delta t}{2}}{1 - \frac{s\Delta t}{2}} \tag{4. 36}$$

where Δt is the numerical integration of the time step size of the trapezoidal rule used in the bilinear transform derivation. Therefore, in the s-plane, the approximation for the bilinear transform can be given as:

$$s = \frac{1}{\Delta t}\ln z = \frac{2}{\Delta t}\left[\frac{z-1}{z+1} + \frac{1}{3}\left(\frac{z-1}{z+1}\right)^3 + \frac{1}{5}\left(\frac{z-1}{z+1}\right)^5 + \frac{1}{7}\left(\frac{z-1}{z+1}\right)^7 + \cdots\right] \quad (4.37)$$

$$\approx \frac{2}{\Delta t}\frac{1-z^{-1}}{1+z^{-1}}$$

The implementation of the digital filtering technique for the braid's transfer impedance can be derived in equations (4.38) – (4.40).

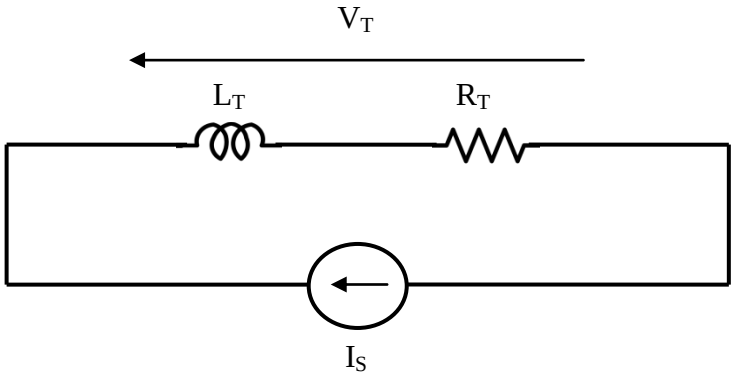

Figure 4.2.13*: Coaxial braid's transfer impedance, Z_T*, with a source current, I_S

From Figure 4.2.13:

$$V_T = I_S(R_T + sL_T) \quad (4.38)$$

where s is described in (4.37), thus, giving:

$$V_T = I_S\left\{R_T + \frac{2}{\Delta t}\frac{1-z^{-1}}{1+z^{-1}}L_T\right\} = I_S R_T + \frac{2}{\Delta t}\frac{1-z^{-1}}{1+z^{-1}}I_S L_T \quad (4.39)$$

After further simplifying (4.40), the final equation to calculate V_T is given by:

$$V_T = I_S\left(R_T + \frac{2L_T}{\Delta t}\right) + z^{-1}\left\{I_S\left(R_T - \frac{2L_T}{\Delta t}\right) - V_T\right\} \quad (4.40)$$

where z^{-1} denotes a delay in time step or previous time step.

4.3 Numerical Model of Two Coaxial Cables in Free Space

The case of crosstalk between two coaxial cables in free space is explained in Chapter 2. Numerically, the coupling modelled by the transfer impedance of the coaxial braid in both the tertiary and victim circuits create a source voltage, V_T, as illustrated in Figures 4.3.1 and 4.3.2, respectively. L and R indicate the line to the left and right respectively, at node n, at time step k.

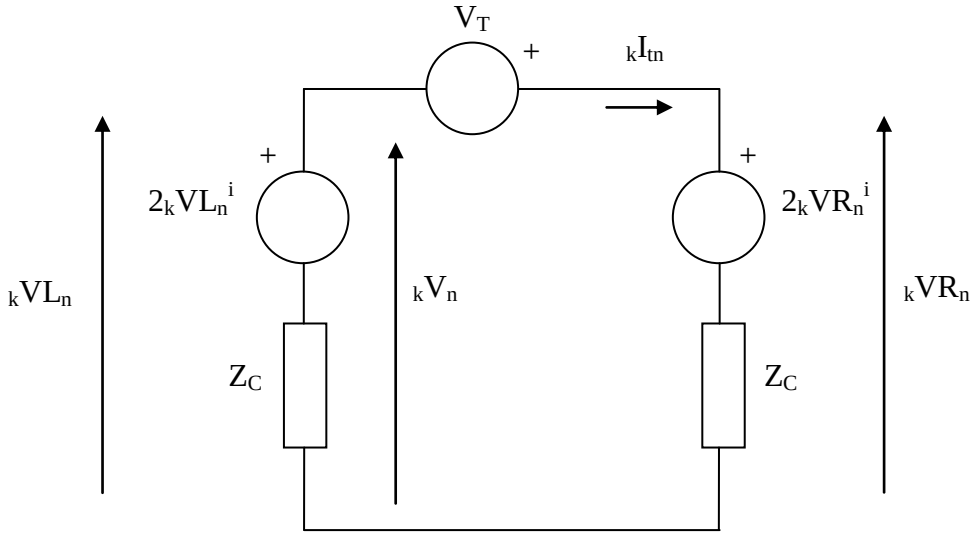

Figure 4.3.1: A node in the tertiary circuit where the coupling path is modelled by the *braid's transfer impedance,* V_T

Solving its Thevenin equivalent, the total voltage of the node of the victim circuit is given by:

$$ {}_kV_n = \frac{\frac{2\ {}_kVL_n^i}{Z_C} + \frac{2\ {}_kVR_n^i - V_T}{Z_C}}{\frac{2}{Z_C}} \tag{4. 41} $$

The reflected voltages would then be given by:

$$ {}_kVL_n^r = {}_kV_n - {}_kVL_n^i \tag{4. 42} $$

$$ {}_kVR_n^r = {}_kV_n - {}_kVR_n^i + V_T \tag{4. 43} $$

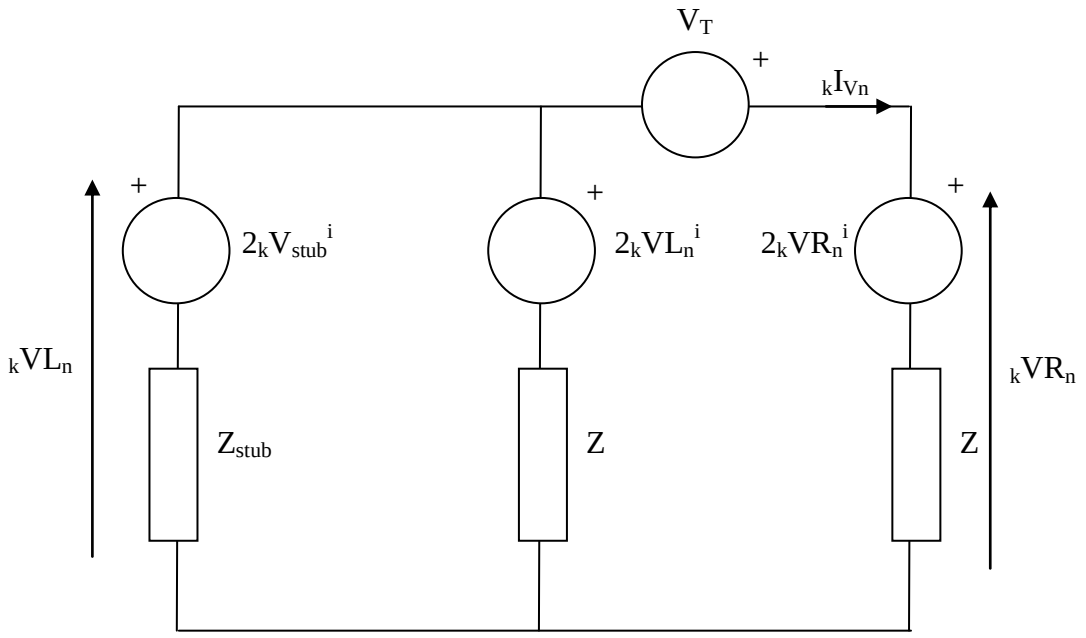

Figure 4.3.2: A node in the victim circuit where the coupling path is modelled by the *braid's transfer impedance,* V_T

Similarly, solving its Thevenin equivalent of the tertiary circuit, the total voltage of the node is given by:

$$ {}_kV_n = \frac{\frac{2\ {}_kV_{stub}^i}{Z_{stub}} + \frac{2\ {}_kVL_n^i}{Z} + \frac{2\ {}_kVR_n^i - V_T}{Z}}{\frac{1}{Z_{stub}} + \frac{2}{Z}} \tag{4. 44} $$

The reflected voltages would then be given by:

$$ {}_kV_{stub}^r = {}_kV_n - {}_kV_{stub}^i \tag{4. 45} $$

$$ {}_kVL_n^r = {}_kV_n - {}_kVL_n^i \tag{4. 46} $$

$$ {}_kVR_n^r = {}_kV_n - {}_kVR_n^i + V_T \tag{4. 47} $$

Subsequently, the victim circuit current, I_V, obtained is used to calculate the coupling degree of the two coaxial cables, giving (from Chapter 2):

$$ V_{V0} = {}_kI_{V1}R_{0L} \tag{4. 48} $$

The flow chart of the simulation procedure is presented in Figure 4.3.3:

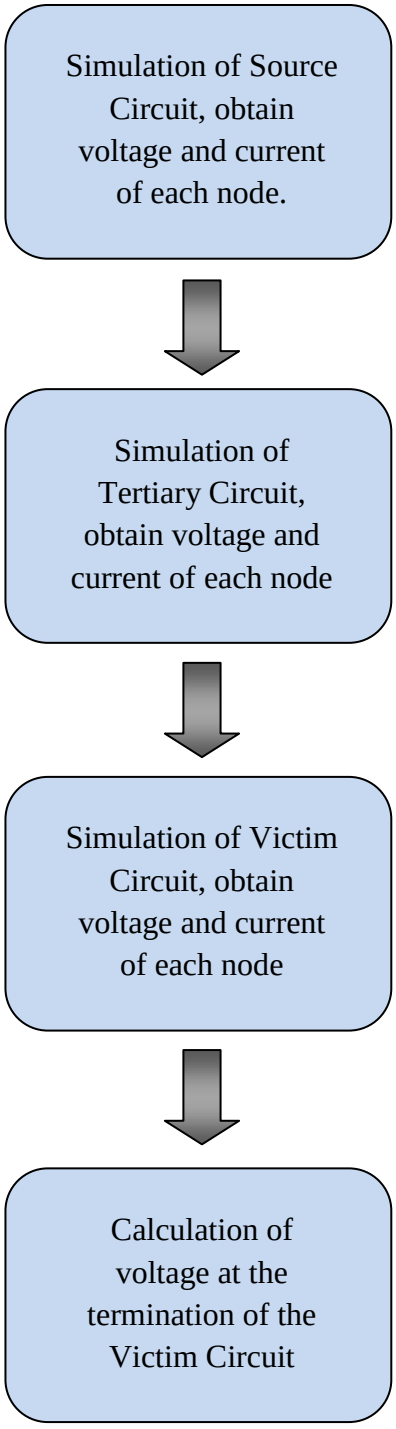

Figure 4.3.3: A flow chart showing the simulation procedure of the numerical approach.

4.3.1 Comparison between the Digital Filter and Stub Inductance Model of the Surface Transfer Impedance

Simulation was performed using the 1D TLM model developed on the crosstalk of two RG-58 coaxial cables in free space. The cell dimension, Δx, was chosen to be 0.01m. The cables are both 1.22m long and divided into 122 segments. The inner conductor of the source circuit is excited by a Gaussian voltage, V_S, in series with a 50Ω resistance. The inner conductors of the source and victim circuits are terminated with a 50Ω resistance. The voltage at the victim circuit, V_{V0}, is obtained. Hence, the crosstalk between the two cables, S_{21}, can be calculated from:

$$S_{21} = 20\log_{10}\left|\frac{\widetilde{V_{V0}}}{\widetilde{V_S}/2}\right| \qquad (4.\ 49)$$

where the accent ~ denotes Fourier Transformed quantities.

The numerical model was simulated for 16384 time-steps. Figures 4.3.4 – 4.3.7 present the crosstalk comparison of the two modelling techniques incorporating only the surface transfer impedance – Digital Filter Model and Stub Inductance Model. It is shown that both the digital filter and stub impedance models match exactly with each other.

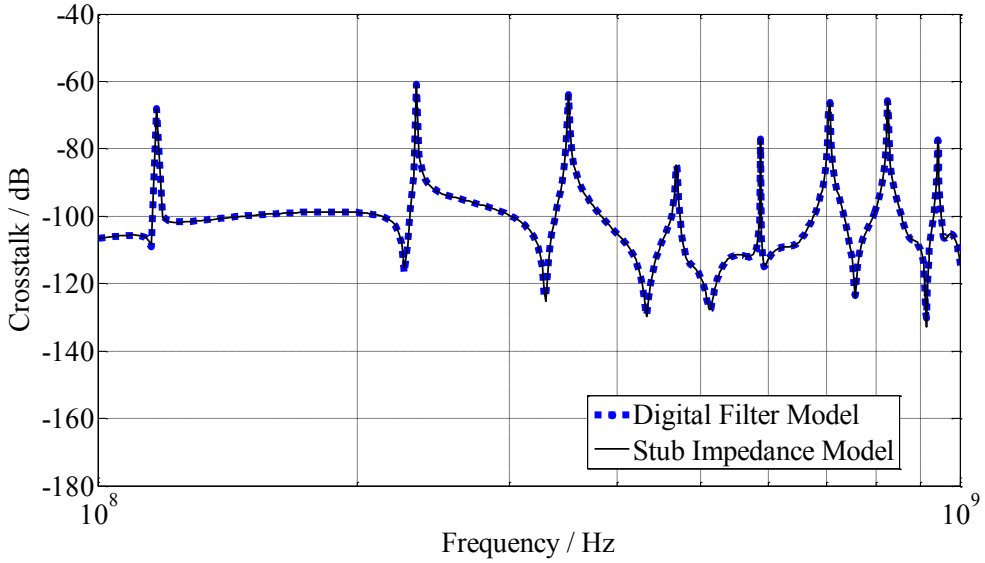

Figure 4.3.4: The crosstalk comparison of two modelling techniques of the surface transfer impedance for a separation, s = 2cm

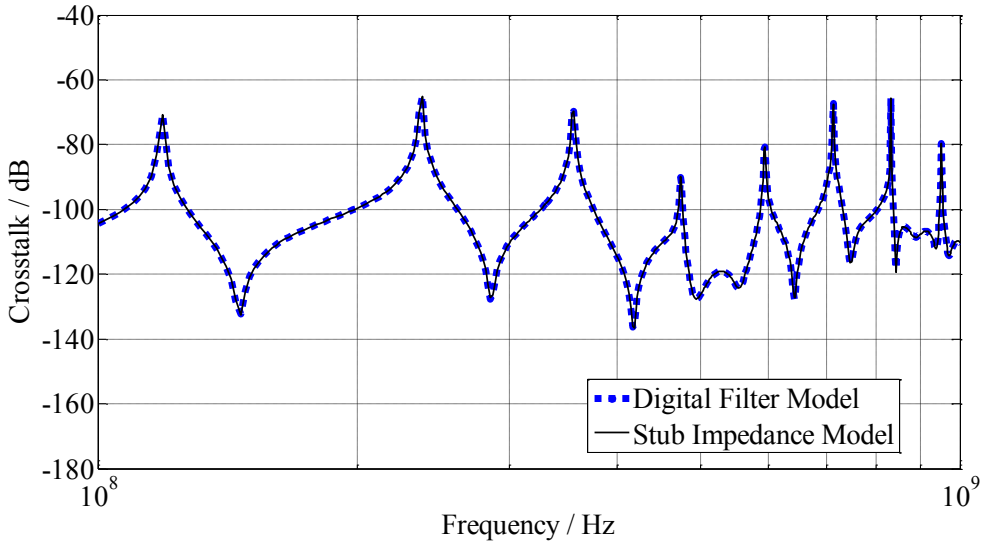

Figure 4.3.5: The crosstalk comparison of two modelling techniques of the surface transfer impedance for a separation, s = 5cm

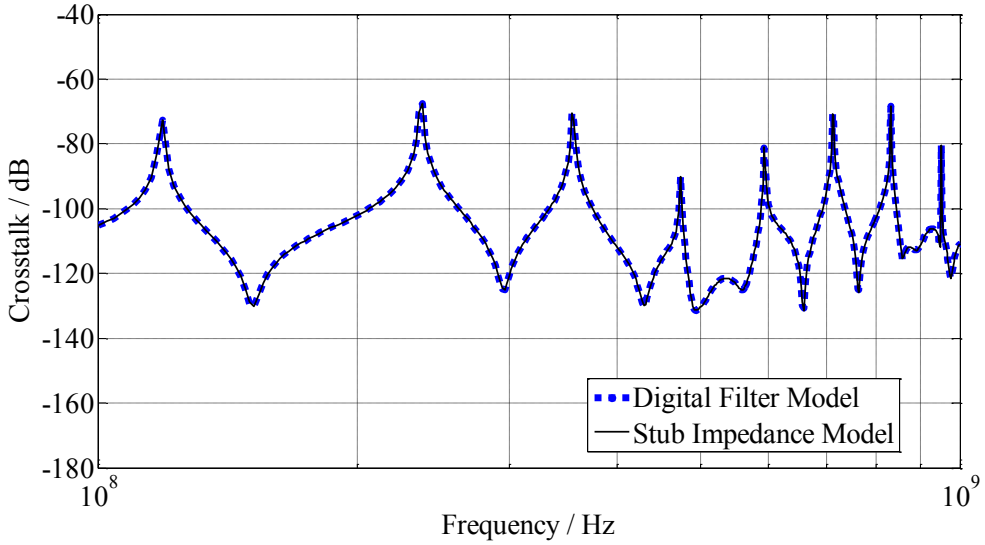

Figure 4.3.6: The crosstalk comparison of two modelling techniques of the surface transfer impedance for a separation, s = 10cm

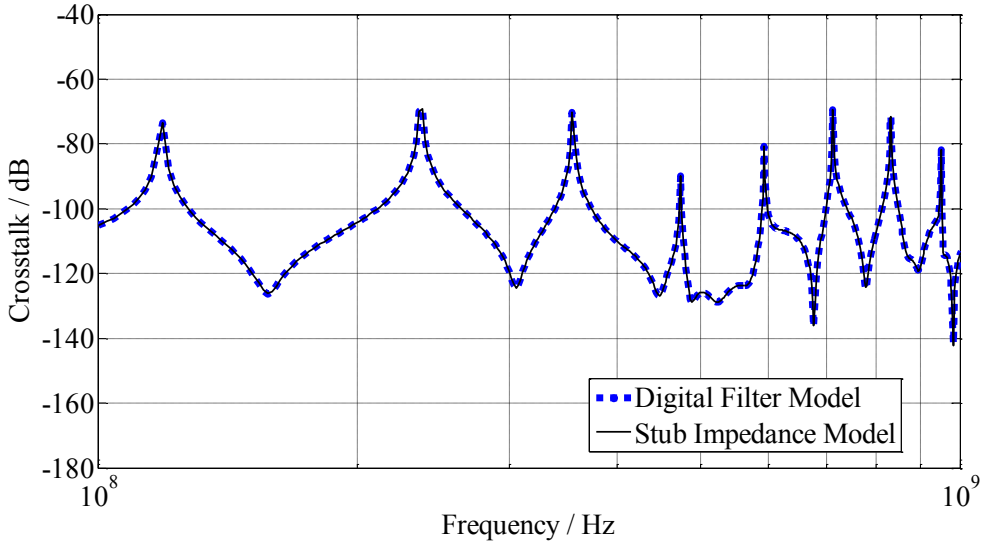

Figure 4.3.7: The crosstalk comparison of two modelling techniques of the surface transfer impedance for a separation, s = 15cm

4.4 The Multimode Model

The principles of propagation in two coaxial cables above ground system are studied in detail in order to establish the main features of propagation in a multiconductor system. This treatment is followed by a generalization to more complex configurations [4.3]. In a case of two coaxial cables above ground shown in Figure 2.3.6 in Chapter 2, the coaxial braids each possess a self-capacitance, C_1, to ground, self-inductance, L_S, and with a mutual capacitance and inductance between the braids, C_2 and M, respectively, illustrated in Figure 4.4.1.

Christopoulos [4.3] and Naylor et al. [4.9] noted that the matrix products of (4.58) and (4.59) are not diagonal, implying that the total voltage and current on any coaxial braid line is dependent on the voltages and currents on all the lines and that part of the electromagnetic energy are transported at different modes of propagation velocities. In order to incorporate the multimode into the TLM model, it is necessary to first decouple the line interaction using a suitable transformation matrix.

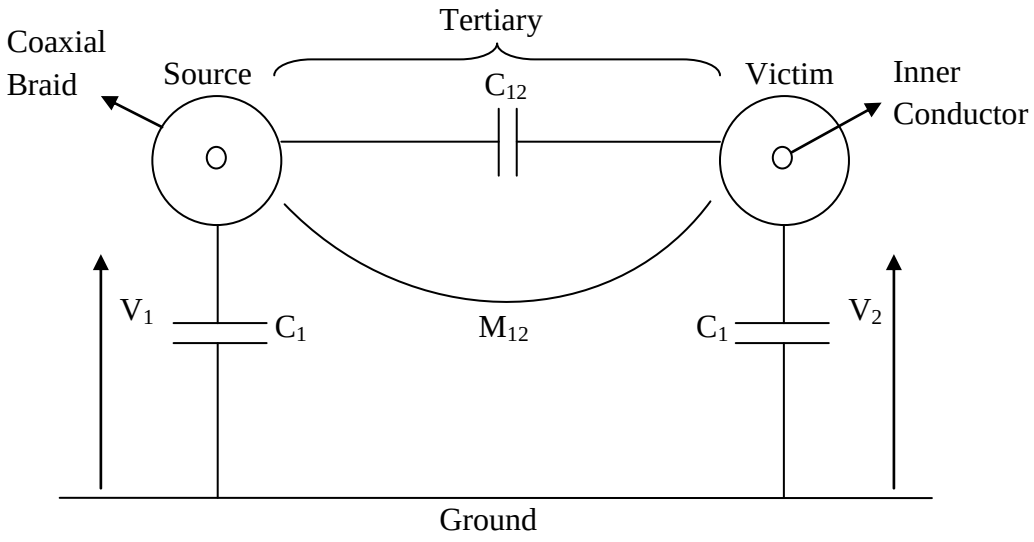

Figure 4.4.1: An illustration of two coaxial cables above a ground plane system

By applying Kirchoff's Voltage Law (KVL), the following relationships can be derived:

$$-\frac{\partial V_1}{\partial x} = L_S \frac{\partial I_1}{\partial t} + M_{12} \frac{\partial I_2}{\partial t} \tag{4. 50}$$

$$-\frac{\partial V_2}{\partial x} = M_{12} \frac{\partial I_1}{\partial t} + L_S \frac{\partial I_2}{\partial t} \tag{4. 51}$$

By applying Kirchoff's Current Law (KCL), the following relationships can be given as:

$$-\frac{\partial I_1}{\partial x} = C_1 \frac{\partial V_1}{\partial t} + C_{12} \frac{\partial V_1}{\partial t} - C_{12} \frac{\partial V_2}{\partial t} \tag{4. 52}$$

$$-\frac{\partial I_2}{\partial x} = C_1 \frac{\partial V_2}{\partial t} + C_{12} \frac{\partial V_2}{\partial t} - C_{12} \frac{\partial V_1}{\partial t} \tag{4. 53}$$

Rearranging equations (4.50) – (4.53), simplifying them in matrix form gives:

$$-\left[\frac{\partial V}{\partial x}\right] = [L]\left[\frac{\partial I}{\partial t}\right] \tag{4. 54}$$

$$-\left[\frac{\partial I}{\partial x}\right] = [C]\left[\frac{\partial V}{\partial t}\right] \tag{4. 55}$$

where

$$[L] = \begin{bmatrix} L_S & M \\ M & L_S \end{bmatrix} \tag{4. 56}$$

$$[C] = \begin{bmatrix} C_1 + C_{12} & -C_{12} \\ -C_{12} & C_1 + C_{12} \end{bmatrix} \tag{4. 57}$$

For the tertiary circuit, [L] and [C] are as given in Chapter 2, section 2.4.1B. The derivatives of equations (4.54) and (4.55) are then given by:

$$-\left[\frac{\partial^2 V}{\partial x^2}\right] = [L][C]\left[\frac{\partial^2 V}{\partial t^2}\right] \tag{4. 58}$$

$$-\left[\frac{\partial^2 I}{\partial x^2}\right] = [C][L]\left[\frac{\partial^2 I}{\partial t^2}\right] \tag{4. 59}$$

Hence, simplifying equations (4.58) and (4.59) gives:

$$-\left[\frac{\partial^2 V}{\partial x^2}\right] = [L][C]\left[\frac{\partial^2 V}{\partial t^2}\right] \tag{4. 60}$$

where

$$[L][C] = \begin{bmatrix} a & b \\ b & a \end{bmatrix} \tag{4. 61}$$

$$\begin{bmatrix} a & b \\ b & a \end{bmatrix} = \begin{bmatrix} L_S(C_1 + C_{12}) - MC_{12} & M(C_1 + C_{12}) - L_S C_{12} \\ M(C_1 + C_{12}) - L_S C_{12} & L_S(C_1 + C_{12}) - MC_{12} \end{bmatrix} \tag{4. 62}$$

Equation (4.63) indicates that voltages V_1 and V_2 are coupled through the off-diagonal elements b [4.3]. It is convenient to introduce a set of new modal voltages, V_{m1} and V_{m2}, where the transmission lines are decoupled. The new modal voltages are related to V_1 and V_2 through a transformation matrix S, given by [4.3]:

$$\begin{bmatrix} V_1 \\ V_2 \end{bmatrix} = [S]\begin{bmatrix} V_{m1} \\ V_{m2} \end{bmatrix} \tag{4. 63}$$

where matrix S can be defined as:

$$[S] = \begin{bmatrix} S_{11} & S_{12} \\ S_{21} & S_{22} \end{bmatrix} \tag{4. 64}$$

By substituting (4.63) into (4.60) and through calculations of the elements of the matrix known as eigenvalues and eigenvectors, the variation of the two modal voltages can be described in equations (4.65) and (4.66) as:

$$\frac{\partial^2 V_{m1}}{\partial x^2} = (a + b)\frac{\partial^2 V_{m1}}{\partial t^2} \tag{4. 65}$$

$$\frac{\partial^2 V_{m2}}{\partial x^2} = (a - b)\frac{\partial^2 V_{m2}}{\partial t^2} \tag{4. 66}$$

Equations (4.67) and (4.68) describe the two independent modes of propagation, where the propagation velocity for modes 1 and 2 are respectively expressed as:

$$u_1 = \frac{1}{\sqrt{a+b}} \tag{4. 67}$$

$$u_2 = \frac{1}{\sqrt{a-b}} \tag{4. 68}$$

Since the modal voltages are related to the actual line voltages, the transformation matrix S can be equated in (4.69) as:

$$[S] = \begin{bmatrix} 1 & 1 \\ 1 & -1 \end{bmatrix} \tag{4. 69}$$

Through diagonalisation, the common and differential mode signals of the modal voltages are equated as:

$$\begin{bmatrix} V_1 \\ V_2 \end{bmatrix} = \begin{bmatrix} 1 & 1 \\ 1 & -1 \end{bmatrix} \begin{bmatrix} V_{m1} \\ V_{m2} \end{bmatrix} = \begin{bmatrix} V_{m1} + V_{m2} \\ V_{m1} - V_{m2} \end{bmatrix} \tag{4. 70}$$

Hence:

$$V_1 = V_{m1} + V_{m2} \tag{4. 71}$$

$$V_2 = V_{m1} - V_{m2} \tag{4. 72}$$

For simplicity, substituting in the values for [L] and [C] as given in section 2.4.1B, it is found that $b = 0$; so that the velocity of propagation for both modes are the same and correspond to the speed of light, c.

Naylor [4.9] et al. presented the modal currents in a more direct approach that is more convenient for numerical applications. Simplifying equations (4.58) and (4.59) give:

$$-\left[\frac{\partial^2 I}{\partial x^2}\right] = [C][L]\left[\frac{\partial^2 I}{\partial t^2}\right] \tag{4. 73}$$

Similarly, by introducing new sets of modal currents, the new modal currents are related to I_1 and I_2 through a transformation matrix Q, given by [4.9]:

$$\begin{bmatrix} I_1 \\ I_2 \end{bmatrix} = [Q] \begin{bmatrix} I_{m1} \\ I_{m2} \end{bmatrix} \tag{4. 74}$$

where

$$[Q] = \{[S]^{-1}\}^T = \frac{1}{2}\begin{bmatrix}1 & 1\\ 1 & -1\end{bmatrix} \quad (4.75)$$

By comparison with (4.74), the current equations are given by:

$$I_1 = \frac{1}{2}(I_{m1} + I_{m2}) \quad (4.76)$$

$$I_2 = \frac{1}{2}(I_{m1} - I_{m2}) \quad (4.77)$$

The modal impedance, Z_m, which relates modal voltages to modal currents, is required. The equation relating actual line quantities with modal voltages is given by:

$$-\left[\frac{\partial I}{\partial x}\right] = [C][S]\left[\frac{\partial V_m}{\partial t}\right] \quad (4.78)$$

As the modal voltages vary as a function of time, space and velocity [4.9], they can be given by:

$$V_m = f(x - tu) \quad (4.79)$$

Substituting:

$$x_s = x - tu \quad (4.80)$$

Then:

$$\frac{\partial V_m}{\partial t} = \frac{\partial V_m}{\partial x_s}\frac{\partial x_s}{\partial t} = -u\frac{\partial V_m}{\partial x_s} \quad (4.81)$$

Hence, (4.81) can be written as:

$$-\left[\frac{\partial I}{\partial x_S}\right] = -[C][S][u]\left[\frac{\partial V_m}{\partial x_s}\right] \quad (4.82)$$

By integrating (4.82) with respect to distance, x_s, it becomes:

$$[I] = [C][S][u]\int\left[\frac{\partial V_m}{\partial x_s}\right]dx_S = [C][S][u][V_m] \quad (4.83)$$

Substituting (4.81) to (4.83), gives:

$$[Q][I_m] = [C][S][u][V_m] \tag{4. 84}$$

Hence:

$$[V_m] = [u]^{-1}[S]^{-1}[C]^{-1}[Q][I_m] \tag{4. 85}$$

where the modal characteristic impedance $[Z_m]$ is given by:

$$[Z_m] = [u]^{-1}[S]^{-1}[C]^{-1}[Q] \tag{4. 86}$$

After derivation, (4.86) gives:

$$\begin{bmatrix} Z_{m1} \\ Z_{m2} \end{bmatrix} = \frac{1}{4}\left\{\frac{1}{u_1 u_2}\right\}\left\{\frac{1}{C_1^2 - C_{12}^2}\right\}\begin{bmatrix} 2(u_2 C_1 - u_2 C_{12}) & 0 \\ 0 & 2(u_1 C_1 + u_1 C_{12}) \end{bmatrix} \tag{4. 87}$$

4.4.1 Implementation of the Multimode Model into TLM Model

The first step in computation is to obtain the modal components and the corresponding propagation velocities for each mode. The system is then separated into external coupling regions, mode conversion and mode propagation regions, shown in Figure 4.4.2 [4.3]. Between the coupling regions propagation of the modal quantities takes place along fictitious conductors chosen to sustain the independent propagation of each mode [4.9]. At each segment Δx, the modal voltages and currents are converted to line components and are combined with the source term for external coupling from the adjacent source braid. The resulting victim braid components are then converted into modal components, which propagate along the two coaxial braids represented by appropriate modal impedances. Reconversion to modal quantities is then implemented to allow propagation to the next coupling region. This process is repeated for the total number of segments in the TLM model.

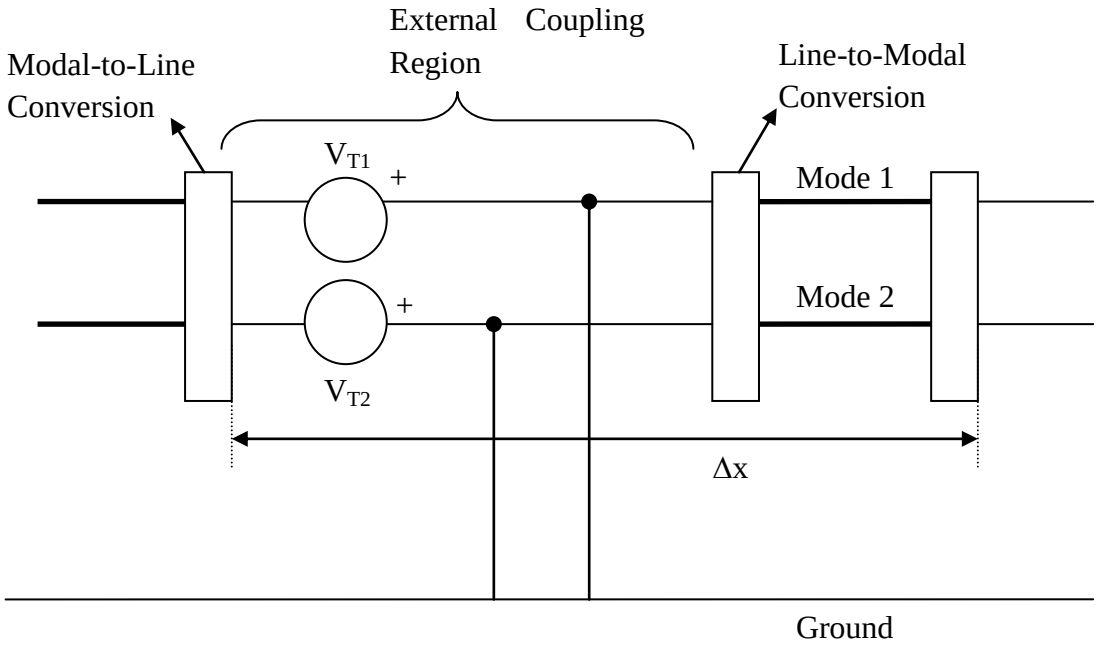

Figure 4.4.2: Model of multimode propagation on the source braid coupled to the victim braid through the surface transfer impedance V_{T1} and V_{T2}.

Thus, for each of the braids of the source and victim coaxial lines there is a voltage source which models the external coupling at the nodes. This voltage source is a real line quantity and in order to incorporate into each of the nodes, it is necessary to convert from modal parameters to actual line parameters, add in the source term and finally converting it back.

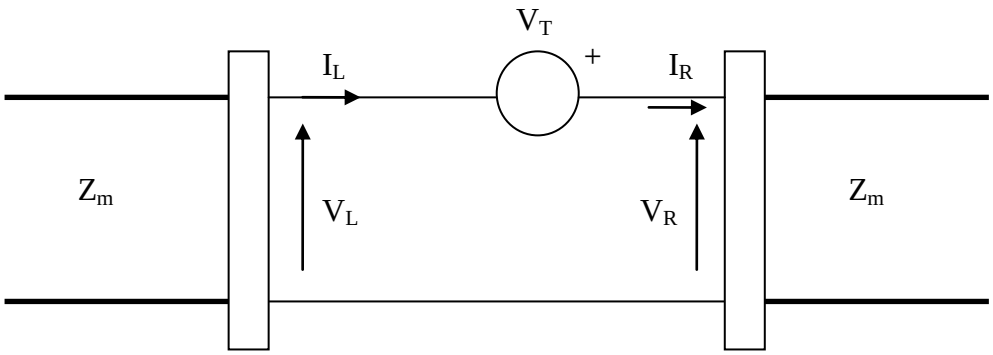

Figure 4.4.3: External coupling source in one segment of the source and victim braid coaxial line

From Figure 4.4.3, it can be deduced that:

$$[I_L] = [I_R] \tag{4. 88}$$

$$[V_L] + [V_T] = [V_R] \tag{4. 89}$$

where the subscripts L and R denote the line to the left or to the right of the node. Through the transformation matrix S and Q, (4.88) and (4.89) can be given as:

$$[V_L] = [S][V_{mL}] \tag{4. 90}$$

$$[V_R] = [S][V_{mR}] \tag{4. 91}$$

$$[I_L] = [Q][I_{mL}] \tag{4. 92}$$

$$[I_R] = [Q][I_{mR}] \tag{4. 93}$$

The current in the transmission line can be described as:

$$[I_{mL}] = \left[I_{mL}^{i}\right] + [I_{mL}^{r}] \tag{4. 94}$$

$$[I_{mL}] = [Z_m]^{-1}\{\left[V_{mL}^{i}\right] - [V_{mL}^{r}]\} \tag{4. 95}$$

Similarly:

$$[I_{mR}] = \left[I_{mR}^{i}\right] + [I_{mR}^{r}] \tag{4. 96}$$

$$[I_{mR}] = [Z_m]^{-1}\{[V_{mR}^{r}] - \left[V_{mR}^{i}\right]\} \tag{4. 97}$$

From equations (4.92), (4.93), (4.95) and (4.97), it can be written that:

$$[I_L] = [Q][Z_m]^{-1}\{\left[V_{mL}^{i}\right] - [V_{mL}^{r}]\} \tag{4. 98}$$

$$[I_R] = [Q][Z_m]^{-1}\{[V_{mR}^{r}] - \left[V_{mR}^{i}\right]\} \tag{4. 99}$$

Similarly, equations (4.90) and (4.91) can be written as:

$$[V_L] = [S]\{\left[V_{mL}^{i}\right] + [V_{mL}^{r}]\} \tag{4. 100}$$

$$[V_R] = [S]\{\left[V_{mR}^{i}\right] + [V_{mR}^{r}]\} \tag{4. 101}$$

Combining equations (4.100) and (4.101), (4.102) can be written as:

$$[S]\{[V_{mL}^{i}] + [V_{mL}^{r}]\} + [V_T] = [S]\{[V_{mR}^{i}] + [V_{mR}^{r}]\} \quad (4.102)$$

Similarly, combining equations (4.98) and (4.99), (4.103) can be written as:

$$[Q][Z_m]^{-1}\{[V_{mL}^{i}] - [V_{mL}^{r}]\} = [Q][Z_m]^{-1}\{[V_{mR}^{r}] - [V_{mR}^{i}]\} \quad (4.103)$$

Equations (4.102) and (4.103) are manipulated to obtain two further expressions relating the known parameters (incident pulses and source terms) to the unknown parameters (reflected pulses) through simultaneous equations, given by [4.9]:

$$[V_{mR}^{i}] = [V_{mL}^{r}] + \frac{1}{2}[S]^{-1}[V_T] \quad (4.104)$$

$$[V_{mL}^{i}] = [V_{mR}^{r}] - \frac{1}{2}[S]^{-1}[V_T] \quad (4.105)$$

where

$$\frac{1}{2}[S]^{-1} = \frac{1}{4}\begin{bmatrix} 1 & 1 \\ 1 & -1 \end{bmatrix} \quad (4.106)$$

Figure 4.4.4 and Figure 4.4.5 both show one segment of how the two propagation modes are implemented into the TLM model. Note that both the modes comprise of the braid where the signal travels at the speed of light, c. The subscripts m1 and m2 indicate modes 1 and 2 respectively; L and R indicate the line to the left and right respectively; at node n, at time step k.

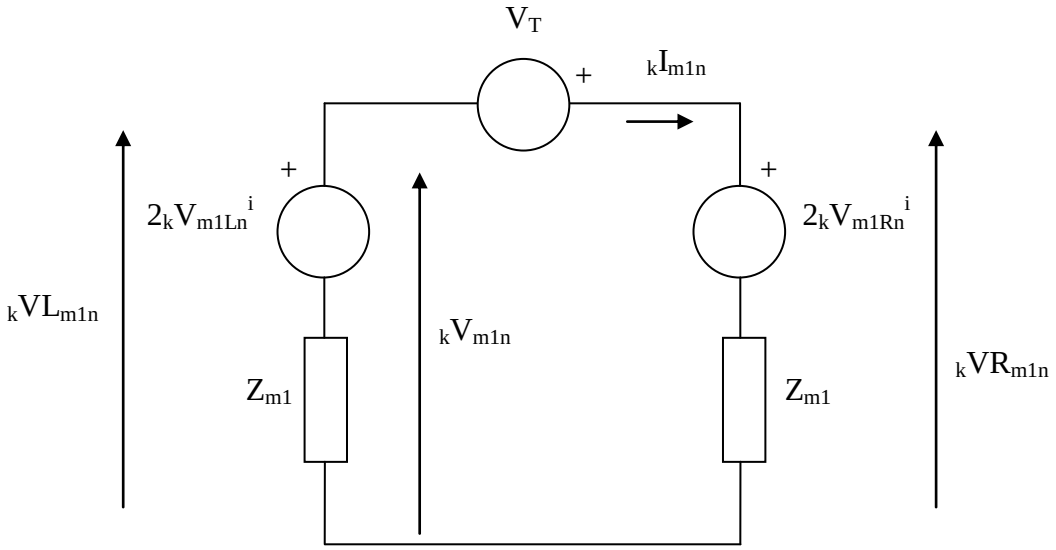

Figure 4.4.4: One segment of the TLM model on the differential mode of the system (Mode 1)

Solving the Thevenin Equivalent circuit as illustrated in Figure 4.4.4, for each node, the total voltage of the node is given by:

$$ {}_kV_{m1} = \frac{\frac{2V_{m1L}^i}{Z_{m1}} + \frac{2V_{m1R}^i - V_T}{Z_{m1}}}{\frac{2}{Z_{m1}}} \tag{4. 107} $$

Following equations (4.108) and (4.109), the reflected pulses would then be given by:

$$ {}_kV_{m1L}^r = {}_kV_{m1R}^i + \frac{1}{4}V_T \tag{4. 108} $$

$$ {}_kV_{m1R}^r = {}_kV_{m1L}^i - \frac{1}{4}V_T \tag{4. 109} $$

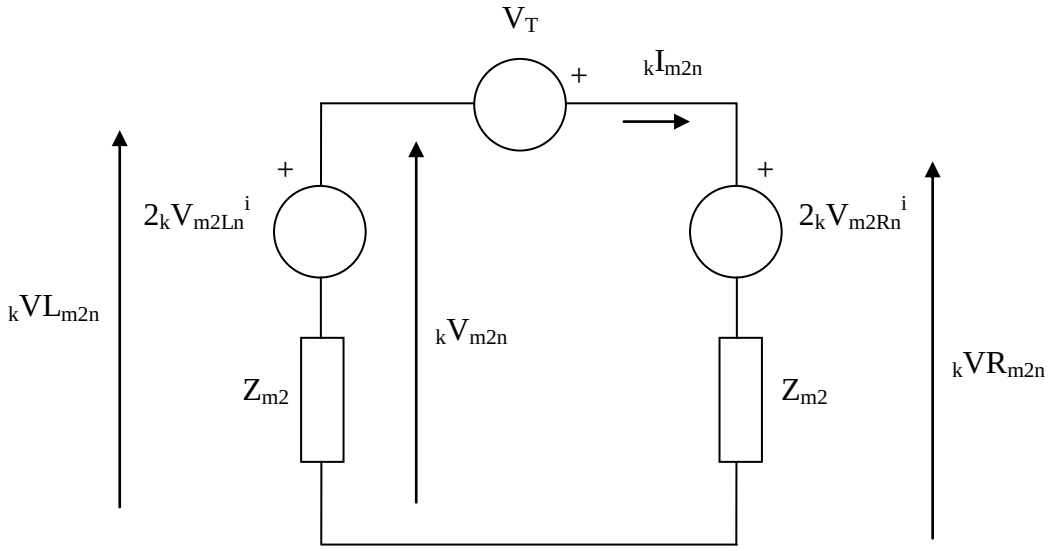

Figure 4.4.5: One segment of the TLM model on the common mode of the system (Mode 2)

Similarly, solving for the Thevenin Equivalent circuit as illustrated in Figure 4.4.5, for each node, the total voltage of the node is given by:

$$ {}_kV_{m2} = \frac{\frac{2V_{m2L}^{i}}{Z_{m2}} + \frac{2V_{m2R}^{i} - V_T}{Z_{m2}}}{\frac{2}{Z_{m2}}} \tag{4. 110} $$

Following equations (4.111) and (4.112), the reflected pulses would then be given by:

$$ {}_kV_{m2L}^{r} = {}_kV_{m2R}^{i} + \frac{1}{4}V_T \tag{4. 111} $$

$$ {}_kV_{m2R}^{r} = {}_kV_{m2L}^{i} - \frac{1}{4}V_T \tag{4. 112} $$

Therefore, with NT denoting the total number of segments in the transmission line, the real quantity of the current in the victim line's coaxial braid can be deduced to be:

$$ {}_kI_2 = \frac{1}{2}\left\{\sum_{n=1}^{NT}\left({}_kI_{m1n} - {}_kI_{m2n}\right)\right\} \tag{4. 113} $$

The current obtained from (4.113) can be used to calculate the transfer impedance in section 4.2.2 and finally included into the calculation of the current, I_V, of the victim line. Subsequently, the coupling degree of the two coaxial cables above ground system can then be obtained from (4.49).

4.5 Numerical Modelling Results – Effects of Brass End Plates

4.5.1 Coupling between Two RG-58 Coaxial Cables in Free Space

Simulation was performed using the 1D TLM model developed in section 4.3. Figures 4.5.1 – 4.5.4 show a simulated lossless crosstalk system between two RG-58 coaxial cables in free space for different separations, s, between the cables (2, 5, 10 and 15cm) compared against measurement, where the differential mode inductive effects of the brass end plates can be observed from the discrepancy in the peaks of the resonant frequencies when omitting the inductance effects.

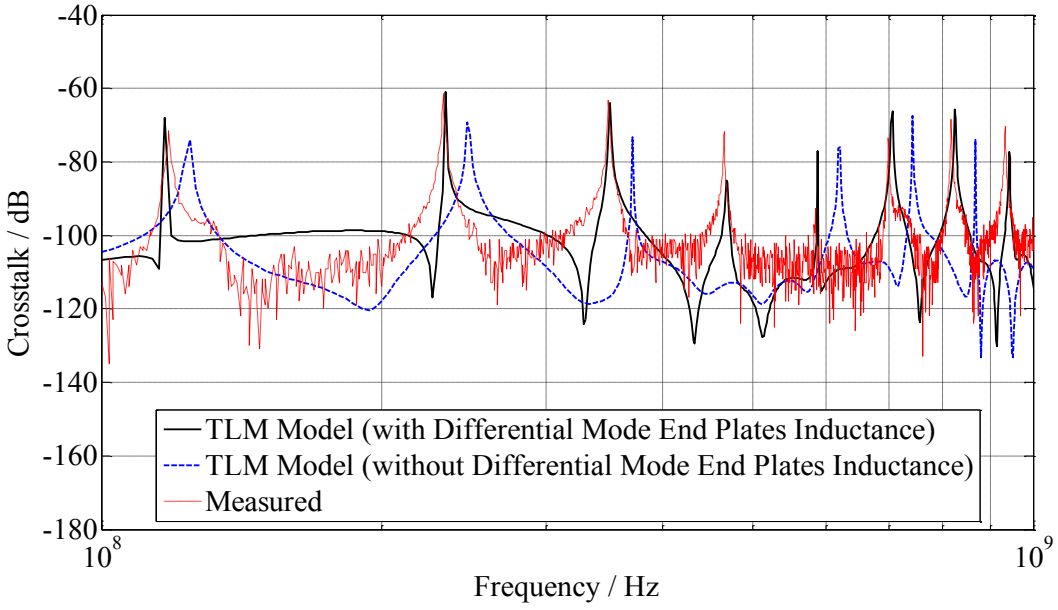

Figure 4.5.1: Crosstalk showing the effects of brass end plates at the terminations of the tertiary circuit with s = 2cm

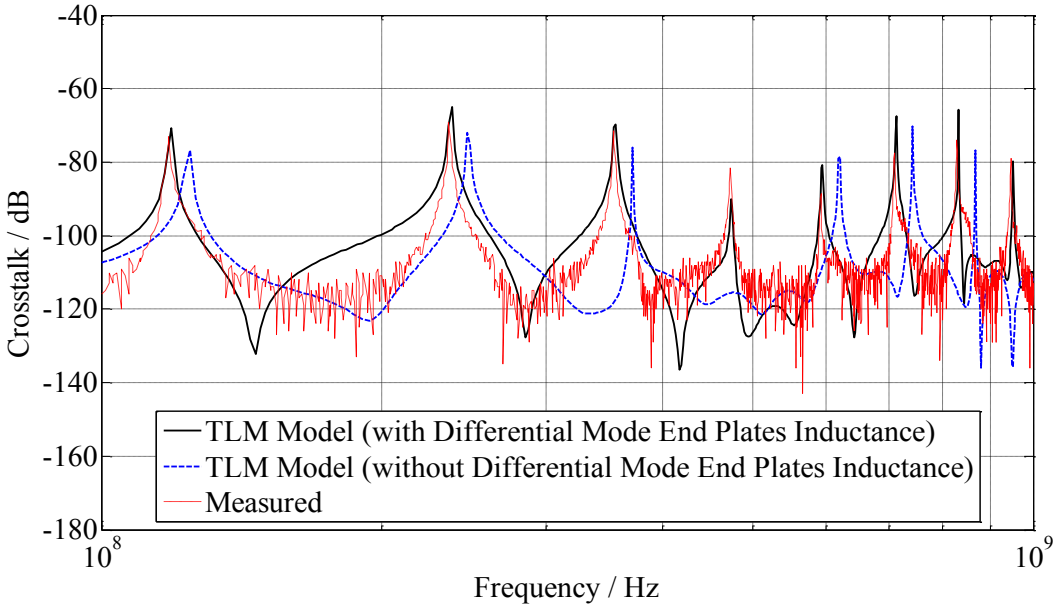

Figure 4.5.2: Crosstalk showing the effects of brass end plates at the terminations of the tertiary circuit with s = 5cm

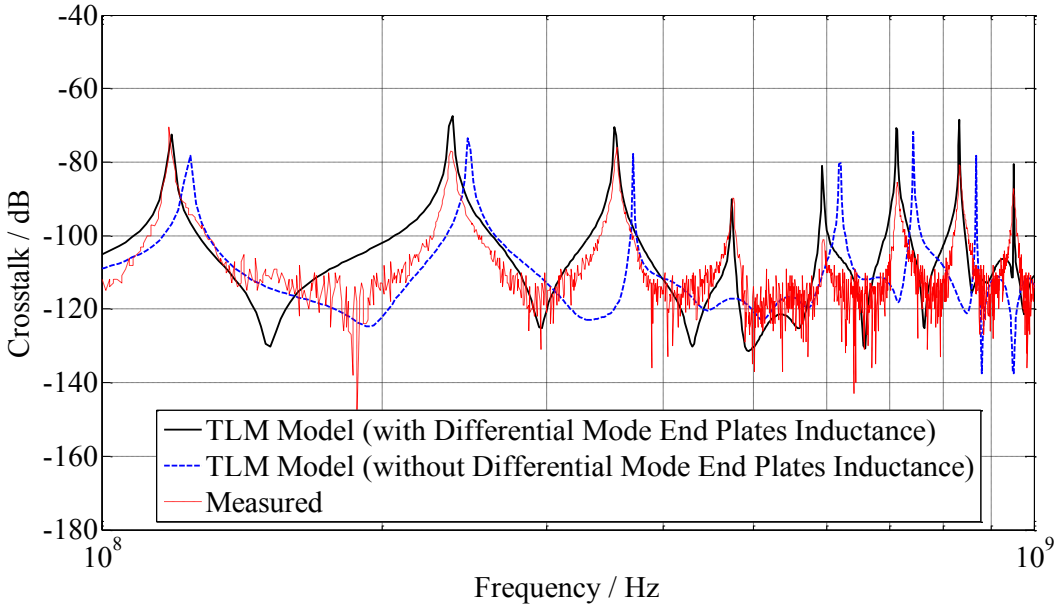

Figure 4.5.3: Crosstalk showing the effects of brass end plates at the terminations of the tertiary circuit with s = 10cm

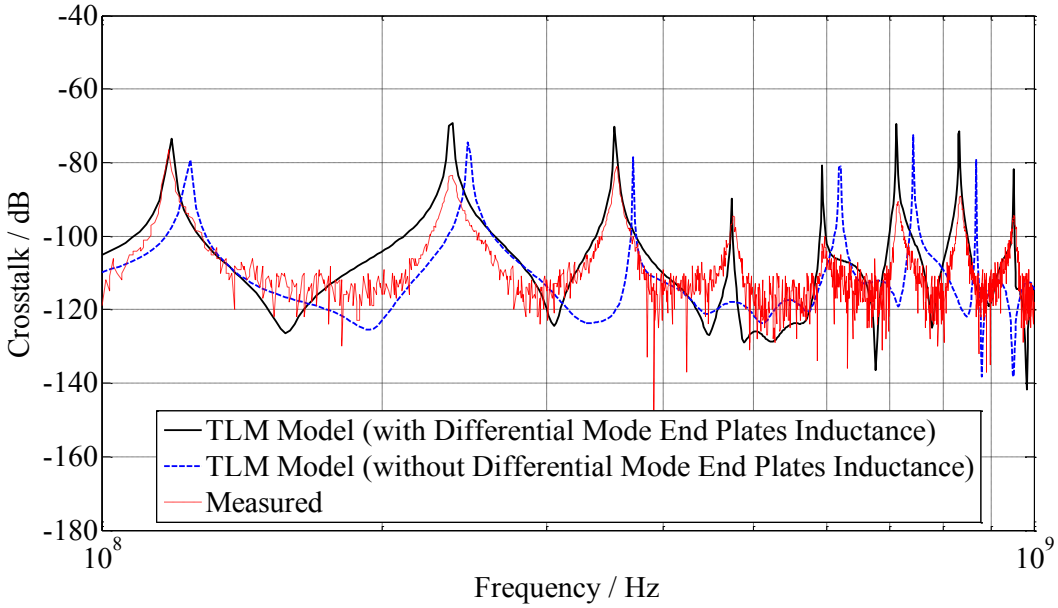

Figure 4.5.4: Crosstalk showing the effects of brass end plates at the terminations of the tertiary circuit with s = 15cm

The close separation and the presence of dielectric surrounding the coaxial cable braid accounts for the frequency discrepancy in the measurement. As the separation increases, the effects of the dielectric decrease; and so does the frequency discrepancy. In general, the peaks of the resonant frequencies correspond to the resonant frequencies of the differential mode current in the tertiary circuit (formed by the external surfaces of the two cable braids as well as the short circuit at the brass end plates).

For a length of 1.22m and assuming that the propagating velocity is the speed of light, c (a good approximation as the tertiary circuit is air insulated apart from the plastic sheath over the braids) the resonances are at 128, 247, 369, 492, 615, 739MHz etc. These are the resonances predicted including end plate inductance in Figures 4.5.1 – 4.5.4, with an assumption that the terminations of the tertiary circuit are short circuited. Results of the investigation performed in Chapter 3, section 3.3, show that the peak resonant frequencies between simulated and measured results can be matched by including the predicted inductance measured for the terminations of the tertiary circuit. The addition of an inductance at the terminations of the tertiary circuit increases the resonant frequency of the tertiary circuit to approximately 118, 233, 351, 469, 588, 706MHz etc.

4.5.2 Coupling between Two RG-58 Coaxial Cables via a Ground Plane

Similar to section 4.5.1, simulations were also performed using the 1D TLM model developed in section 4.4. Figures 4.5.5 – 4.5.11 show a lossless crosstalk system between two RG-58 coaxial cables over a metallic ground plane, where the common mode effects of the brass end plates' inductance can be observed from the difference in the peaks of the resonant frequencies. The models were simulated, including only the differential mode effects of the end plates' inductance. Keeping the height of the cables from the ground plane, h, constant at 11.5cm; Figures 4.5.5 – 4.5.8 show frequency domain results for varying separations between the cables, s, (2, 5, 10 and 15cm). In conjunction, by keeping the separation, s, constant at 5cm, Figures 4.5.9 – 4.5.11 show frequency domain results by varying h (16.5, 21.5 and 26.5cm).

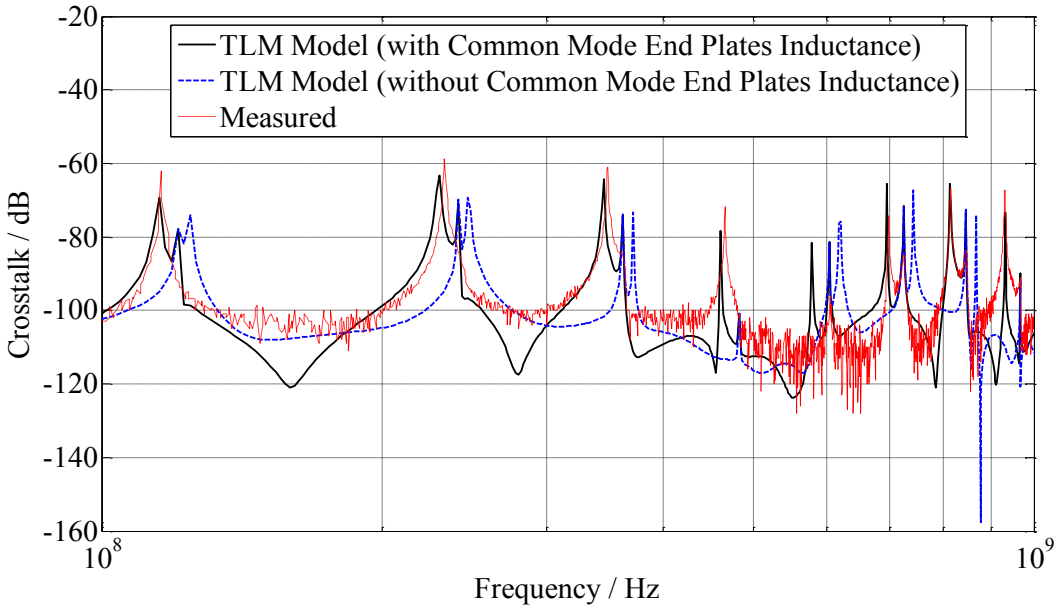

Figure 4.5.5: Crosstalk showing the effects of brass end plates at the terminations of the tertiary circuit with s = 2cm and h = 11.5cm

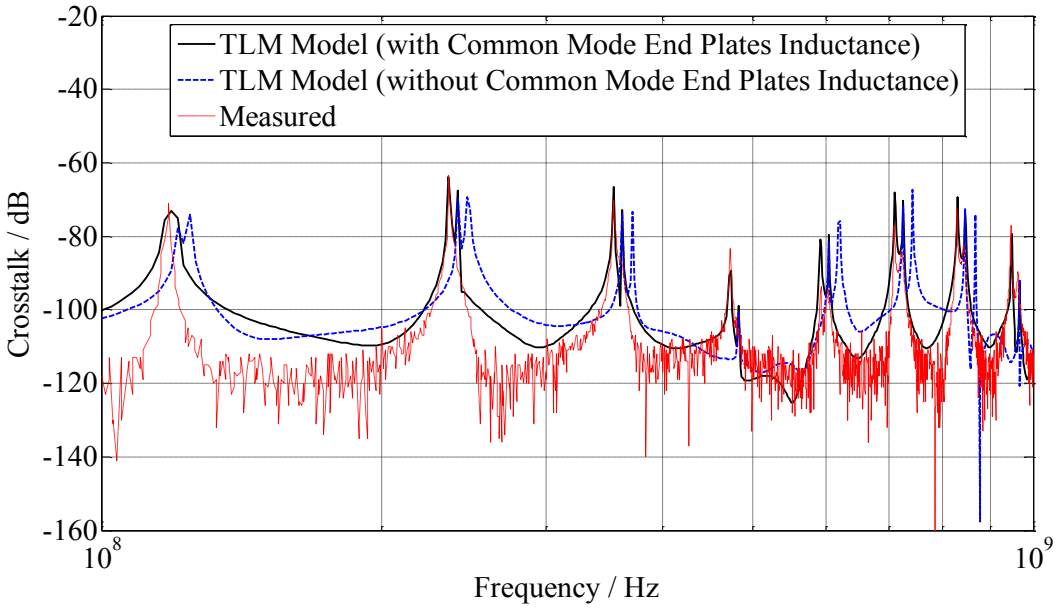

Figure 4.5.6: Crosstalk showing the effects of brass end plates at the terminations of the tertiary circuit with s = 5cm and h = 11.5cm

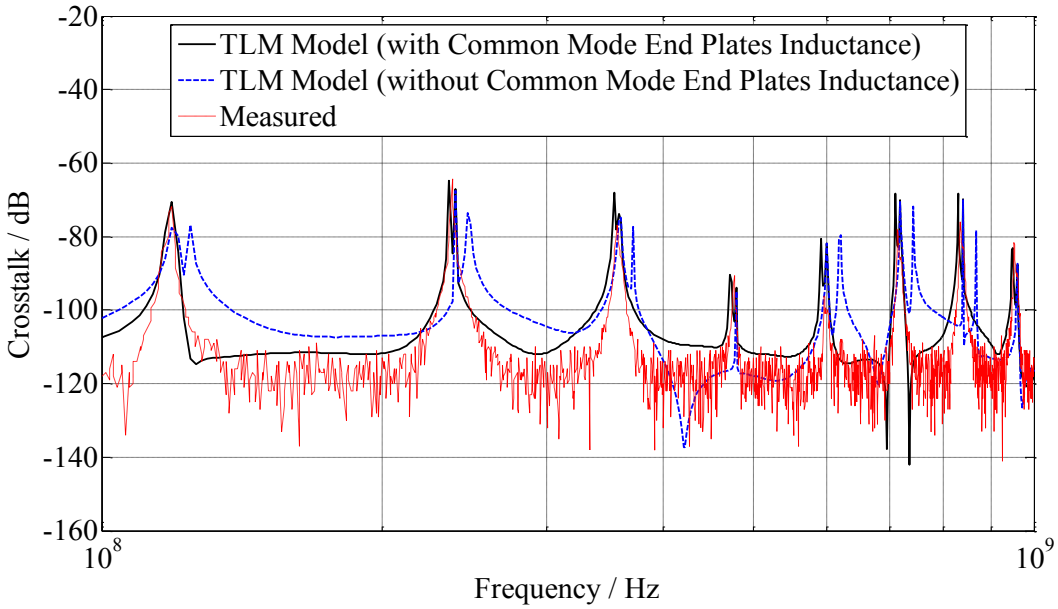

Figure 4.5.7: Crosstalk showing the effects of brass end plates at the terminations of the tertiary circuit with s = 10cm and h = 11.5cm

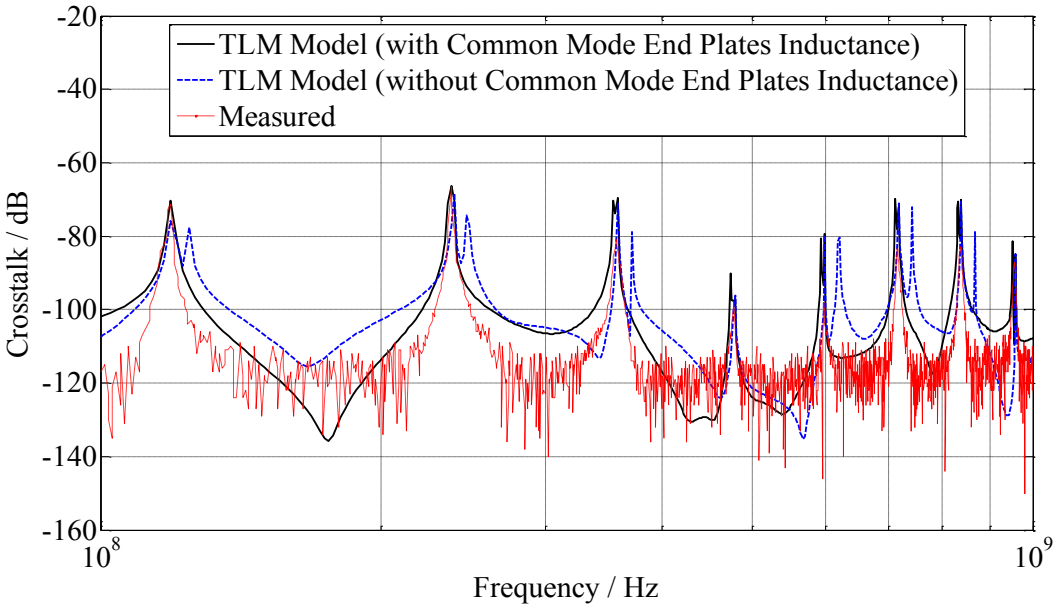

Figure 4.5.8: Crosstalk showing the effects of brass end plates at the terminations of the tertiary circuit with s = 15cm and h = 11.5cm

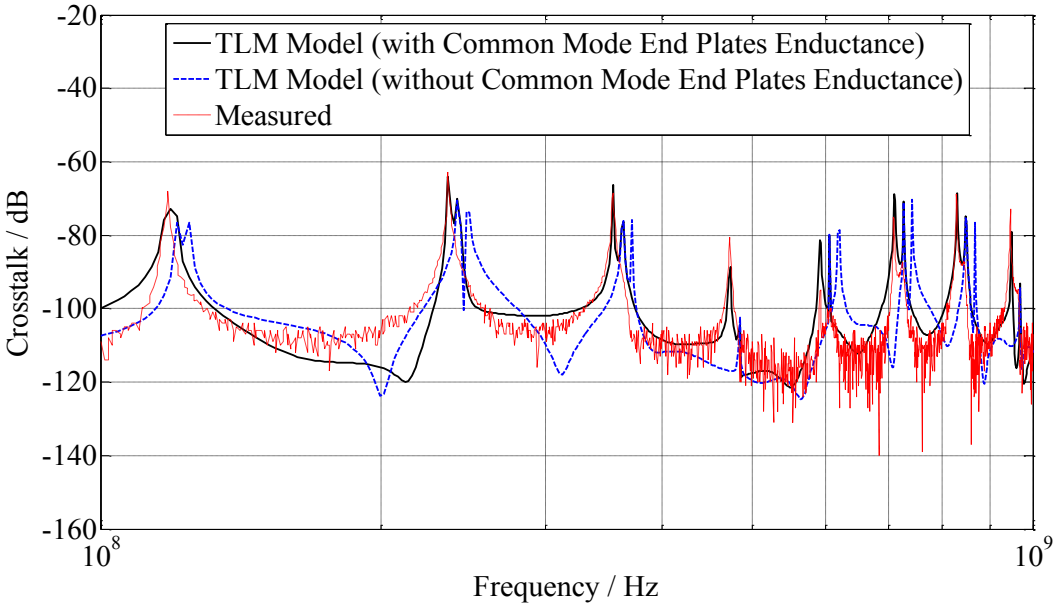

Figure 4.5.9: Crosstalk showing the effects of brass end plates at the terminations of the tertiary circuit with s = 5cm and h = 16.5cm

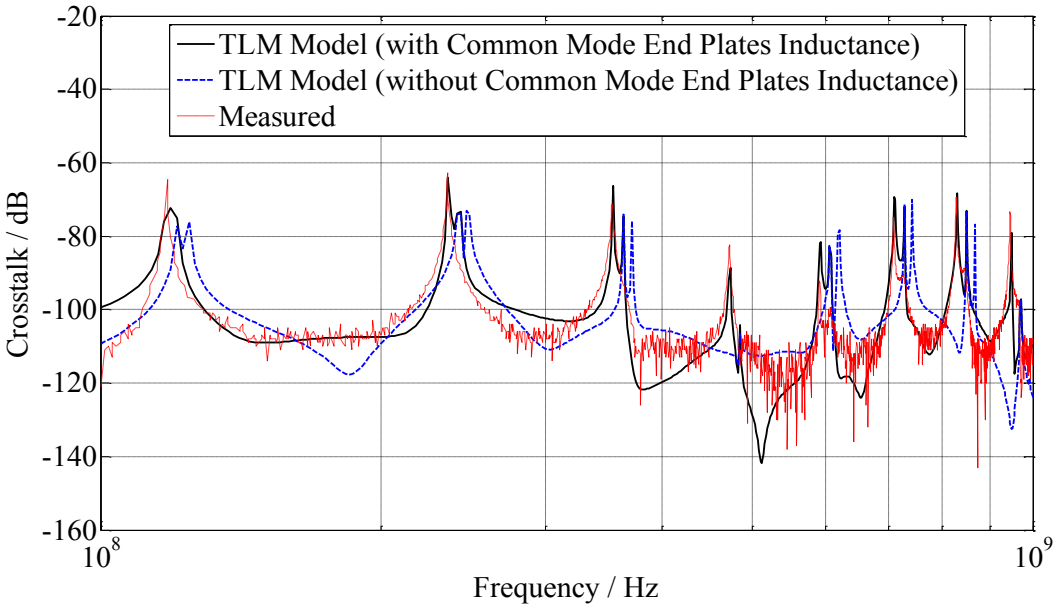

Figure 4.5.10: Crosstalk showing the effects of brass end plates at the terminations of the tertiary circuit with s = 5cm and h = 21.5cm

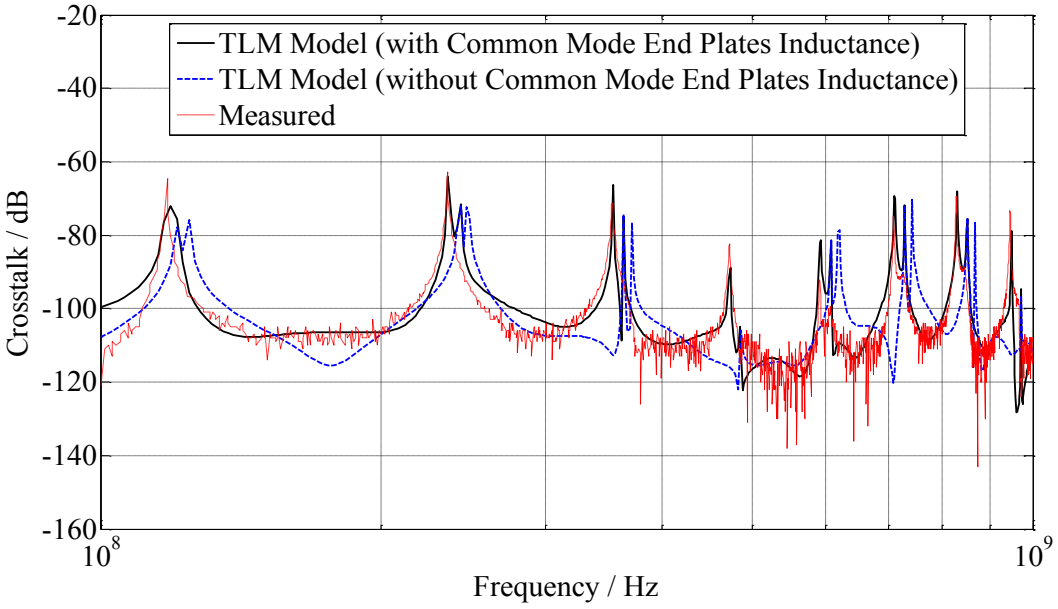

Figure 4.5.11: Crosstalk showing the effects of brass end plates at the terminations of the tertiary circuit with s = 5cm and h = 26.5cm

The discrepancy in the resonances observed in Figures 4.5.5 – 4.5.11 are the effects of the assumption that the terminations of the common mode path in the tertiary circuit is short circuited. Studies performed in Chapter 3, section 3.3, show

that the peak resonant frequencies between simulated and measured results can be matched by including the predicted inductance measured for the terminations of the tertiary circuit.

In the multimode model, the peaks of the resonant frequencies in the tertiary circuit are formed by two different current modes (differential and common mode currents, I_{td} and I_{tc}). Similar to the crosstalk between two cables in free space, the differential mode current is formed by the external surfaces of the two RG-58 cables and the brass end plates at the terminations. On the other hand, the common mode current is formed by the return path between the surfaces of the cables and the metallic ground plane.

Unlike the resonant peaks of the crosstalk observed in section 4.5.1, it is observed that the extra resonant peaks are effects caused by the common mode currents in the tertiary circuit. The measurements show that the resonant effects caused by the common mode currents are more distinctive at high frequencies (>500MHz). As the height of the cables above the ground plane, h, increases, the resonant peaks caused by the common mode currents gradually disappears. However, with the same conditions; although visible, the simulated results show a gradual decrease in the resonant peaks as h increases. The common mode resonant peaks are not entirely visible in the measurements as due to the relatively high Q the peak of the resonances, maximum coupling may be missed in a frequency domain study.

4.6 Conclusions

In this chapter, the numerical modelling technique based on the 1D Transmission Line Modelling (TLM) method was introduced. In implementing this method for crosstalk simulation, several factors are considered such as time synchronisation of all three circuits (source, tertiary and victim circuits); and also numerically modelling the cable braid's surface transfer impedance using two techniques, the stub inductance model and digital filter model. For ease of computation, it is necessary to synchronise the time and space steps to be the same by adjusting the propagation velocities for all three circuits. The crosstalk of two conductors in free space is governed by the differential mode current. However, when the two conductors are placed over a

conducting ground plane, the crosstalk is governed by both the differential and common modes, which are modelled using the multimode model.

It can be concluded that the numerical model of the system is successfully modelled using the TLM technique. Predictions show that the characterisation of the braid's transfer impedance is insufficient to predict accurate results when compared against measurements. The results also successfully compared the effects of including the brass end plates into the system and can finally be concluded that the peaks of the resonant frequencies correspond to the resonant frequencies in the tertiary circuit.

References

[4.1] Christopoulos C., The Transmission-Line Modelling Method: TLM, John Wiley & Sons, Inc., 1995.

[4.2] Taflove A. and Hagness C., Computational Electrodynamics: The Finite-Difference Time-Domain Method, Norwell, MA: Artech House, second edition, 2000.

[4.3] Christopoulos C., Principles and Techniques of Electromagnetic Compatibility, second edition, CRC Press, Taylor & Francis Group, 2007.

[4.4] J. L. Herring, Developments in the Transmission-Line Modelling Method for Electromagnetic Compatibility Studies, PhD. Dissertation, the University of Nottingham, 1993.

[4.5] Yew Kwan Choong, Advanced Modal Expansion Techniques for the Transmission Line Modelling Method, PhD. Dissertation, the University of Nottingham, 2003.

[4.6] John D. Kraus, Electromagnetics, Fourth Edition, McGraw-Hill, Inc, 1991.

[4.7] G. Nerukh and N. A. Khizhnyak, "Modern problems in nanostationary microscopic electromagnetic," Kharkov, Russia: Test-Radio, 1991.

[4.8] Boctor, S.A, Electric Circuit Analysis, Englewood Cliffs, NJ: Prentice-Hall, 1987.

[4.9] P. Naylor and C. Christopoulos, "Coupling between electromagnetic fields and multimode transmission systems using TLM," Intl. Journal of Numerical Modelling: Electronic Networks, Devices and Fields, vol. 2, 1989, pp. 227 – 240.

[4.10] Thomas Kley, "Optimized single-braided cable shields," IEEE Transactions on Electromagnetic Compatibility, vol. 35, no. 1, February 1993.

[4.11] John Paul, Christopoulos C and D.W.P. Thomas, "Generalized material models in TLM – part I: materials with frequency-dependent properties," IEEE Transactions on Antennas and Propagation, vol. 47, no. 10, October 1999, pp. 1528 – 1534.

[4.12] John Paul, Modelling of General Electromagnetic Material Properties in TLM, Ph.D. Theses, University of Nottingham.

[4.13] Clayton R. Paul, Analysis of Multiconductor Transmission Lines, John Wiley & Sons, Inc, 1994.

CHAPTER 5

SKIN DEPTH EFFECT

5.1 Analysis of the Skin Depth Effect

This chapter presents the overall crosstalk results for all configurations; in both time and frequency domain. Results are compared between numerical predictions and measurements, showing the effects of skin depth in the tertiary circuit.

The skin depth effect is an important factor in the modelling of a transmission line. Although much research has been done in investigating the system of two-conductors in free space [5.2], [5.3], [5.5] and [5.6], not much has been mentioned about the skin depth effect in the coaxial cable braid. It is usually included in the modelling of a conductor itself but not in the tertiary circuit of a coaxial cable system. The skin depth effect can be analytically described as given by Clayton [5.7], which essentially forms the basis for the theory of this loss factor.

If the line conductors are considered to be perfect conductors of infinite conductivity, any currents and charges must exist only on the surfaces of the conductors [5.7]. For realistic line conductors, the conductivities are finite. A line conductor of finite conductivity allows the current to penetrate so that a portion of its magnetic flux links a portion of the current internal to the line conductor and affects a per-unit length internal inductance, L_i. The internal current inevitably produces an internal resistance, R_{dc}. Note that these parameters only apply to solid, round wires. At DC, the current is uniformly distributed over a cross section of a solid conductor. This is illustrated in Figure 5.1.1. As frequency of excitation, f, increases, the current tends to crowd closer to the surface of the conductor. This is referred to as the skin depth effect. For a well-developed skin effect, the current can be considered to be uniformly distributed over an annulus at the surface of the wire of depth, δ; which is the skin depth. For most common cables, electromagnetic fields do not tend to penetrate line conductors at high frequencies. At lower frequencies, the electromagnetic field can penetrate the entire cross section of the current carrying conductor.

dc = low frequencies

hf = high frequencies

r = radius of conductor

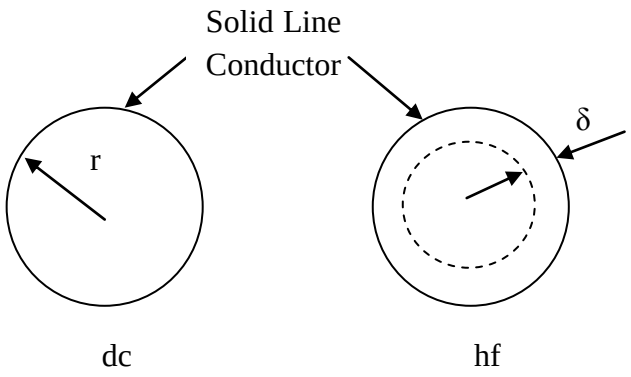

Figure 5.1.1: Illustration of the dependence of the per-unit length resistance of a solid line conductor on frequency (skin effect)

The skin depth, δ, of the current carrying conductor is given by [5.7] as:

$$\delta = \frac{1}{\sqrt{\pi f \mu \sigma}} \; ; \; in \text{ m} \tag{5. 1}$$

where σ denotes the conductivity of the conductor, μ denotes the permeability; and f denotes the frequency.

Figure 5.1.2 shows the skin depth, δ, over a range of frequencies from 10MHz – 1GHz, for a conductivity of copper ($58.82 MS^{-1}$) and permeability of free space ($4\pi \times 10^{-7} NA^{-2}$), and this will be used in investigations throughout this work. With increasing f, the skin depth is decreasing. This reflects that with higher frequencies, the current travels only on the surface of the line conductor.

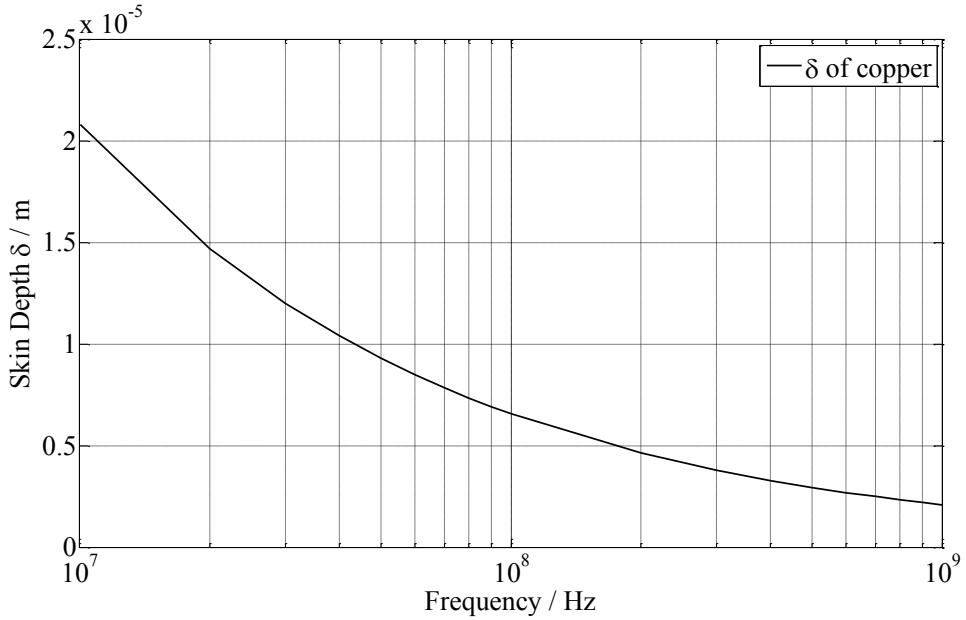

Figure 5.1.2: Pattern of skin depth, δ, with increasing frequency (10MHz – 1GHz)

The DC internal resistance of a solid conductor, R_{dc}, is given by:

$$R_{dc} = \frac{1}{\sigma \pi r^2} \; ; \; \Omega/\mathrm{m} \tag{5. 2}$$

Equation (5.2) is only applicable when $r \ll \delta$. As frequency increases, $r \gg \delta$. Hence, the resistance, R_{cable}, is:

$$R_{cable} = \frac{1}{\sigma 2\pi r^2 \delta} = \frac{R_{dc}}{2\delta} \; ; \; \Omega/\mathrm{m} \tag{5. 3}$$

Thus, the internal inductance of a solid conductor, L_i, can be equated as:

$$L_{i,dc} = \frac{\mu_0}{8\pi} \; ; \; H/\mathrm{m} \tag{5. 4}$$

The internal inductance at other frequencies is [5.7]:

$$L_i = \frac{2\delta}{r} L_{i,dc} \; ; \; H/\mathrm{m} \tag{5. 5}$$

5.2 Modelling the Skin Depth Effect into the Tertiary Circuit

The skin depth effect has been extensively studied on lossy transmission lines [5.8] – [5.14]. However, many methods that have been developed treat the skin effect at only high frequencies, failing to predict the properties of transmission lines at low frequencies [5.10]. Since the skin depth effect is frequency dependent, it would be easier to model in the frequency domain. However, digital signals are best modelled in the time domain, where the change in the rising edges is affected by dispersion due to the skin depth effect [5.8].

In this investigation, the skin effect is modelled for the tertiary circuit to develop a realistic model in this two-wire system. This is developed for the TLM method used in this work. All skin effect models proposed for transient response were developed using R-L lumped circuit models. All methods were successfully modelled to provide relatively accurate response for the skin depth effect, but most developed models tend to produce either large or relatively complicated ladder circuit models, which is a major drawback in computational modelling [5.11], [5.13] and [5.14]. As Dinh et al.

[5.11] suggested, the larger the number of branches in the ladder circuit model, the smaller the error due to discretisation when reconstructing the output signal.

Yen et al. [5.9] introduced a compact circuit model, but this method failed to capture the skin effect at high frequencies accurately, mainly from 100MHz – 1GHz, which falls in the frequency range of interest of this work. It also did not establish clear rules governing the choice of the component values [5.10]. As far as the frequency range is concerned in this investigation, Bidyut et al. [5.8] and Kim et al. [5.10] produced a relatively accurate skin effect response in the time domain. A modified model of Yen et al. [5.9] is developed by Kim et al. [5.10] using simple rules for selecting the values of resistors and inductors for a four deep ladder circuit model. It also clearly shows the equivalent circuit of the ladder circuit model that accurately models the skin effect for circular cross section conductors up to a frequency with a skin depth up to a hundredth of the radius conductor [5.10]. The lumped circuit model developed by Bidyut et al. [5.8] also accurately predicts the skin effect using a six ladder circuit model composed of resistors and inductors, where the selection of the values of the components are clearly stated. Its desired frequency range is from 1 kHz – 1 GHz, which corresponds with the frequency range studied in this thesis. Therefore, models developed by Bidyut et al. [5.8] and Kim et al. [5.10] are investigated and implemented into the tertiary circuit respectively and the results are compared.

5.2.1 Skin Effect Model by Bidyut et al. [5.8]

Since the skin depth, δ, is dependent on frequency, the main difficulty to model the contributions of the skin effect in a lumped circuit model lies in the $\sqrt{f}$ dependence of the skin effect impedance. The bandwidth for this model ranges from 1 kHz – 1 GHz. Hence, the approach is that the L and R variation in the desired frequency range can be mimicked. Figure 5.2.1 shows a cross section of the RG-58 coaxial cables, illustrating how the skin depth effect can be modelled for the tertiary circuit of the two-conductor system.

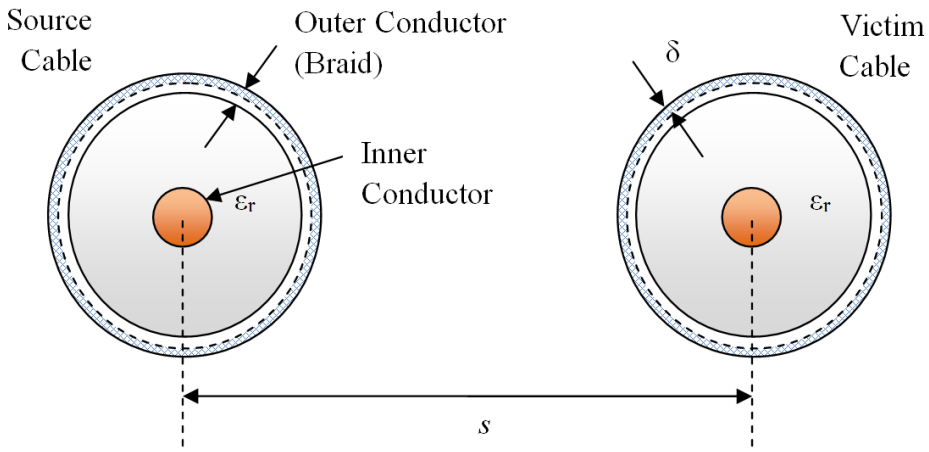

Figure 5.2.1: Configuration showing the two coaxial cables

Since the tertiary circuit is treated as a transmission line, the skin depth effect can easily be implemented into it using this lumped circuit model developed by Bidyut et al. [5.8].

Intuitively, to mimic the skin depth effect, a conductor can be imagined to be made up of concentric segments. All segments carry current at low frequencies, minimising the resistance and maximising the internal inductance. With increasing frequency, the outer segments stay active, thus increasing the resistance and decreasing the internal inductance. This can be modelled using L-R circuits connected in series in each branch of the ladder circuit. Figure 5.2.2 illustrates the ladder circuit model of the skin depth effect.

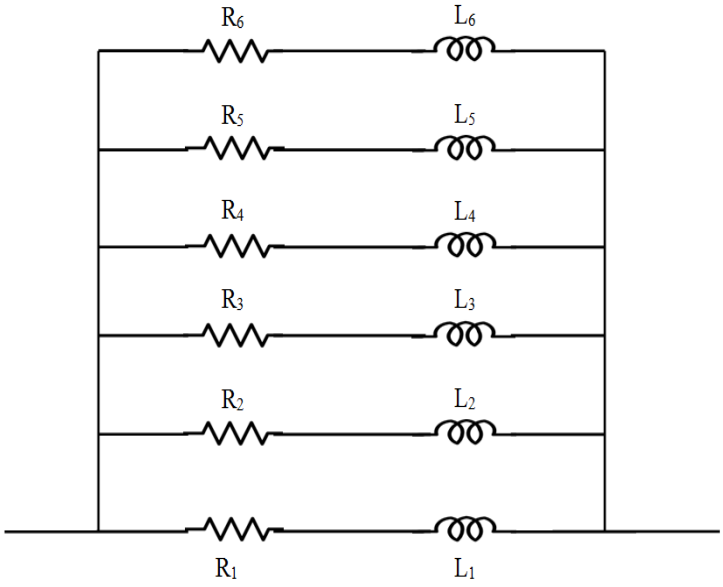

Figure 5.2.2: The ladder circuit model of the skin depth effect proposed by Bidyut et al. [5.8]

Let i denote the branch number 1 – 6. With increasing branch number, the value of the resistance, R_i, of the branch increases by a factor of x, where x is assumed an arbitrary number by Bidyut et al. [5.8] for accurate modelling of the skin depth. Meanwhile, the value of the inductance, L_i, decreases by the same factor, x [5.8].

$$x = \sqrt{10}$$

Therefore, the resistance and inductance for each branch can be equated with a general formula respectively, giving:

$$R_{i+1} = xR_i \tag{5. 6}$$

$$L_{i+1} = \frac{L_i}{x} \tag{5. 7}$$

Note that the parallel combination of all the resistances in each branch must sum up to R_{dc}. Similarly, L_i can be solved iteratively by equating the phase to the combination of the R_{dc}-L_i circuit at low frequencies [5.8]. The solutions for these values are tabulated in Table 5.2.1.

No. of Branches	R1	L1
1	Rdc	Li,dc
2	1.32Rdc	1.68Li,dc
3	1.42Rdc	1.94Li,dc
4	1.45Rdc	2.03Li,dc
5	1.457Rdc	2.06Li,dc
6	1.461Rdc	2.07Li,dc

Table 5.2.1: Skin effect for determining the values for R and L for the first branch depending on the number of branches of the ladder circuit

It is shown by Bidyut et al. [5.8] that for a frequency range from 1 kHz – 1 GHz, the number of branches that the ladder circuit requires are six. Thus, the following equations calculate the values for R_1 and L_1.

$$R_1 = 1.461 R_{dc} \tag{5. 8}$$

$$L_1 = 2.07 L_{dc} \tag{5. 9}$$

The internal resistance of the braid can be approximated by [2.8] and defined in Chapter 2:

$$R_{dc} = \frac{4}{\pi d^2 n N \sigma cos\alpha} \; ; \; \Omega/\mathrm{m} \tag{5. 10}$$

The internal inductance of a solid conductor can be given by (5.5); this is not the case for a coaxial cable braid due to the different structure of the braid. According to [5.10], the internal inductance of the outer conductor (coaxial braid), at low frequencies can be given by:

$$L_{dc} = \frac{\mu_0}{2\pi}\left[\frac{{R_m}^4 \ln\frac{R_m}{R_b}}{\left({R_m}^2 - {R_b}^2\right)} + \frac{{R_b}^2 - 3{R_m}^2}{4\left({R_m}^2 - {R_b}^2\right)}\right] \tag{5. 11}$$

where R_m denotes the radius of the mean braid diameter, D_m, and R_b denotes the outer diameter of dielectric, D_0. The parameters of D_m and D_0 can be found or calculated as in [4.2].

The TLM equivalent circuit from the L-R ladder is given in Figure 5.2.3. The tertiary circuit of the numerical model using the TLM technique, stub models [5.4], are developed to describe the inductances in the ladder circuit. The equivalent TLM circuit is then as shown in Figure 5.2.4.

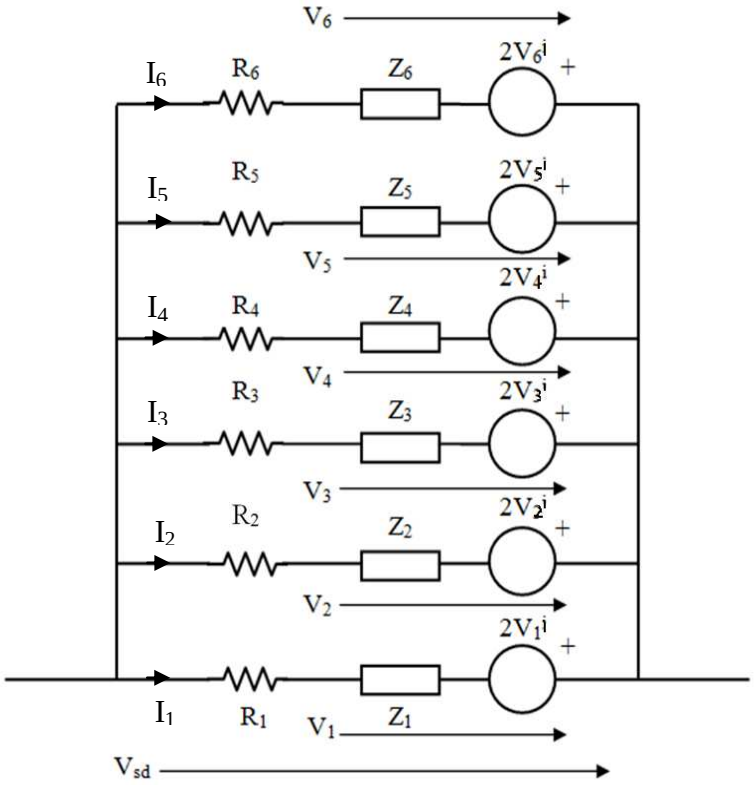

Figure 5.2.3: Equivalent circuit of the ladder circuit model

The skin depth effect occurs throughout the length of the cable. The tertiary circuit consists of the braids of the two coaxial cables, it is necessary to apply the ladder circuit model of the skin effect in both braids, with the same values of L and R in each branch since the cables used are identical. The following equations are derived to solve the tertiary circuit including skin effects. Therefore, the single node Thevenin equivalent circuit can be constructed as in Figure 5.2.4.

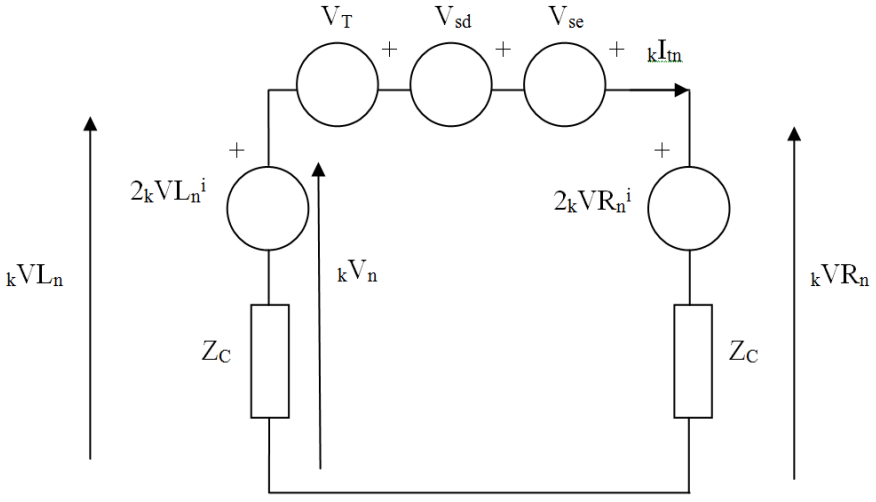

Figure 5.2.4: Thevenin equivalent circuit at a single node in the tertiary circuit including contributions from coupling due to skin effect and due to transfer impedance

The following equations are derived to solve for the interconnect for the skin effect in the tertiary circuit of the numerical TLM model. Let subscripts $_i$ (source braid) and $_j$ (victim braid) denote the branch number 1 – 6. Since the skin effect models in both the source and victim braids are the same, the total impedances, Z_{S_i} and Z_{S_j}, for each branch can be given by a general formula:

$$Z_{S_i} = Z_{S_j} = R_i + Z_i \tag{5. 12}$$

The impedances for the inductive stubs, Z_i and Z_j, are:

$$Z_i = Z_j = \frac{2L_i}{dt} \tag{5. 13}$$

Voltages V_{se} and V_{sd} denote the skin effect in both the source and victim line's braids respectively and V_T denotes the surface transfer impedance of the braid. The voltages V_{sd} and V_{se} are:

$$V_{sd} = \Delta x \left[\frac{\left\{ \sum_{i=1}^{6} \frac{2V_i^i}{Z_{S_i}} \right\} + \frac{2\ {}_kVL_n^i - 2\ {}_kVR_n^i - V_{se}}{2Z_C}}{\left\{ \sum_{i=1}^{6} \frac{1}{Z_{S_i}} \right\} + \frac{1}{2Z_C}} \right] \tag{5. 14}$$

$$V_{se} = \Delta x \left[\frac{\left\{ \sum_{j=1}^{6} \frac{2V_j^i}{Z_{S_j}} \right\} + \frac{2\ {}_kVL_n^i - 2\ {}_kVR_n^i - V_{sd}}{2Z_C}}{\left\{ \sum_{j=1}^{6} \frac{1}{Z_{S_j}} \right\} + \frac{1}{2Z_C}} \right] \tag{5. 15}$$

where Δx denotes the space-step. Thus, V_{sd} and V_{se} can be solved for each branch, giving:

$$V_{sd} = 2\ {}_kV_i^i - I_i Z_{S_i};\ \ i = 1, 2, 3, \ldots 6 \tag{5. 16}$$

$$V_{se} = 2\ {}_kV_j^i - I_j Z_{S_j};\ \ j = 1, 2, 3, \ldots 6 \tag{5. 17}$$

$$I_i = \frac{2V_i^i - V_{sd}}{Z_{S_i}};\ \ i = 1, 2, 3, \ldots 6 \tag{5. 18}$$

$$I_j = \frac{2V_j^i - V_{se}}{Z_{S_j}};\ \ j = 1, 2, 3, \ldots 6; \tag{5. 19}$$

where I_i (source braid) and I_j (victim braid) denote the currents flowing into each branch of the skin depth model. Hence, the stub impedance in each branch can be given as:

$$V_i = 2V_i^i - I_i Z_{S_i} ; \ i = 1, 2, 3, \dots 6 \tag{5. 20}$$

$$V_j = 2V_j^i - I_j Z_{S_j} ; \ j = 1, 2, 3, \dots 6 \tag{5. 21}$$

Next, the reflected voltages, V_i^r and V_j^r, can be derived as:

$$V_i^r = V_i - V_i^i ; \ i = 1, 2, 3, \dots 6 \tag{5. 22}$$

$$V_j^r = V_j - V_j^i ; \ j = 1, 2, 3, \dots 6 \tag{5. 23}$$

where the superscript ^{r} denotes the reflected voltages in the segment.

The interconnection between each node in the tertiary circuit can then be given as:

$${}_{k+1}V_i^i = -{}_kV_i^r ; \ i = 1, 2, 3, \dots 6 \tag{5. 24}$$

$${}_{k+1}V_j^i = -{}_kV_j^r ; \ j = 1, 2, 3, \dots 6 \tag{5. 25}$$

Finally, the overall voltage, V_n; current, I_t; and the reflected voltages, V_L^r and V_R^r; of the node is then:

$${}_kV_n = \frac{\frac{2\ {}_kVL_n^i}{Z_C} - \frac{2\ {}_kVR_n^i - V_T - V_{sd} - V_{se}}{Z_C}}{\frac{2}{Z_C}} \tag{5. 26}$$

$${}_kI_{tn} = \frac{2\ {}_kVL_n^i - {}_kV_n}{Z_C} \tag{5. 27}$$

$${}_kVL_n^r = {}_kV_n - {}_kVL_n^i \tag{5. 28}$$

$${}_kVR_n^r = {}_kV_n + V_T + V_{sd} + V_{se} - {}_kVR_n^i \tag{5. 29}$$

5.2.2 Skin Effect Model by Kim et al. [5.10]

In section 5.2.1, [5.8] models the skin depth effect where the number of branches of the lumped ladder circuit model depends on the range of frequency to be modelled. However, the method proposed in [5.10] models the skin effect via a four deep ladder circuit where it divides the circular cross section conductor into four concentric rings, where each ring is represented by one ladder section, with R_1 being the outermost ring. The skin effect ladder circuit is illustrated in Figure 5.2.7.

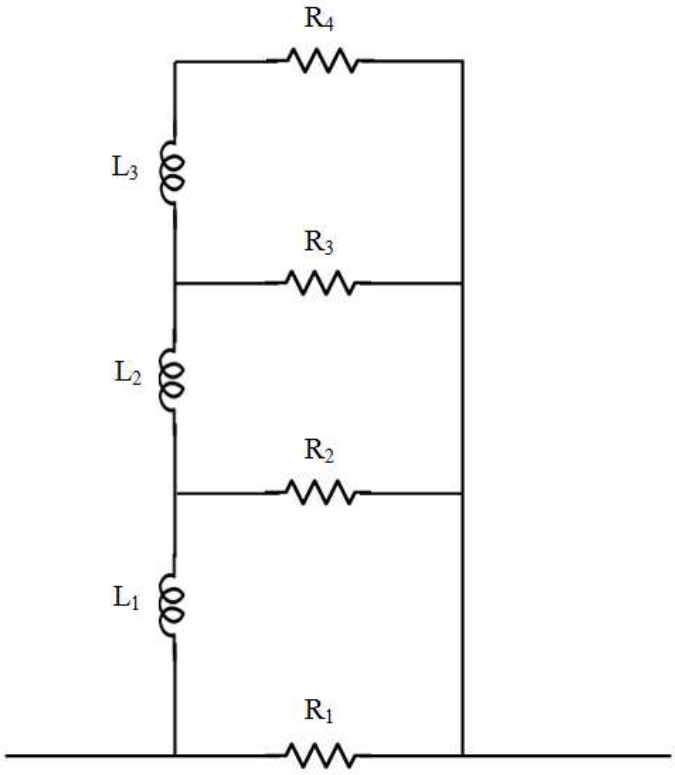

Figure 5.2.7: The ladder circuit model of the skin depth effect proposed by Kim et al. [5.10]

A diagram of how the branches of the four ladder compact circuit are represented by the cross section area of a solid conductor is illustrated in Figure 5.2.8.

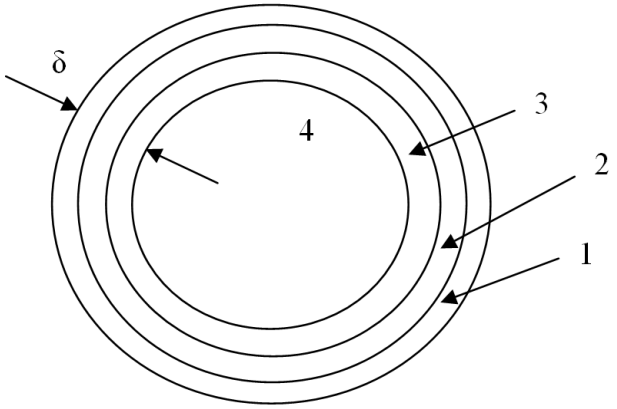

Figure 5.2.8: A schematic illustration representing the four ladder circuit to a solid conductor

Note that the ladder circuit model comprises four resistances R_i, where $i = 1, 2, 3$, and three inductors, L_i, where $i = 1, 2$. RR denotes the resistance factor. Thus, in this case, the resistance values can be derived from a general formula:

$$R_{i+1} = \frac{R_i}{RR} \tag{5. 30}$$

It is required in this model that the DC resistance of the braid, R_{dc}, is equal to the DC resistance of the ladder circuit. Hence, R_1 is:

$$R_1 = \alpha_R R_{dc} \tag{5. 31}$$

where R_{dc} can be obtained in (5.10).

In order to match the resistance of the conductor at high frequencies, the selection of the outermost ring, R_1, is the most crucial step which would affect the entire model's accuracy in modelling the skin effect. As proposed in [5.10], it is found that if the maximum desired frequency is ω_{max} (1 GHz), then α_R is:

$$\alpha_R = 0.53 \frac{wire\ radius}{\delta_{max}} \tag{5. 32}$$

where

$$\delta_{max} = \sqrt{\frac{2}{\omega_{max}\mu_0\sigma}} \tag{5. 33}$$

and the wire radius is the radius of the coaxial braid used to calculate R_{dc} in (5.10).

The unknowns in (5.34) are constrained by asymptotic behaviour at low frequencies and that Kim et al. [5.10] proposed that R_{dc} and α_R are related by:

$$RR^3 + RR^2 + RR + (1 - \alpha_R) = 0 \tag{5. 34}$$

Similarly, LL denotes the inductance factor and the inductance values can be found using a general formula:

$$L_{i+1} = \frac{L_i}{LL} \tag{5. 35}$$

It is required in this model that the low frequency inductance of the braid, L_{lf}, is equal to the low frequency inductance of the ladder circuit. Hence, L_1 can be gven as:

$$L_1 = \frac{L_{lf}}{\alpha_L} \tag{5. 36}$$

To ensure the frequency response is modelled accurately across the frequency range, α_L can be given as:

$$\alpha_L = 0.315\alpha_R \tag{5. 37}$$

The inductance factor, LL, can then be solved, as proposed by Kim et al. [5.10], given by:

$$\left[\frac{1}{LL}\right]^2 + \left[1 + \frac{1}{RR}\right]^2 \frac{1}{LL} + \left\{\left[\frac{1}{RR}\right]^2 + \frac{1}{RR} + 1\right\}^2 - \alpha_L\left\{\left[1 + \frac{1}{RR}\right]\left[\left(\frac{1}{RR}\right)^2 + 1\right]\right\}^2 = 0 \tag{5. 38}$$

By implementing the ladder network for the skin depth effect as given in Figure 5.2.7 into the tertiary circuit of the numerical model using the TLM technique, stub models [5.4], are used to describe the inductances in the ladder circuit. The equivalent TLM circuit is as shown in Figure 5.2.8.

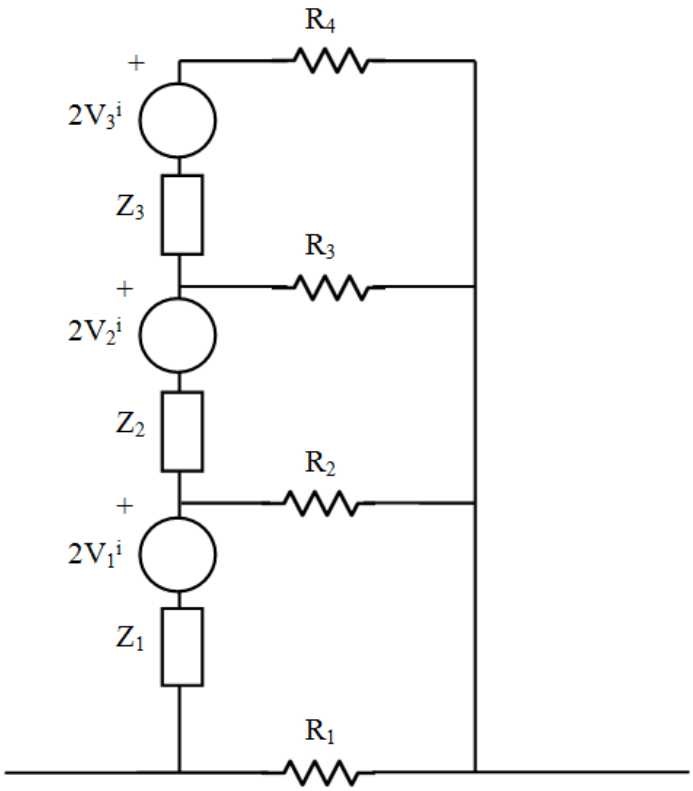

Figure 5.2.8: Equivalent circuit of the ladder circuit model

In TLM, the length of the cable is divided into segments. Since the skin depth effect occurs throughout the length of cable, Figure 5.2.9 shows the Thevenin equivalent circuit using the ladder circuit model for the skin effect as implemented in each segment. Taking one segment as an example.

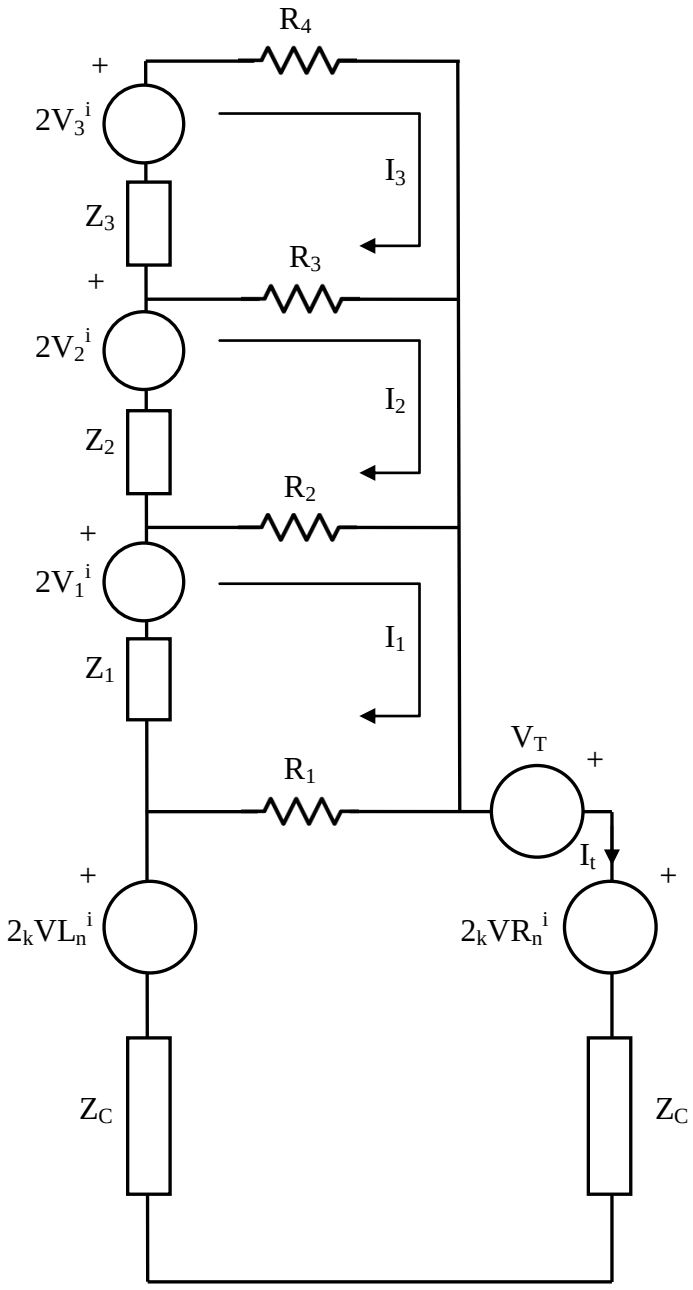

Figure 5.2.9: Thevenin equivalent circuit for one segment implementing the skin effect

The following equations are derived to solve for the interconnects for the skin effect in the tertiary circuit of the numerical TLM model. The impedance for the inductive stubs, Z_i, are shown in (5.13). In Figure 5.2.9, the incident voltages can be solved for each branch via a matrix formation as given in (5.39).

$$\begin{bmatrix} 2\ {}_kVL_n^i + V_T - 2\ {}_kVR_n^i \\ 2V_1^i \\ 2V_2^i \\ 2V_3^i \end{bmatrix} -$$

$$\begin{bmatrix} 2Z_C + R_1 & -R_1 & 0 & 0 \\ -R_1 & Z_1 + R_1 + R_2 & -R_2 & 0 \\ 0 & -R_2 & Z_2 + R_2 + R_3 & -R_3 \\ 0 & 0 & -R_3 & Z_3 + R_3 + R_4 \end{bmatrix} \begin{bmatrix} I_t \\ I_1 \\ I_2 \\ I_3 \end{bmatrix} = 0 \tag{5. 39}$$

Hence, the currents can be solved through:

$$[I] = [Z]^{-1}[V] \tag{5. 40}$$

The inverse for the impedance matrix $[Z]^{-1}$ can be obtained through a matrix solving package such as MATLAB and need only be derived initially in the simulation.

5.3 Results – Comparison between the Two Models

The results for models developed by Bidyut et al. [5.8] and Kim et al. [5.10] are compared in this section. One way to compare the results between them is to simulate the crosstalk of the two coaxial cables in free space system. The results given in Figures 5.3.1 – 5.3.4 are compared in the frequency domain after Fourier transformation of the time domain numerical results. The cable configuration is as given in Figure 2.3.2 in Chapter 2, section 2.3.1.

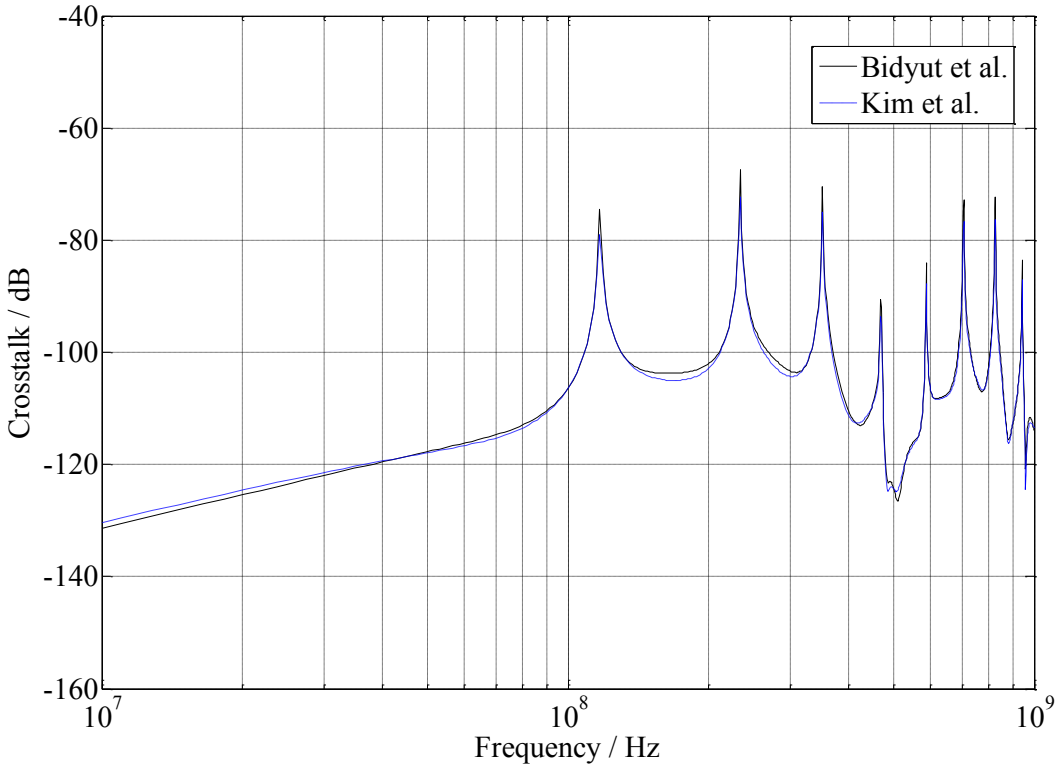

Figure 5.3.1: Model Comparison with separation of 2cm

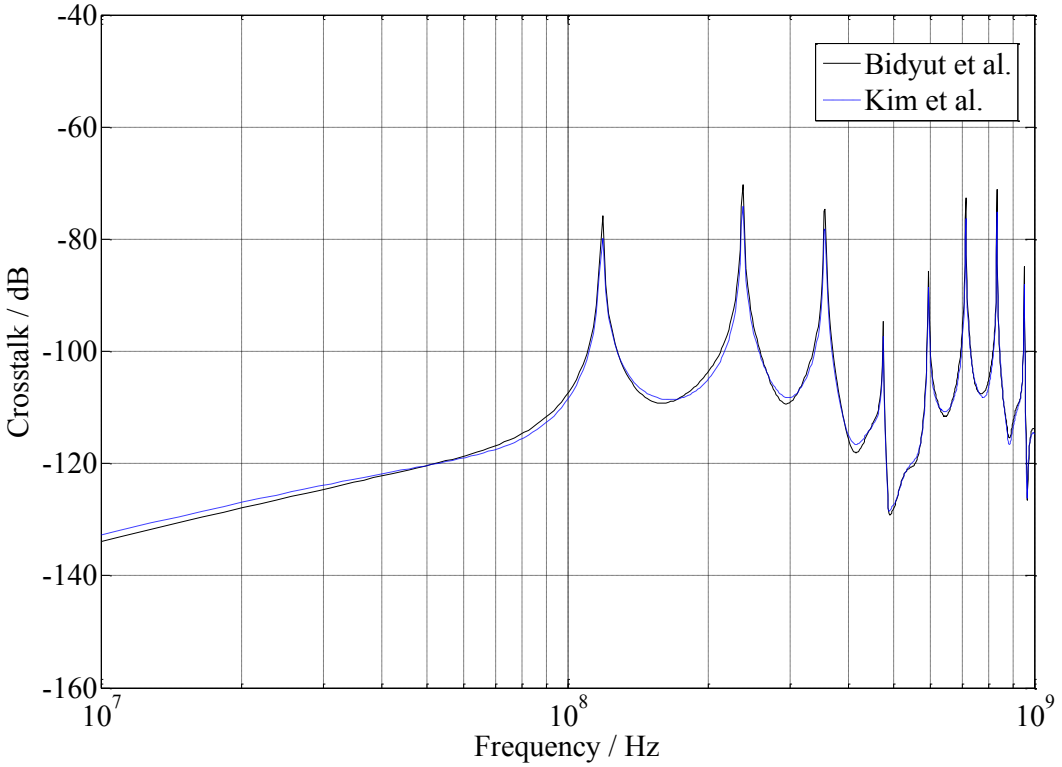

Figure 5.3.2: Model Comparison with separation of 5cm

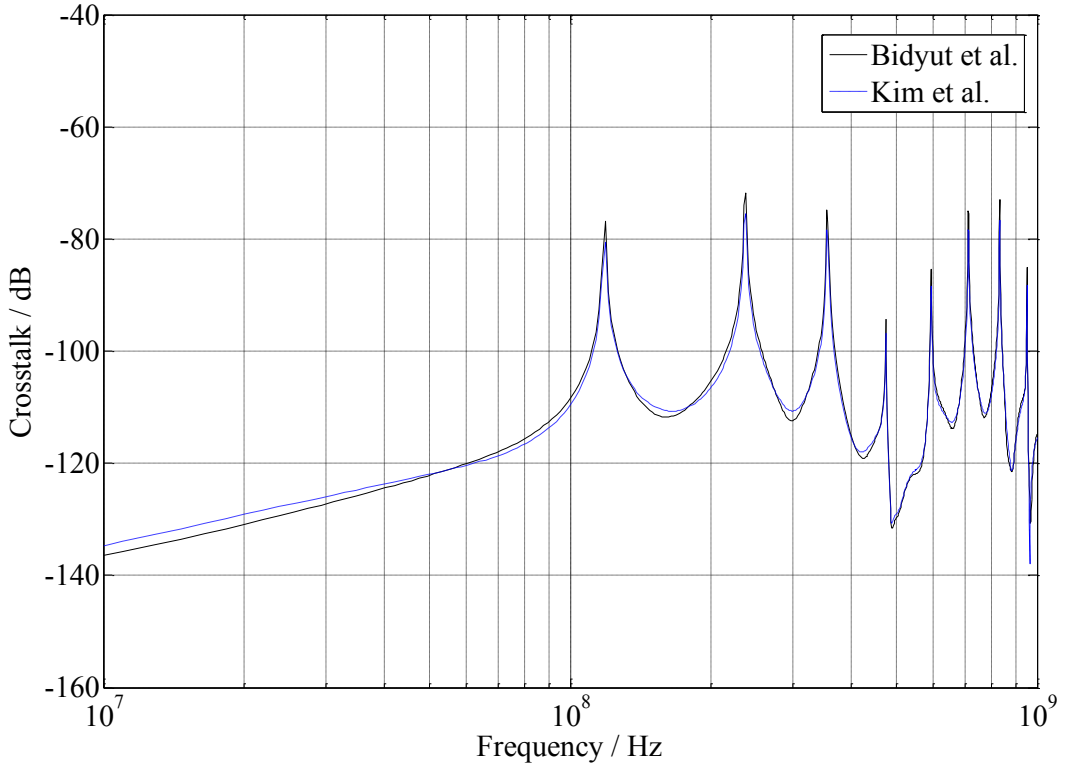

Figure 5.3.3: Model Comparison with separation of 10cm

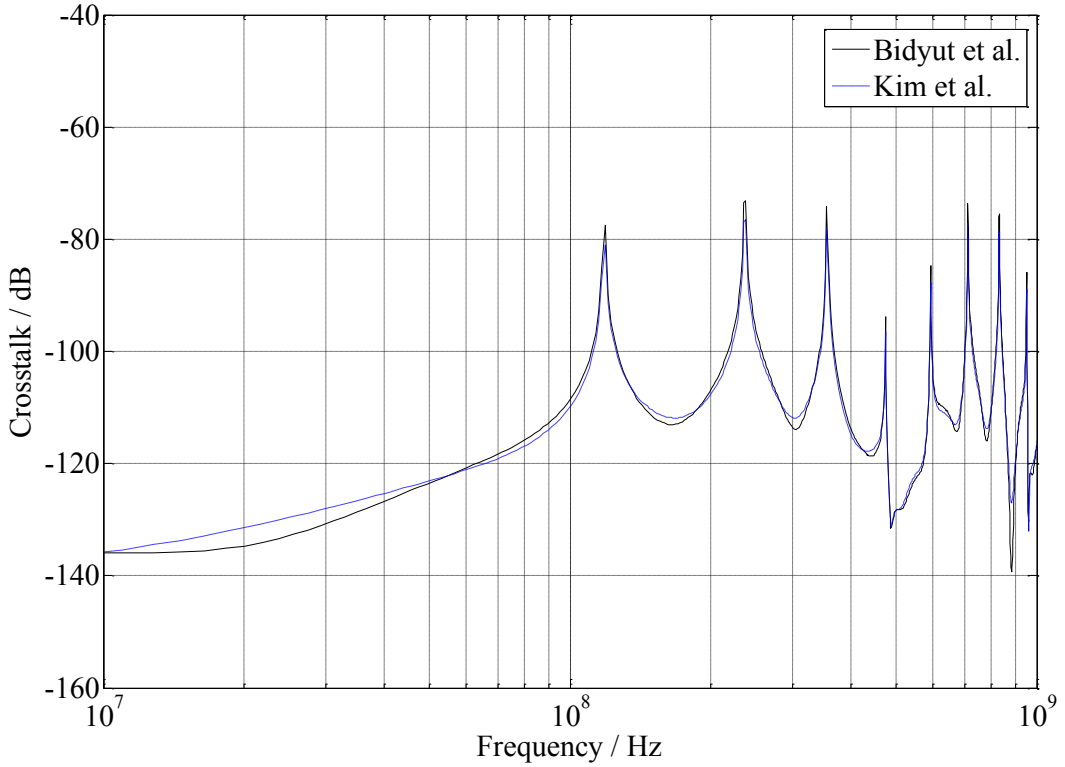

Figure 5.3.4: Model Comparison with separation of 15cm

Using the exact same simulation criterions in Chapter 4, Figures 5.3.1 – 5.3.4 show excellent agreement between the two models proposed. The comparison between the peaks of the resonant frequencies can be clearly seen in the frequency domain. The skin depth model proposed by Bidyut et al. [5.8] is convenient to implement since the incident and reflected stub voltages in each branch can easily be derived and calculated using the TLM technique [5.4]. However, this model is only effective for low frequencies. As frequency increases, the number of branches required to accommodate for the desired frequency increases, thus, causing it to be a drawback for circuitry design and computational simulation. As for the skin depth model proposed by Kim et al. [5.10], the compact four ladder circuit can be implemented for any desired frequency since its resistance factor, RR, in (5.34); and inductance factor, LL, in (5.38) are determined by its maximum desired frequency in equations (5.32) and (5.33). Therefore, the more preferable skin depth model to be implemented is the model developed by Kim et al. [5.10], as its matrix implementation can easily be derived through any matrix solving software such as MATLAB.

5.4 Results – Complete Characterisation of the Tertiary Circuit

5.4.1 Coupling between Two RG-58 Coaxial Cables in Free Space

A. Frequency Domain Results

Simulation was performed using the 1D TLM model developed in Chapter 4, section 4.3. Figures 5.4.1 – 5.4.4 show results with different separations, s, between the cables (2, 5, 10 and 15cm), where the results obtained from TLM simulations is compared with the measured crosstalk, with and without including the skin depth effect for the tertiary circuit. The frequency domain measurements were presented in Chapter 3, section 3.2.1.

(a)

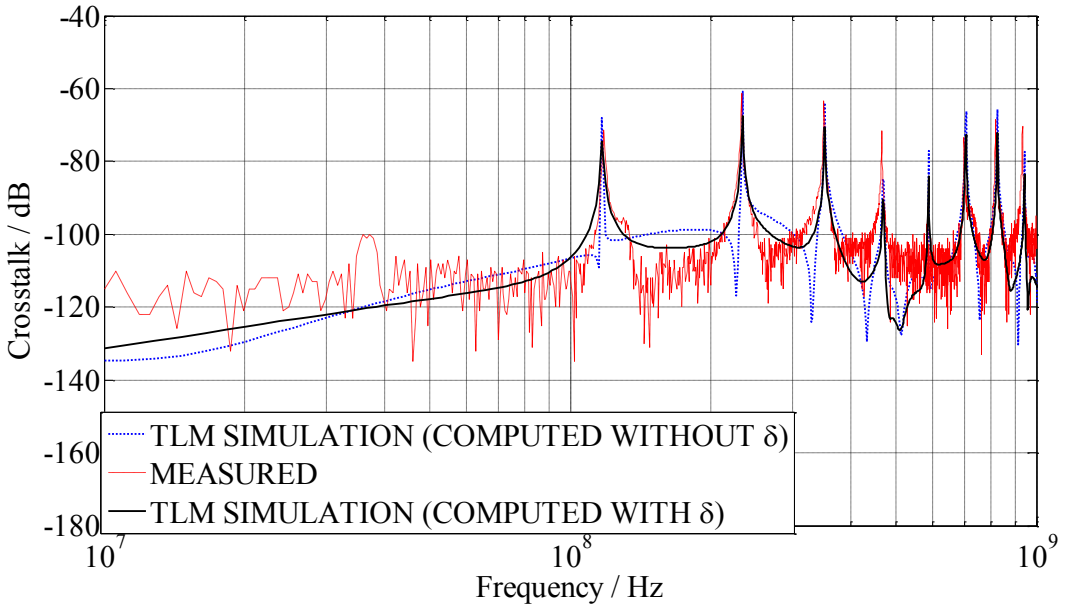

(b)

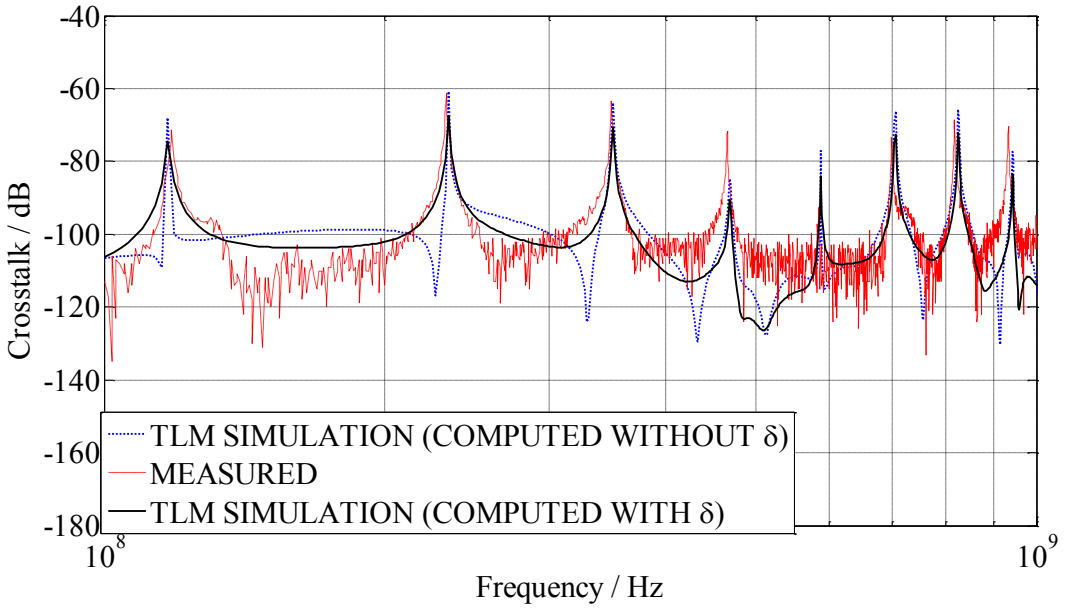

Figure 5.4.1: Crosstalk between two parallel RG-58 coaxial cables in free space with s = 2cm. (a) Frequency: 10MHz – 1GHz. (b) Frequency: 100MHz – 1GHz.

(a)

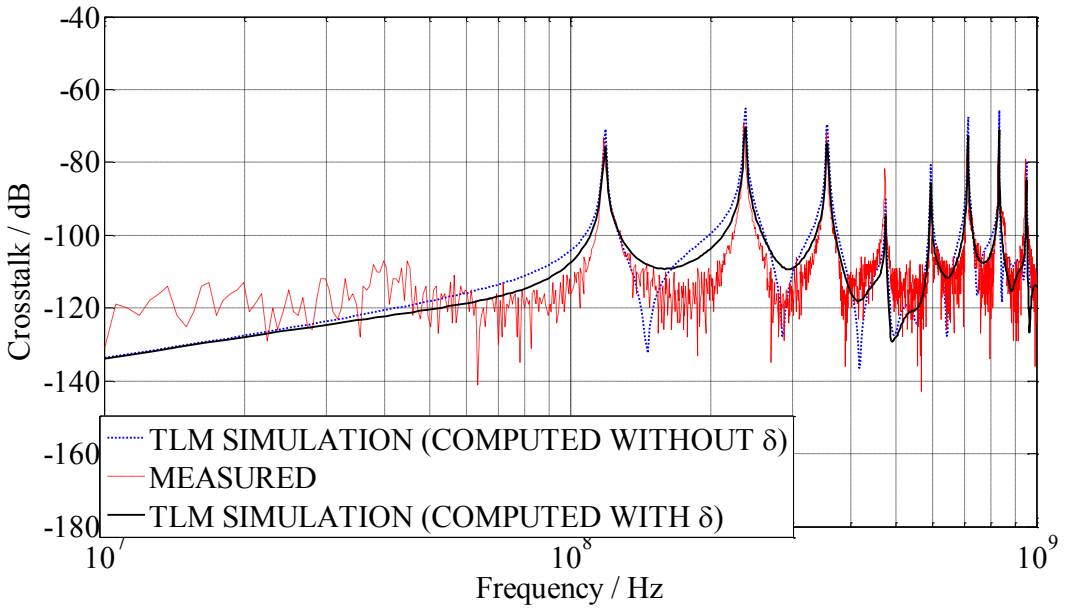

(b)

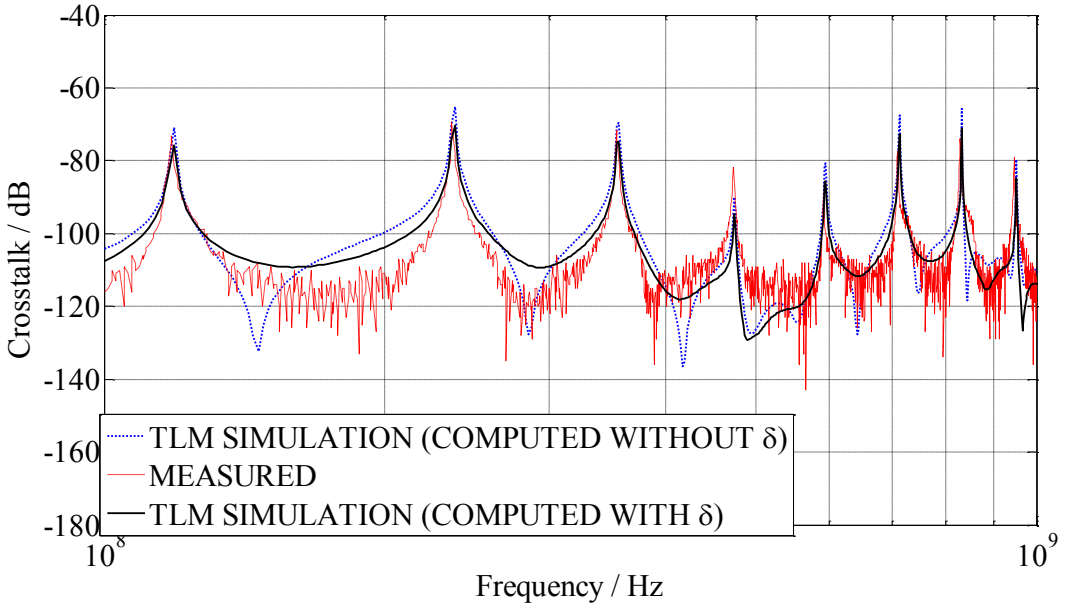

Figure 5.4.2: Crosstalk between two parallel RG-58 coaxial cables in free space with s = 5cm. (a) Frequency: 10MHz – 1GHz. (b) Frequency: 100MHz – 1GHz.

(a)

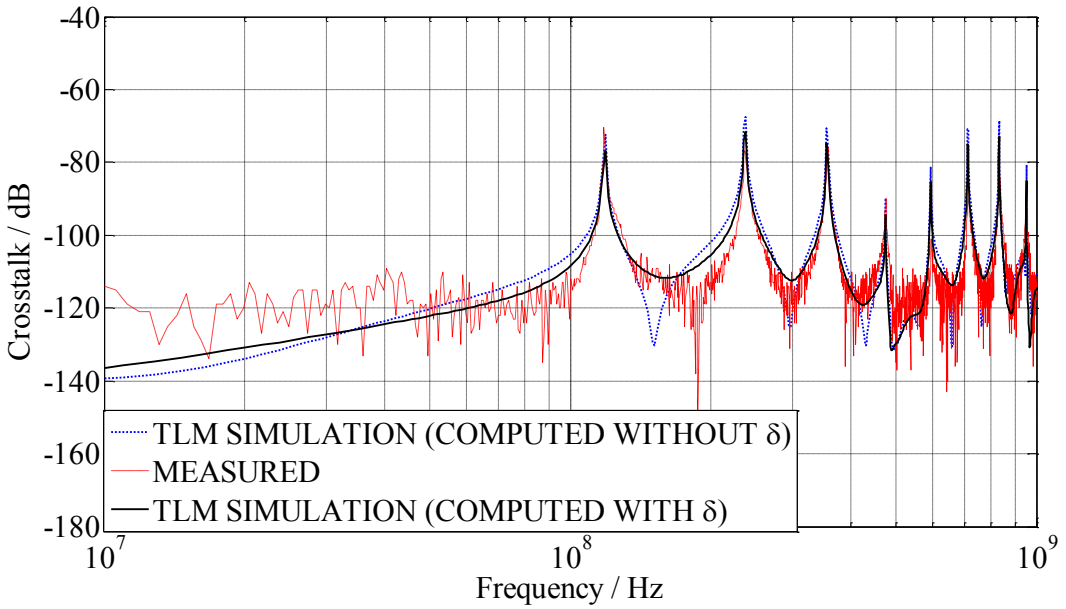

(b)

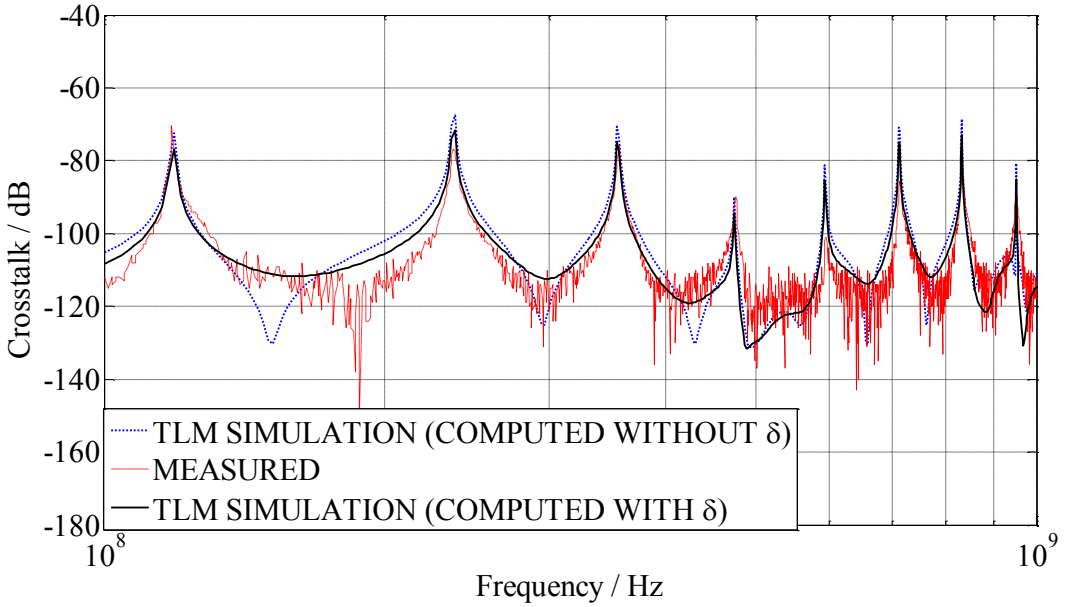

Figure 5.4.3: Crosstalk between two parallel RG-58 coaxial cables in free space with s = 10cm. (a) Frequency: 10MHz – 1GHz. (b) Frequency: 100MHz – 1GHz.

(a)

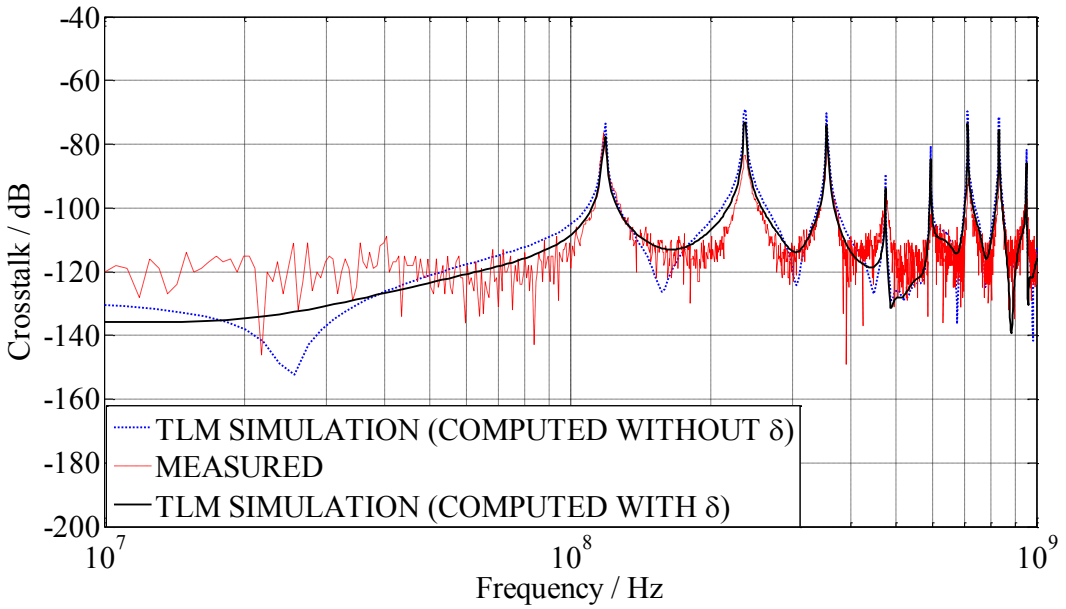

(b)

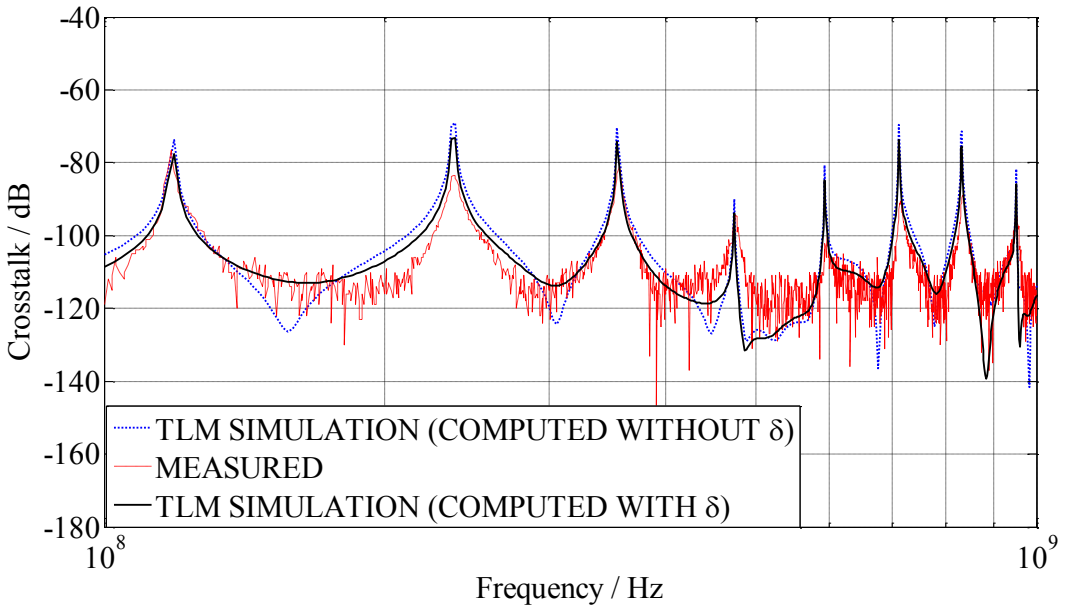

Figure 5.4.4: Crosstalk between two parallel RG-58 coaxial cables in free space with s = 15cm. (a) Frequency: 10MHz – 1GHz. (b) Frequency: 100MHz – 1GHz.

As observed in Figures 5.4.1 – 5.4.4, the simulated results have very good agreement with the measurement results. It is observed that by including the skin depth effect, δ, in both the braids of the coaxial lines, better agreement in shape as well as magnitude is observed between the peak crosstalk resonant frequencies in the

TLM solution and the peaks of the measurements for all separations. When δ is omitted, the peak resonant frequencies appear to be higher, especially at high frequencies, generally above 500MHz. At low frequencies, where the line length is very much less than $\frac{\lambda}{10}$, the coupling can be determined by a lumped model where the entire cross section are of the braid is dominated by the loop coupling inductance in the tertiary circuit (penetration of the magnetic field). The coupling in the tertiary circuit is completely defined by the composite effects of the DC impedance of the braid and the loop inductance, together with the resistive losses in the tertiary circuit. Hence, at these frequencies, the skin depth effect is not a significant factor. As frequency increases, the skin depth effect in the tertiary circuit gradually takes effect, where the crosstalk is controlled by the increasing resistance in the tertiary circuit. It is proven that the inclusion of the skin depth effect is essential in the tertiary circuit as it significantly improves the Q-factor in the peaks of the resonant frequencies.

B. Time Domain Results

Similarly, simulations were performed using the model as proposed in Chapter 4, section 4.3, where the time domain crosstalk between the two RG-58 coaxial cables in free space can be observed from the voltage, V_{V0}, obtained from the adjacent cable. In order to obtain similar output, the source voltage simulated has to be comparable to the source generated by the instrument. Figure 5.4.5 shows a comparison of the square wave generated by the pulse function arbitrary generator (PFAG) presented in Chapter 3, section 3.2.2C, and a TLM simulated square wave. The rise and fall time of the imperfect square wave generated by the PFAG is measured accordingly to the corresponding fundamental frequency.

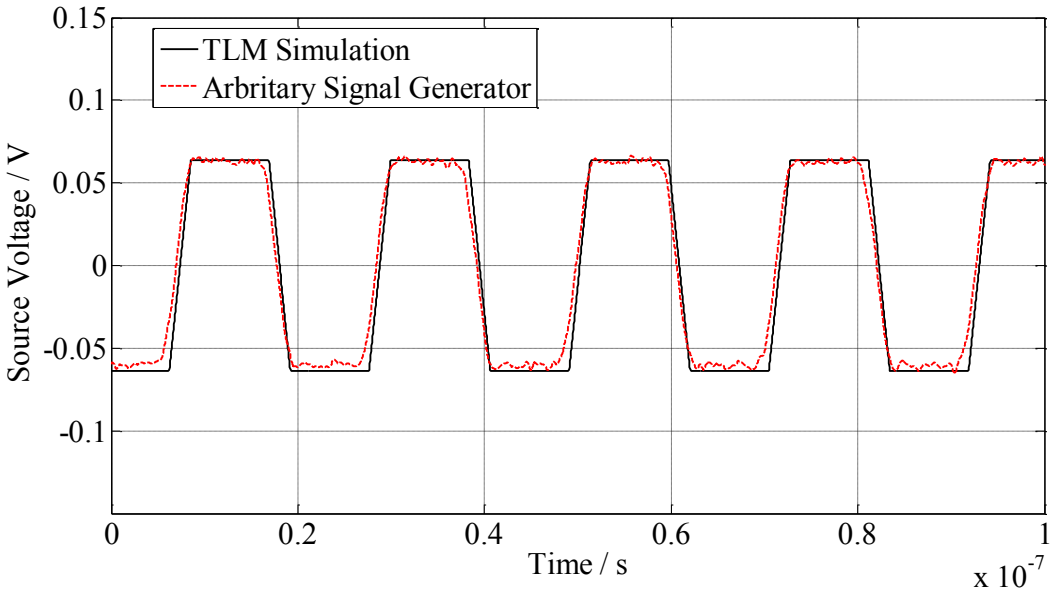

Figure 5.4.5: Comparison between generated and simulated square wave

However, in section 3.2.2C, it has been proven that the broadband amplifier does not provide a linear gain, causing the output of the square wave input signal to slightly deviate from its original shape. Based on the configuration used in section 3.2.2C, V'_{IN} in Figure 3.2.12 can be approximated by generating the corresponding square wave for better crosstalk comparisons.

The fundamental frequency as depicted in Figure 5.4.5 is 46.67MHz. By varying the fundamental frequency of the time domain input, the harmonics of the input fundamental frequency is observed from the output peaks of the resonant frequencies in the frequency domain, as presented in section 5.4.1A.

The PFAG has a limited frequency range, where frequencies above approximately 60MHz cause a distortion in the square wave. Therefore, the fundamental frequency generated is limited to frequencies below 50MHz; depending on the harmonics of the fundamental frequency, in which the coupling strength appears to be strong at the resonant peaks. The Time Domain Oscilloscope (TDO) is also unable to observe a voltage scale of less than 1mV per division. As the separation, s, between the cables increases, its coupling strength decreases. Therefore, in order to obtain a clear comparison of the time domain coupling, both the simulation and measurement are performed with a fundamental frequency input, where the harmonics at low frequency resonant peaks can be observed.

In section 5.4.1A, the first 2 peak resonant frequencies were observed to be at approximately 118MHz and 233MHz, within the frequency range of 10MHz – 1GHz. To obtain the corresponding resonant peak harmonics, the fundamental frequencies fed into the square wave are 39.33MHz and 46.67MHz respectively, presented in Figures 5.4.6 – 5.4.8, for separations, s (2, 5 and 10cm).

(a)

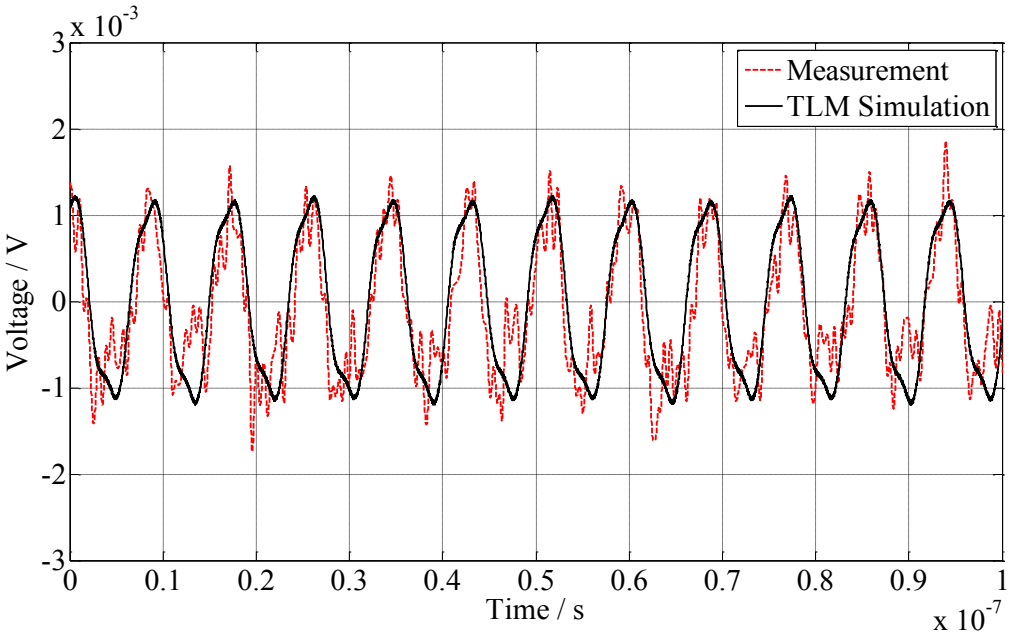

(b)

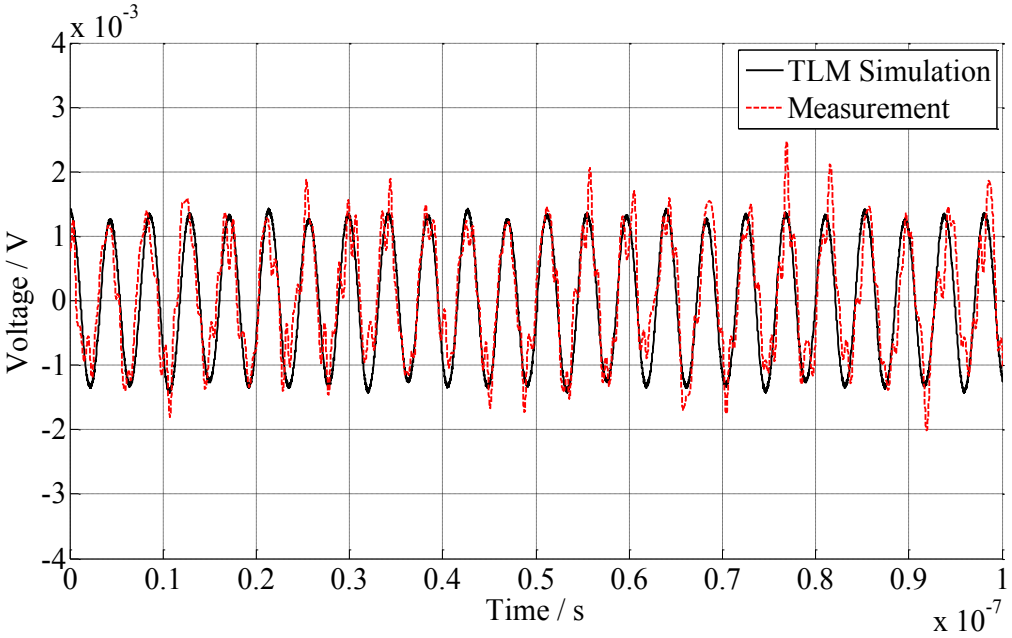

Figure 5.4.6: Time domain crosstalk of two RG-58 coaxial cables in free space for a separation, s = 2cm, and input of fundamental frequency (a) 39.33MHz. (b) 46.67MHz.

(a)

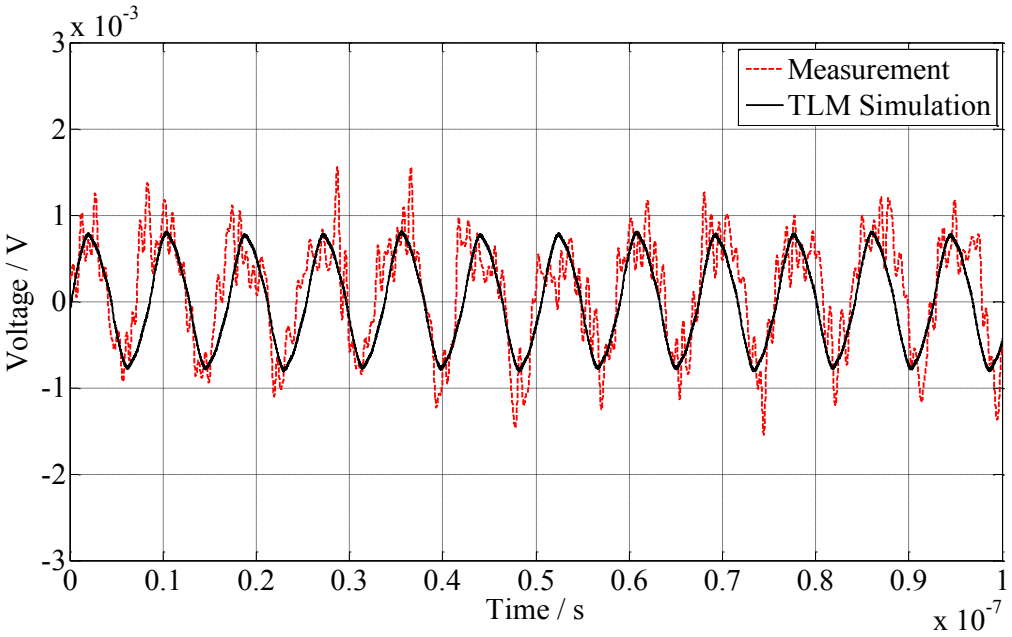

(b)

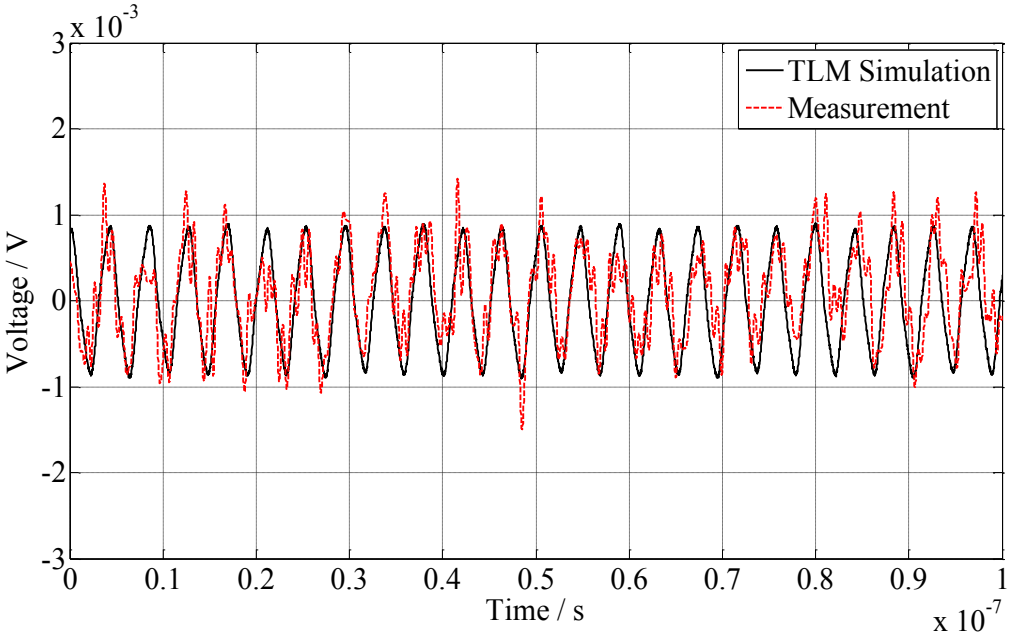

Figure 5.4.7: Time domain crosstalk of two RG-58 coaxial cables in free space for a separation, s = 5cm, and input of fundamental frequency (a) 39.33MHz. (b) 46.67MHz

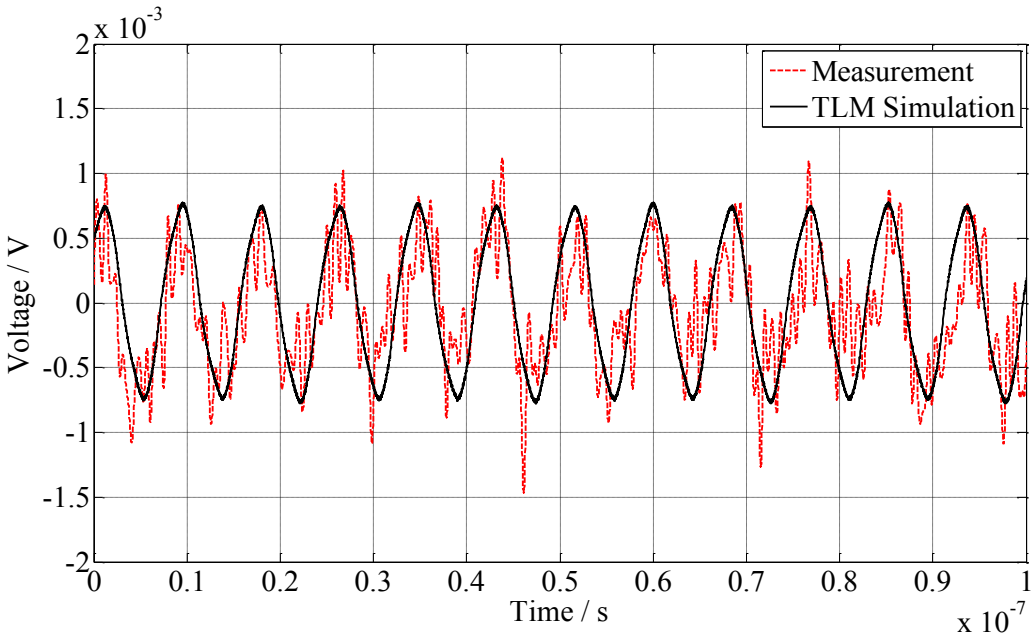

Figure 5.4.8: Time domain crosstalk of two RG-58 coaxial cables in free space for a separation, s = 10cm, and input of fundamental frequency 39.33MHz.

It is found that whenever a harmonic of the source square waveform is close to one of the resonances of the tertiary circuit a strong coupling is observed. Taking Figure 5.4.6 as an example; from Figure 5.4.1 in section 5.4.1A, it is observed that there are resonances at approximately 118, 233, 351MHz etc. Typically, an output yields a voltage signal of same frequency as the input signal. However, no coupling peak is observed at the fundamental frequency of the source voltage which is 39.33MHz. Therefore, the output yields a frequency of approximately 118MHz, which denotes the 3rd harmonic of the input fundamental frequency, which also represents the 1st peak resonant frequency of the crosstalk within the frequency range of 100MHz – 1GHz, depicted in Figure 5.4.1.

Similarly, no coupling peak is observed at fundamental frequency 46.67MHz. The output yields a frequency of approximately 233MHz, denoting the 5th harmonic of the input fundamental frequency, which represents the 2nd peak resonant frequency of the crosstalk. The critical factor in the coupling strength is due to the resonances in the tertiary circuit. The resonances are close to the resonances observed in Figure 5.4.1.

From the time domain results measured, most of the crosstalk output signal is subjected to noise. The time domain coupling for separations 10cm (input fundamental frequency 46.67MHz) and 15cm are not presented since the coupling

cannot be recorded below -75dB on the TDO. Moreover, there is difficulty in capturing clear signals even with coupling between -70dB – -75dB. In all, the simulated results agree reasonably well with the measured results.

For some applications, time domain signal representation is preferred over frequency domain analysis since the crosstalk is often useful when presented as a transient signal, where digital information is often conveyed using voltage as a function of time. Aspects such as jitter and propagation delay can be studied and included. Moreover, the change in pattern of the transient signal can only be observed in the time domain as compared to the frequency domain.

C. Validation of Time Domain Results

In order to validate the accuracy of the time domain results obtained, they are Fourier transformed into the frequency domain. For the same separations, s, between the cables (2, 5 and 10cm) in section 5.4.1B, Figures 5.4.9 – 5.4.11 show the peaks of the resonant frequencies of Figures 5.4.6 – 5.4.8 respectively.

It is observed from the Fourier Transformed time domain results in section 5.4.1B that the resonant frequency presented perfectly matches the resonances obtained from the frequency domain results in section 5.4.1A, both at approximately 118MHz and 233MHz respectively, where strong coupling is observed. No other resonances are seen to occur in both cases. From Fourier analysis it is found that the measurements obtained in section 5.4.1B contain only the resonant frequency harmonics of 118MHz and 233MHz; and most of the output signal is subjected to noise. However, when a square wave of fundamental frequency 39.33MHz is fed into the system, both resonances of 118MHz and 233MHz are observed to be of significant value; as presented in Figures 5.4.9a, 5.4.10a and 5.4.11a. The resonance of 233MHz represents the 6^{th} harmonic frequency of the input fundamental frequency of 39.33MHz, denoting that the system yields even harmonics at the output. Such phenomenon only occurs when the periodical input positive peak amplitude is different from the negative peak value, which can be observed from Figure 5.4.5 in section 5.4.1B. The cause for such situation lies in the discrepancy of the instrument – Pulse Function Arbitrary Generator (see Chapter 3).

(a)

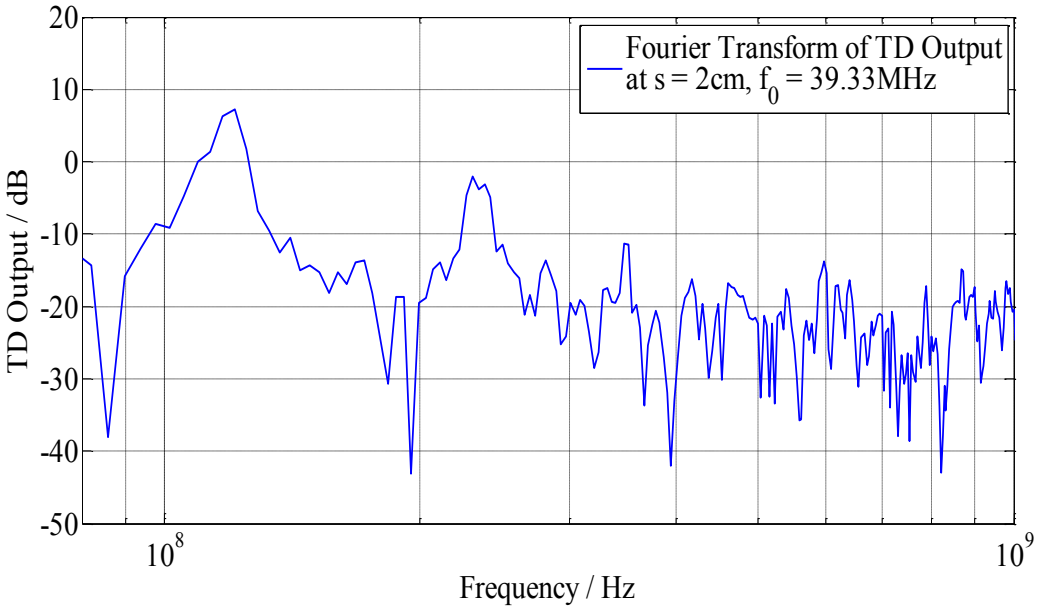

(b)

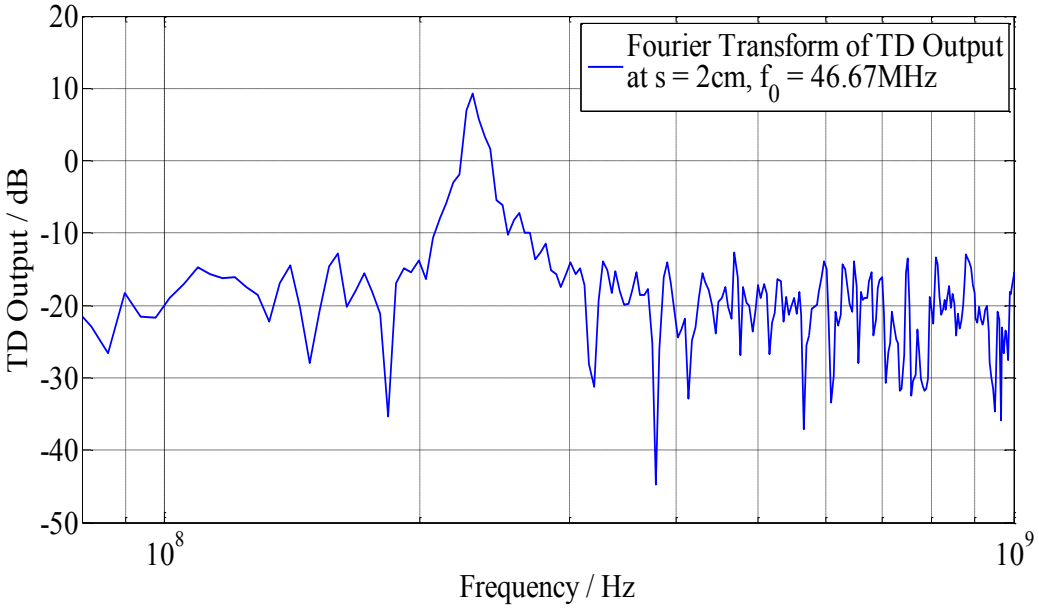

Figure 5.4.9: Fourier Transform of measurement data in Figure 5.4.6, for a separation, s = 2cm, and input of fundamental frequency (a) 39.33MHz. (b) 46.67MHz

(a)

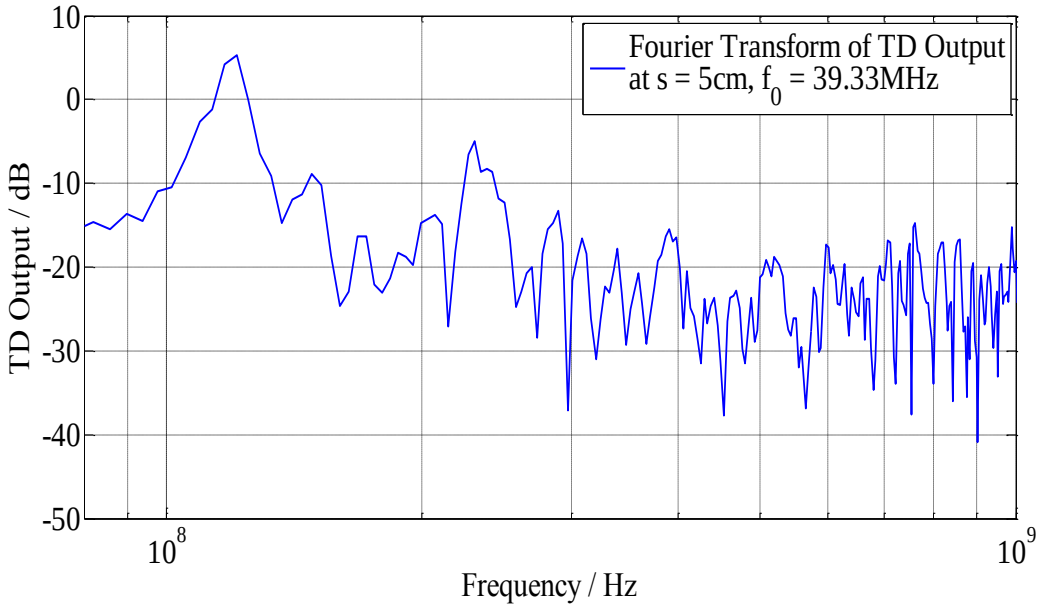

(b)

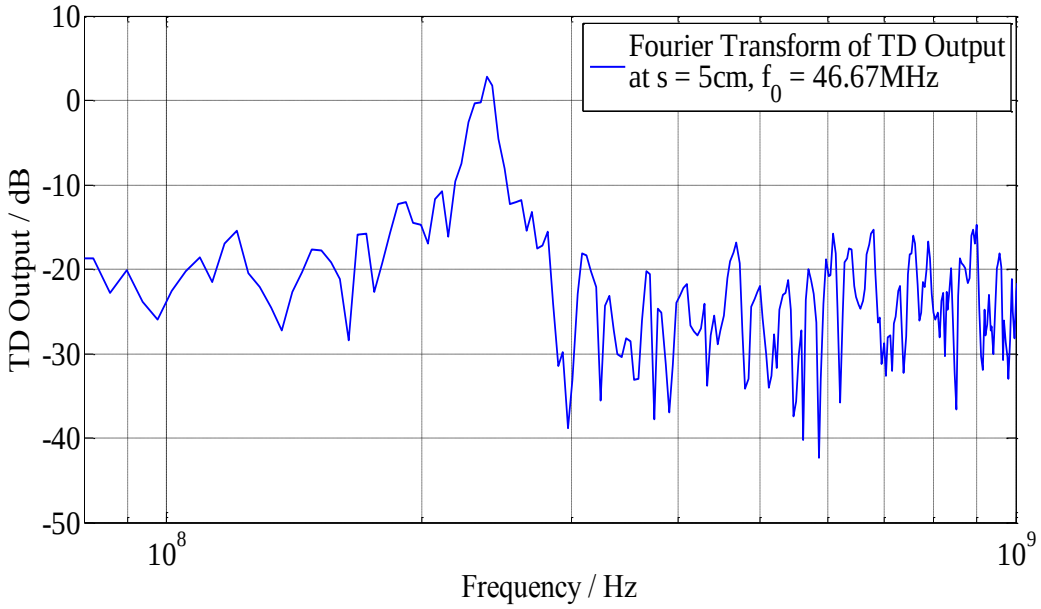

Figure 5.4.10: Fourier Transform of measurement data in Figure 5.4.7, for a separation, s = 5cm, and input of fundamental frequency (a) 39.33MHz. (b) 46.67MHz

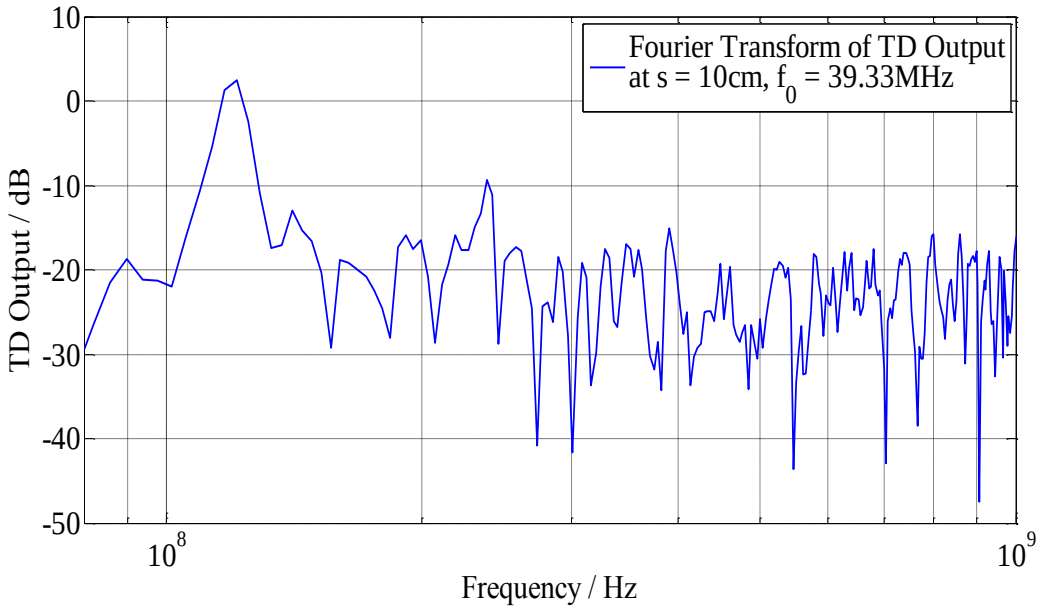

Figure 5.4.11: Fourier Transform of measurement data in Figure 5.4.8, for a separation, s = 10cm, and input of fundamental frequency of 39.33MHz.

5.4.2 Coupling between Two RG-58 Coaxial Cables via a Ground Plane

A. Frequency Domain Results

Similar to section 5.4.1, simulations were also performed using the 1D TLM model developed in Chapter 4, section 4.4. In comparison with the crosstalk measurement results and including both the differential and common mode of the end plates' inductance, Figures 5.4.12 – 5.4.15 show results for various separations, s (2, 5, 10 and 15cm) and keeping h constant at 11.5cm; while Figures 5.4.16 – 5.4.18 show results for various h (16.5, 21.5 and 26.5cm) and keeping s constant at 5cm; with and without including the skin depth effect into the tertiary circuit.

(a)

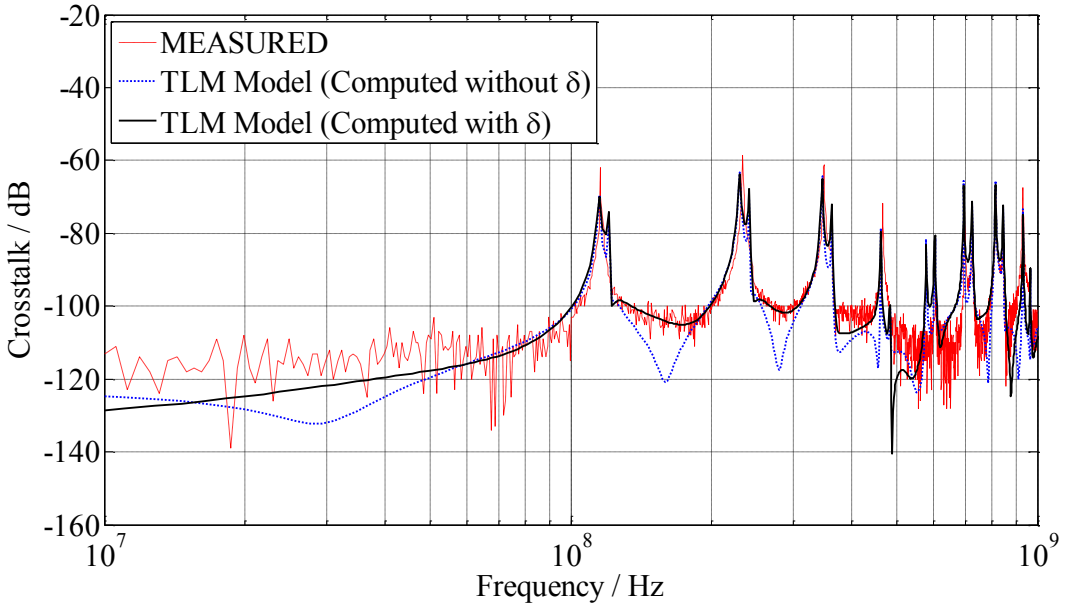

(b)

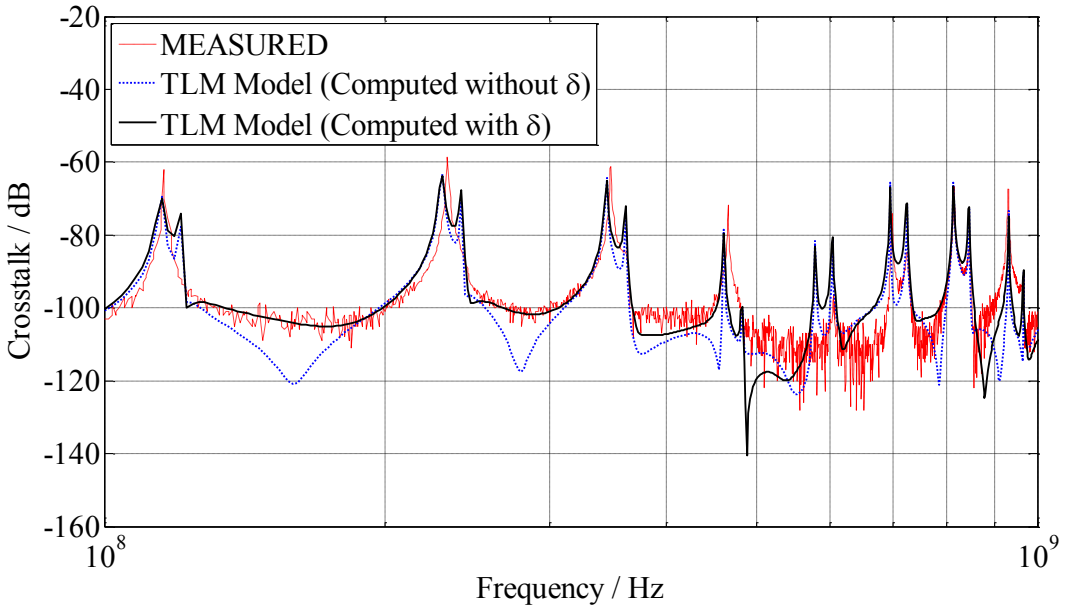

Figure 5.4.12: Crosstalk between two parallel RG-58 coaxial cables via ground plane with s = 2cm and h = 11.5cm. (a) Frequency: 10MHz – 1GHz. (b) Frequency: 100MHz – 1GHz.

(a)

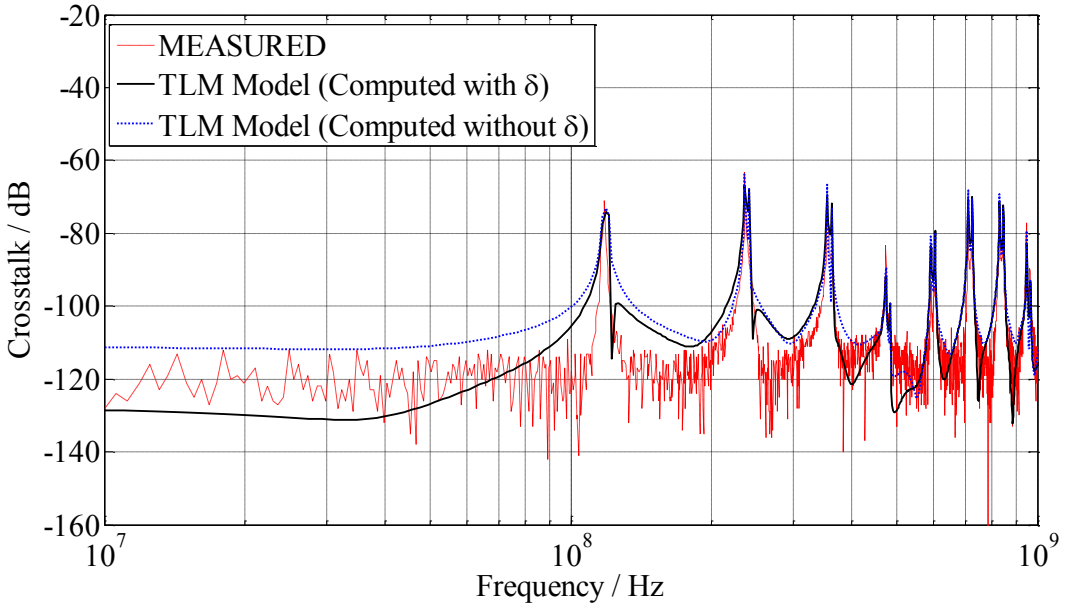

(b)

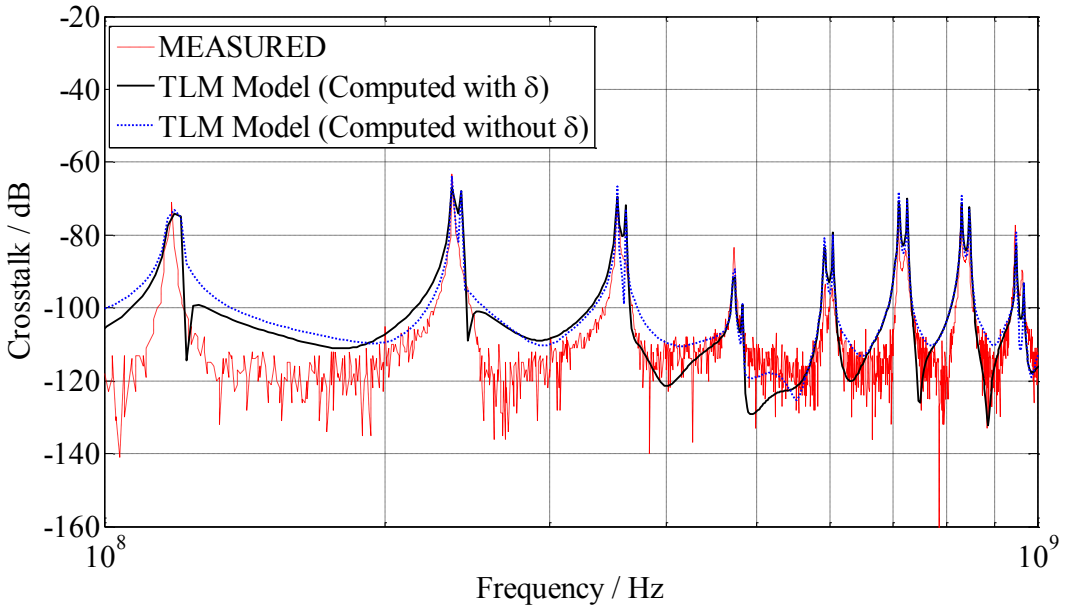

Figure 5.4.13: Crosstalk between two parallel RG-58 coaxial cables via ground plane with s = 5cm and h = 11.5cm. (a) Frequency: 10MHz – 1GHz. (b) Frequency: 100MHz – 1GHz.

(a)

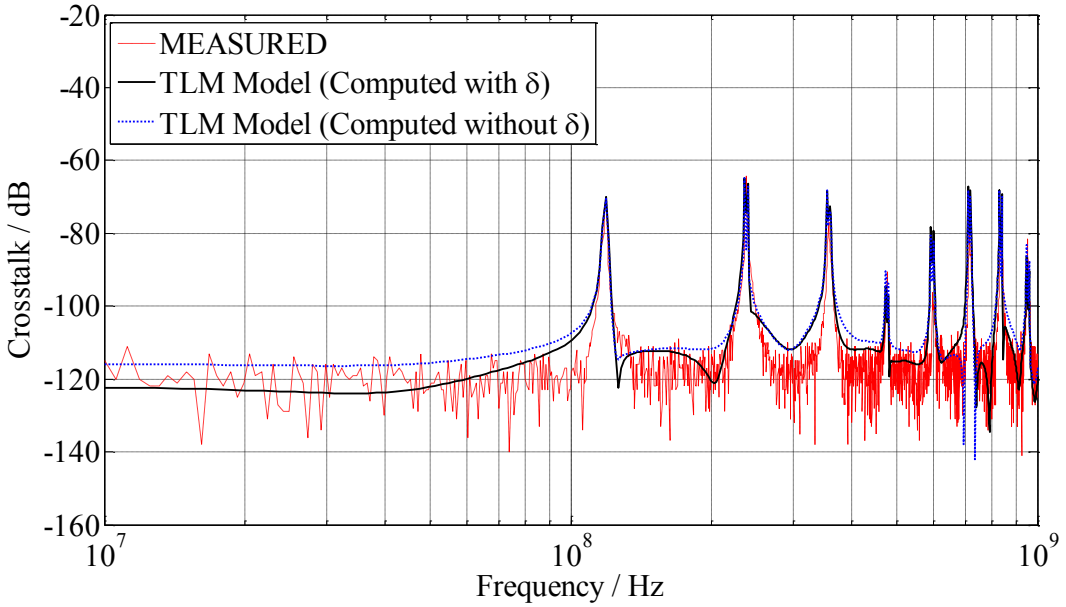

(b)

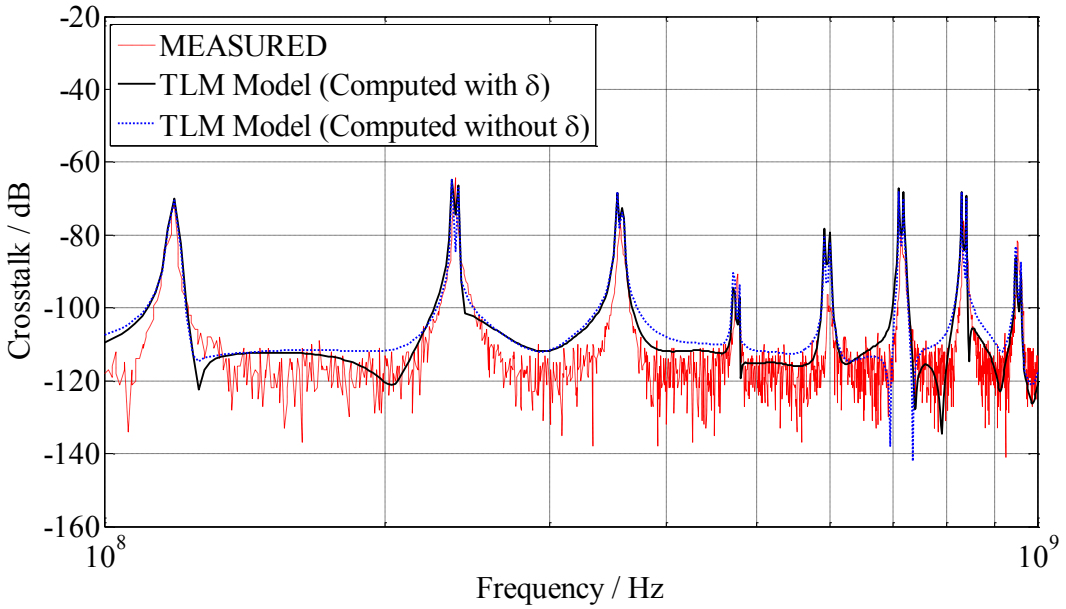

Figure 5.4.14: Crosstalk between two parallel RG-58 coaxial cables via ground plane with s = 10cm and h = 11.5cm. (a) Frequency: 10MHz – 1GHz. (b) Frequency: 100MHz – 1GHz.

(a)

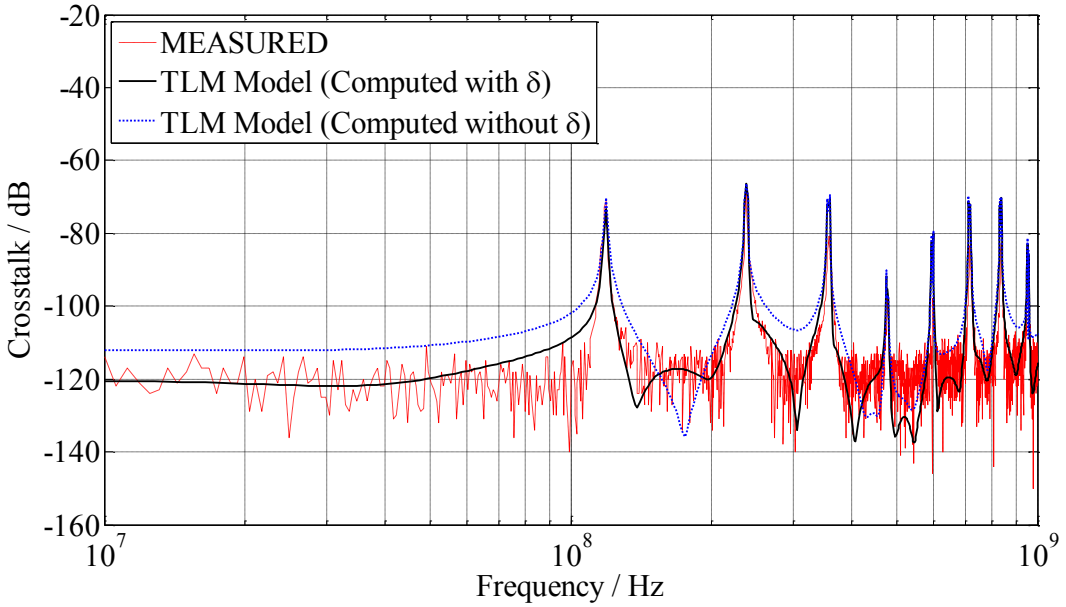

(b)

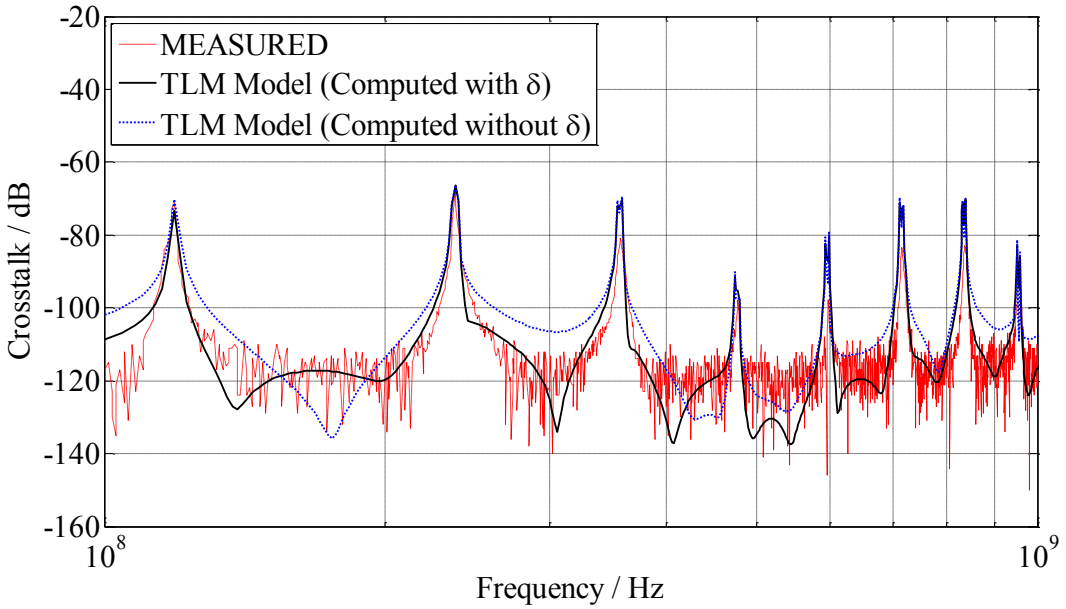

Figure 5.4.15: Crosstalk between two parallel RG-58 coaxial cables via ground plane with s = 15cm and h = 11.5cm. (a) Frequency: 10MHz – 1GHz. (b) Frequency: 100MHz – 1GHz.

(a)

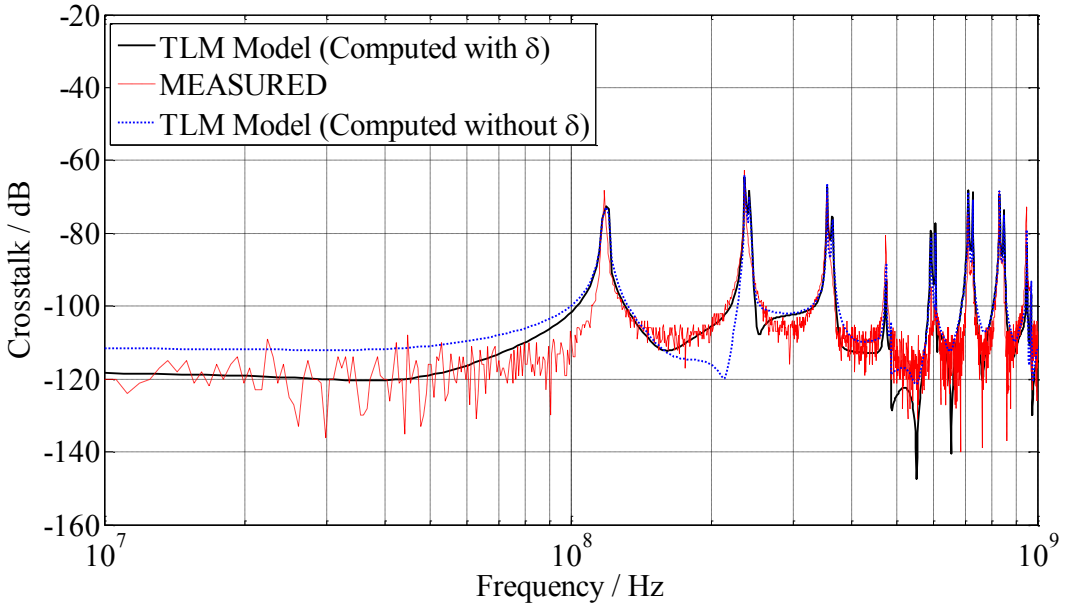

(b)

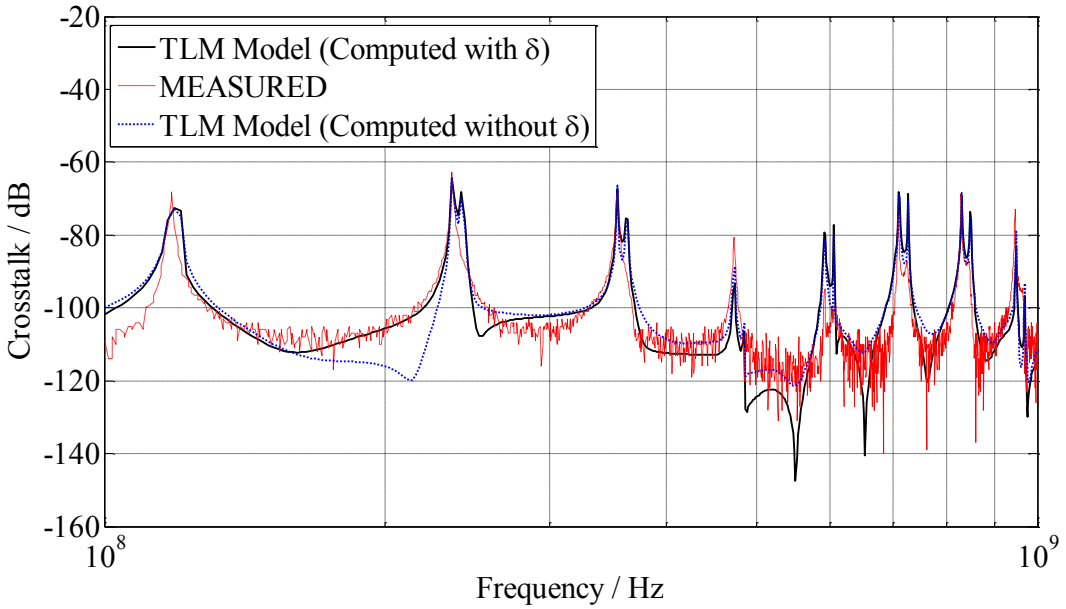

Figure 5.4.16: Crosstalk between two parallel RG-58 coaxial cables via ground plane with s = 5cm and h = 16.5cm. (a) Frequency: 10MHz – 1GHz. (b) Frequency: 100MHz – 1GHz.

(a)

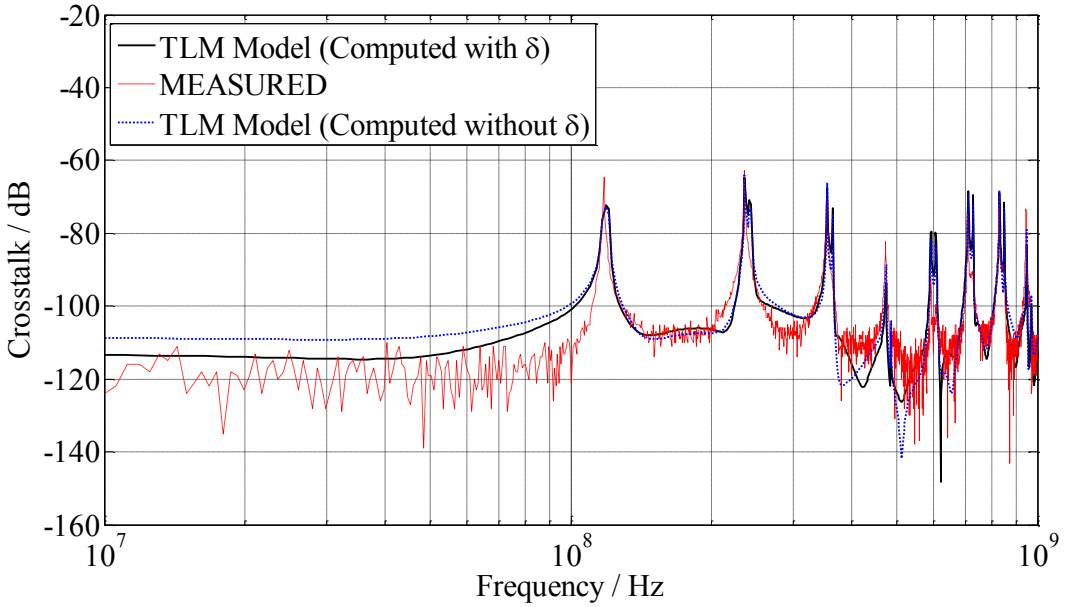

(b)

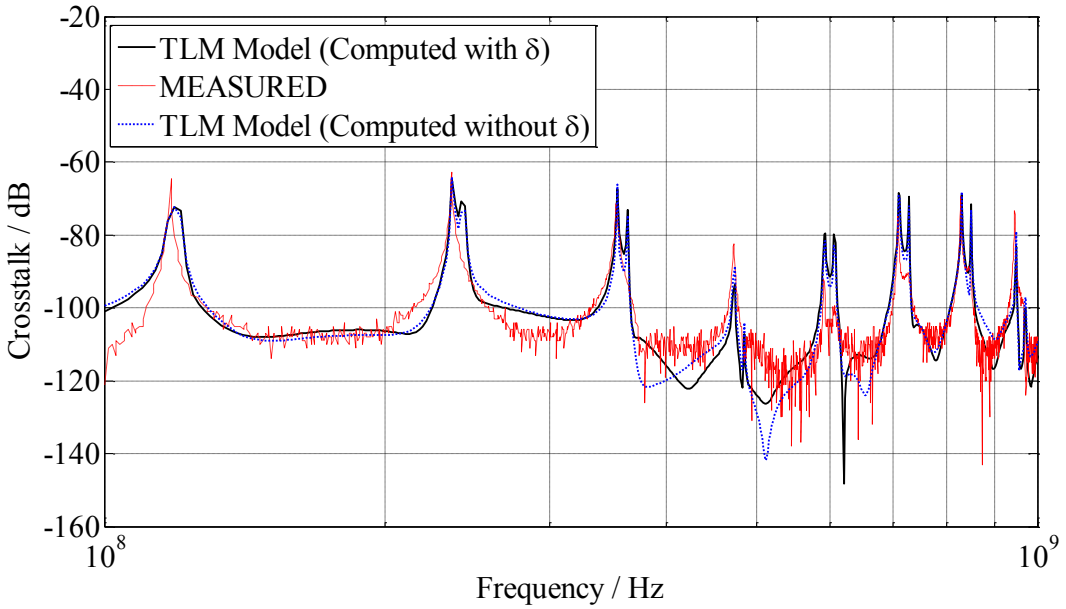

Figure 5.4.17: Crosstalk between two parallel RG-58 coaxial cables via ground plane with s = 2cm and h = 21.5cm. (a) Frequency: 10MHz – 1GHz. (b) Frequency: 100MHz – 1GHz.

(a)

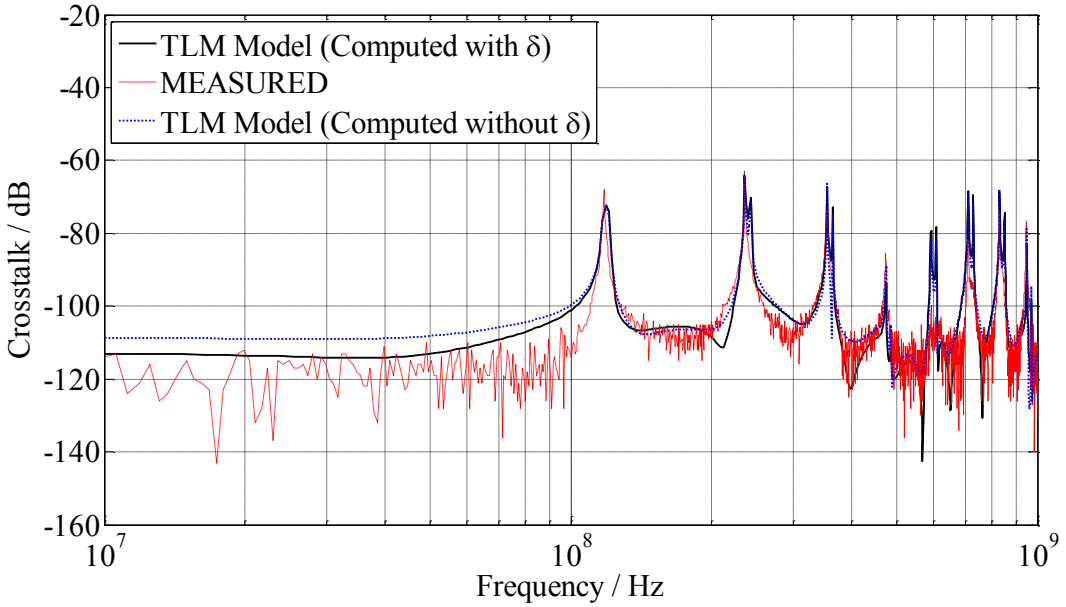

(b)

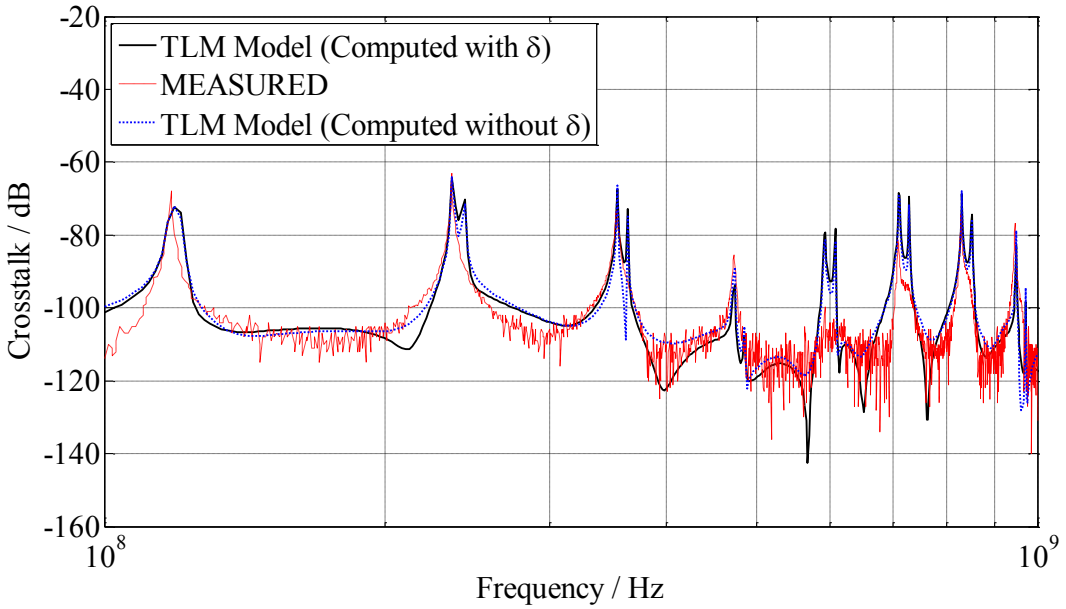

Figure 5.4.18: Crosstalk between two parallel RG-58 coaxial cables via ground plane with s = 5cm and h = 26.5cm. (a) Frequency: 10MHz – 1GHz. (b) Frequency: 100MHz – 1GHz.

As observed from Figures 5.4.12 – 5.4.18, the simulated results have good agreement with the measurement results. It is observed that by including the skin depth effect, δ, in both the braids of the coaxial lines, better improvement in shape is observed between the peak crosstalk resonant frequencies in the TLM solution and the peaks of the measurements for all separations, along the wide band of frequencies. There is not much improvement in the predicted magnitude observed by including δ, into the braids of the cables as the tertiary circuit is dominated by the common mode currents ($I_{tc} >> I_{td}$), formed by the return path of the metallic ground plane. However, it is proven that the inclusion of the skin depth effect is essential in the tertiary circuit as it significantly improves the Q-factor in the peaks of the resonant frequencies.

B. Time Domain Results

Similarly, simulation was performed using criterions as proposed in Chapter 4, section 4.4, where the time domain crosstalk between the two RG-58 coaxial cables via a ground plane can be observed from the voltage, V_{V0}, obtained from the adjacent cable. The same simulated square wave generated in section 5.4.1B is used as the source fed into the source line. In section 5.4.2A, the first 2 peak resonant frequencies were observed to be at approximately 118MHz and 235MHz, within the frequency range of 10MHz – 1GHz. In comparison with the crosstalk measurement results, Figures 5.4.19 – 5.4.21 show the time domain results for various separations, s (2, 5 and 10cm) and keeping the height, h, constant at 11.5cm; while Figures 5.4.22 and 5.2.23 show the time domain results for various h (16.5 and 26.5cm) and keeping s constant at 5cm.

(a)

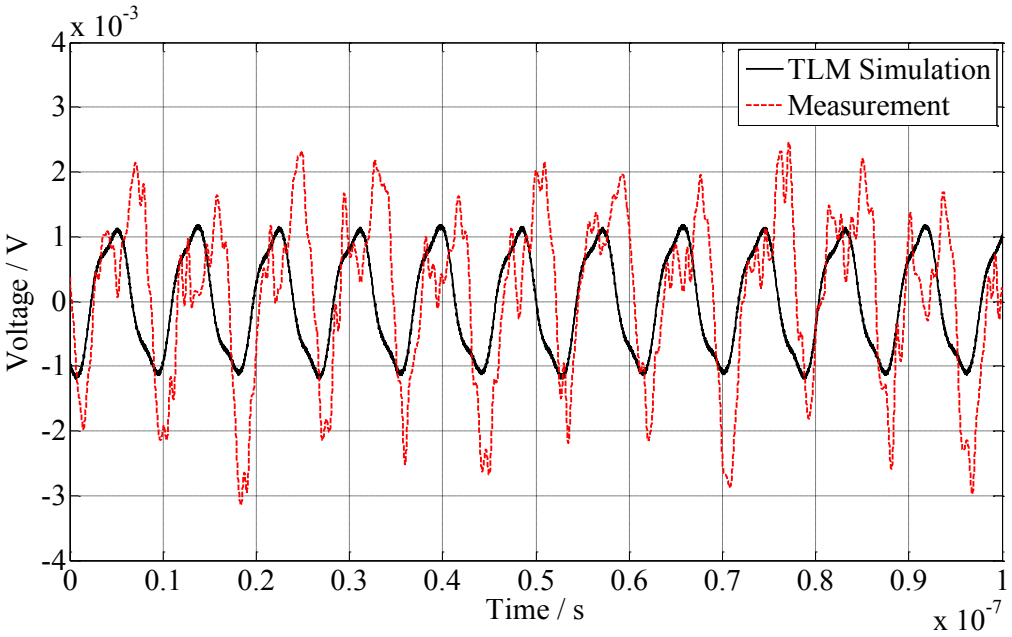

(b)

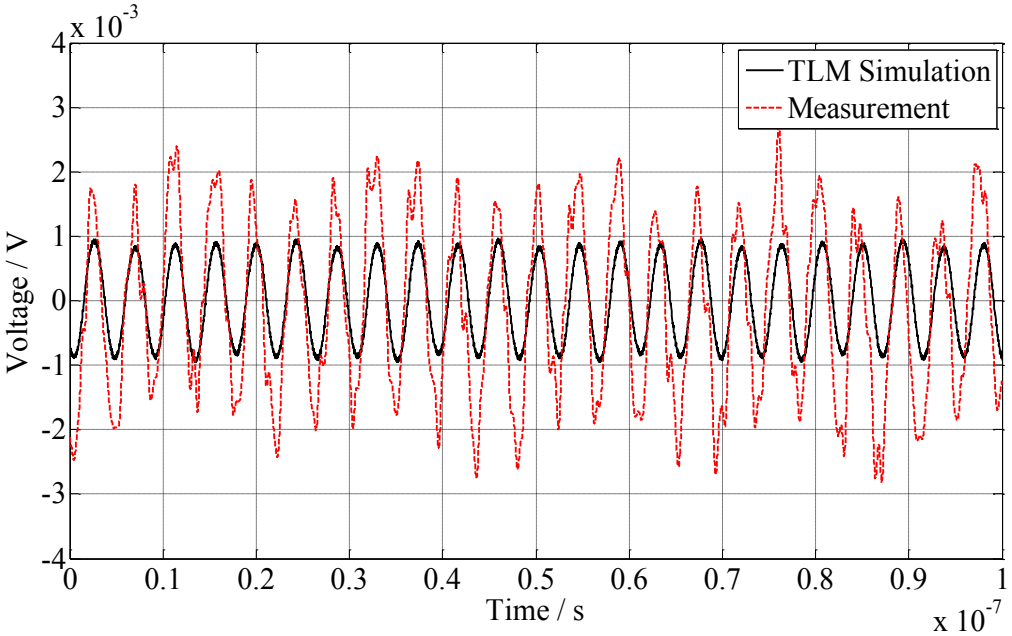

Figure 5.4.19: Time domain crosstalk between two parallel RG-58 coaxial cables via ground plane with s = 2cm and h = 11.5cm, and input of fundamental frequency (a) 38.4MHz (b) 46.1MHz

(a)

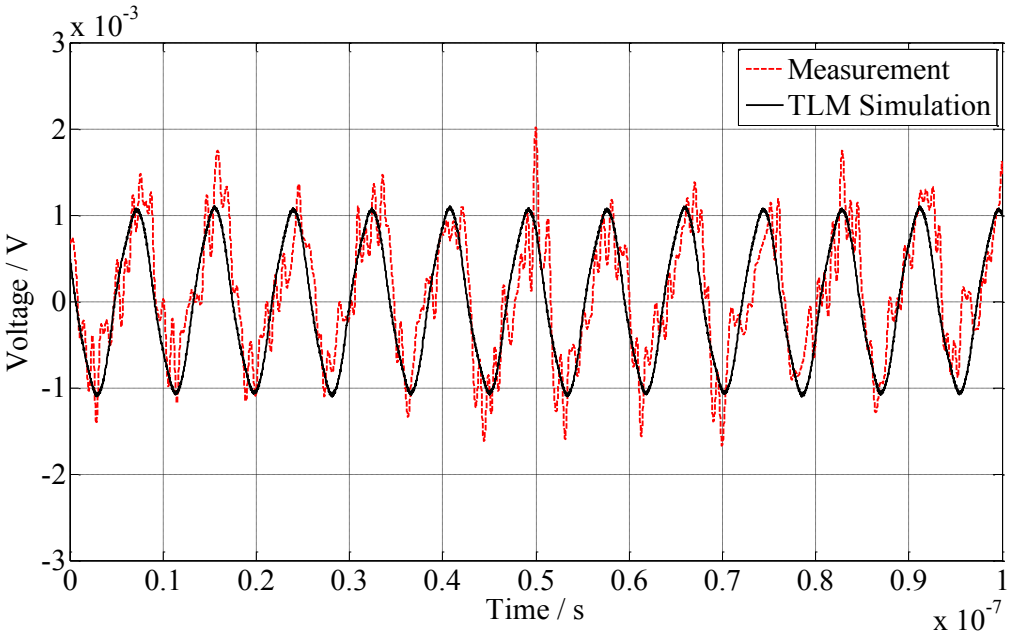

(b)

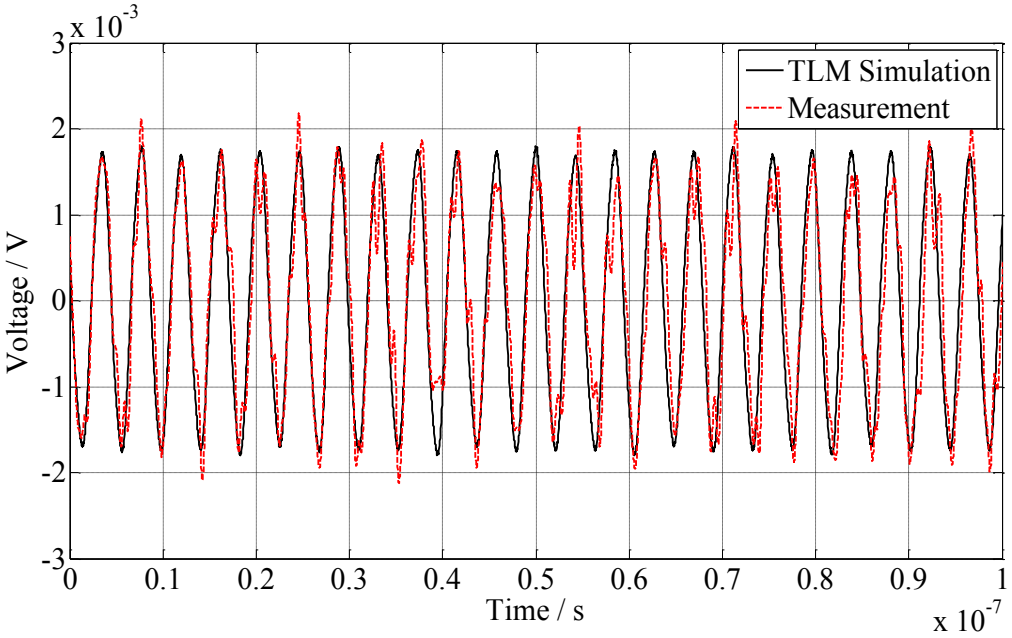

Figure 5.4.20: Time domain crosstalk between two parallel RG-58 coaxial cables via ground plane with s = 5cm and h = 11.5cm, and input of fundamental frequency (a) 39.63MHz (b) 47.2MHz

(a)

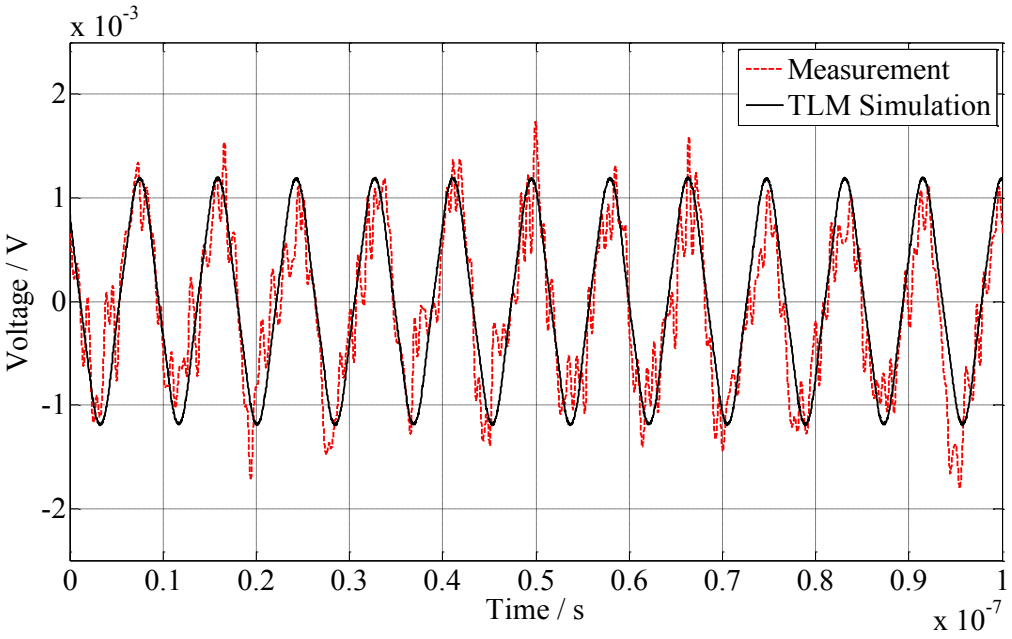

(b)

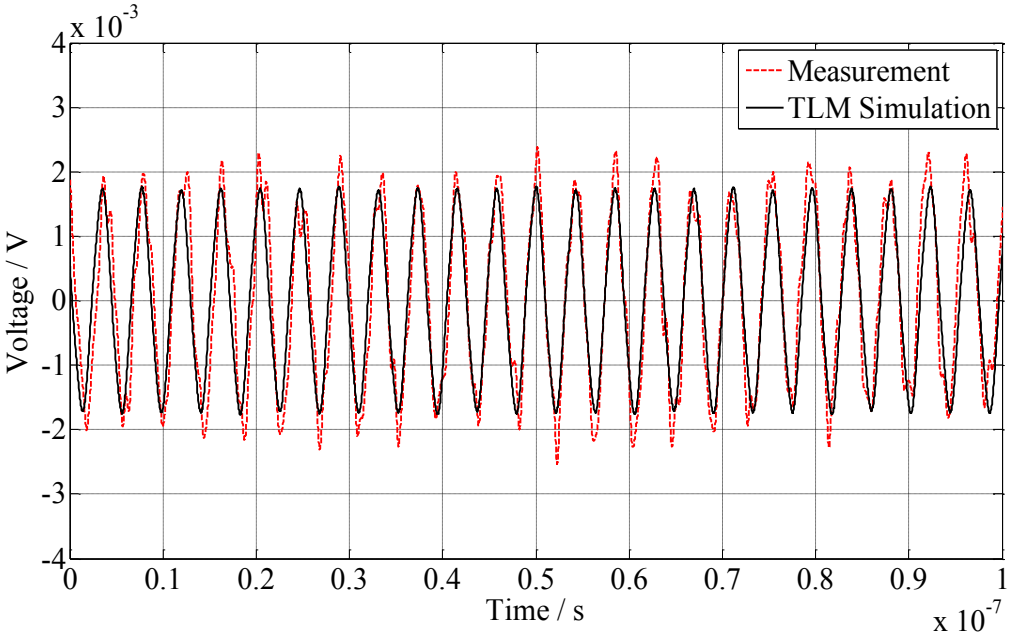

Figure 5.4.21: Time domain crosstalk between two parallel RG-58 coaxial cables via ground plane with s = 10cm and h = 11.5cm, and input of fundamental frequency (a) 39.63MHz (b) 47.2MHz

(a)

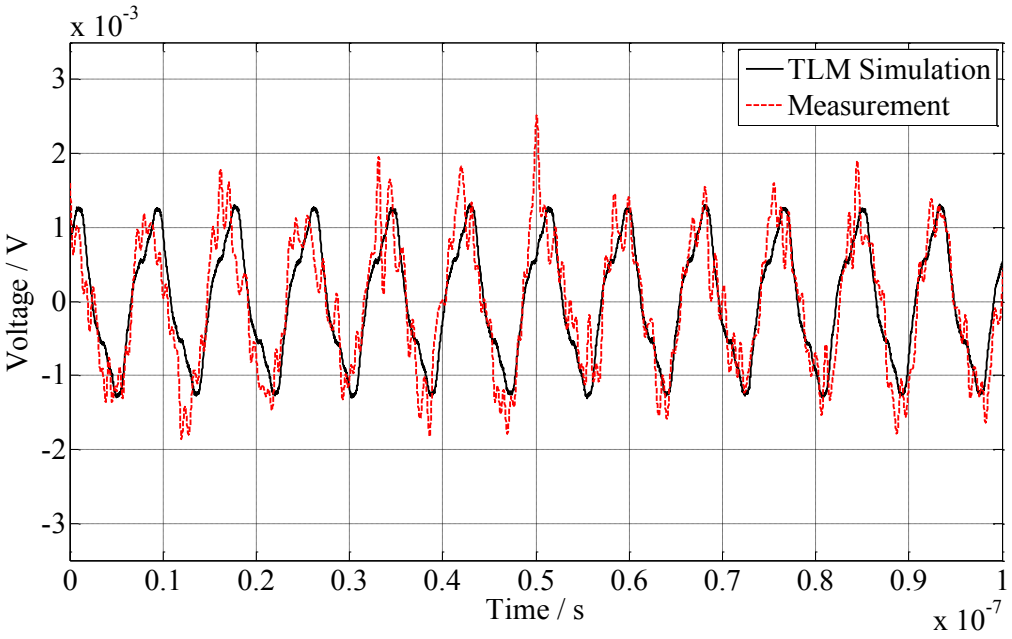

(b)

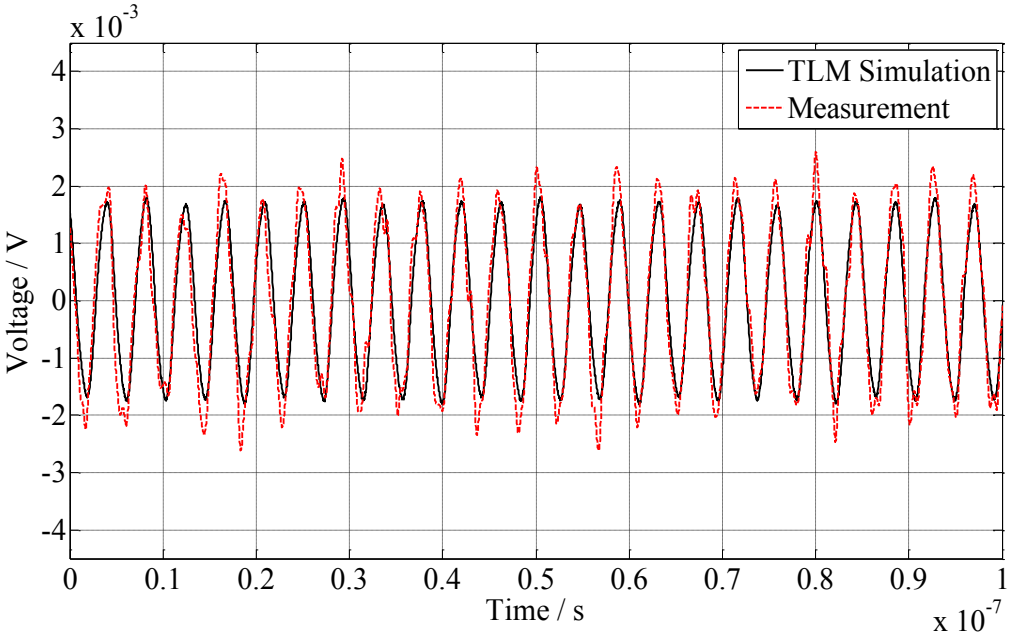

Figure 5.4.22: Time domain crosstalk between two parallel RG-58 coaxial cables via ground plane with s = 5cm and h = 16.5cm, and input of fundamental frequency (a) 39.63MHz (b) 47.2MHz

(a)

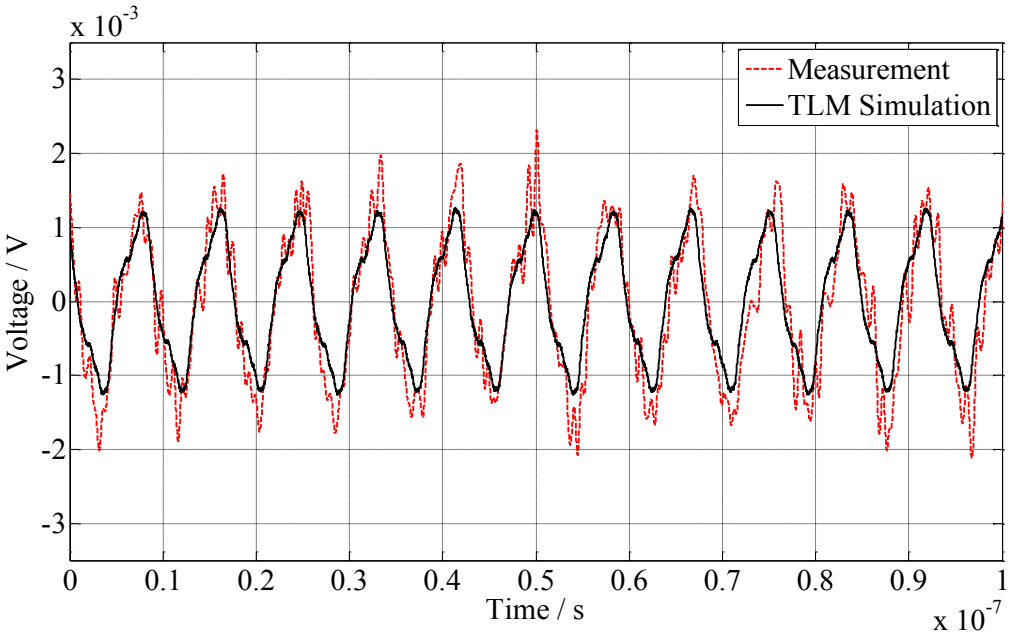

(b)

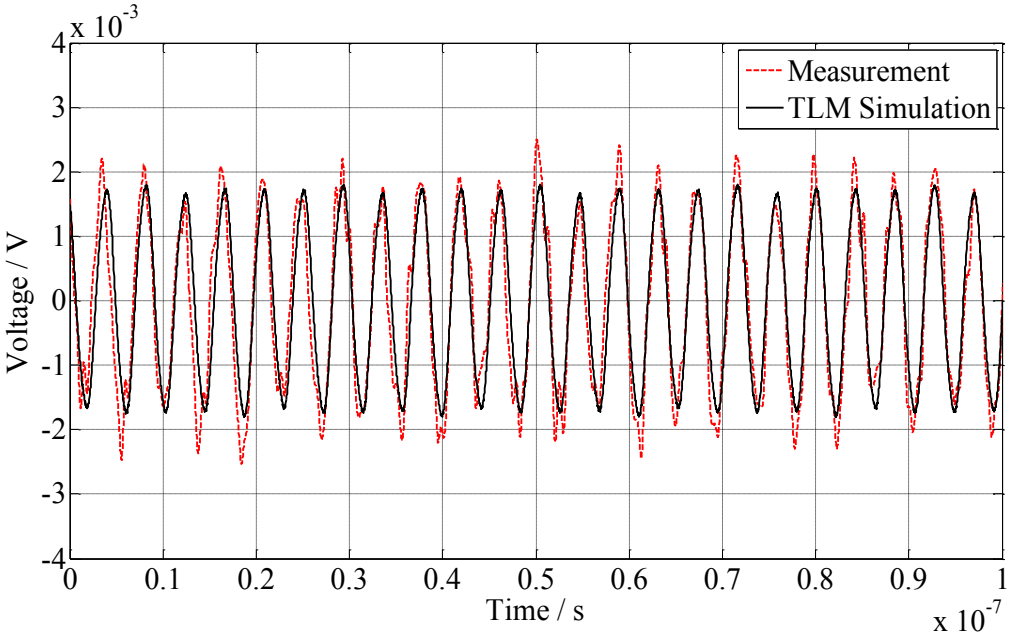

Figure 5.4.23: Time domain crosstalk between two parallel RG-58 coaxial cables via ground plane with s = 5cm and h = 26.5cm, and input of fundamental frequency (a) 39.63MHz (b) 47.2MHz

Similar effects in section 5.4.1B are observed from the results obtained in this section. Therefore, it can be deduced that whenever a harmonic of the source square waveform is close to one of the resonant of the tertiary circuit, strong coupling is observed. From Figure 5.4.19, the discrepancy in the amplitude in the time domain results is observed from the frequency domain results in Figure 5.4.12, section 5.4.2A. Of all the results it shows the largest discrepancy and requires more investigation.

C. Validation of Time Domain Results

Similarly, in order to validate the accuracy of the time domain results obtained, a Fourier Transform is performed on the time domain measurement results to verify the output frequency in which the peak of the resonant frequency resides. For the various separations, s, between the cables (2, 5 and 10cm) and keeping the height, h, constant at 11.5cm in section 5.4.2B, Figures 5.4.24 – 5.4.26 show the peaks of the resonant frequencies of Figures 5.4.19 – 5.4.21; while for various h (16.5 and 26.5cm) and keeping s constant at 5cm in section 5.4.2B, Figures 5.4.27 and 5.4.28 show the peaks of the resonant frequencies of Figures 5.4.22 and 5.4.23, respectively.

Similarly, it is observed from the Fourier Transformed time domain results in section 5.4.2B that the resonant frequency presented perfectly matches the resonances obtained from the frequency domain results in section 5.4.2A, both at approximately 118MHz and 236MHz respectively, where strong coupling is observed. No other resonances are seen to occur in both cases. It can be proven that the measurements obtained in section 5.4.2B contain only the resonant frequency harmonics of 118MHz and 236MHz; and most of the output signal is subjected to noise. Similarly, even harmonics are also observed in the output. Such phenomenon only occurs when the periodical input positive peak amplitude is different from the negative peak value, which can be observed from Figure 5.4.5 in section 5.4.1B. The cause for such situation lies in the discrepancy of the instrument – Pulse Function Arbitrary Generator (see Chapter 3). However, the even harmonics at the output are seen to be more distinctive when the ground plane is included into the system. This may be due to the effects of both propagating modes, the common and differential modes, travelling in the system.

(a)

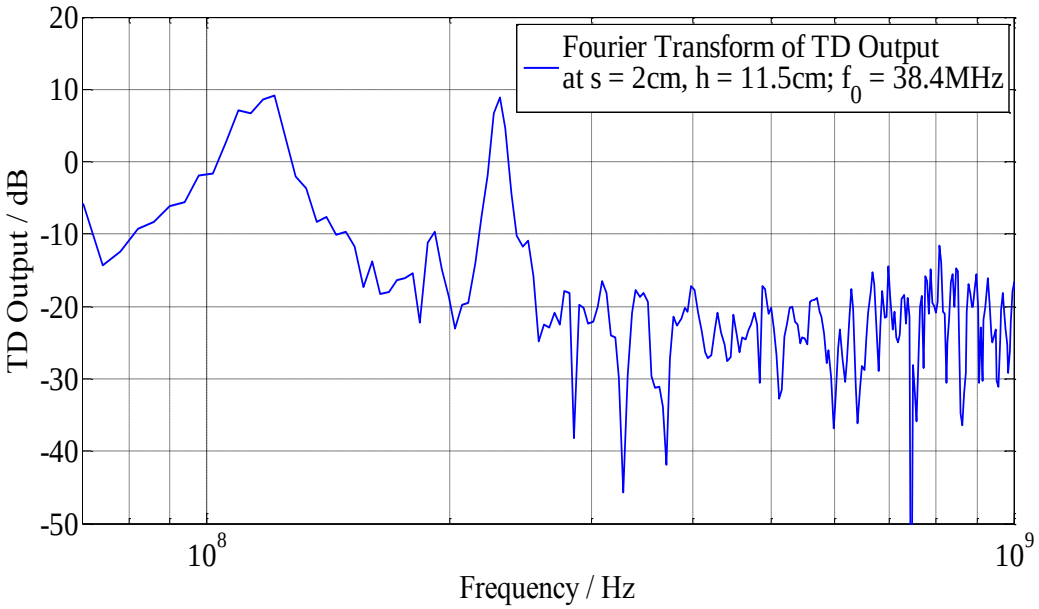

(b)

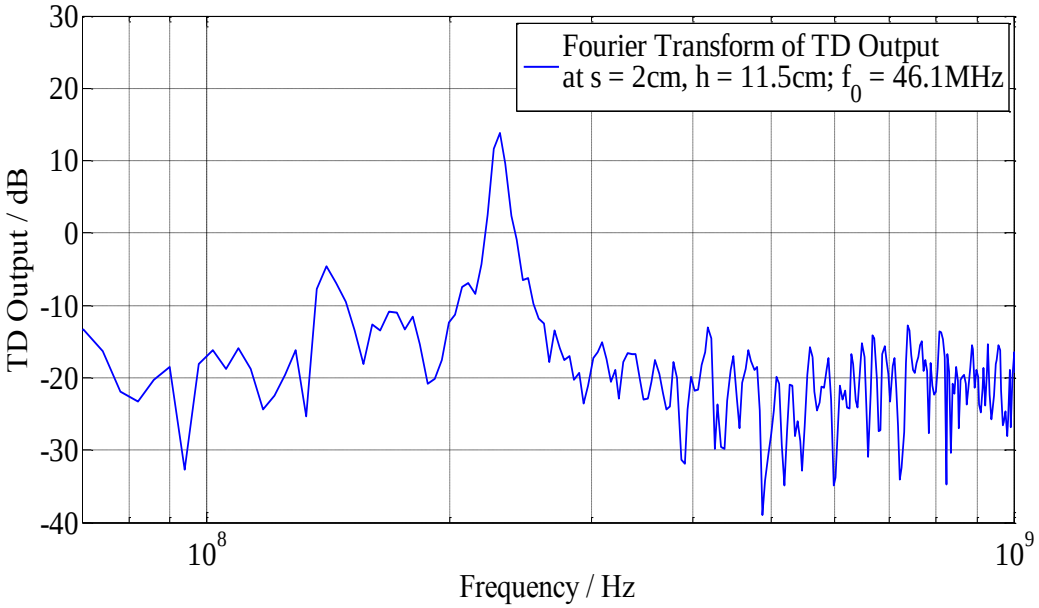

Figure 5.4.24: Fourier Transform of measurement data in Figure 5.4.19, with s = 2cm, h = 11.5cm and input of fundamental frequency (a) 38.4MHz. (b) 46.1MHz

(a)

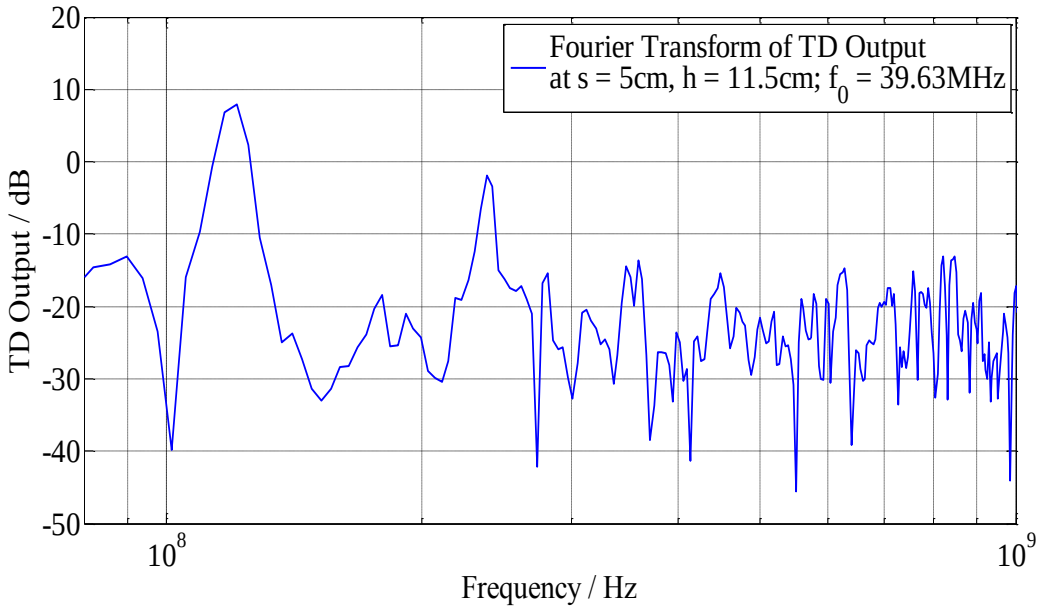

(b)

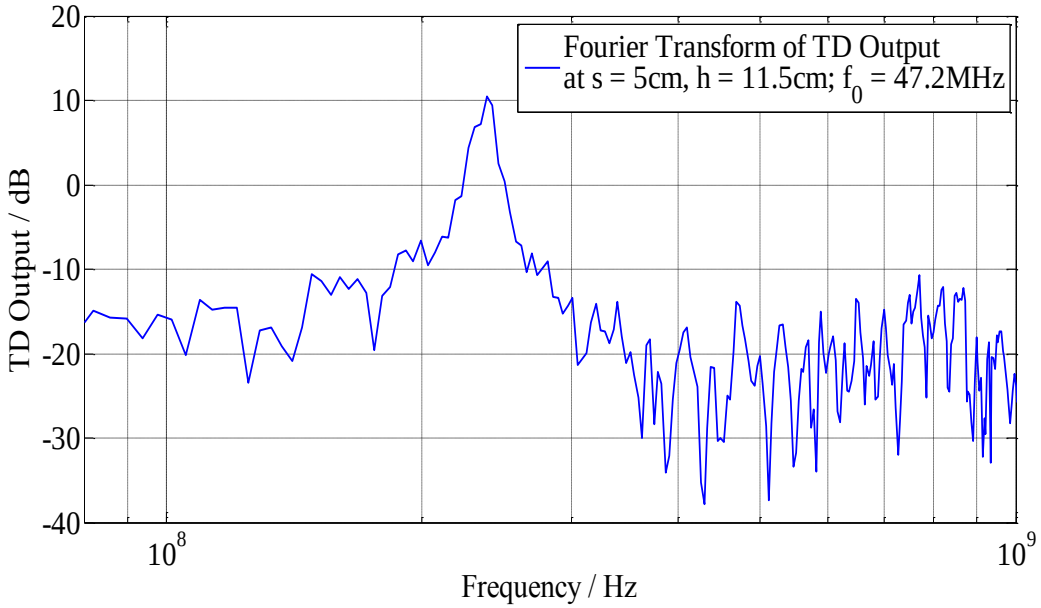

Figure 5.4.25: Fourier Transform of measurement data in Figure 5.4.20, with s = 5cm, h = 11.5cm and input of fundamental frequency (a) 39.63MHz. (b) 47.2MHz

(a)

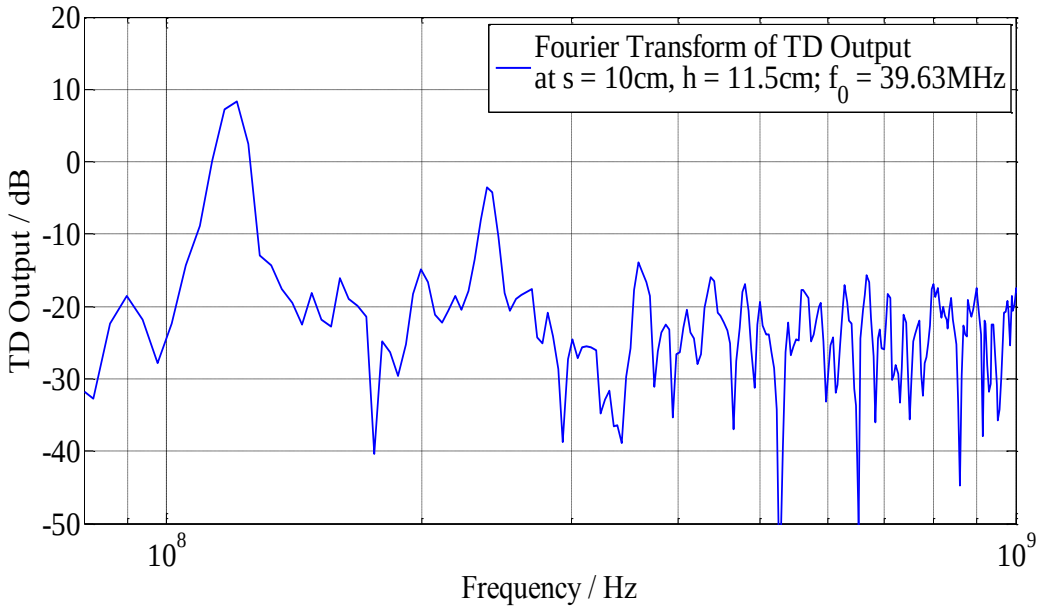

(b)

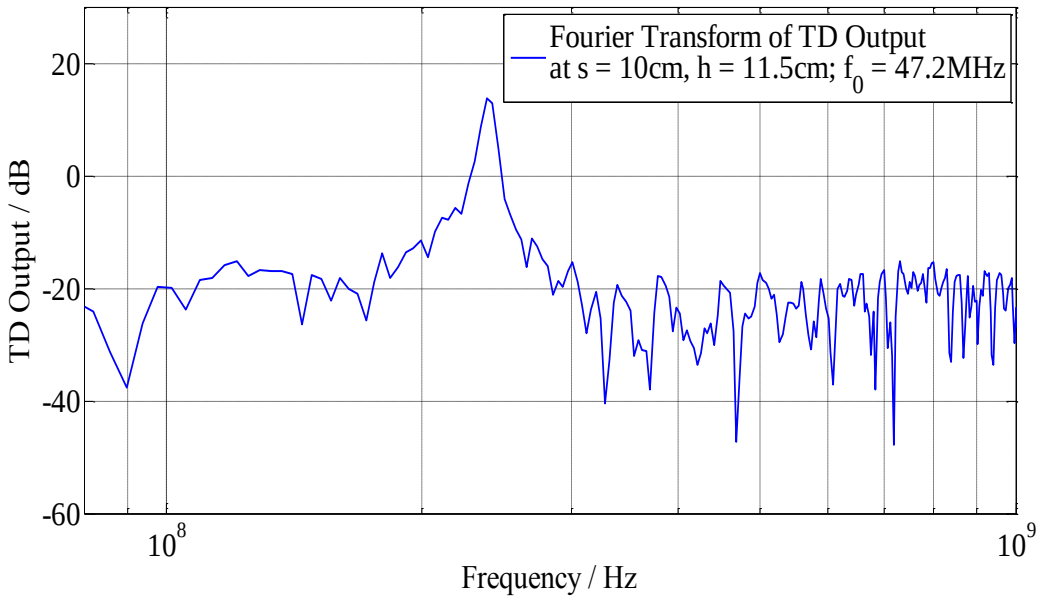

Figure 5.4.26: Fourier Transform of measurement data in Figure 5.4.21, with s = 10cm, h = 11.5cm and input of fundamental frequency (a) 39.63MHz. (b) 47.2MHz

(a)

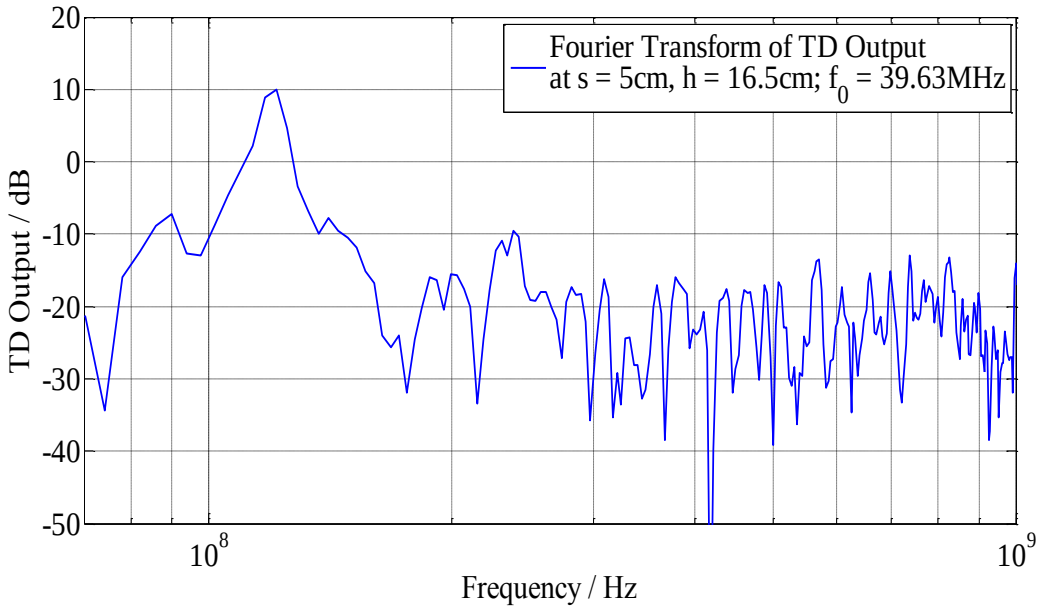

(b)

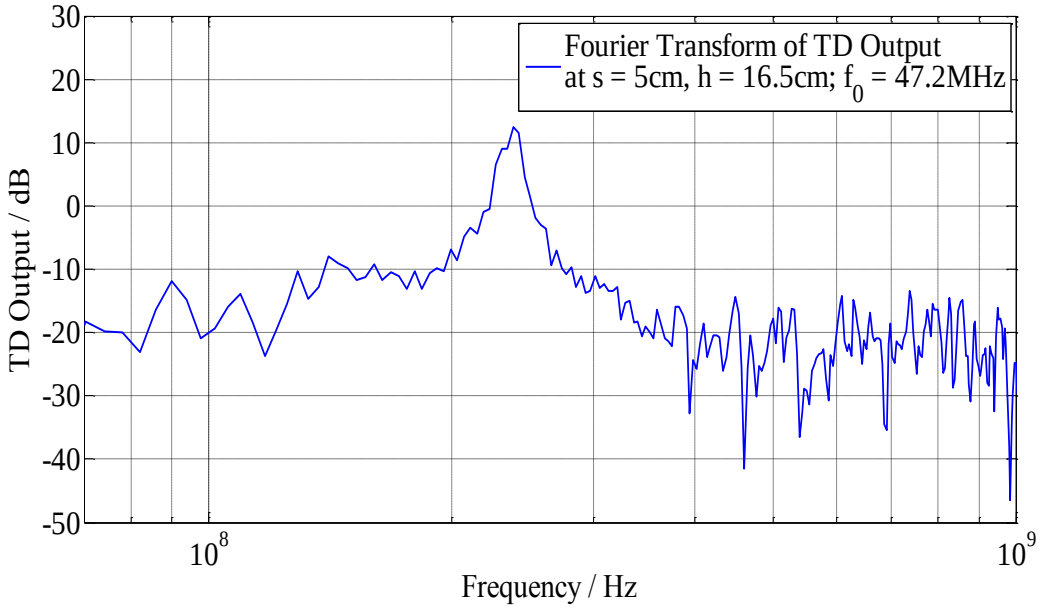

Figure 5.4.27: Fourier Transform of measurement data in Figure 5.4.22, with s = 5cm, h = 16.5cm and input of fundamental frequency (a) 39.63MHz. (b) 47.2MHz

(a)

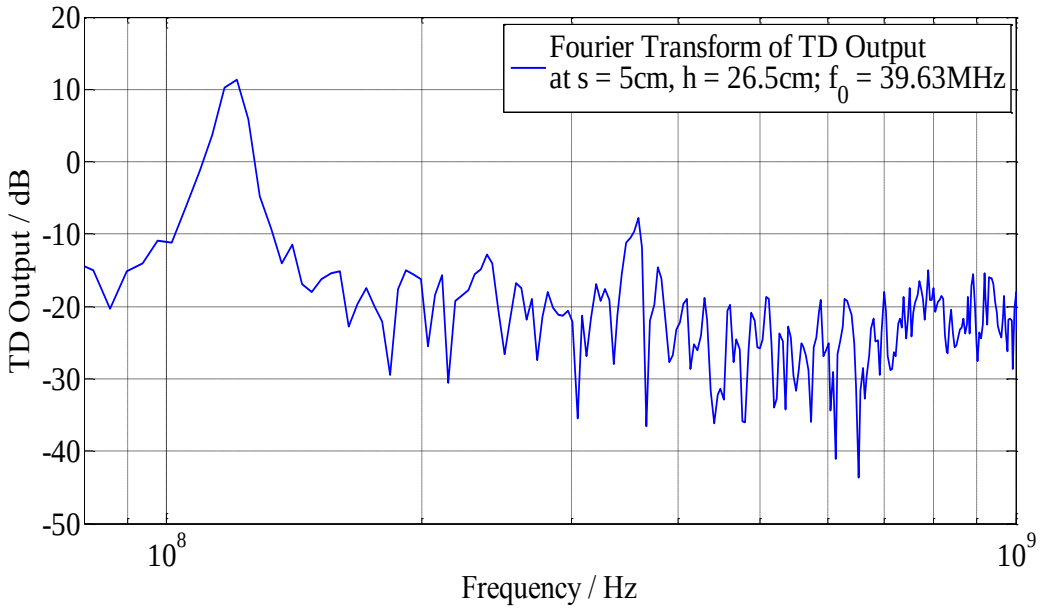

(b)

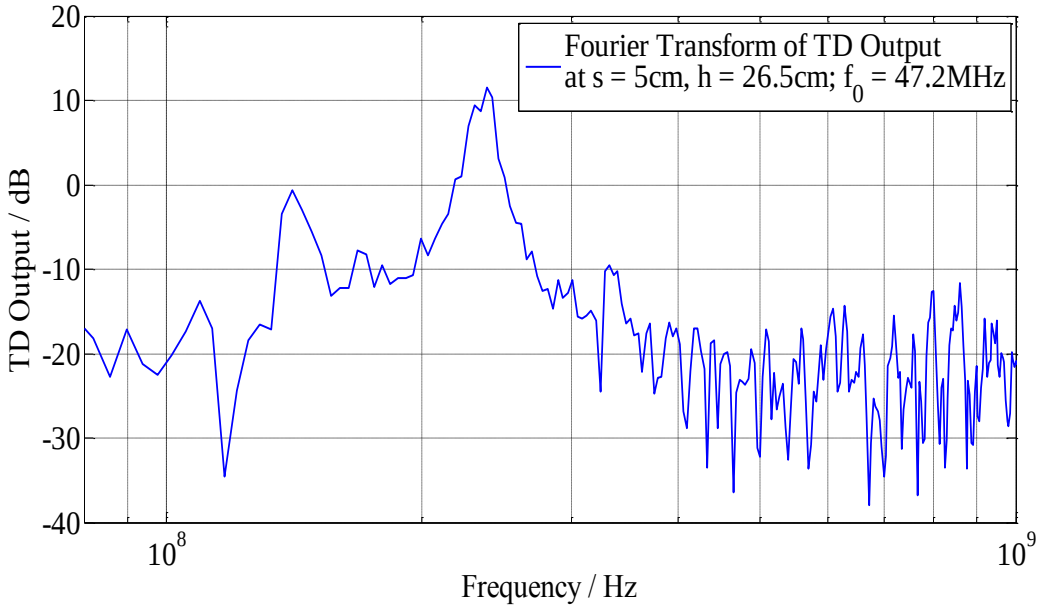

Figure 5.4.28: Fourier Transform of measurement data in Figure 5.4.23, with s = 5cm, h = 26.5cm and input of fundamental frequency (a) 39.63MHz. (b) 47.2MHz

5.5 Conclusions

In this chapter, the analysis of the skin depth effect is included as a loss factor in the characterisation of the tertiary circuit (braided shield). Skin depth effects are usually modelled in the frequency domain. Time domain skin depth models comprise of branches of R-L lumped circuits. Most proposed time domain models have relatively large number of R-L branches, resulting in slow computation. The two most suitable models are due to (Kim et al. [5.10] and Bidyut et al. [5.8]). The two models were investigated and compared; and both agree very well with each other.

It can be concluded that good agreement is obtained for both the crosstalk configurations; two coaxial cables in free space as well as over a perfectly conducting ground plane; presented in both time and frequency domains when compared against the measurement results. Predictions include characterisation of the tertiary circuit through the braid's transfer impedance, the impedance at the connector plates, and skin depth effect.

Comparison between measured and numerical solution show that the TLM solution successfully models coupling. However, it is shown that the coupling becomes less accurate in the TLM model at higher frequencies, which may be due to factors such as radiation loss etc. This study proved that noticeable discrepancies are observed between measurements and the TLM solution when the skin depth effect and the excess impedance at the connector plates are omitted from the tertiary circuit.

In all, the characterisation of the tertiary circuit is successfully modelled in order to obtain accurate crosstalk comparison between measurements and the TLM simulation model. In addition to the importance of crosstalk to EMC studies, the presentation of results in the time domain is also valuable for Signal Integrity studies, showing importance for the correct operation of fast digital circuits.

References

[5.1] Thomas Kley, "Optimized single-braided cable shields," IEEE Transactions on Electromagnetic Compatibility, vol. 35, no. 1, February 1993.

[5.2] S. Sali, Prof. F.A. Benson and J.E. Sitch, "General crosstalk equations between two coaxial cables in free space," IEE Proceedings, vol. 130, no. 6, September 1983.

[5.3] Anatoly Tsaliovich, Cable Shielding for Electromagnetic Compatibility, Van Nostrand Reinhold, 1995.

[5.4] Christopoulos. C., The Transmission-Line Modelling Method: TLM, John Wiley & Sons, Inc, 1995.

[5.5] S. Sali, "A circuit based approach for crosstalk between coaxial cables with optimum braided shields," IEEE Transactions on Electromagnetic Compatibility, vol. 35, no. 2, 1993, pp. 300 – 311.

[5.6] D.W.P. Thomas, C. Christopoulos, F. Leferink and H. Bergsma, "Practical measure of cable coupling," IEEE Computer Science Press, September 2005.

[5.7] Clayton R. Paul, Introduction to Electromagnetic Compatibility, Wiley Series in Microwave and Optical Engineering, 1992.

[5.8] Bidyut K. Sen and Richard L. Wheeler, "Skin effect models for transmission line structures using generic SPICE circuit simulators," IEEE 7th Topical Meeting, 1998.

[5.9] Chu-Sun Yen, Zvonko Fazarinc and Richard L. Wheeler, "Time-domain skin effect model for transient analysis of lossy transmission lines," IEEE Proceedings, vol. 70, no. 7, July 1982, pp. 750 – 757.

[5.10] S. Kim and D. P. Neikirk, "Compact equivalent circuit model for the skin effect," IEEE Proceedings, pp. 1815 – 1818.

[5.11] T. Vu Dinh, B. Cabon and J. Chilo, "Time domain analysis of skin effect on lossy interconnections," Electronics Letters, vol. 26, no. 25, 6th December 1990, pp. 2057 – 2058.

[5.12] S. Mei and Y. I. Ismail, "Modelling skin effect with reduced decoupled R-L circuits," Electrical and Computer Engineering, Northwestern University, IEEE Proceedings 2003, pp. 588 – 591.

[5.13] Z. Song, W. Yahyaoui, F. Duval, D. Su and A. Louis, "Capturing skin effect with an effective non-uniform mesh and coupled R-L circuits," Electronics Letters, vol. 47, no. 2, 20th January 2011, pp. 94 – 95.

[5.14] Shizhong mei, Chirayu Amin and Yehea I. Ismail, "Efficient model order reduction including skin effect," Nation Science Foundation Career Award, 2nd June 2003, pp. 232 – 237.

CHAPTER 6

PREDICTED RADIATION EMISSION

6.1 Introduction

In recent years, with processor clock rates are reaching into the GHz region such that significant energy is present well into the microwave frequency range. At higher frequencies, the energy is more difficult to contain. Subtle factors like enclosure slots, length of individual component interconnections and radiation directly from terminated high-speed circuit boards all are potential causes for unwanted radiation. Moreover, radiated fields generated by transmission lines such as multiconductor lines and tracks on a printed circuit board, are also a major concern in electromagnetic compatibility (EMC) studies. The increasing use and demand for high-frequency electrical and electronic equipment in modern applications require an increasing effort in developing better designs to avoid electromagnetic interference (EMI). Therefore, to ensure normal functions of circuitries, control units, and massive data commutation networks, the radiated electromagnetic fields must be accurately calculated.

Many problems for EMC and interferences are caused by interconnects such as coaxial cables, which either radiate in free space or couple by imperfect shields into other cables, devices and antennas; or any receiving circuit, which then cause induced voltages and currents, potentially resulting in the malfunction of the victim devices. In modern systems where cables play such a dominant role (ie: an aircraft which comprises several kilometres of cables or in the automotive industry), it is crucial that such radiation effects involving cables are taken into account in the design process of electromagnetic systems from an EMC perspective. As the most fundamental model in wiring, it is important to investigate theoretically the radiation from a transmission line of finite length [6.11]. Since the transmission line considered here is of much smaller cross-sectional dimensions than the wavelength of the travelling wave in the line concerned, the principal propagation mode is essentially TEM mode. This chapter aims to present an estimation of the electromagnetic field radiation from a bare copper

wire above ground; and a RG-58 coaxial cable above ground, using time and frequency domain models.

6.2 Electric Field Estimates

It is known that charge and current distributions on conductors set up electric and magnetic fields around them. Two techniques have been developed to compute the radiated electromagnetic field from interconnects: the exact analytical solution [6.8] and the Hertzian dipole approximation approach [6.9] – [6.12] and [6.15] – [6.17].

6.2.1 Analytical Solution

The first approach is to resolve the travelling current signal into a series of transient functions, where the resultant field is a superposition of all the functions. As to the achievement of a practical EMC modelling method, the exact analytical solutions apply only to a limited and impractical range of geometries. To solve most practical problems such as a coaxial cable radiation, full wave numerical solvers must be used. However typical problems require excessive computational time. Therefore, an intermediate level modelling method aims to provide a faster solution with less computing resources to obtain the results required. A closed-form solution for the total power radiated by a multiconductor line above a ground plane was proposed by Cozza et al. [6.6], although this solution is very powerful and accessible, the radiation due to the discontinuities introduced by the line terminations, ie: brass end plates and coaxial connection transitions, was assumed to be negligible and no direct comparison with measured radiated fields was provided. To the best of our knowledge, the critical mechanism of electromagnetic radiation from a circular cross section cylinder wire is more likely to be the discontinuous termination rather than the straight line itself [6.18].

6.2.2 Hertzian Dipole Technique

The dipole technique can be used to calculate the electric and magnetic fields

from a known distribution of currents and charges [1.1] – [6.5]. It is most commonly used in the theory of antennas including radiating fields from cables, where it requires only the knowledge of source current density as a function of time and space [6.11]. In most cases only static and quasistatic solutions are found in the frequency domain.

Any radiating sections in an electrical circuit may be regarded to be made up of a chain of short ideal radiating dipoles [6.3]. These Hertzian dipoles are short enough for the current to be approximated as constant along the length of each of the dipoles. The total radiated electromagnetic field is the sum of each constituent dipole element. For a single dipole element of length dl, in free space, the radiated fields can be obtained in the frequency domain, as given in [6.3]. The current, I, is assumed to be the same in magnitude and phase, at all points along the element length [6.4]. A spherical coordinate system is commonly used to describe antennas, as illustrated in Figure 6.2.1 [6.4].

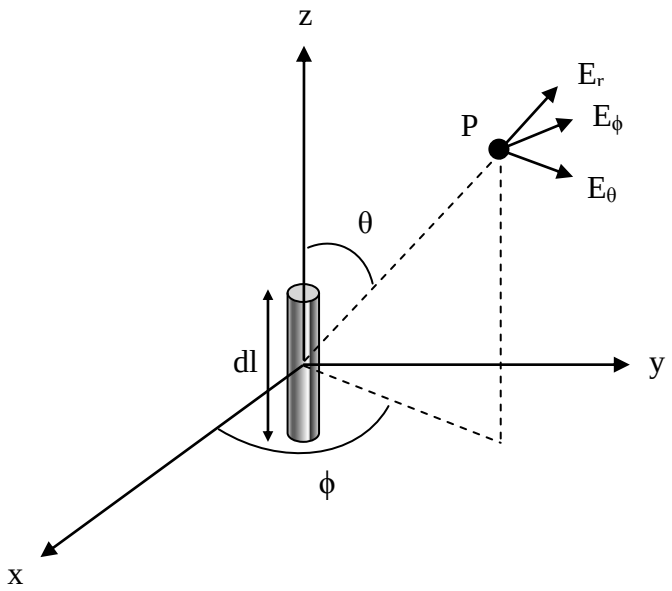

Figure 6.2.1: A Hertzian dipole element with its coordinate system

The Hertzian dipole method can be expressed in both time and frequency domains, depending on the application. In the past, spectrum analysers and network analysers are more efficient in the frequency domain, using heterodyne receivers. However, recent developments are making time domain approaches more attractive, prompting EMC designers to develop computational simulations in the time domain.

6.3 Frequency Domain Radiated Field

This section reviews the mathematical basis for linear antennas as described by Rao [6.5] and Balanis [6.18], in the frequency domain. The behavior of a linear antenna begins with an analysis of an incremental antenna, ie: an antenna of incremental length (substantially less than the wavelength of the driving signal). Given the electromagnetic fields of such an incremental antenna, a Hertzian dipole, at a distance from the antenna substantially larger than the wavelength of the signal, the electromagnetic field produced by a linear antenna of larger length can be obtained by suitable integration of the contribution from each elemental Hertzian antenna over the length of that antenna.

The Hertzian dipole shown in Figure 6.2.1, corresponds to a short length wire (of length $\overrightarrow{dl} << \lambda$ where λ is the wavelength of the signal) driven by an AC current of frequency ω, where the wire is directed along the z-axis in a rectangular coordinate system.

The current in the wire leads to a magnetic field encircling the wire, where the magnetic field is given by [6.3]:

$$\vec{B} = \frac{\mu_0 I}{4\pi}\left(\frac{\overrightarrow{dl} \times \vec{n}_r}{r^2}\right) \tag{6. 1}$$

where $\overrightarrow{n_r}$ is the unit vector along the line joining the current element and the observation at r distance from the current element. The magnetic field can also be expressed in terms of the vector potential [6.3]:

$$\vec{B} = \vec{\nabla} \times \vec{A} \tag{6. 2}$$

where the magnetic vector potential due to the current element is [6.18]:

$$\vec{A} = \frac{\mu_0 I \overrightarrow{dl}}{4\pi r} = \left(\frac{\mu_0 I dl}{4\pi r}\right)\vec{n}_z \tag{6. 3}$$

where $\overrightarrow{n_z}$ is the unit vector in the z-direction.

Let the current at the dipole element be given by:

$$I(t, r = 0) = I_0 \cos(\omega t) \tag{6. 4}$$

At distances away from the dipole, there is a retardation effect due to the time required for the electromagnetic field to propagate to the point $r \neq 0$. Therefore, (6.3) can be rewritten as:

$$\vec{A} = \left(\frac{\mu_0 I_0 dl}{4\pi r}\right) \cos(\omega t - \beta r)\vec{n}_z \tag{6. 5}$$

After being taken the curl of $\vec{A}$ in a spherical coordinates, the magnetic field intensity $\vec{H}$ is given by:

$$\vec{H} = \frac{\mu_0 I_0 \sin\theta}{4\pi}\left[\frac{\cos(\omega t - \beta r)}{r^2} - \frac{\beta \sin(\omega t - \beta r)}{r}\right]\vec{n}_\phi \tag{6. 6}$$

Given $\vec{H}$, from Maxwell's equations the electric field in free space is given by:

$$\vec{E} = E_r\vec{n}_z + E_\theta\vec{n}_\theta \tag{6. 7}$$

where the two components of $\vec{E}$ are:

$$E_r = \frac{2I_0 dl \cos\theta}{4\pi\varepsilon_0\omega}\left[\frac{\sin(\omega t - \beta r)}{r^3} + \frac{\beta \cos(\omega t - \beta r)}{r^2}\right] \tag{6. 8}$$

$$E_\theta = \frac{I_0 dl \sin\theta}{4\pi\varepsilon_0\omega}\left[\frac{\sin(\omega t - \beta r)}{r^3} + \frac{\beta \cos(\omega t - \beta r)}{r^2} - \frac{\beta^2 \sin(\omega t - \beta r)}{r}\right] \tag{6. 9}$$

For a general field calculation of a system, which may contain many radiating bodies in widely different attitudes, summation of the field components can best be achieved using Cartesian coordinates. The radiation fields can be found in Cartesian coordinates by using the following transformation described by Kraus [6.3]:

$$\begin{bmatrix} E_x \\ E_y \\ E_z \end{bmatrix} = \begin{bmatrix} \cos\theta\cos\phi & \sin\theta\cos\phi & -\sin\phi \\ \cos\theta\sin\phi & \sin\theta\sin\phi & \cos\phi \\ -\sin\theta & \cos\theta & 0 \end{bmatrix}\begin{bmatrix} E_\theta \\ E_r \\ E_\phi \end{bmatrix} \tag{6. 10}$$

where

$$\sin\phi = \frac{y}{\sqrt{x^2+y^2}}\ ;\ \cos\phi = \frac{x}{\sqrt{x^2+y^2}} \tag{6. 11}$$

$$\sin\theta = \frac{\sqrt{x^2+y^2}}{r}\ ;\ \cos\theta = \frac{z}{r} \tag{6. 12}$$

Figure 6.3.1 shows the cable configuration causing radiated fields investigated in this thesis. Note that the transmission line is terminated by two brass end plates at each end, which also contribute to the total radiating field of the system.

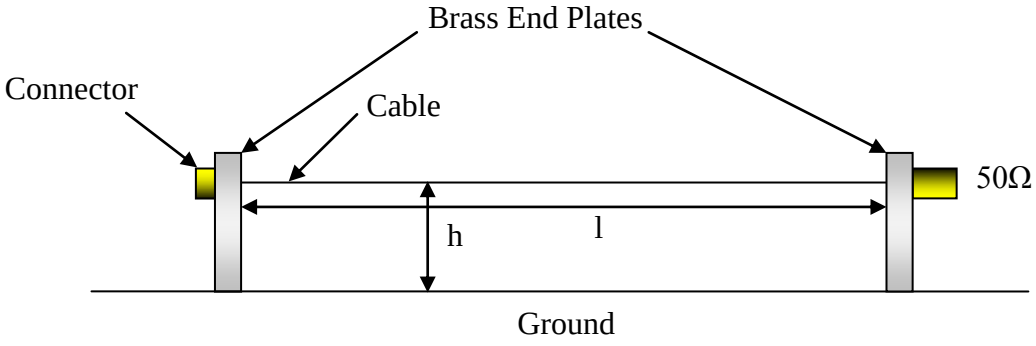

Figure 6.3.1: Radiated field configuration

The length of each dipole element, l_1 to l_N, is short enough to permit the assumption that the current along each segment is constant. Current values, $I_1 – I_N$, can be obtained by numerical means, namely through simulation using frequency domain transmission line model [6.21], as depicted in Figure 6.3.2.

(a)

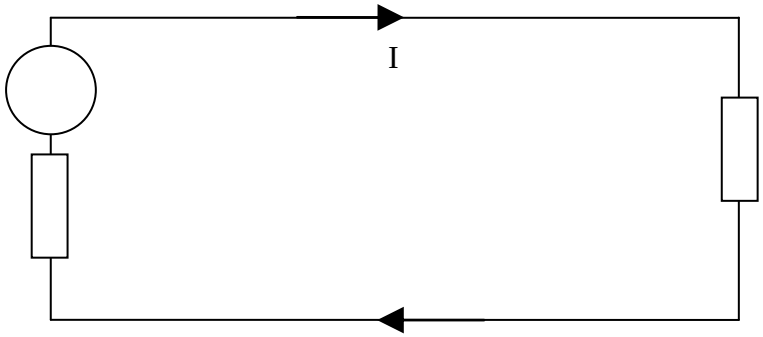

(b)

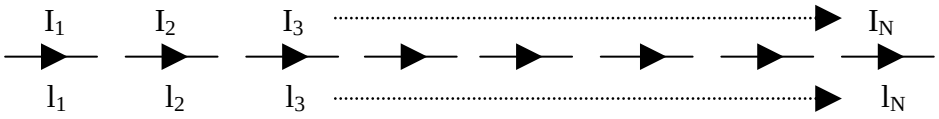

Figure 6.3.2: (a) A circuit of a simple one-wire above ground transmission line. (b) The segmentation of the one-wire above ground transmission line for field calculation.

Since the radiation model for the configuration presented in this paper are for cables over a perfect infinite ground plane, the image current has to be considered into the model. Due to the ground plane, the radiated field can be represented using an image of the transmission line with the return current of the primary conductor. In Figure 6.3.1, the cable is connected to a brass plate at each end as support. Therefore, another important factor that should be taken into account is the radiated field emitted by the current on the brass end plates. The current flowing through the brass end plates is assumed to be in the y-direction and is treated as individual dipole elements. Figure 6.3.3 presents a detailed radiated field model for the configuration in Figure 6.3.1.

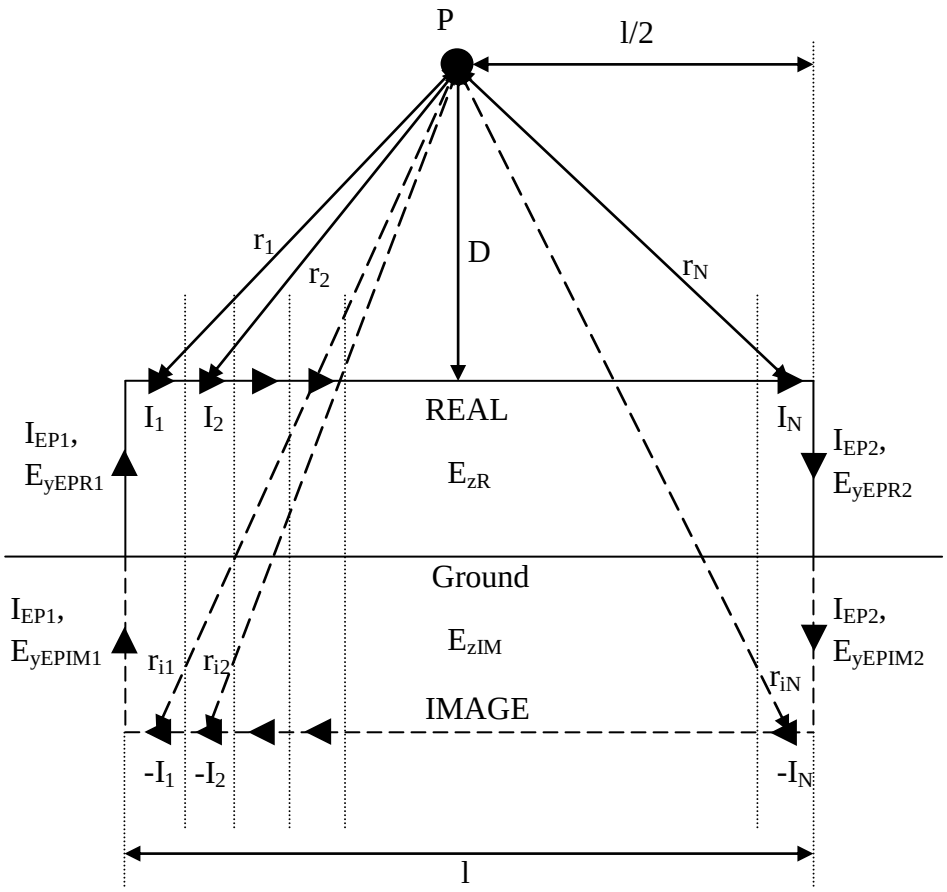

Figure 6.3.3: Detailed radiated field calculation for the configuration in Figure 2

where $r_1 - r_N$ and $r_{i1} - r_{iN}$ represent the distance between each dipole element of the transmission line to the observation point, P, of the real and image parts respectively. I_{EP1} and I_{EP2} denote the currents flowing in the end plates. $E_{yEPR1} - E_{yEPR2}$ and $E_{yEPIM1} - E_{yEPIM2}$ represent the radiated field from the end plates in its real and image parts respectively in the y-direction.

To determine the radiated field generated by the transmission line system as shown in Figure 6.3.3, one can regard the transmission line as being made up of a large number of short dipole radiators. As shown in Figure 6.3.2, the length of each dipole is chosen to be short enough to permit the assumption of a Hertzian dipole.

$$\overrightarrow{I_\xi}(\omega) = I\left(\frac{\xi l}{N}\right)\vec{n}_z;\ \xi = 1,2,\dots N \qquad (6.\ 13)$$

where ξ is the segment number and N is the total number of segments.

The end plate currents can subsequently be defined as:

$$\vec{I}_{EP1} = I_1(\omega)\vec{n}_z \tag{6. 14}$$

$$\vec{I}_{EP2} = I_N(\omega)\vec{n}_z \tag{6. 15}$$

Given the observation point coordinates P(x, y, z), according to the Hertzian dipole field theory addressed in section 6.2.2, one can compute the radiated fields from all aspects in Figure 6.3.2. The total radiated field from the total transmission line system can subsequently be calculated as:

$$\begin{aligned}\vec{E}_{TOTAL}(\omega) = &\left\{\sum_{\xi=0}^{N} \vec{E}_{zR}(\xi,\omega) + \vec{E}_{yEPR1}(\omega) + \vec{E}_{yEPR2}(\omega)\right\}_{Conductor} \\ &+ \left\{\sum_{\xi=0}^{N} \vec{E}_{zIM}(\xi,\omega) + \vec{E}_{yEPMI1}(\omega) + \vec{E}_{yEPMI2}(\omega)\right\}_{Image}\end{aligned} \tag{6. 16}$$

6.4 Time Domain Radiated Field

Similarly, for a general time domain field calculation of a system, which may contain many radiating bodies in widely different attitudes, the Cartesian coordinate system is more convenient for the summation of the field contributions, using the transformation addressed by Kraus [6.3] in section 6.3. Hence, the time dependent equations for the radiated electromagnetic fields are then given by [6.7]:

$$E_x(t) = \frac{(dl)xz}{4\pi\varepsilon_0 r^2}\left[\frac{3I(t-{}^{r}/_{c})}{cr^2} + \frac{3\int_0^t I(t-{}^{r}/_{c})dt}{r^3} + \frac{1}{c^2 r}\frac{\partial I(t-{}^{r}/_{c})}{\partial(t-{}^{r}/_{c})}\right] \tag{6. 17}$$

$$E_y(t) = \frac{(dl)yz}{4\pi\varepsilon_0 r^2}\left[\frac{3I(t-{}^{r}/_{c})}{cr^2} + \frac{3\int_0^t I(t-{}^{r}/_{c})dt}{r^3} + \frac{1}{c^2 r}\frac{\partial I(t-{}^{r}/_{c})}{\partial(t-{}^{r}/_{c})}\right] \tag{6. 18}$$

$$\begin{aligned}E_z(t) = &\frac{(dl)z^2}{4\pi\varepsilon_0 r^2}\left[\frac{3I(t-{}^{r}/_{c})}{cr^2} + \frac{3\int_0^t I(t-{}^{r}/_{c})dt}{r^3} + \frac{1}{c^2 r}\frac{\partial I(t-{}^{r}/_{c})}{\partial(t-{}^{r}/_{c})}\right] \\ &- \frac{(dl)}{4\pi\varepsilon_0 r^2}\left[\frac{I(t-{}^{r}/_{c})}{cr^2} + \frac{\int_0^t I(t-{}^{r}/_{c})dt}{r^3} + \frac{1}{c^2 r}\frac{\partial I(t-{}^{r}/_{c})}{\partial(t-{}^{r}/_{c})}\right]\end{aligned} \tag{6. 19}$$

$$H_x(t) = \frac{-(dl)y}{4\pi}\left[\frac{1}{r^3}I(t - {}^{r}/_{c}) + \frac{1}{cr^2}\frac{\partial I(t - {}^{r}/_{c})}{\partial(t - {}^{r}/_{c})}\right] \quad (6.\ 20)$$

$$H_y(t) = \frac{(dl)x}{4\pi}\left[\frac{1}{r^3}I(t - {}^{r}/_{c}) + \frac{1}{cr^2}\frac{\partial I(t - {}^{r}/_{c})}{\partial(t - {}^{r}/_{c})}\right] \quad (6.\ 21)$$

$$H_z(t) = 0 \quad (6.\ 22)$$

where the term $(t - {}^{r}/_{c})$ denotes the retarded time [6.3], I is the current amplitude of the dipole element and r is the distance of the observation point, P, at location (x, y, z) from the dipole at the origin (0, 0, 0).

With the known current value from the radiating dipole at a retarded time $(t - {}^{r}/_{c})$, the radiated electromagnetic field can be calculated using equations (6.17) – (6.19) at the observation point, P, a distance r from the dipole centre. The integral terms in equations (6.17) – (6.19) denotes the charge function, which calculates the electrostatic field in the near field. The derivative terms in equations (6.17) – (6.22) represents the induction fields with respect to the function of the dipole currents. These equations were derived from [6.7] to determine the radiation field due to current carrying conductors (transmission lines), such as PCBs and ribbon cables [6.21]. For a more advanced use, this method is also used to calculate the electromagnetic fields from isolated radiators such as a lightning source [6.12].

Using formulas (6.17) – (6.19), the radiating field of the circuit can be defined by dividing the transmission line into small segments, where each segment is assumed to be an individual dipole element with its own current amplitude [6.12]. Time domain current values, I_1 – I_N, can be obtained by numerical means, namely through simulation using TLM method (see Chapter 4) [6.7], as depicted in Figure 6.3.2.

The TLM numerical solution (See Chapter 4) calculates the transient cable currents at nodal points that are, by necessity for accurate simulation, of separation much less than the minimum transient wavelength. These divided nodal points together with their associated transient currents are treated as a chain of Hertzian dipole elements for the field calculation process, as shown in Figure 6.3.3. The centre of each dipole element of the cable is the node connection points of the TLM numerical model. The simulated transient currents are also discrete in time-step k (see Chapter 4). The value of $k\Delta t$ must be significantly less than the minimum period of the

current transients. Therefore, the retardation factor ${}^{(r/c)}/_{\Delta t}$ of the retarded time, between an observation point P and a radiating dipole element can also be rounded to the nearest simulation step of k without introducing a significant error [6.7].

Using the discrete form of the integral and derivative terms of the transient current at a retarded time in equations (1) – (6), approximations derived by [6.7] is given by:

$$\int_0^t I(t - {}^{r}/_{c})dt = \sum_{k=1}^{NT-1} I(k\Delta t - {}^{r}/_{c})\Delta t + \frac{[I(-{}^{r}/_{c}) + I(NT\Delta t - {}^{r}/_{c})]\Delta t}{2} \quad (6.\ 23)$$

$$I(t - {}^{r}/_{c}) = I(k\Delta t - {}^{r}/_{c}) \quad (6.\ 24)$$

$$\frac{\partial I(t - {}^{r}/_{c})}{\partial (t - {}^{r}/_{c})} = \frac{I(k\Delta t - {}^{r}/_{c}) - I((k-1)\Delta t - {}^{r}/_{c})}{\Delta t} \quad (6.\ 25)$$

The total radiated field calculated is the sum of both the real and image parts of the radiated field in the transmission line, given by:

$$\vec{E}_{TOTAL}(t) = \left\{ \vec{E}_{yEPR1}(t) + \left\{ \sum_{I_1}^{I_N} \vec{E}_{zR} \right\}(t) + \vec{E}_{yEPR2}(t) \right\}_{Conductor} + \left\{ \vec{E}_{yEPIM1}(t) + \left\{ \sum_{-I_1}^{-I_N} \vec{E}_{zIM} \right\}(t) + \vec{E}_{yEPIM2}(t) \right\}_{Image} \quad (6.\ 26)$$

6.5 Frequency Domain Transmission Line Model

6.5.1 Single Bare Copper Wire above Ground

A bare wire is investigated as the radiating line; the equivalent transmission network circuit can be modelled as in Figure 6.5.1. R_b, L_b, C_b and G_b are the per-unit-length resistance [6.21], inductance, capacitance, and conductance, respectively. The circuit is driven by a source voltage, V_G. The source impedance, Z_G is 50Ω and the circuit is either terminated by an open circuit or 50Ω impedance. Z_0 denotes the characteristic impedance of transmission line system. C_{t1} and C_{t2} denote the connector capacitances on each end (line-end discontinuities), which are similar in magnitude

and given an estimated impedance value, $C_{t1} = C_{t2} = 2.78pF$ from S_{11} measurements (see Appendix C).

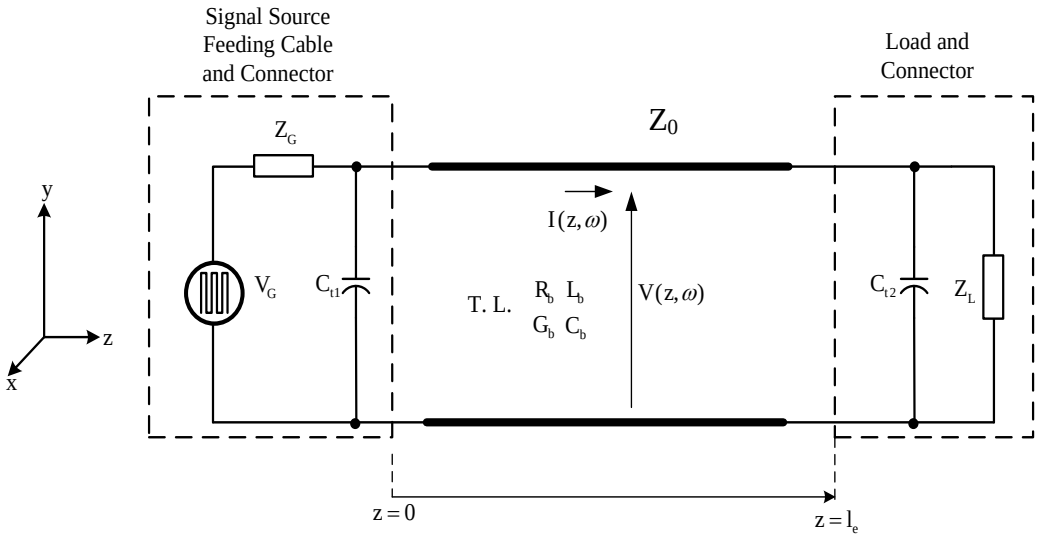

Figure 6.5.1: Equivalent transmission line circuit of a bare wire above ground

The solution of the bare wire above ground can be treated as two-conductor transmission line system [6.21]. In the case of a periodic or non-periodic waveform, the signal can be decomposed into a continuum of sinusoidal components via Fourier Transform and the frequency analysis remains unchanged. One of the advantages in frequency domain modelling is that losses of the conductors and its surrounding dielectric can be easily handled in the frequency domain. The frequency domain transmission line equations for a two-conductor bare wire circuit have been well developed as:

$$\frac{dV(z,\omega)}{dz} = -(R_b + j\omega L_b)I(z,\omega) \tag{6. 27}$$

$$\frac{dI(z,\omega)}{dz} = -(G_b + j\omega C_b)V(z,\omega) \tag{6. 28}$$

(a) (b)

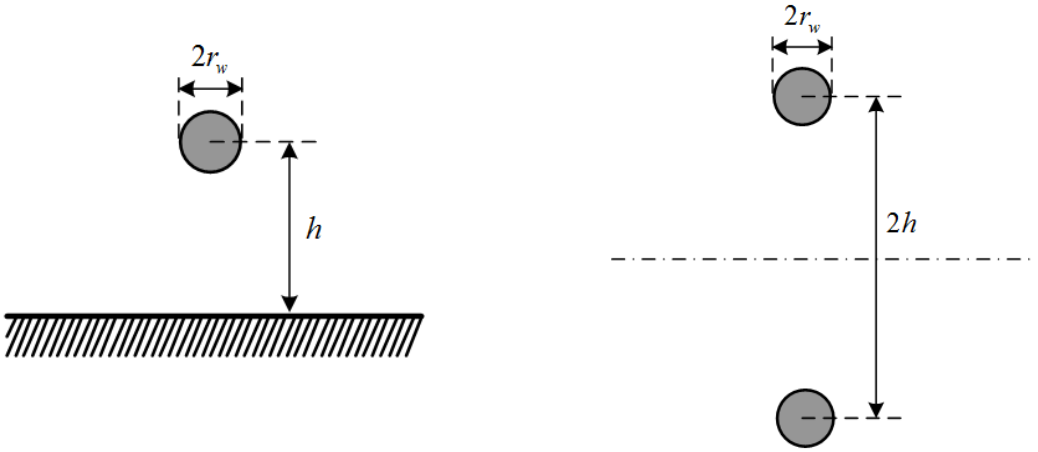

Figure 6.5.2: (a) Bare wire above ground plane. (b) Equivalent two-conductor transmission line.

The bare wire transmission line geometry is as shown in Figure 6.5.2. By method of images, the parameters of this configuration are thoroughly described by Paul [6.21], giving:

$$R_b = \frac{2\sqrt{\frac{\pi f \mu_0}{\sigma_{CU}}}}{\pi\left(1 - e^{-\frac{r_w}{\delta}}\right)\left(2r_w - \delta\left(1 - e^{-\frac{r_w}{\delta}}\right)\right)} \; ; \; \Omega/\text{m} \tag{6. 29}$$

$$L_b = \frac{\mu_0}{\pi}\cosh^{-1}\left(\frac{h}{r_w}\right) \; ; \; H/\text{m} \tag{6. 30}$$

$$C_b = \frac{\pi\varepsilon_0}{\cosh^{-1}\left(\frac{h}{r_w}\right)} \; ; \; F/\text{m} \tag{6. 31}$$

$$G_b = \frac{2\pi\sigma_{AIR}}{\cosh^{-1}\left(\frac{h}{r_w}\right)} \; ; \; S/\text{m} \tag{6. 32}$$

where f is the frequency of the transmitted signal, μ_0 is the permeability of air, ε_0 is the permittivity of air, δ is the skin depth, σ_{CU} is the copper conductivity and σ_{AIR} is air conductivity (≈ 0). The two equations (6.27) and (6.28) are solved simultaneously to determine the current in each segment on the transmission line, finally obtaining the reflection coefficients at the source and load in closed forms, given by:

$$I(z,\omega) = \frac{1 - T_L e^{-\gamma_b l} e^{2\gamma_b z}}{1 - T_S T_L e^{-\gamma_b l}} \frac{V_{th}}{Z_{th1} + Z_b} e^{-\gamma_b z} \tag{6. 33}$$

where

$$T_S = \frac{Z_{th1} - Z_b}{Z_{th1} + Z_b} \; ; \; T_L = \frac{Z_{th2} - Z_b}{Z_{th2} + Z_b} \tag{6. 34}$$

$$Z_{th1} = \frac{Z_G}{1 + j\omega C_{t1} Z_G} \; ; \; Z_{th2} = \frac{Z_L}{1 + j\omega C_{t2} Z_L} \tag{6. 35}$$

$$V_{th} = \frac{V_G}{1 + j\omega C_{t1} Z_L} \tag{6. 36}$$

$$\gamma_b = \sqrt{(R_b + j\omega L_b)(G_b + j\omega C_b)} \tag{6. 37}$$

$$Z_b = \sqrt{\frac{(R_b + j\omega L_b)}{(G_b + j\omega C_b)}} \tag{6. 38}$$

6.5.2 Single Coaxial Cable above Ground

To investigate the radiated fields from shielded coaxial cables, the bare wire in section 6.5.1 was replaced by a RG-58 coaxial cable. Based on the conventional shielded cable analysis method, Figure 6.5.3 gives the three-conductor system with reference directions and notation [6.23] and [6.25].

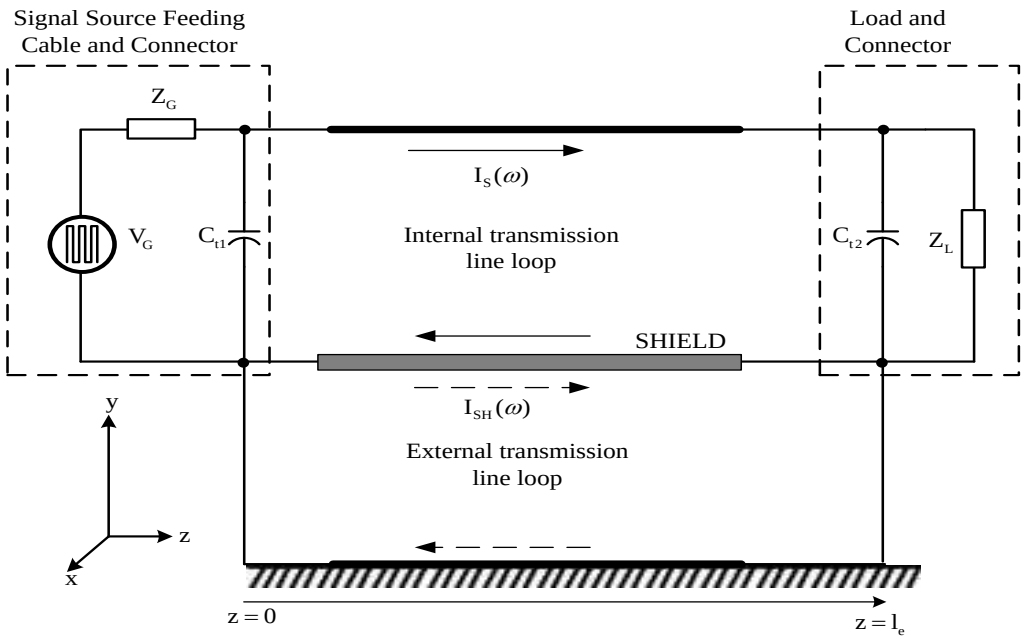

Figure 6.5.3: Shielded coaxial cable model for transmission line analysis

The whole system is interpreted as two transmission-line (TL) loops, where the internal TL loop represents the internal conductor of the coaxial cable, while the external TL loop represents the current return path between the coaxial braid and the ground. Adopting the two current notations shown in Figure 6.5.4 for the inner and outer system cable representation, the outer braid current flowing between the cable sheath and the ground plane can be treated as the radiated field excitation current.

(a) (b)

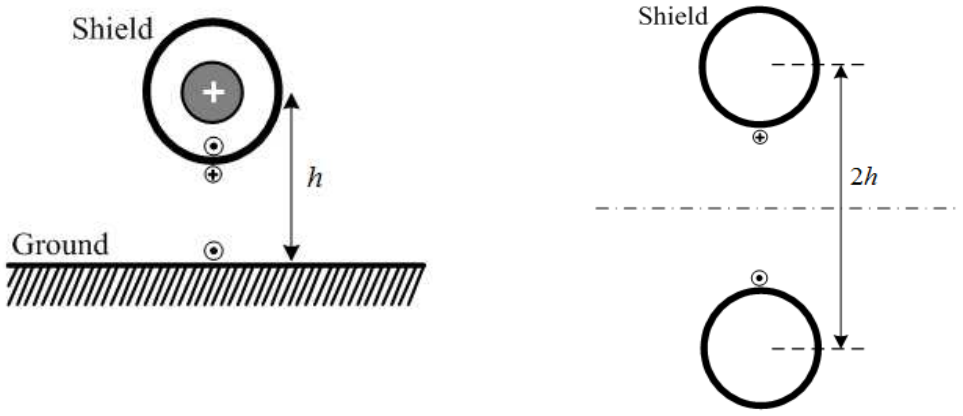

Figure 6.5.4: (a) Notation of the current in a shielded cable above ground. (b) Equivalent two-conductor transmission line for external current loop.

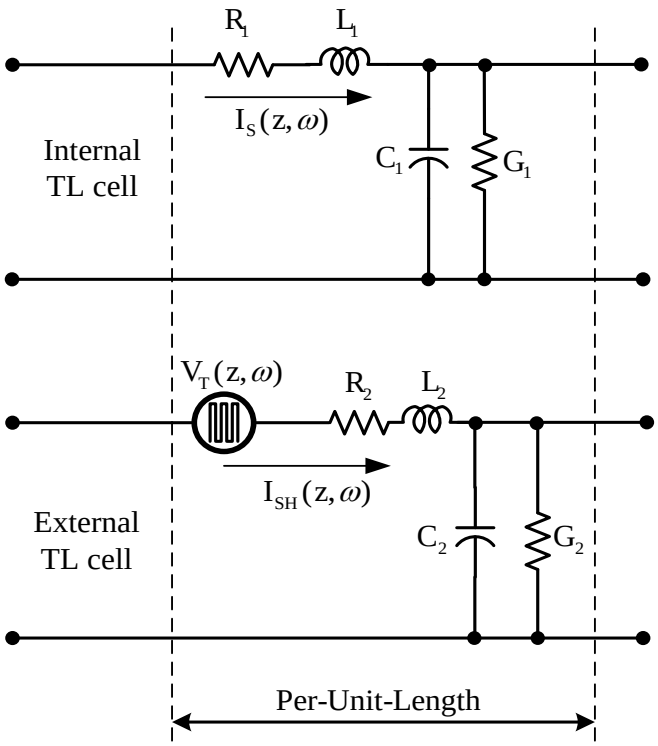

Figure 6.5.5: Equivalent transmission line circuit of Figure 6.5.3

Figure 6.5.5 shows a segment of the internal and external TL loops illustrated in Figure 6.5.3. The internal circuit of the coaxial cable can be also described by the frequency differential equations (6.27) and (6.28). Solve these two simultaneous equations (6.27) and (6.28) to determine the inner current of the core conductor:

$$I_S(z,\omega) = \frac{1 - T_L e^{-\gamma_1 l} e^{2\gamma_1 z}}{1 - T_S T_L e^{-\gamma_1 l}} \frac{V_{th}}{Z_{th} + Z_{C1}} e^{-\gamma_1 z} \tag{6. 39}$$

where

$$\gamma_1 = \sqrt{(R_1 + j\omega L_1)(G_1 + j\omega C_1)} \tag{6. 40}$$

$$Z_{C1} = \sqrt{\frac{(R_1 + j\omega L_1)}{(G_1 + j\omega C_1)}} \tag{6. 41}$$

The per-unit length parameters of the internal transmission line formed by the core conductor and the braided shield are given by:

$$R_1 = \frac{1}{2\pi}\left(\frac{1}{a}+\frac{1}{b}\right)\sqrt{\frac{\pi f \mu_0}{\sigma_{CU}}}\ ;\ \ \Omega/\mathrm{m} \tag{6. 42}$$

$$L_1 = \frac{\mu_0}{2\pi}\ln\left(\frac{b}{a}\right)\ ;\ \ H/\mathrm{m} \tag{6. 43}$$

$$C_1 = \frac{2\pi\varepsilon_0\varepsilon_r}{\ln\left(\frac{b}{a}\right)}\ ;\ \ F/\mathrm{m} \tag{6. 44}$$

$$G_1 = \frac{2\pi\sigma_r}{\ln\left(\frac{b}{a}\right)}\ ;\ \ S/\mathrm{m} \tag{6. 45}$$

where a is the core conductor radius, b is the radius under braid, ε_r is the permittivity of dielectric material, σ_r is the conductivity of dielectric material.

The transfer mechanism between the internal voltages and currents and the external voltages and currents is modelled by the transfer impedance, Z_T (See Chapter 2). Current flowing between the braid and the ground return is given by Sali [6.26] and [6.27]:

$$I_b(z,\omega) = k\cosh(\gamma_2 z) - \int_0^z \frac{1}{Z_{C2}}\sinh[\gamma_2(z-\xi)]V_T(z,\omega)d\xi \tag{6. 46}$$

where

$$V_T(z,\omega) = Z_T I_S(z,\omega) \tag{6. 47}$$

$$k = \frac{\int_0^l \cosh[\gamma_2(z-\xi)]V_T(z,\omega)\,d\xi}{Z_{C2}\sinh(\gamma_2 l)} \tag{6. 48}$$

$$\gamma_2 = \sqrt{(R_2+j\omega L_2)(G_2+j\omega C_2)} \tag{6. 49}$$

$$Z_{C2} = \sqrt{\frac{(R_2+j\omega L_2)}{(G_2+j\omega C_2)}} \tag{6. 50}$$

The per-unit length parameters of the external transmission line formed between the braided shield and ground plane are given by:

$$R_2 = \frac{1}{2\pi}\left(\frac{1}{b}\right)\sqrt{\frac{\pi f \mu_0}{\sigma_{CU}}}\ ;\ \ \Omega/\mathrm{m} \tag{6. 51}$$

$$L_2 = \frac{\mu_0}{2\pi}\ln\left(\frac{8h}{\pi D_m} + \frac{\pi D_m}{4h}\right)\ ;\ \ H/\mathrm{m} \tag{6. 52}$$

$$C_2 = \frac{2\pi\varepsilon_0}{\ln\left(\frac{8h}{\pi D_m} + \frac{\pi D_m}{4h}\right)}\ ;\ \ F/\mathrm{m} \tag{6. 53}$$

$$G_2 = \frac{2\pi\sigma_{CU}}{\ln\left(\frac{8h}{\pi D_m} + \frac{\pi D_m}{4h}\right)}\ ;\ \ S/\mathrm{m} \tag{6. 54}$$

6.6 Experimental Set Up

6.6.1 Frequency Domain (FD) Measurement

Significant research has been done to obtain the predicted radiated field from current carrying conductors [6.10], [6.12] and [6.15] – [6.17]. The radiated field measurement arrangement is illustrated in Figure 6.6.1. The radiation measurements were performed in a semi-anechoic chamber to reduce external interference reflections and improve experimental accuracy. The Device under Test (DUT) includes a single bare copper wire of 1.02m in length; or a RG-58 coaxial cable of 1.22m in length. The DUT is placed above a 2m×0.5m aluminium ground plane, where it is placed on the floor of the semi-anechoic chamber.

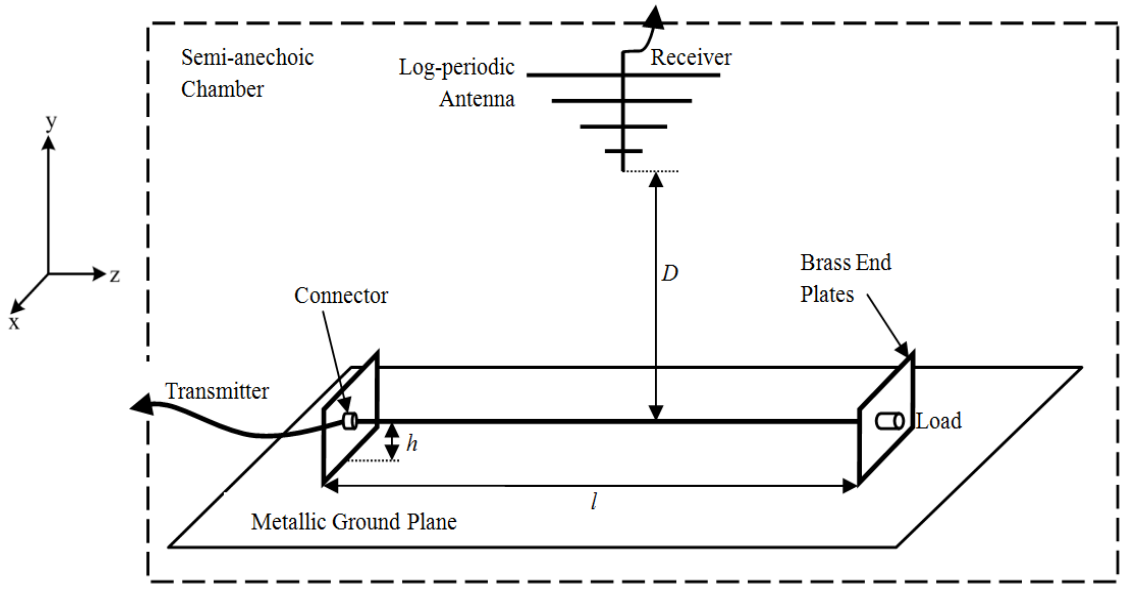

Figure 6.6.1: Radiated electromagnetic field measurement set up for the DUT over a finite ground plane

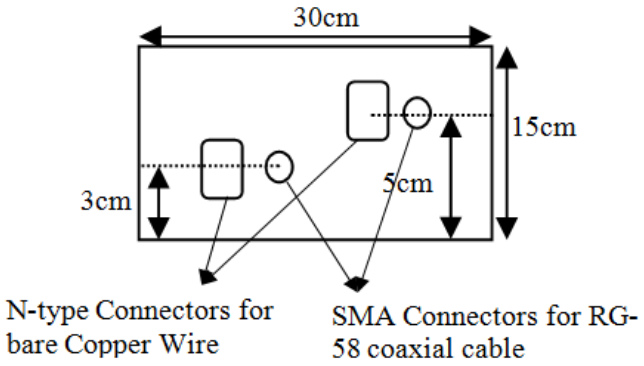

Figure 6.6.2: Details of the brass end plates used as support for the DUT for the radiated field measurement

Figure 6.6.2 shows the details of the two brass end plates with dimensions 15cm×30cm, which are used to support the DUT. Two N-type connectors are used as the connecting points for the copper wire at each end; whereas two SMA connectors are used for the RG-58 coaxial cable. One end of the DUT is connected to a source; and the other is attached to the load. A log periodic antenna Model 3146 is placed in the yz plane above the cable to measure the z-direction of the radiated electromagnetic field. The antenna is placed at 1.03m above the aluminium ground plane. Measurements were carried out under two different termination cases, ie: 50Ω load and an open circuit for both DUTs. Measurements were also performed with two different heights where h = 3cm; and h = 5cm.

A vector network analyzer (VNA) was used to provide the signal source and detection. The cable is connected to Port 1, where it acts as a transmitter, of the VNA and the log periodic antenna is in turn connected to Port 2 of the VNA, where it acts as a receiver. Through calibration or the use of the antenna factor, the VNA is set up to measure the radiated field emitted by the cable (S_{21}) in dB, with a power of 10dBm sweeping over a frequency range of 200MHz to 1GHz, sampling over 1601 points (see Appendix A). The instrument and test leads were calibrated with an electronic calibration module N4691-60003 (See Chapter 3).

6.7 Results

Simulation was performed for both cables, both in the frequency and time domain. The cell dimension was chosen to be 0.01m for both cables. The copper wire is 102 segments long while the RG-58 coaxial cable is 122 segments long. Both the cables are excited by a source Gaussian pulse, in series with a 50Ω resistance. The radiated field for both the cables, E_{rad}, can be calculated as:

$$E_{rad} = 20\log_{10}\left|\frac{\widetilde{V_{V0}}}{\widetilde{V_S}/_2}\right| + 107\ ;\ dB\mu V/\mathrm{m} \qquad (6.55)$$

where the accent ~ denotes Fourier Transformed quantities.

6.7.1 Bare Wire above Ground

Figure 6.7.1 shows the comparison between the predicted and measured current (see Appendix B) while Figure 6.7.2 shows the comparison between the predicted and measured radiated field, for a bare wire above ground at height, h = 5cm, for both cases of an open circuit and 50Ω termination, for both the frequency domain and TLM models. Figure 6.7.3 shows the comparison between predicted and measured radiated field at a height of h = 3cm.

(a)

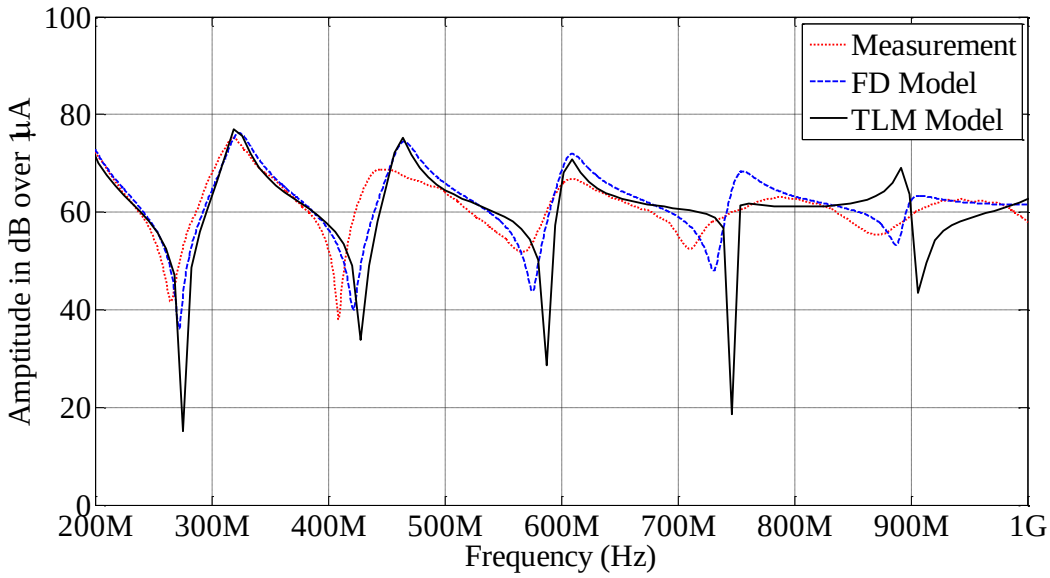

(b)

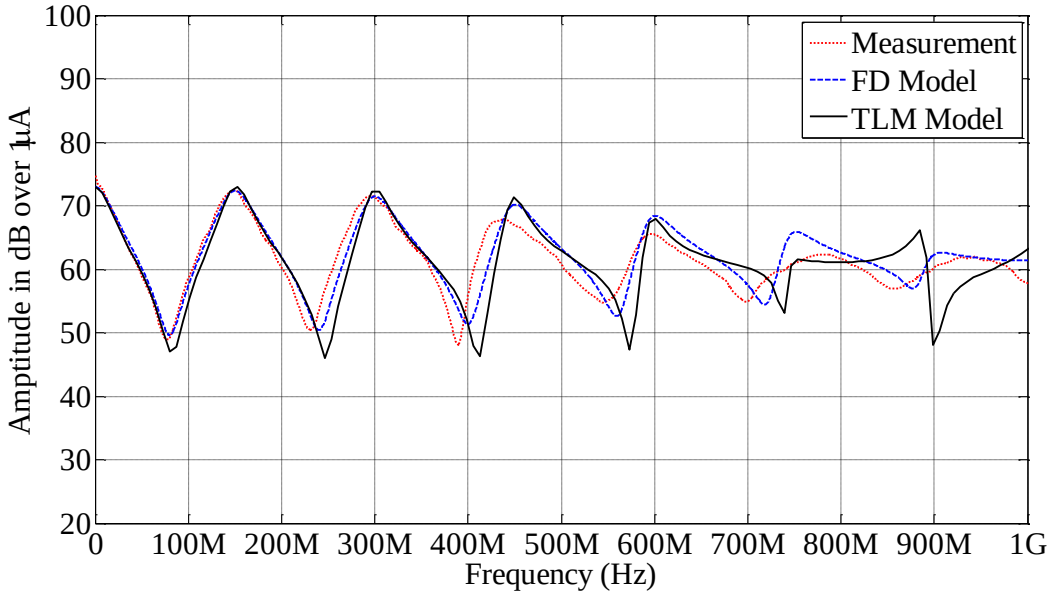

Figure 6.7.1: Comparison of current for a bare wire over ground, h = 5cm, measured position z = 0.1m. *(a) Open circuit termination. (b) 50Ω termination.*

(a)

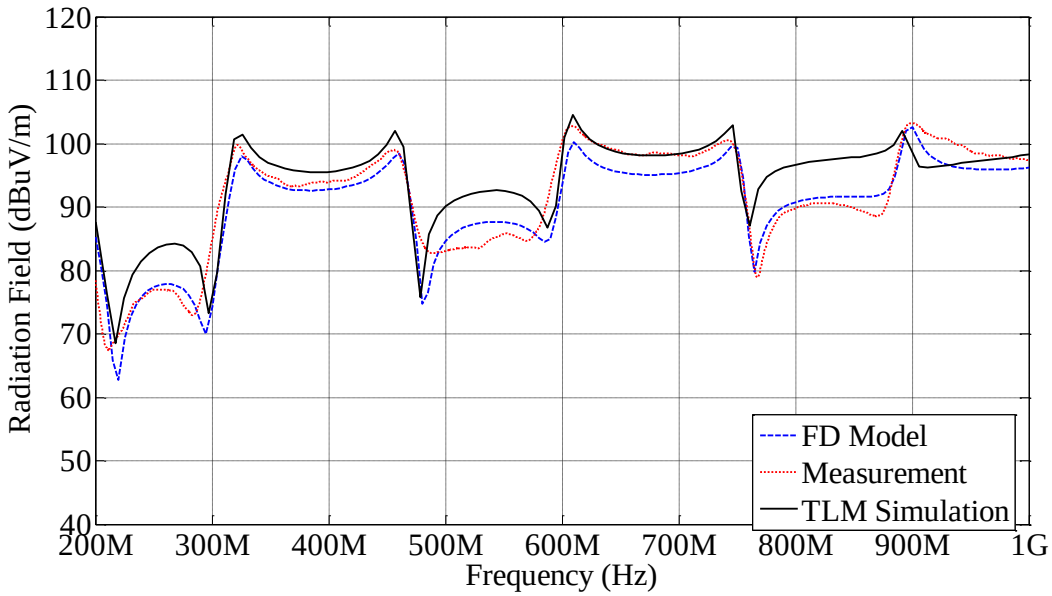

(b)

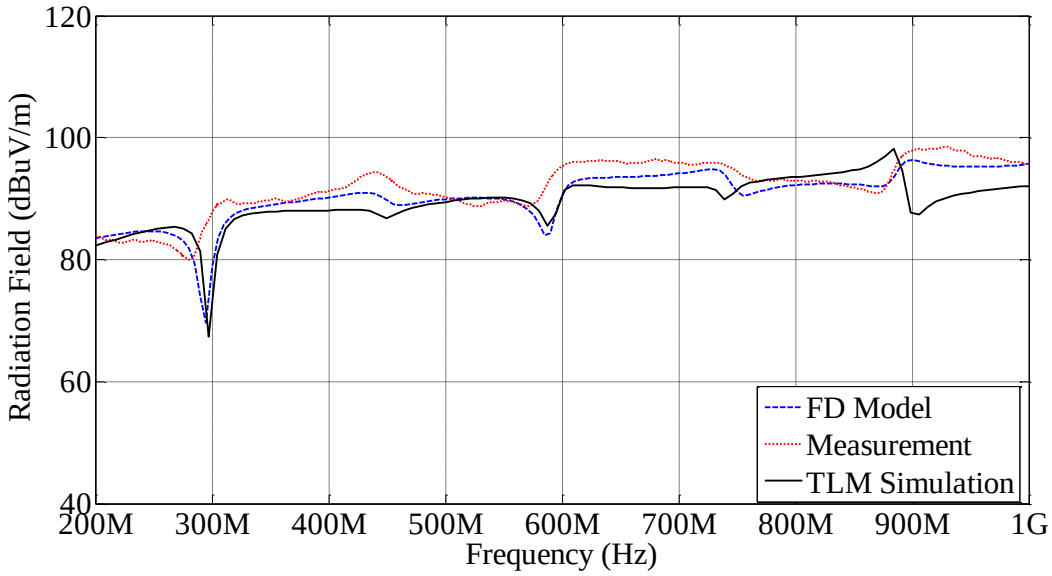

Figure 6.7.2: Comparison of radiated field for a bare wire over ground, h = 5cm. (a) *Open circuit termination. (b) 50Ω termination.*

(a)

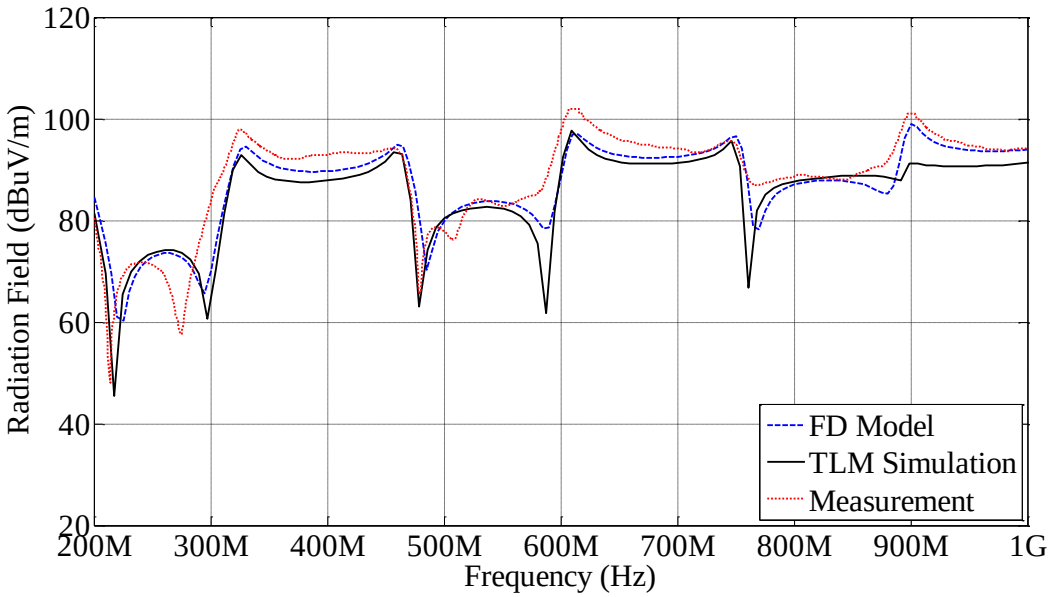

(b)

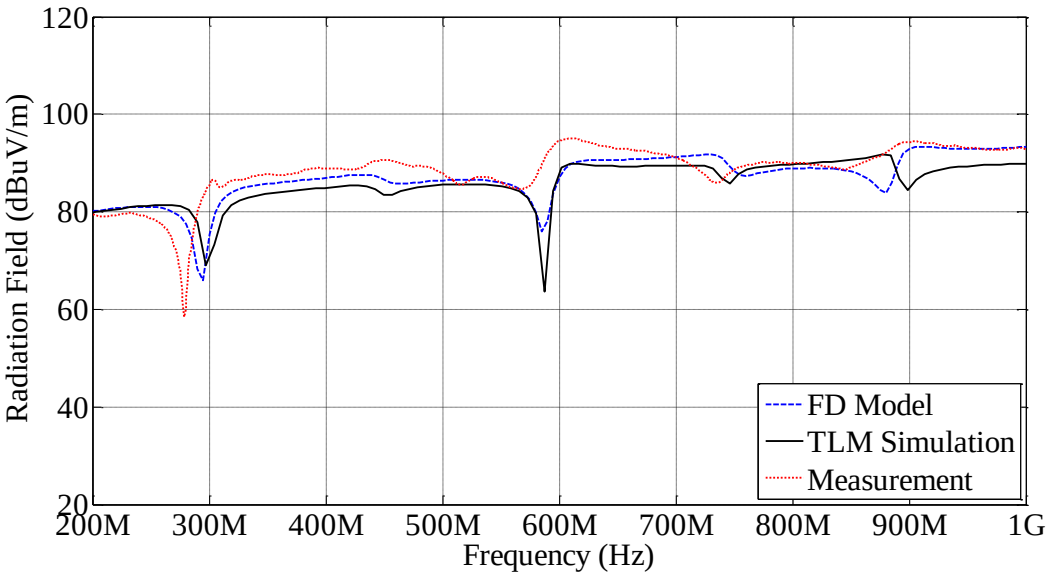

Figure 6.7.3: Comparison of radiated field for a bare wire over ground, h = 3cm. (a) *Open circuit termination. (b) 50Ω termination.*

6.7.2 RG-58 Coaxial Cable above Ground

In order to validate the accuracy of the TLM model, the predicted radiated field is presented in the frequency domain by Fourier transforming the time domain quantities, given in (6.26). Figure 6.7.4 shows the comparison between the predicted and measured current (see Appendix B) while Figure 6.7.5 shows the comparison between the predicted and measured radiated field, for a RG-58 coaxial cable above ground at height, h = 5cm, for both cases of an open circuit and 50Ω termination, for both the frequency domain and TLM models. Figure 6.7.6 shows the comparison between predicted and measured radiated field with a height of h = 3cm.

(a)

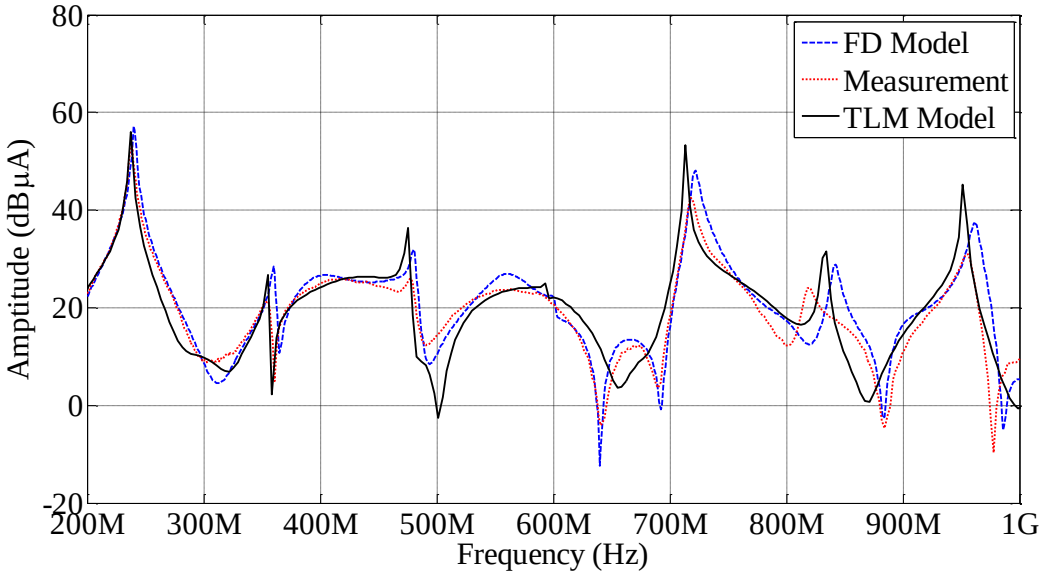

(b)

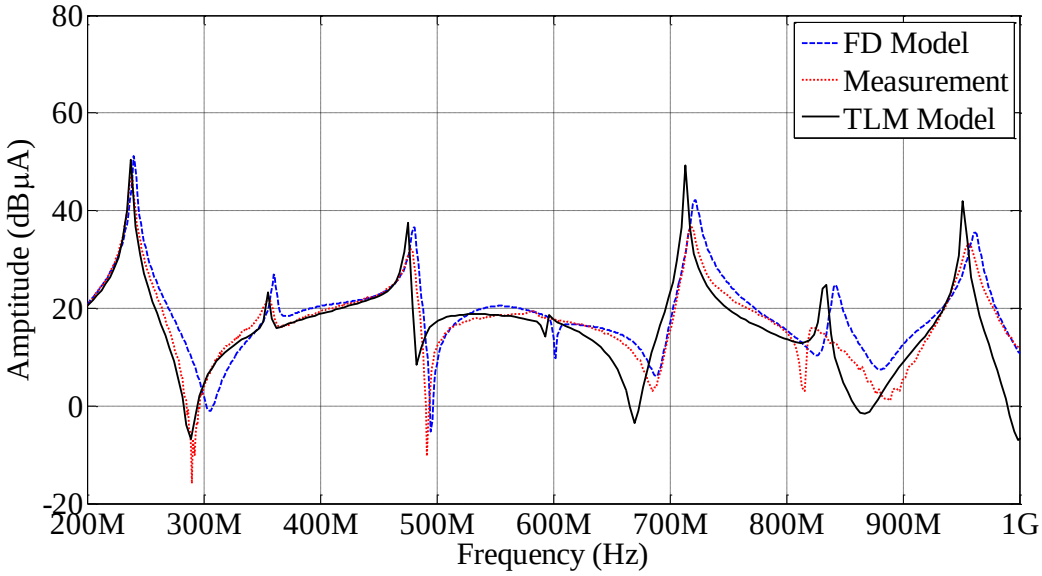

Figure 6.7.4: Comparison of current for a RG-58 coaxial cable over ground, h = 5cm, measured position z = 0.1m. *(a) Open circuit termination. (b) 50Ω termination.*

(a)

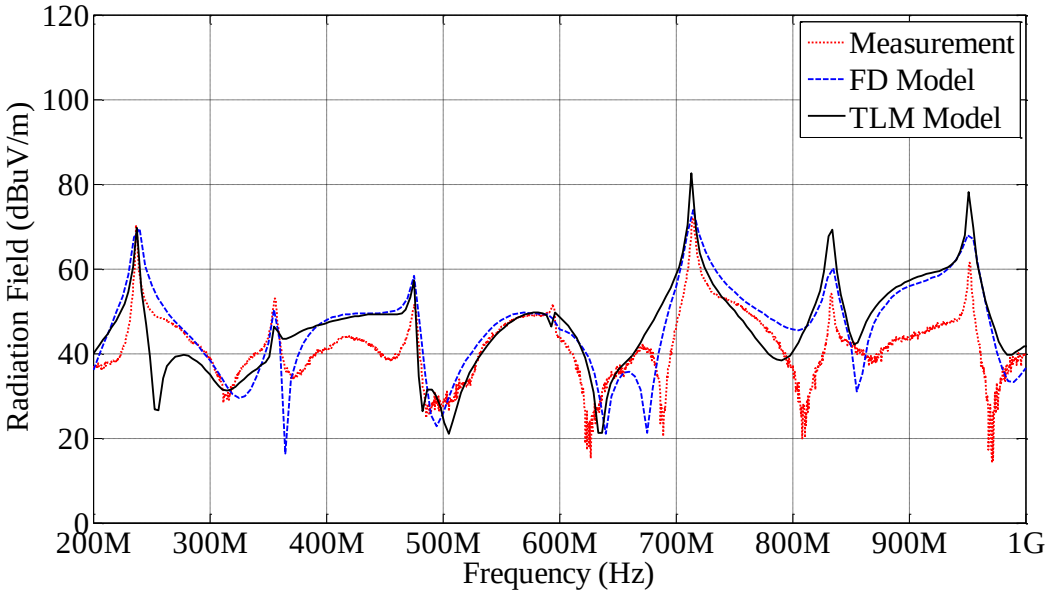

(b)

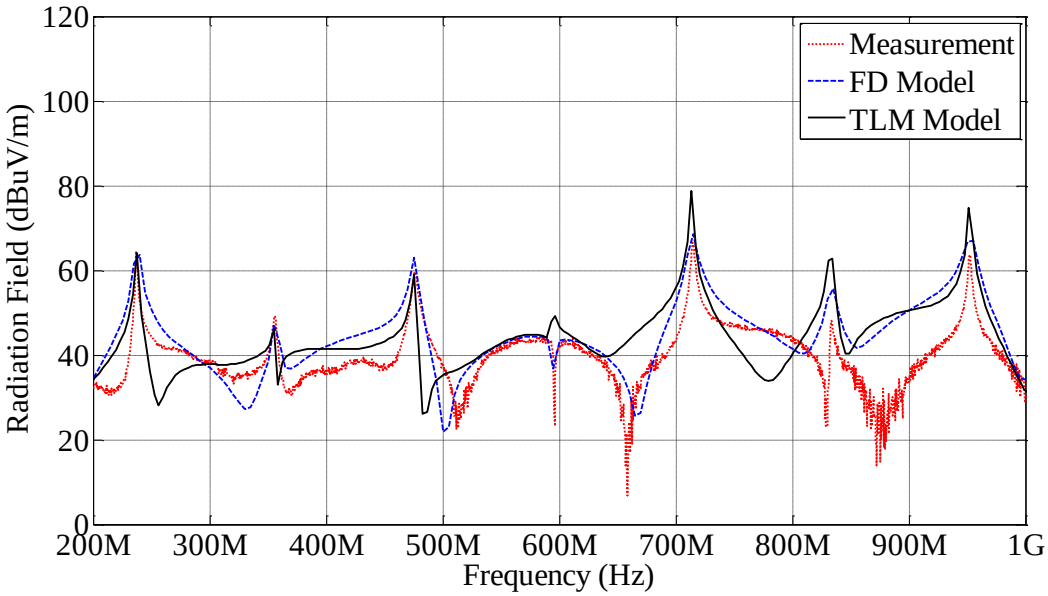

Figure 6.7.5: Comparison of radiated field for a RG-58 coaxial cable over ground, h = *5cm. (a) Open circuit termination. (b) 50Ω termination.*

(a)

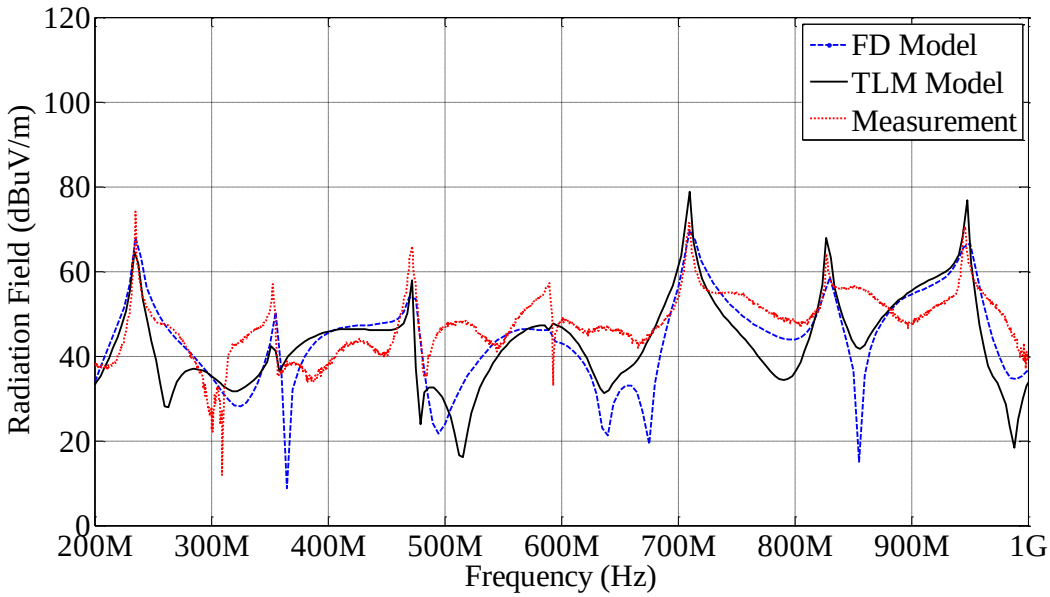

(b)

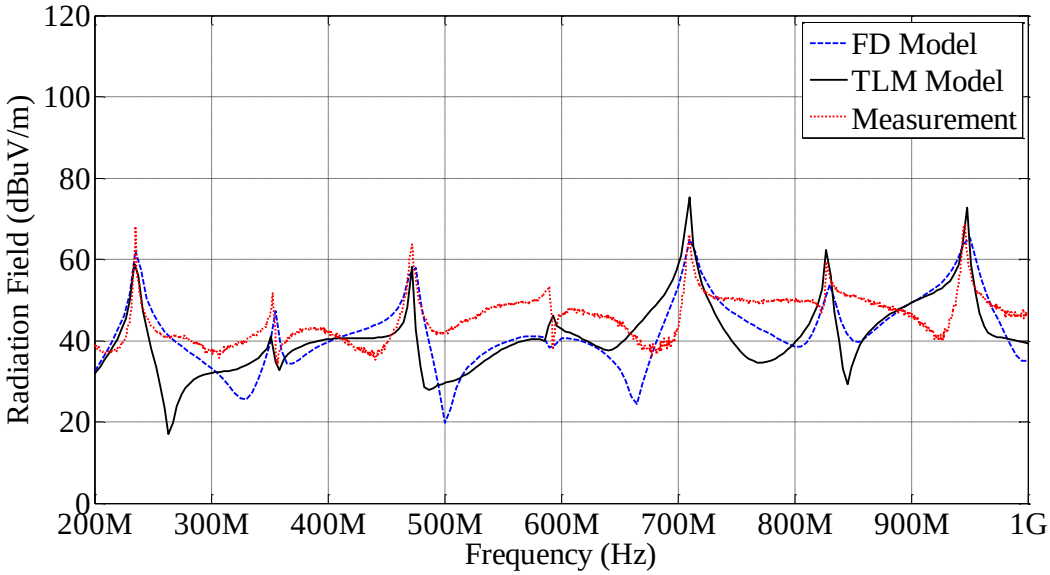

Figure 6.7.6: Comparison of radiated field for a bare wire over ground, h = 3cm. (a) *Open circuit termination. (b) 50Ω termination.*

Figures 6.7.1 and 6.7.4 compares between the calculated current spectra and measured results using the current probe for both the bare wire and coaxial cable above ground, respectively. Both the open load and 50Ω resistive load results show good agreement between the simulation models and measurement. Meanwhile, Figures 6.7.2 and 6.7.3 present the radiated field comparison of calculated results and

measured results from the bare wire while Figures 6.7.5 and 6.7.6 show the radiated field comparison of calculated results and measured results from the RG-58 coaxial cable. Notice that both the open circuit results and 50Ω resistive load results show relatively good agreement between the measured and simulated results, with respect to both the several resonant frequencies and the peak values.

It is observed that the radiated field prediction for a bare copper wire is in better agreement as compared to the RG-58 coaxial cable. This may be due to the inaccuracies in the modelling of the coaxial braid current. Nonetheless, the peak resonant frequencies can be clearly captured in both cases. The difference in some of the peaks of the resonant frequencies may be due to the inaccurate placing of the antenna position. The antenna is placed above and in the middle of the cable, as seen in Figure 6.6.1. Any uncertainty in the position of the antenna during measurement procedures causes significant discrepancy in the radiated field results.

Notice that when radiated field measurements were performed, the brass end plates in section 3.2.1 are replaced with one with smaller dimensions, as presented in section 6.6.1. The reason to this is that for larger connector plates, the larger the amount of radiated field from the connector plates. As illustrated in Figure 6.7.7, if the original connector plates from section 3.2.1 are used, the top of the connector plates becomes isolated (shown in red). Thus, it is assumed to be a monopole, with its excess radiating field being picked up by the antenna, causing inaccurate readings.

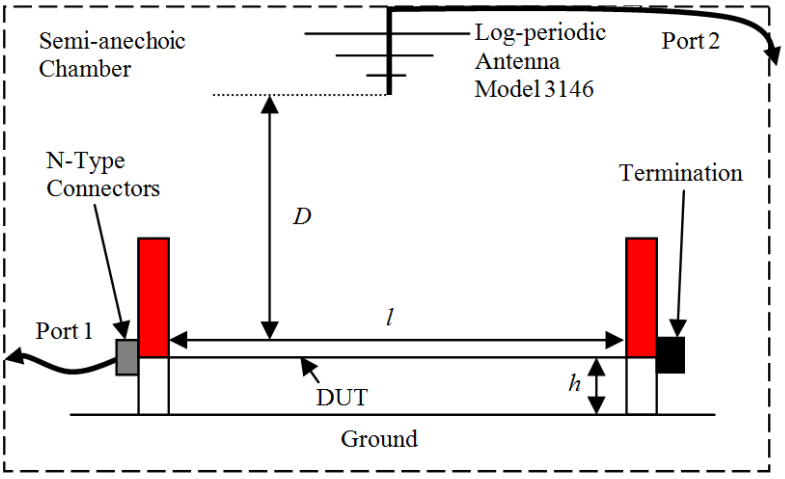

Figure 6.7.7: The monopole effect causing inaccurate radiated field measurement if a larger brass end plate is used.

Another important problem that may require future investigation would be the brass end plates. The current flowing through the end plates is too complicated to model in a 1D TLM model, which may explain the slight difference in pattern in the radiated field results.

6.8 Conclusions

In this chapter, a modelling technique has been presented to evaluate the predicted radiated electromagnetic fields from interconnect cables, known as the Hertzian dipole technique. Based on the Hertzian dipole theory, the radiating cable comprise of a large number of short dipoles. Subsequently, the radiated field emitted by the cable is the summation of all current contributions from each of the dipole. Two transmission line modelling techniques have been implemented in the prediction of the radiated field, ie: time domain model (TLM), and frequency domain analysis. Two types of interconnects are investigated, ie: bare copper wire and the RG-58 coaxial cable. In both cases, the transient current derived from the numerical model is used to calculate the radiated field. Experimental verifications were performed to validate the radiated field prediction accuracy of both the time and frequency domain models. Comparison between the predicted and measured electromagnetic fields radiated by both types of interconnects show very good agreement within the validity of the modelling assumptions and measurement uncertainties.

References

[6.1] Christopoulos, C., Principles and Techniques of Electromagnetic Compatibility, second edition, CRC Press, Taylor & Francis Group, 2007.

[6.2] Jasper Goedbloed, “Electromagnetic compatibility,” Philips Research Laboratories, Eindhoven, Prentice Hall International (UK) Ltd, 1992.

[6.3] John D. Kraus, Electromagnetics, Fourth Edition, McGraw-Hill, Inc, 1991.

[6.4] Clayton R. Paul, Introduction to Electromagnetic Compatibility, Wiley Series in Microwave and Optical Engineering, 1992.

[6.5] N. N. Rao, Elements of Engineering Electromagnetics, 3rd Edition, Englewood Cliffs, NJ: Prentice Hall, 1992.

[6.6] A. Cozza and B. Denoulin, "Close-form expressions for the total power radiated by an electrically long multiconductor line," IEEE Trans. on EMC, vol. 51, no. 1, Feb. 2009, pp. 119 – 130.

[6.7] E. T. Pereira, D. W. P. Thomas, A. F. Howe and C. Christopoulos, "Computation of electromagnetic switching transients in a substation," IEEE Intl. Conference on Computation in Electromagnetics, 1991, pp. 331-334.

[6.8] R. S. Shi, A. Darcherif, and J. C. Sabonnadiere, "Computation of transient electromagnetic fields radiated by a transmission line: an exact model," IEEE Trans. Magnetics, vol. 31, no. 4, July 1995, pp. 2423-2431.

[6.9] C. R. Paul and D. R. Bush, "A comparison of the contribution of common-mode and differential-mode currents in radiated emissions," IEEE Trans. Electromagn. Compat., vol. 31, no. 2, May 1989, pp. 189-193.

[6.10] S. K. Das, W. T. Smith, C. R. Paul, "Radiated Emissions of Interconnect Cables," IEEE Intl. Symposium on EMC, 1992, pp 423-427.

[6.11] Marcos Rubinstein and Martin A. Uman, "Methods for calculating the electromagnetic fields from a known source distribution: application to lightning," IEEE Trans. on EMC, vol. 31, no. 2, May 1989, pp. 183-189.

[6.12] David W. P. Thomas, Christos Christopoulos and Elisete T. Pereira, "Calculation on radiated electromagnetic fields from cables using time-domain simulation," IEEE Trans. on EMC, vol. 36, no. 3, August 1994, pp. 201-205.

[6.13] B. U. Musa, W. H. Siew, and M. D. Judd, "Computation of transient electromagnetic fields due to switching in high-voltage substations," IEEE Trans. Power Delivery, vol. 25, no. 2, April 2010, pp. 1154-1161.

[6.14] Y. Kami and R. Sato, “Analysis of radiation characteristics of a finite-length transmission line using a circuit-concept approach,” IEEE Trans. Electromagn. Compat., vol. 30, no. 2, May 1988, pp. 114-121.

[6.15] Ugo Reggiani, Antonio Massarini, Leonardo Sandrolini, Marco Ciccotti, Xilei Liu, David W. P. Thomas and Christos Christopoulos, “Experimental verification of predicted electromagnetic fields radiated by straight interconnect cables carrying high-frequency currents,” IEEE Bologna Power Tech Conference, June 2003.

[6.16] X. L. Liu, D. W. P. Thomas and C. Christopoulos, “Prediction and experimental verification of radiated fields from interconnect cables due to common-mode currents,” EMC Europe 2004 International symposium on electromagnetic compatibility, Eindhoven, the Netherlands, Sept. 06-10 2004, pp. 590-594.

[6.17] C. R. Paul and D. R. Bush, “Radiated fields of interconnect cables,” Proc. Intl. Conf. on EMC, IERE, London, UK, Sept 1984.

[6.18] C. A. Balanis, Antenna Theory: Analysis and Design. Hoboken, NJ: John Wiley & Sons, 2005, pp. 151–154.

[6.19] Y. Tang, H. Chen, H. Wang, F.Dai, and S. Jiang,”Transmission line models used in travelling wave studies,” IEEE Proc. in Transmission Distribution Conf., vol. 2, 1999, pp. 797 – 803.

[6.20] A. Cozza, F. Canavero and B. Denoulin, “High-frequency extension for the transmission-line theory for an open line,” IEEE Proc. Intl. Symp. in EMC, vol. 1, March 2004, pp. 165 – 170.

[6.21] Clayton R. Paul, Analysis of Multiconductor Transmission Lines, Jogn Wiley & Sons, Inc, 1994.

[6.22] M. M. Al-Asadi, A. P. Duffy, A. J. Willis, K. Hodge, and T. M. Benson, “A simple formula for calculating the frequency-dependent resistance of a round wire,” Microwave and Optical Technology Letters, vol. 19, no. 2, Oct. 1998. pp. 84-87.

[6.23] S. Caniggia and F. Maradei, "SPICE-like models for the analysis of the conducted and radiated immunity of shielded cables," IEEE Trans. Electromagn. Compat., vol. 46, no. 4, Nov. 2004,pp. 606-616.

[6.24] T. Kley, "Optimized single-braided cable shields," IEEE Trans. Electromagn. Compat., vol. 35, no. 1, pp. 1-9, Feb. 1993.

[6.25] R. Tiedemann, "Current flow in coaxial braided cable shields," IEEE Trans. Electromagn. Compat., vol. 45, no. 3, Aug. 2003, pp. 531-537.

[6.26] S. Sali, "Response of externally excited coaxial cables with wire braided shields," IEE Proc. Sci. Meas. Technol., vol. 141, no. 4, pp. 266-272, July 1994.

[6.27] S. Sali, "A circuit-based approach for crosstalk between coaxial cables with optimum braided shields," IEEE Transactions in EMC, vol.35, no. 2, May 1993, pp. 300 – 311.

CHAPTER 7

CONCLUSIONS AND FUTURE WORK

7.1 Conclusions

The main objective of this thesis is the modelling of interconnects, mainly coaxial cables and multiconductor lines. It involves the time domain numerical simulation and prediction of crosstalk between two coaxial cables in free space and over a perfect conducting ground plane; as well as numerical time and frequency domain radiated field models to predict radiated field emission from a single bare copper wire and a single coaxial cable above a perfectly conducting ground plane. The research work includes both measurements and modelling techniques (based on the TLM method). For the experimental verification of crosstalk, the degree of coupling is observed at the near end of the adjacent (victim) cable; for which numerical solution is developed and compared with the measurements. The near-field radiated field measurement is obtained from a log-periodic antenna. A method of predicting the resultant electromagnetic field (Hertzian dipole technique) using simulated data from the time (TLM method) and frequency domains is employed and results are compared against measurements. The conclusions of this research can be summarised as below.

In Chapter 2, theoretical knowledge of coaxial cable coupling is presented. In this work, the cable coupling due to transfer impedance alone is considered as the effect of transfer admittance is negligible for non-optimised cable braids [7.1]. A comparison is made between three different transfer impedance modelling techniques (Tyni, Vance and Kley models) of the coaxial cable, where the model with best accuracy proposed by Kley is chosen for this work. The coupling due to the transfer impedance occurs when the cables are laid in parallel along a common path. It is found that the nature of the terminations strongly affects the degree of coupling at high frequencies due to the stray reactance they introduce. If the cables are terminated at a common equipment cabinet, the stray reactance is mostly inductive. However, if the cables are connected to electrically isolated units, the stray reactance will be primarily capacitive.

The coupling path between the driven source cable and the victim cable is via the tertiary circuit, which serves as a conduit transferring EMI to the victim circuit through the currents in the braided shield. The two configurations investigated in this work were the coupling between two coaxial cables in free space and the coupling between two coaxial cables over a perfect conducting ground plane. By assuming that both cables are identical; and the metallic ground plane is perfect and infinitely large, the tertiary circuit parameters were correspondingly derived in [7.2] for the two configurations investigated.

In Chapter 3, the crosstalk experiment together with the measurement configurations are presented. The configuration involves coupling measurements between two RG-58 coaxial cables in free space and over a metallic ground plane; with results obtained in both the time and frequency domains. Various measurement results were taken by varying the separation between the two cables and the height between the cables and the metallic ground plane. The external impedance of the connector plates were also measured using a Time Domain Reflectometer (TDR) to obtain an approximation of the tertiary circuit termination's stray inductance since the cables are placed in parallel along common brass connector plates, as presented in Chapter 2. Measurements were taken for both modes; the differential mode, formed by the external surfaces of the two cable braids as well as the connector plates; and the common mode, formed by the return path between the cable braid and the metallic ground plane.

In Chapter 4, the numerical modelling technique based on the 1D Transmission Line Modelling (TLM) method was introduced. The 1D TLM model can be divided into three main tasks, starting with the initial problem definition and followed by the calculation of voltages and currents, which propagate by "scatter" and "connection". In implementing this method for crosstalk simulation, several factors are considered such as time synchronisation of all three circuits (source, tertiary and victim circuits); and also numerically modelling the cable braid's surface transfer impedance using two techniques, the stub inductance model and digital filter model.

Propagation of the tertiary circuit is in free space while both the source and victim coaxial lines have polymer insulation. For ease of computation, it is necessary for the time and space steps to be the same for all three circuits. A time synchronisation

method is implemented in the 1D TLM model by an addition of a capacitive stub into both the source and victim coaxial lines to adjust the propagation velocities in all three circuits.

The coupling path from one circuit to another is numerically modelled through the frequency dependent models of the surface transfer impedance. The surface transfer impedance is approximated by a simple L-R circuit where the inductance can be represented as a stub for modelling it in the time domain. As for the alternative digital filter model, the inductance is represented using the bilinear z-transform method. The bilinear z-transform is a first-order approximation of the differential equations that maps the z-(digital) plane to the s-(analog) plane. The inductance of the transfer impedance is derived in the s-plane using the z-plane representation before solving for the entire transfer impedance function. Nonetheless, both stub inductance and digital filter models agree exactly with each other.

The crosstalk of two conductors in free space is governed by the differential mode current. However, when the two conductors are placed over a conducting ground plane, the crosstalk is governed by both the differential and common modes. In this case, a multimode model is developed and implemented using 1D TLM model. The modal components and the corresponding propagation velocities for each mode were initially introduced and obtained. The system is then separated into external coupling regions, mode conversion and mode propagation regions. Coupling path was attained by converting the modal quantities, combined with the coupling source terms, into line parameters; each propagation mode (differential and common modes) of the coupling path was represented by their corresponding modal impedances. The reconversion of the adjacent victim cable line parameters to modal quantities was finally implemented to allow propagation to the next coupling region.

It can be concluded that the numerical model of the system is successfully modelled using the TLM technique. Predictions show that the characterisation of the braid's transfer impedance is insufficient to predict accurate results when compared against measurements. The results also successfully compared the effects of including the brass end plates into the system and can finally be concluded that the peaks of the resonant frequencies correspond to the resonant frequencies in the tertiary circuit.

In Chapter 5, the analysis of the skin depth effect is included as a loss factor in the characterisation of the tertiary circuit (braided shield). Skin depth effects are usually modelled in the frequency domain. Time domain skin depth models comprise of branches of R-L lumped circuits. Most proposed time domain models have a relatively large number of R-L branches, resulting in slow computation. The two most suitable models are due to (Kim et al. [7.4] and Bidyut et al. [7.3]). The two models were investigated and compared; and both agree very well with each other.

The model proposed by Bidyut et al. [7.3] consists of a six branch ladder circuit and is convenient to implement at low frequencies. As frequency increases, the number of branches required increases, resulting in slow computation. The model proposed by Kim et al. [7.4] consists of a compact four ladder circuit and can be implemented over any desired frequency range using a matrix model.

It can be concluded that good agreement is obtained for both the crosstalk configurations; two coaxial cables in free space as well as over a perfectly conducting ground plane; presented in both time and frequency domains when compared against the measurement results. Predictions include a complete characterisation of the tertiary circuit through the braid's transfer impedance, the impedance at the connector plates, and skin depth effect.

In Chapter 6, a modelling technique has been presented to predict the radiated electromagnetic fields from interconnect cables, known as the Hertzian dipole technique. Based on the Hertzian dipole theory, the radiating cable is split up in a large number of short dipoles. The total radiated field emitted by the cable is the summation of all current contributions from each of the dipoles. Two transmission line modelling techniques have been implemented in the prediction of the radiated field, ie: time domain model based on TLM, and frequency domain analysis. Two types of interconnect are investigated, ie: bare copper wire and the RG-58 coaxial cable. In both cases, the transient current derived from the numerical model is used to calculate the radiated field. Experimental verifications were performed to validate the radiated field prediction accuracy of both the time and frequency domain models.

Radiating sections of the TLM equivalent circuit are assumed to behave as ideal radiating antennas with a transient current given from a time-domain simulation of the circuit. In both cases, the transient current derived from the numerical model is used to

calculate the radiated field. In this study, radiated field measurements obtained using an antenna agree with the radiation calculated using the transient currents obtained from the TLM numerical model. The approach is general and it enables solution of practical interconnect configurations.

It was found that the radiated field prediction for a bare copper wire was in better agreement with measurements compared to the RG-58 coaxial cable. This may be due to inaccuracies in the modelling of the coaxial braid current. Another factor governing the slight discrepancy in the results may also be due to the uncertainty in the position of the antenna during measurement procedures. Nonetheless, comparison between the predicted and measured electromagnetic fields radiated for both types of interconnects show very good agreement with measurements within the validity of the modelling assumptions and measurement uncertainties.

It can be concluded that good agreement is obtained for both the configurations, in both time and frequency domains when compared to the measurements. It was shown that the amplitude and resonance frequencies of crosstalk are dependent on the geometry of the tertiary circuit. In most situations, the cable geometry is poorly defined in practical situations so therefore resonant peaks and frequencies may not match accurately with the numerical solutions. Comparison between measured and numerical solution show that the TLM solution successfully models the coupling. However, it is observed that the coupling prediction become less accurate at higher frequencies. This is due to that factors such as radiation loss etc. were not included in the numerical model. This study proved that when the skin depth effect and the excess impedance at the connector plates are omitted from the tertiary circuit, noticeable discrepancies are observed between measurements and the TLM solution. A further advantage of this study is that in addition to the importance of crosstalk to EMC studies, the presentation of results in the time domain is also valuable for Signal Integrity studies where the exact shape of the waveforms is important for the correct operation of fast digital circuits.

7.2 Future Works

The factors affecting the degree coupling in multiconductor lines are clearly identified and modelled in the current research. This work can be regarded as a basis to develop intermediate design tools for EMC problems from multiconductor lines. Some future work is proposed in this section.

The equivalent circuits formulas developed in this work may be further improved to solve more complex and realistic systems and subsequently to obtain more accurate results; more specifically the following aspects are worth considering:

7.2.1 The Effects of Transfer Admittance at High Frequencies

The concept of transfer admittance of a cable braid is briefly discussed in Chapter 2 (see section 2.2). In addition to coupling produced by penetration of the magnetic field through apertures in the shield (transfer impedance), there is also electric coupling produced by an electric field, which would otherwise terminate on the outer surface of the shield, penetrating through the holes in the shield and terminating on the inner conductors [7.5]. Coupling of this form is represented by transfer admittance, Y_T, between the return path for the shield current and the inner conductors as illustrated in Figure 7.2.1.

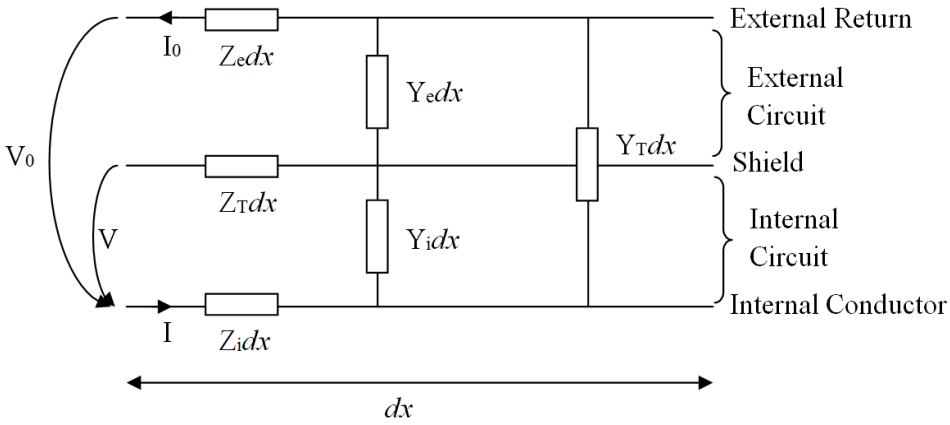

Figure 7.2.1: Coupled line showing transfer impedance Z_T and transfer admittance Y_T of a segment, dx, of a transmission line [7.5]

where Z_i and Y_i denote the impedance and admittance of the internal conductor respectively; Z_e and Y_e denote the impedance and admittance of the external circuit (tertiary circuit) respectively; V_0 and I_0 denote the voltage and current between the external return from the source cable and the internal conductor respectively; and V and I denote the voltage and current between the shield and the internal conductor respectively.

As discussed in Chapter 2 (see section 2.3), the effects of transfer admittance, Y_T, is negligible in non-optimised cable braids [7.6]. However, this investigation is only proven for frequencies up to 1GHz. The relevance of the transfer admittance should be included in the model to observe its effects at frequencies above 1GHz. Investigation should also be carried out to compare the relevance of transfer admittance in optimised and standard cable braids at high frequencies.

7.2.2 High Frequency Time Domain Crosstalk

In current research, the time domain crosstalk can only be measured at low frequencies due to the Time Domain Oscilloscope (TDO) and Pulse Arbitrary Function Generator (PAFG) limitations. It would be interesting to observe the crosstalk pattern in the time domain when a square wave of high frequency, sufficient to cover at least two resonant frequency peaks in the desired range of frequencies, is applied.

7.2.3 Three-Dimensional TLM Model

Work in this thesis is based on using the 1D TLM method. To fully study the current flow patterns in open waveguide, 3D TLM model is required [7.8]. This is essential especially in modelling the brass connector plates. A 1D TLM model cannot fully model the current in the end plates. The reason is illustrated in Figure 7.2.2. This figure shows that current, I_t, is non-uniformly distributed as it travels through the brass end plates. This in turn affects the termination inductance which will vary with frequency.

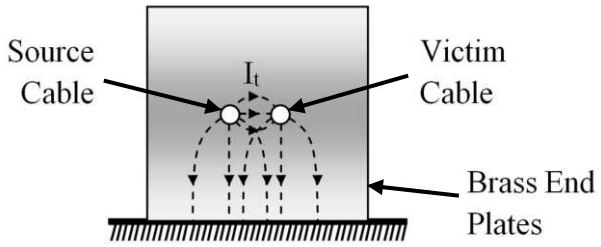

Figure 7.2.2: Complex current flow in the tertiary circuit which requires 3D TLM

References

[7.1] D. W. P. Thomas, C. Christopoulos, F. Leferink and H. Bergsma, "Practical measure of cable coupling," Intl. Conf. on Electromagnetics in Advanced Applications, September 2009, pp. 803 – 806.

[7.2] Christopoulos, C., Principles and Techniques of Electromagnetic Compatibility, second edition, CRC Press, Taylor & Francis Group, 2007.

[7.3] Bidyut K. Sen and Richard L. Wheeler, "Skin effect models for transmission line structures using generic SPICE circuit simulators," IEEE 7th Topical Meeting, 1998.

[7.4] S. Kim and D. P. Neikirk, "Compact equivalent circuit model for the skin effect," IEEE Proceedings, pp. 1815 – 1818.

[7.5] Edward F. Vance, "Shielding effectiveness of braided-wire shields," IEEE Transactions on EMC, vol. EMC-17, no. 2, May 1975, pp. 71 – 77.

[7.6] S. Sali, "Screening performances of trixial cables with optimum braided shields," IEEE 7th Intl. Conference on EMC, Aug. 1990, pp. 24 – 29.

[7.7] R. S. Shi and A. Darcherif, "Computation of transient electromagnetic fields radiated by a transmission line: an exact model," IEEE TEMC, vol.31, no. 4, July 1995.

[7.8] Christopoulos C., The Transmission-Line Modelling Method: TLM, John Wiley & Sons, Inc., 1995.

APPENDIX

A. Log-Periodic Antenna Calibration

In general, an antenna can be used to receive, as well as emit, electromagnetic radiation. An antenna which transmits most of their radiation in a particular direction is also preferentially sensitive to the radiation incident from the corresponding direction. In section 6.6.1, before the radiated field measurements were carried out, the calibration of the log-periodic antenna Model 3146 is done in a semi-anechoic chamber in order to obtain its antenna factor (AF). The AF is used by radio frequency (RF) or EMC antenna engineers to describe the required electric field strength that produces 1 Volt at the terminals of an antenna. Alternatively, the AF is defined as what the received voltage is in the presence of an electric field, given by:

$$AF = \frac{E_{incident}}{V_{received}} \quad \text{(A. 1)}$$

For the specified log-periodic antenna Model 3146, which spans from frequencies 200MHz – 1GHz, its AF characterisation is illustrated in Figure A.1.

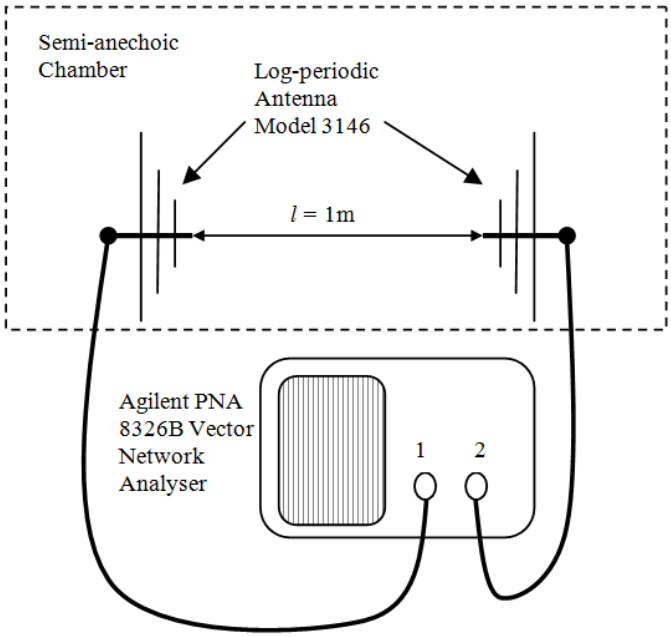

Figure A.1: The characterisation of the log-periodic antenna Model 3146

The calculation of the AF is given by (see [6.4], pp. 160):

$$|AF|_{dB} = 20\log_{10}\sqrt{\frac{1}{|S_{21}|}\frac{\eta_0}{Z_0}\frac{1}{l\lambda_0}}\ ;\ \ in\ \text{dB} \qquad \text{(A. 1)}$$

where S_{21} denotes the coupling between two antennas in dB; η_0 denotes the intrinsic impedance in free space (≈377Ω); Z_0 denotes the input impedance of the receiving antenna from the network analyser (50Ω); l denotes the separation between the two antennas, where in this case, the 1m calibration is performed. Finally, λ_0 denotes the wavelength which is given by:

$$\lambda_0 = \frac{c}{f}\ ;\ \ in\ \text{m} \qquad \text{(A. 2)}$$

where c is defined as the speed of light (≈3×10^8ms^{-1}) and f denotes the frequency.

Figure A.2 shows the comparison of the AF (in dB) values between data sheet and the calibrated data of the log-periodic antenna Model 3146, using (A.1).

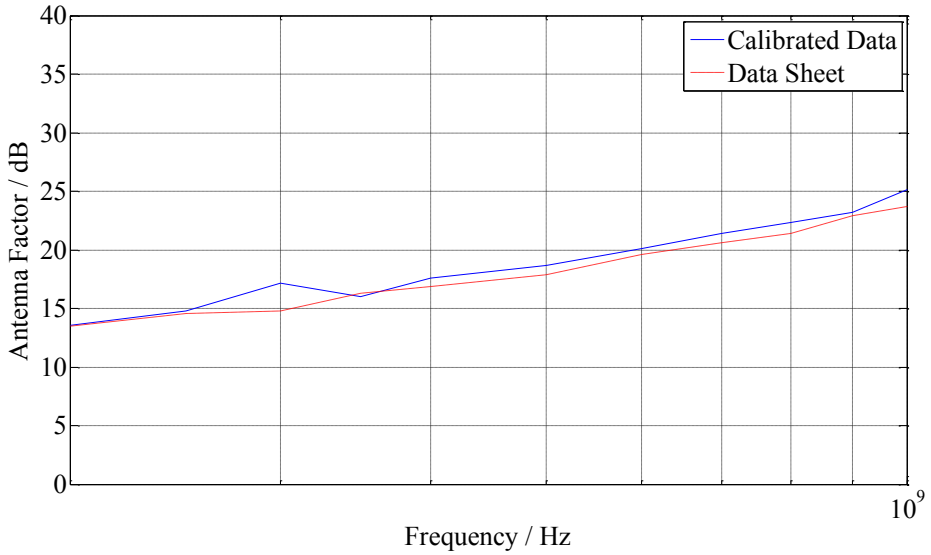

Figure A.2: Comparison of AF of the log-periodic antenna between data sheet and calibrated values

B. Current Probe Measurement

In section 6.7, a comparison between the measured and predicted current was presented. In order to measure the current flowing in the cables (DUT), a current probe was used. The specifications of the current probe used are presented in Table A.1.

Model:	Eaton Corp. Model 94111-1 948
Frequency Range:	1MHz - 1GHz

Table A.1: Specifications of the current probe used

With the same instruments and parameters in section 6.6, the antenna is replaced by the said current probe as a receiver, as illustrated in Figure B.1

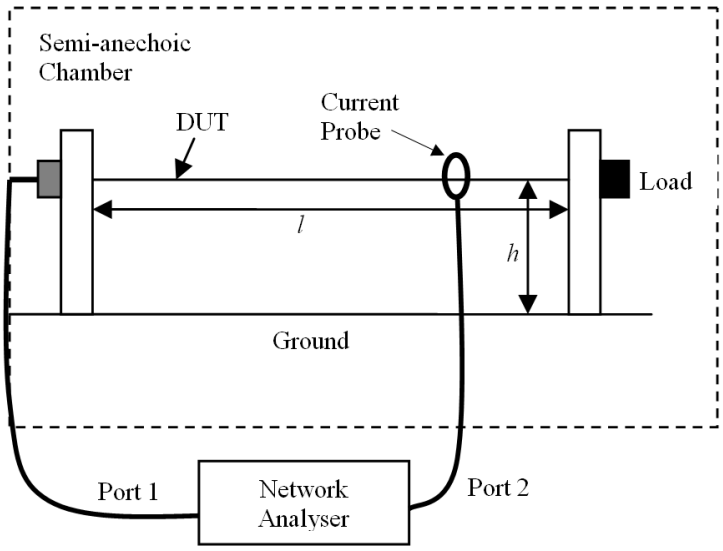

Figure B.1: Current spectra measurement using current probe

The current, I, along the DUT is calculated from the receiver reading of the current probe output in volts divided by the probe transfer impedance, Z_t. If the readings on the receiver, S_{21}, are recorded in dBμV, Z_t in dBΩ is only required to be subtracted in order to convert the readings to dBμA, as given by:

$$I_{dB\mu A} = |S_{21}|_{dB\mu V} - Z_{t\,dB\Omega} \qquad \text{(B. 1)}$$

where Z_t values can be obtained from the data sheet.

C. S_{11} Measurements of the Line-End Discontinuities

The models for the line-end discontinuities have been determined using a 6cm length and 5cm height line configuration shown in Figure C.1. An equivalent model for this structure is developed in Figure C.2, yielding two terminated capacitances to add at the line-ends. Figure C.2 also shows that the short line is represented by connecting two short nominal sections in cascade. A good approximation of the highest frequency range represented by the two cascaded nominal circuits is given by (see [6.19], pp. 185):

$$f_{max} = \frac{Nc}{\pi l} \tag{C. 1}$$

where N denotes the number of segments and l denotes the line length. The representation of this distributed effect by the equivalent lumped model in Figure C.2 is not valid above the frequency of 3.18GHz.

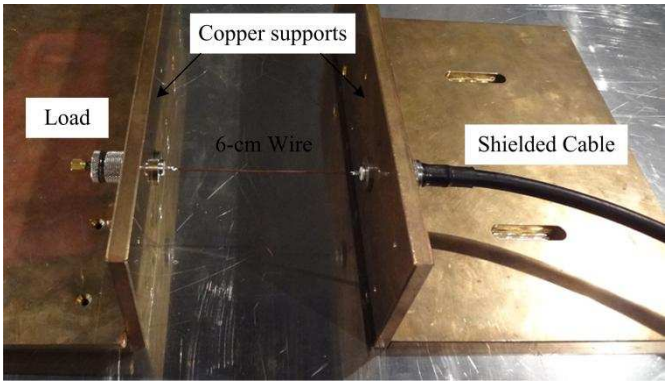

Figure C.1: Short line measurement for the line-end discontinuities characterisation

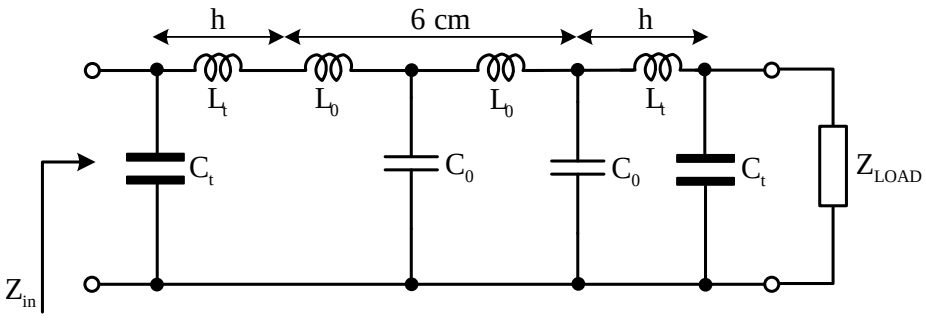

Figure C.2: Equivalent LC network for a 6cm length transmission line

An experimental characterisation, in terms of scattering parameters S_{11}, has been performed to derive the LC model of Figure C.2. It relies on the knowledge of the input impedance, Z_{in}, of the whole circuit, which is extracted from the reflection coefficient, S_{11}, parameter of the circuit obtained from a vector network analyser (VNA):

$$Z_{in} = Z_G \frac{1 + S_{11}}{1 - S_{11}} \tag{C. 2}$$

where Z_G is the nominal impedance of the VNA. The evolution of the cable impedance according to the frequency of a 6cm line length in short circuit (SC) and open circuit (OC) is represented in Figure C.3. At low frequencies, the SC impedance profile is basically inductive, while the OC impedance is capacitive.

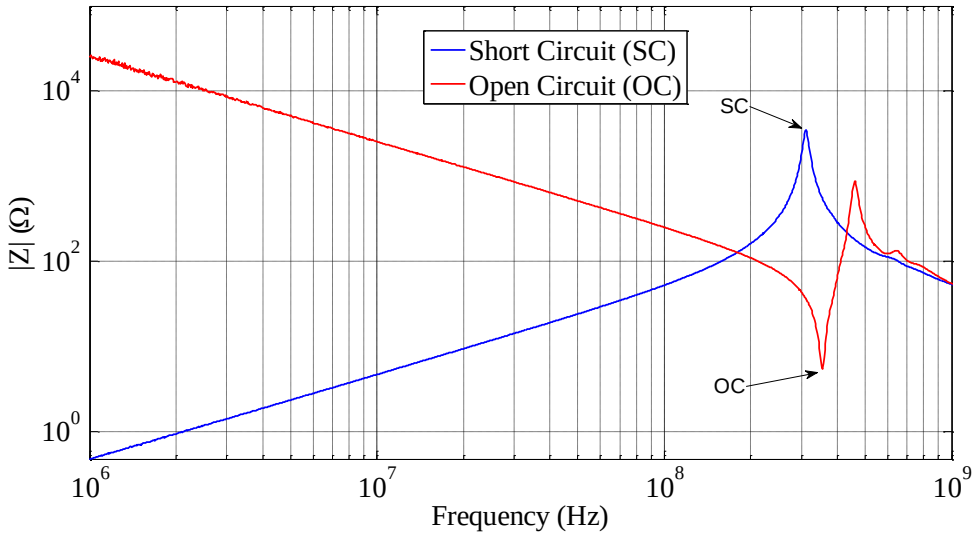

Figure C.3: Evolution of the line impedances (6cm length) comprising short circuit and open circuit configurations

From the measurement data shown in Figure C.3, the equivalent total capacitance and inductance through the impedance profile can be determined as:

$$C_{eq} = 2(C_t + C_0) = \frac{1}{\omega |Z_{in-OC}|} \tag{C. 3}$$

$$L_{eq} = 2(L_t + L_0) = \frac{|Z_{in-SC}|}{\omega} \tag{C. 4}$$

Although the total inductance and capacitance are frequency dependent, it is assumed that the values are approximately constant over the frequency range of interest at 74.75nH and 6.19pF, respectively. Finally, by solving the circuit in Figure C.2, the capacitance and inductance parameters for each segment can be computed (see [6.21], pp. 185), yielding $C_t = 2.78pF$; and $L_t = 5.57nH$, representing the capacitances and inductances for the terminations (end plates), respectively.

The results obtained through this representation are shown in Figures C.4 and C.5. The empirical model proposed by estimates approximately 1pF for the line-end transition. In fact, as shown in Figure C.5, the empirical model predicts the first resonant frequency at an estimated 570MHz, whereas the actual resonance takes place at approximately 310MHz.

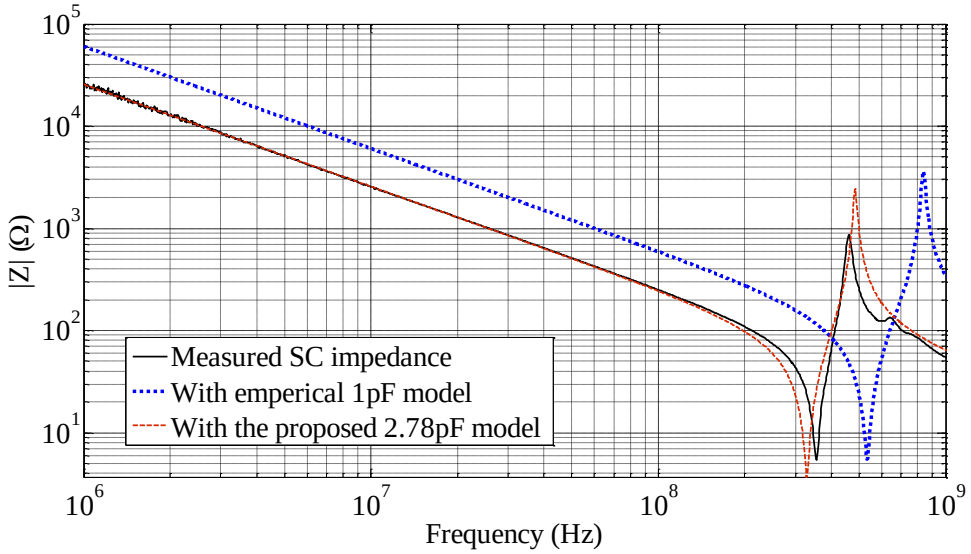

Figure C.4: Comparison of measured and simulated results of an open circuit configuration for the 6cm length wire above ground

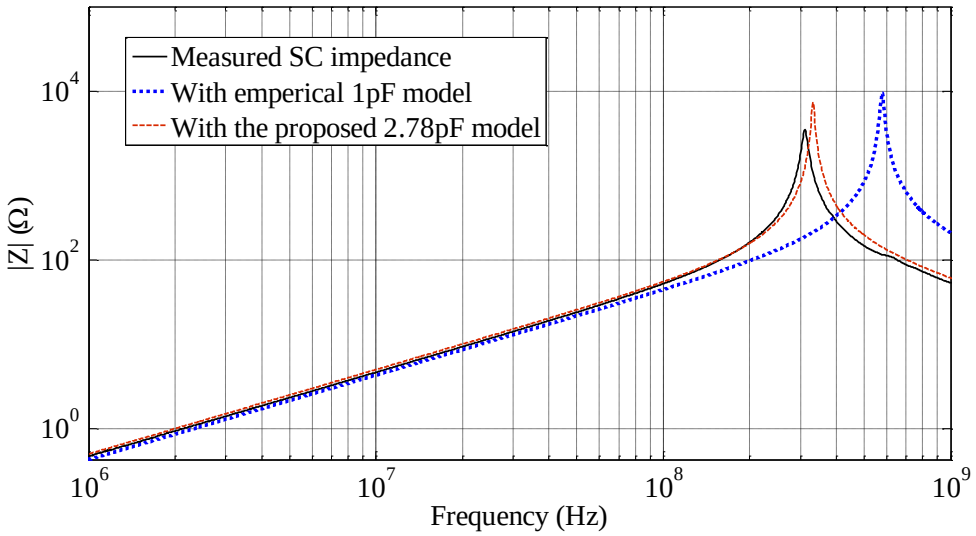

Figure C.5: Comparison of measured and simulated results of a short circuit configuration for the 6cm length wire above ground

For validation purposes, Figure C.6 plots the simulation results of a 30cm length round wire over a conducting ground plane, showing open and short circuit configurations; comparing with the experimental measurements for the same configuration shown in Figure C.1. The results obtained with this proposed model are very satisfying, providing a good description of the line-end discontinuities behaviour.

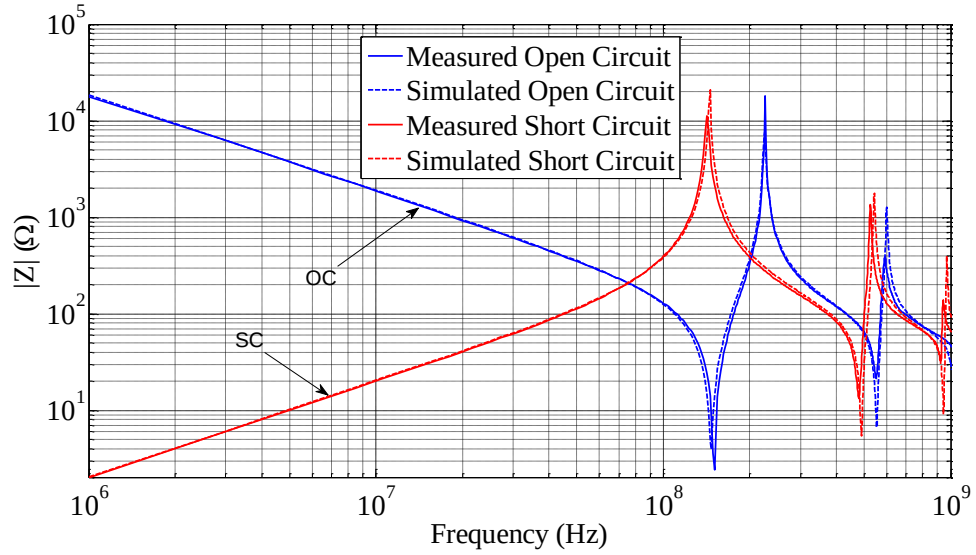

Figure C.6: Evolution of the line impedances (30cm length) comprising short circuit and open circuit configurations (comparing measured and simulated results)

D. RG-58 Coaxial Cable Parameters

RG-58 COAXIAL CABLE PROPERTIES		
Symbol	Quantity	Value
e	number of carriers	9
N	number of wires in each carrier	12
l	length	1.22m
b	hole width	0.377mm
d_r	wire diameter	0.127mm
D_m	mean braid diameter	3.27mm
D_0	outer diameter of dielectric	2.95mm
R_m	mean braid radius	1.635mm
R_b	outer radius of dielectric	1.475mm
α	braid angle	27.42°
σ	conductivity	58.82M Sm^{-1}
ε_r	relative permittivity	2.25

Table D.1: RG-58 coaxial cable properties